DISSERTATION

Simulation of Thermoelectric Devices

ausgeführt zum Zwecke der Erlangung des akademischen Grades
eines Doktors der technischen Wissenschaften

eingereicht an der Technischen Universität Wien
Fakultät für Elektrotechnik und Informationstechnik
von

Martin Wagner

[redacted]

[redacted]

Wien, im November 2007

It is unwise
to be too sure
of one's own wisdom.
It is healthy
to be reminded that
the strongest might weaken
and the wisest might err.

Mahatma Gandhi

To Lena and Jakob

Kurzfassung

THERMOELEKTRISCHE GENERATOREN sind Bauteile zur direkten Umwandlung von Wärme in elektrische Energie. Ihre herausragende Ausfallsicherheit beruhend auf einem Aufbau ohne beweglicher Teile macht sie zu attraktiven Kandidaten für eine Reihe von Anwendungen, jedoch ist die Verwendung heutiger Thermogeneratoren durch ihre niedrige Effizienz und hohe Kosten auf spezielle Nischen eingeschränkt. Die Optimierung thermoelektrischer Bauelemente für thermische und geometrische Gegebenheiten benötigt eine physikalisch basierte Simulationsumgebung. Die vorliegende Arbeit befasst sich mit der Erweiterung und Anwendung der Halbleiter–Bauelementsimulation auf thermoelektrische Strukturen.

In einem theoretischen Teil wird die Beschreibung des Ladungsträgertransports entwickelt. Modelle, die auf verschiedenen Näherungen des Streuoperators der *Boltzmann*–Gleichung beruhen werden systematisch mit Hilfe der Momentenmethode hergeleitet und mit einem phänomenologischen Zugang verglichen. Der theoretische Seebeckkoeffizient, der eine bedeutende Rolle in thermoelektrischen Bauteilen spielt, wird diskutiert und mit Messdaten verglichen.

Nachfolgend sind im materialspezifischen Teil der Arbeit wichtige Eigenschaften thermoelektrischer Materialien sowie mögliche Ansätze zur Optimierung aufgezeigt. Nach einem Überblick der wichtigsten thermoelektrischen Materialien sowie deren Eigenschaften steht Bleitellurid im Mittelpunkt des Interesses, welches ein interessantes Material für den mittleren Temperaturbereich darstellt. Weiters werden detaillierte physikalische Modelle für alle simulationsrelevanten Grössen ausgeführt.

Der praktische Teil beinhaltet Fallstudien für konventionelle Thermogeneratoren sowie für eine neuartige Diodenstruktur. Simulationsergebnisse von Strukturen basierend auf Silizium sowie Bleitellurid werden mit Messdaten verglichen, wobei exzellente Übereinstimmung erreicht wird. In einer ausführlichen Simulationsstudie werden die Einflüsse verschiedener Entwurfsparameter wie Geometrie, Materialzusammensetzung und Dotierprofil auf das Bauteilverhalten untersucht. Weiters ist das Verhalten unter nicht-idealen thermischen Umgebungsbedingungen Gegenstand der Untersuchung. Die neuartige Diodenstruktur weist eine hohe Flexibilität bei der Anpassung an vorgegebene Bedingungen auf.

Abstract

THERMOELECTRIC GENERATORS are devices for direct conversion of heat into electricity. Their outstanding reliability due to the lack of moving parts makes them attractive candidates for a series of applications. However, today's thermoelectric devices are limited by their low efficiency and high costs. Thus, their operation is restricted to highly specialized niches. Optimization of thermoelectric devices to given thermal and geometrical constraints depends on a physics–based simulation framework. This work focuses on the extension and application of semiconductor device simulation, which is a well established tool in mainstream microelectronics to thermoelectrics.

In the theoretical part, proper transport description for thermoelectric devices is developed. Models based on different approximations of the scattering operator within *Boltzmann*'s equation are systematically derived by the method of moments and compared to a phenomenological approach based on the principles of irreversible thermodynamics. Models for the *Seebeck* coefficient, which play a major role in thermoelectric devices are discussed and compared to measurement data.

A material related part highlights important properties of thermoelectric materials as well as mechanisms for possible optimization. After an overview of the most important thermoelectric materials and their attributes, the focus is put on lead telluride, which serves as a thermoelectric material in the intermediate temperature range. A detailed discussion on the physical modeling of several simulation–relevant material properties is carried out.

The practical part incorporates case studies of both conventional thermoelectric devices as well as a novel structure containing a large scale pn–junction. Simulation results for both silicon and lead telluride structures are compared to measurement data, whereby excellent agreement is achieved. In a detailed simulation study, the influences of several design parameters like geometry, material composition, and doping profiles on the device performance of thermoelectric generators are assessed. Furthermore, the device behavior is discussed within non–ideal thermal environments. The novel structure incorporating a large scale pn–junction turns out to be highly adaptable to given environmental conditions.

Acknowledgment

FIRST AND FOREMOST I want to thank my adviser *Prof. Tibor Grasser* for opening the floodgates to the world of microelectronics and giving me the opportunity to join his research group. He did not get tired of motivating me to work at the Institute for Microelectronics for several projects over the years, whereby he only failed once temporarily when I left for the Himalayas. He impressed me not only with his persistent way of solving scientific problems but also with his widely diversified talents from social capabilities to playing the piano in an amazing manner. Sometimes, I envy him for the length of his days, which must be 48 hours at least...

I thank *Prof. Emmerich Bertagnolli* for serving on my examination committee. Furthermore, I am indebted to *Prof. Siegfried Selberherr* for the excellent working conditions, the opportunity to attend several scientific conferences, and not at last the calm working climate at the Institute, which serves as a basis for world–class scientific work. I also thank *Prof. Erasmus Langer*, the head of the Institute for Microelectronics, who delighted long working days with his sarcastic comments regularly. *Prof. Hans Kosina* impressed me with his deep theoretical knowledge as well as his ability to pass it on. He always found the time to answer my questions, even during the most hectic days.

Gerhard Span provided me with the industrial background of my work as well as the confidence to represent him at two conferences on short notice. It was always a pleasure to collaborate in an uncomplicated and productive way.

The history of my roommates at the Institute is not too short. *Johannes Mesa* introduced me to the Institute and was always open for discussions. His regular phone calls to the western parts of Austria considerably extended my vocabulary. At the same time, we shared our room with *Mahdi Pourfath*, whom I thank for occasional cultural discussions. He impressed me with a phenomenal diligence and endless working hours. Later, *Martin Vasicek* joined our room, who accompanied me on an essential part of my theoretical derivations and soon became a good friend. Special thank goes to him for uncountable discussions on semiconductor physics, computer problems, our fatherhood, or just the source of our daily lunch. The last year, *Wolfgang Gös* shared our room, whom I have never seen in a bad temper.

I want to thank the proofreaders of this thesis, who greatly improved this work by their numerous suggestions. *Enzo Ungersböck* supported me on several issues on Monte Carlo simulations. His deep physical background and programming skills combined with his calm nature and modesty made him a good colleague and friend. The man behind his tie, *Stefan Holzer* proved to solve even the trickiest optimization tasks with just the adaption of one or two short scripts. I remember *Vassil Palankovski* for his elaborate knowledge on hetero–structure devices as well as his ingenious tactics on research and publication, who was one of the Institute's biggest coffee sinks. I do not remember even one weekend at the office, when he was not also there.

I had the pleasure to attend numerous conferences on three continents with a couple of colleagues. *Siddhartha Dhar* accompanied me to India and the USA, whereby interestingly his navigational skills where developed far better in New York than in his hometown, Delhi. My fascination for his homeland and his openness served as a basis for a good friendship. The outcome of a trip to Mexico together with *Gerhard (Monte–)Karlowatz* was an impressive number of high–quality photographs. The attendance of a summer school in Grenoble together with *Philipp Schwaha* and *Oliver Triebl* as well as a conference in Nice together with *Alexandre Nentchev* opened essential insights to the French cuisine.

Probably the Institute's most successful "hacker" was *Johann Cervenka*. His disrespect for complicated code constructs within MINIMOS-NT has turned out to be very useful on several occasions. Besides his support in many cases, I want to thank him and all other colleagues who spent plenty of their leisure time on the professional administration of the computer network. Special acknowledgment goes to *Robert Entner* for infecting me with a deep devotion for Linux.

Markus Karner proved to host brilliant ideas below his amazing tailwind haircut. His immortal optimism was one of the cornerstones for the software projects we collaborated on, whose quality has been ensured by one of the most destructive software testers I know, *Oskar Baumgartner*.

My namesake *Paul–Jürgen Wagner* not only amused me with his humorous comments, but also had an open ear for countless questions regarding the typesetting system LaTeX. Whenever I got stuck in some theoretical questions, *Viktor Sverdlov* had the right Russian book and some helpful translations for me. *Andreas Gehring* and *Wilfried Wessner* were always good conversation partners whenever my inner motor requested some motivation refill.

If I had the right to, I would award *Gregor Meller* as the Institute's universal genius. There was not a single topic he could not handle in a well–founding presentation of at least 15 minutes immediately.

Manfred Katterbauer, *Ewald* and *Christoph Haslinger*, and *Renate Winkler* took care of the administrative work at the Institute, which is much too often totally undervalued. Thank goes to all former members of the Institute for Microelectronics for leaving a precious heritage for all coming generations and to all other colleagues for their assistance and the stimulating working atmosphere they created.

Above all, I want to thank my family. My parents made possible all of my studies by their continuous support, which they gave as a matter of course. Obviously, my father's recommendation not to come after his profession was not fruitful... While my mother–in–law *Elfi* assisted me with countless little things she handled, *Peter* detached me from my laptop from time to time in order to remind me of the beauty of our neighborhood. More than any other support, my better half *Lena* provided me with love and understanding for endless working days. She encouraged and assisted me whenever possible. Only she knows how much I am indebted to her. And of course there is *Jakob*, most probably the best achievement of my life!

Contents

List of Symbols

Notation

x . . . Scalar
$\boldsymbol{x}$ . . . Vector
$\underline{A}$ . . . Matrix
A_{ij} . . . Elements of the matrix $\underline{A}$
$\mathrm{tr}\,(\underline{A})$ . . . Trace of the matrix $\underline{A}$
$\hat{\mathrm{X}}$ . . . Tensor

$\boldsymbol{x} \cdot \boldsymbol{y}$ . . . Scalar (in) product
$\boldsymbol{x} \times \boldsymbol{y}$ . . . Vector (ex) product
$\boldsymbol{x} \otimes \boldsymbol{y}$ . . . Tensor product

$\partial_t(\cdot)$ . . . Partial derivative with respect to t
∇ . . . Nabla operator
∇x . . . Gradient of x
$\nabla \cdot \boldsymbol{x}$ . . . Divergence of $\boldsymbol{x}$

$\langle\!\langle \cdot \rangle\!\rangle$ . . . Statistical average
$\langle \cdot \rangle$ . . . Normalized statistical average

$\Gamma(\cdot)$ . . . Gamma function
$f(\mathbf{r}, \mathbf{k}, t)$ . . . Distribution function
$\mathcal{Q}(\cdot)$ . . . Collision operator
$\mathcal{H}$ . . . *Hamilton*ian operator
s_ν . . . Carrier charge sign

$\{\cdot, \cdot\}$ . . . *Poisson* bracket

Physical Quantities

Symbol	Unit	Description
α	$\mathrm{VK^{-1}}$	*Seebeck* coefficient
ϵ	$\mathrm{AsV^{-1}m^{-1}}$	Dielectric permittivity
ϵ_r	1	Relative dielectric permittivity
ϵ_s	1	Relative low frequency dielectric permittivity
ϵ_∞	1	Relative high frequency dielectric permittivity
$\mathcal{E}$	eV	Energy
$\mathcal{E}_0$	eV	Reference energy
$\mathcal{E}_\mathrm{c}$	eV	Conduction band edge energy
$\Delta\mathcal{E}_\mathrm{c}$	eV	Conduction band edge narrowing
$\mathcal{E}_\mathrm{f}$	eV	*Fermi* energy
$\mathcal{E}_\mathrm{g}$	eV	Band gap energy
$\mathcal{E}_\mathrm{T}$	eV	Trap energy
$\mathcal{E}_\mathrm{v}$	eV	Valence band edge energy
$\Delta\mathcal{E}_\mathrm{v}$	eV	Valence band edge narrowing
κ	$\mathrm{WK^{-1}m^{-1}}$	Thermal conductivity
κ_ν	$\mathrm{WK^{-1}m^{-1}}$	Carrier contribution to thermal conductivity
κ_L	$\mathrm{WK^{-1}m^{-1}}$	Lattice contribution to thermal conductivity
κ_n	$\mathrm{WK^{-1}m^{-1}}$	Electron contribution to thermal conductivity
κ_p	$\mathrm{WK^{-1}m^{-1}}$	Hole contribution to thermal conductivity
η	1	Conversion efficiency
μ_ν	$\mathrm{m^2V^{-1}s^{-1}}$	Carrier mobility
μ_n	$\mathrm{m^2V^{-1}s^{-1}}$	Electron mobility
μ_p	$\mathrm{m^2V^{-1}s^{-1}}$	Hole mobility
μ_ν^u	$\mathrm{m^2V^{-1}s^{-1}}$	Energy flux mobility
μ_n^u	$\mathrm{m^2V^{-1}s^{-1}}$	Electron energy flux mobility
μ_p^u	$\mathrm{m^2V^{-1}s^{-1}}$	Hole energy flux mobility
ν	$\mathrm{m^{-3}}$	Carrier concentration
π	V	*Peltier* coefficient
ρ	$\mathrm{kg\ m^{-3}}$	Mass density
σ	$\mathrm{AV^{-1}m^{-1}}$	Electric conductivity
τ_0	s	Relaxation time constant in power law approximation
$\tau_\mathcal{E}$	s	Energy dependent microscopic relaxation time
$\tau_{\boldsymbol{j}}$	s	Macroscopic particle flux relaxation time
$\tau_{\boldsymbol{u}}$	s	Macroscopic energy flux relaxation time
τ_x	s	Relaxation time of quantity x
φ	V	Electrostatic potential
$\tilde{\varphi}$	V	Effective electrostatic potential
Φ_ν	V	Electrochemical potential

Φ_n	V	Electrochemical potential of electrons
Φ_p	V	Electrochemical potential of holes
Φ_ν^{c}	V	Chemical potential
c_{L}	$\mathrm{JK^{-1}m^{-3}}$	Lattice heat capacity
c_n	$\mathrm{JK^{-1}m^{-3}}$	Heat capacity of the electron subsystem
c_p	$\mathrm{JK^{-1}m^{-3}}$	Heat capacity of the hole subsystem
c_{tot}	$\mathrm{JK^{-1}m^{-3}}$	Total heat capacity
$\boldsymbol{F}$	N	Force vector
G	$\mathrm{s^{-1}}$	Net carrier generation rate
H	$\mathrm{Wm^{-3}}$	Heat source density
$\boldsymbol{J}$	$\mathrm{s^{-1}}$	Particle flux vector
$\boldsymbol{J}^{\mathrm{q}}$	$\mathrm{Js^{-1}}$	Heat flux vector
$\boldsymbol{j}$	$\mathrm{m^{-2}s^{-1}}$	Flux density vector
$\boldsymbol{j}_\nu$	$\mathrm{m^{-2}s^{-1}}$	Particle flux density vector
$\boldsymbol{j}_n$	$\mathrm{m^{-2}s^{-1}}$	Electron flux density vector
$\boldsymbol{j}_p$	$\mathrm{m^{-2}s^{-1}}$	Hole flux density vector
$\boldsymbol{j}_\nu^{\mathrm{q}}$	$\mathrm{Jm^{-2}s^{-1}}$	Heat flux density vector
$\boldsymbol{j}_n^{\mathrm{q}}$	$\mathrm{Jm^{-2}s^{-1}}$	Heat flux density vector of the electron subsystem
$\boldsymbol{j}_p^{\mathrm{q}}$	$\mathrm{Jm^{-2}s^{-1}}$	Heat flux density vector of the hole subsystem
$\boldsymbol{j}_\nu^{\mathrm{u}}$	$\mathrm{Jm^{-2}s^{-1}}$	Energy flux density vector
$\boldsymbol{j}_n^{\mathrm{u}}$	$\mathrm{Jm^{-2}s^{-1}}$	Electron energy flux density vector
$\boldsymbol{j}_p^{\mathrm{u}}$	$\mathrm{Jm^{-2}s^{-1}}$	Hole energy flux density vector
$\boldsymbol{J}^{\mathrm{q}}$	$\mathrm{Js^{-1}}$	Heat flux vector
$\boldsymbol{k}$	$\mathrm{m^{-1}}$	Wave number vector
m^*	kg	Density of states effective mass
m_{t}^*	kg	Transversal effective mass
m_{l}^*	kg	Longitudinal effective mass
m_{c}^*	kg	Density of states effective mass of the conduction band
m_{v}^*	kg	Density of states effective mass of the valence band
$m_{\mathrm{c,l}}^*$	kg	Longitudinal effective mass of the conduction band
$m_{\mathrm{v,l}}^*$	kg	Longitudinal effective mass of the valence band
$m_{\mathrm{c,t}}^*$	kg	Transversal effective mass of the conduction band
$m_{\mathrm{v,t}}^*$	kg	Transversal effective mass of the valence band
$M_{\mathrm{c,v}}$	1	Valley multiplicity
n	$\mathrm{m^{-3}}$	Electron density
n_{i}	$\mathrm{m^{-3}}$	Intrinsic carrier concentration
N_A	$\mathrm{m^{-3}}$	Concentration of acceptors
N_{c}	$\mathrm{m^{-3}}$	Effective density of states in the conduction band
N_D	$\mathrm{m^{-3}}$	Concentration of donors
N_{T}	$\mathrm{m^{-3}}$	Trap density
N_{tot}	$\mathrm{m^{-3}}$	Total dopant concentration
N_{v}	$\mathrm{m^{-3}}$	Effective density of states in the valence band
p	$\mathrm{m^{-3}}$	Hole density

$\boldsymbol{p}$	kg ms^{-1}	Pulse vector
P_{el}	W	Electric power
Q	J	Heat
$\boldsymbol{r}$	m	Space vector
r_ν	1	Scattering parameter
r_n	1	Scattering parameter for electrons
r_p	1	Scattering parameter for holes
R	s^{-1}	Net carrier recombination rate
R_{l}	VA^{-1}	Load resistance
R_{i}	VA^{-1}	Inner resistance
R_{th}	KW^{-1}	Thermal resistance
S	JK^{-1}	Entropy
t	s	Time
T	K	Temperature
T_ν	K	Carrier temperature
T_{C}	K	Temperature at the cooled end of a thermoelectric device
T_{H}	K	Temperature at the heated end of a thermoelectric device
T_{L}	K	Lattice temperature
T_n	K	Electron temperature
T_p	K	Hole temperature
U	V	Voltage
U_{c}	V	Contact voltage
v	ms^{-1}	Velocity
$\boldsymbol{v}$	ms^{-1}	Velocity vector
v_{s}	ms^{-1}	Average sound velocity
v_{st}	ms^{-1}	Transversal sound velocity
v_{sl}	ms^{-1}	Longitudinal sound velocity
w	Jm^{-3}	Energy density
X	1	Microscopic density
X_0	1	Microscopic density in equilibrium
x	m^{-3}	Macroscopic density
Z	K^{-1}	Thermoelectric figure of merit

Constants

h	...	*Planck*'s constant,	$6.6260755 \times 10^{-34}\,\mathrm{J\,s}$
$\hbar$	...	Reduced *Planck*'s constant,	$\mathrm{h}/(2\,\pi)$
k_{B}	...	*Boltzmann*'s constant,	$1.3806503 \times 10^{-23}\,\mathrm{JK}^{-1}$
q	...	Elementary charge,	$1.6021892 \times 10^{-19}\,\mathrm{C}$
m_0^*	...	Electron rest mass,	$9.1093897 \times 10^{-31}\,\mathrm{kg}$
ϵ_0	...	Vacuum permittivity,	$8.8541878 \times 10^{-12}\,\mathrm{Fm}^{-1}$

List of Figures

List of Tables

'The best way to predict the future is to invent it.'
Alan Kay

Chapter 1

Introduction

AVAILABILITY OF ENERGY is an important cornerstone for wealth and social stability. The continuous economical growth in the last two centuries went hand in hand with a steady growth of energy demand in the industrial, public, and private sector. While very early facilities had to deal with locally available energy sources, the beginning of the oil era with the vision of apparently unlimited resources has brought an immense impact on industry, culture, lifestyle, but also environment. These days, the end of fossil fuels as the major energy source for the civilization in its current way is foreseeable, and environmental concerns have become topics of international political discussions and daily news.

In the last decades, uprising efforts in science and engineering to increase fuel efficiency was by far not able to compensate economical growth in order to at least keep the consumption of limited fossil reserves on a constant level. The current scenario incorporates increasing energy demand facing short running resources, which implies the need for tremendous efforts on an exit strategy. While the awareness about the worth of our energy supply has to generally increase, a new consciousness of consumption has to gain impact on the international markets. Politics has to honestly deal with the problem in a holistic point of view and provide the background for the right measures.

The role of science and engineering to develop technologies for providing electric energy from renewable sources on a broad basis incorporates an immense responsibility for environment, living space, wealth, and security for the next generations. Therefore, ecological, economical, and social considerations have to enter engineering processes beside technical excellence. On the one hand, decentralized power facilities based on renewable resources will play a significant role in the future. On the other hand, the potentials of improvement in efficiency has to be exhausted in a wide range of applications. Therefore, both existing technologies have to be further developed as well as new innovative and unconventional ideas have to enter well established solutions. Besides the power consumption optimization of single devices and components, interdisciplinary research has to combine single optimization potentials by system wide considerations to intelligent global solutions.

Thermoelectric energy conversion is one of the technologies with a potential to play a role in future energy technology. It incorporates the direct energy conversion from temperature gradients to electric energy, whereby the fundamental existence of its underlying physical effect has been well known for almost two centuries. However, in spite of ongoing efforts, their low conversion efficiency currently limits the application of thermoelectric devices to a few highly specialized niches. In the last decades, tremendous efforts on material research has provided both novel materials for thermoelectric energy conversion as well as a principle understanding of the demands for higher efficiencies. Thus, a directed search for according materials has been made possible. Furthermore, recent developments in nanotechnology and low dimensional systems include promising potentials for increased efficiencies.

The contribution of this thesis is a fruitful extension and application of semiconductor device simulation to thermoelectric devices. Technology Computer Aided Design (TCAD) has been established as an important tool to shorten development cycles in mainstream microelectronics. Based on a physically rigorous framework, it incorporates the possibility of device investigations by elaborate simulation studies as well as the optimization of several device parameters for given constraints.

Chapter 2 starts with an overview of important milestones in the history of thermoelectrics. Furthermore, the three thermoelectric effects as well as their relationships are discussed on a phenomenological basis. A glimpse on current as well as potential future applications accomplishes this chapter.

The focus of **Chapter 3** is directed to the proper description of electrical transport in semiconductors. After a delimitation within the hierarchy of physical simulation approaches, the fundamentals of macroscopic transport models are sketched. The main part incorporates the systematic derivation of macroscopic transport models from *Boltzmann*'s equation by the method of moments. Thereby, different approximations of the scattering operator are investigated and the resulting equations are summarized in a final comparison. Based on the equations of up to the third moment, a transport model is formulated assuming local thermal equilibrium. The compatibility of this model with the principles of phenomenological irreversible thermodynamics is demonstrated. Special attention is payed to the *Seebeck* coefficient by a comparison of measurement data with its theoretical formulation inherently contained in the transport model.

Chapter 4 is devoted to materials for thermoelectric energy conversion. Based on the thermoelectric figure of merit, the influence of single material properties on device characteristics are investigated and possibilities for performance optimization are discussed. In addition, relevant parameters of the three most important material classes for thermoelectric applications are presented. Besides silicon–germanium alloys, the material systems of lead telluride and bismuth telluride are briefly introduced.

In **Chapter 5**, the material properties of lead telluride are collected. Thereby, special attention is drawn to the temperature dependence of several physical quantities. One of its ternary alloys, lead tin telluride is used to highlight interesting aspects of the physical behavior. Models of all relevant parameters for device simulation are formulated based on comprehensive measurement data available in literature as well as theoretical considerations.

Finally, **Chapter 6** contains case studies of both classical thermoelectric devices and a novel structure incorporating a large scale pn-junction. The influences of several design parameters on device behavior are assessed in elaborate simulation studies. Results for both silicon and lead telluride devices are compared to measurement data, whereby excellent agreement is achieved. Furthermore, the influence of non-ideal thermal environments on device performance are discussed. **Chapter 7** gives some closing remarks.

'Any sufficiently advanced technology is indistinguishable from magic.'

Arthur C. Clarke

Chapter 2

Fundamentals of Thermoelectric Devices

THE HISTORY OF THERMOELECTRIC DEVICES began back in 1821, when *Seebeck* discovered the deviation of a compass needle when keeping the two junctions of different metals at different temperatures [1]. Today's understanding of his discovery, the formation of a potential difference due to the temperature slope, which further causes an electric current was named after his discoverer, the *Seebeck* effect. Thirteen years later, *Peltier* observed that an electrical current driven through a junction of two different metals causes a temperature change at the junction [2]. However, it took until 1838 to discover an important property of *Peltier*'s experiment, when *Lenz* realized, that both material combination and current direction control if the junction is heated or cooled [3]. This behavior is known today as the *Peltier* effect. The theoretical explanation as well as the connection between the *Seebeck* and the *Peltier* effect has been performed by *Thomson* (later Lord *Kelvin*) within the framework of thermodynamics in 1851 [4]. Furthermore, he predicted the third thermoelectric effect, later named *Thomson* effect.

An important foundation for the theory of thermoelectric materials was built by *Altenkirch* [5,6]. He concluded that high quality thermoelectric materials are characterized by high *Seebeck* coefficients and electrical conductivities, while thermal conductivities should be low. Based on this attributes, the thermoelectric figure of merit has been formulated later, which became an important cornerstone of the systematic search for novel thermoelectric materials. Due to the availability of first artificially manufactured semiconductors, *Ioffe* intensified the research on semiconductor based thermoelectric devices in the mid of the last century and formulated the basis of modern thermoelectric theory [7,8]. The efficiency of thermoelectric generators could be raised to about 5 % due to the favorable material properties of semiconductors compared to metals.

Intense material research in the sequel lead to the successive discovery of materials with increasing thermoelectric figures of merit suitable for several temperature ranges. Independent of the materials used, the basic structure of thermoelectric generators has been established as a combination of n–type and p–type semiconductor rods, which are arranged thermally parallel and electrically serial. In the following, this chapter gives an overview about the thermodynamic foundation as well as today's and possible future applications.

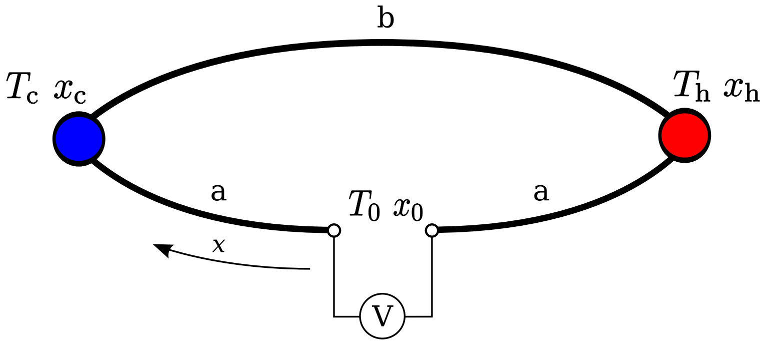

Figure 2.1: Thermocouple made of two metal rods.

2.1 Thermoelectric Phenomena

In the following section, the three thermoelectric phenomena are described in the order of their discovery. These effects build a phenomenological cornerstone for the description of thermoelectric materials as well as the functioning basis for several thermoelectric devices and applications.

2.1.1 *Seebeck* Effect

Named after his discoverer, the *Seebeck* effect describes the occurrence of an electrical voltage induced by a temperature gradient. While the theoretical interpretation in *Seebeck*'s pioneering paper [1] is surpassed by his general discovery by far, he also gave an overview of several material combinations usable in thermocouples as illustrated in Fig. 2.1.

Two rods of different materials are soldered together and the soldered points are held at the temperatures T_H and T_C, respectively maintaining a temperature difference ΔT and thus an according temperature gradient along the rods. On device level, the given temperature difference causes a certain voltage measured at the device's contacts

$$U_\mathrm{Seebeck} \propto \Delta T\,. \tag{2.1}$$

In contrast to the frequently occurring idea in literature, that the *Seebeck* effect is based on the temperature dependence of the contact potential, the reason has to be looked for inside the device. Having a closer look on the microscopic description, the definition of the *Seebeck* coefficient is obtained by approaching infinitesimal small temperature differences. Then, a local potential gradient is caused by an according temperature gradient, which are connected by the temperature dependent *Seebeck* coefficient. Thus, the definition of the *Seebeck* coefficient reads

$$\alpha(T) = \lim_{\Delta T \to 0} \frac{\Delta U}{\Delta T} \tag{2.2}$$

The total voltage measured at the ends of one rod is given by the path integral along the rod as

$$U_\mathrm{Seebeck} = \varphi_2 - \varphi_1 = \int\limits_{x_1}^{x_2} \partial_x \varphi \,\mathrm{d}x = \int\limits_{x_1}^{x_2} \alpha(T)\partial_x T \,\mathrm{d}x = \int\limits_{T_1}^{T_2} \alpha(T)\partial_x T \,\mathrm{d}T\,. \tag{2.3}$$

For the entire device, the path integral around the rods has to be evaluated. Beside the two constitutions of the single rods, the according contact potentials at the soldered points have to be added. However, the contact potentials cancel out each other and thus the voltage is given by

$$U_{\mathrm{Seebeck}} = \int_{T_0}^{T_c} \alpha_{\mathrm{a}}(T)\partial_x T \,\mathrm{d}T + \int_{T_{\mathrm{C}}}^{T_{\mathrm{H}}} \alpha_{\mathrm{b}}(T)\partial_x T \,\mathrm{d}T + \int_{T_{\mathrm{H}}}^{T_0} \alpha_{\mathrm{a}}(T)\partial_x T \,\mathrm{d}T\,. \tag{2.4}$$

By averaging the temperature dependent *Seebeck* coefficients along the rods, a combined coefficient for the material couple under given thermal conditions can be given as the difference of the single constituents of each rod

$$U_{\mathrm{Seebeck}} = (\bar{\alpha}_{\mathrm{b}} - \bar{\alpha}_{\mathrm{a}}) \int_{T_{\mathrm{C}}}^{T_{\mathrm{H}}} \partial_x T \,\mathrm{d}T = (\bar{\alpha}_{\mathrm{b}} - \bar{\alpha}_{\mathrm{a}})\,\Delta T\,. \tag{2.5}$$

Normally, two materials with *Seebeck* coefficients of different signs are chosen in order to gain an accordingly large voltage.

While the *Seebeck* coefficient of most metals is in the range of 1–10 μV/K, values of 1 mV/K and more are obtained with semiconductors. Both metals with positive and negative *Seebeck* coefficients exist. The choice of according material combinations depends on the intention of use. For example in measurement applications, high total *Seebeck* coefficients are less important than a linear behavior in the desired temperature range. In semiconductors, the *Seebeck* coefficient can be varied by appropriate doping. While n–type semiconductors have negative *Seebeck* coefficients, the ones of p–type materials are positive. Quantitative values obtained in semiconductors can be obtained by analysis of carrier transport. Based on *Boltzmann*'s equation, expressions for the coefficients are derived throughout Chapter 3.

2.1.2 *Peltier* Effect

To some extent, the *Peltier* effect describes the phenomenologically reverse effect of the *Seebeck* effect. However, the physical effect is different, since the *Peltier* effect is only present at the presence of an electric current, while the *Seebeck* effect also causes a voltage at open circuit conditions. An electrical current driven through two connected rods causes a temperature difference between the two soldered points. Accordingly, heat is absorbed and rejected, respectively and thus a heat flux throughout the rods is induced. The heat flux at the junctions can be understood by considering energy conservation within the junction and a change of the total energy of the carriers when passing the junction.

The heat flux throughout the rods depends on the charge current as well as the *Peltier* coefficient and is given by

$$\boldsymbol{J}^{\mathrm{q}}_{\mathrm{Peltier}} = \pi_{\mathrm{ab}}\mathrm{q}\boldsymbol{J} \tag{2.6}$$

where the *Peltier* coefficient of a junction π_{ab} is defined by the difference of the coefficients of the constituent materials $\pi_{\mathrm{ab}} = \pi_{\mathrm{a}} - \pi_{\mathrm{b}}$. The direction of heat flow at a junction is thus defined by the choice of materials as well as the direction of the passing current. Furthermore, the *Peltier* coefficients are temperature dependent, just as the *Seebeck* coefficients.

Peltier coefficient and *Seebeck* coefficient are not independent of each other. From both a systematic approach using the method of moments as carried out in Chapter 3 as well as phenomenological thermodynamics (first *Kelvin* relation) [9], it follows that

$$\pi_{\mathrm{ab}} = \alpha_{\mathrm{ab}} T \,. \tag{2.7}$$

2.1.3 *Thomson* Effect

Beside the *Seebeck* and *Peltier* effect, *Thomson* (later Lord *Kelvin*) observed the third thermoelectric effect. Assuming a homogeneous conductor with a temperature gradient applied, carriers traversing the temperature gradient gain or release energy depending on their relative direction to the temperature gradient. Applying local energy balance, the energy change of the traversing carriers is absorbed or released as heat, respectively. The total *Thomson* heat absorbed or released along one rod is given by

$$J^{\mathrm{q}}_{\mathrm{Thomson}} = \int\limits_{T_{\mathrm{C}}}^{T_{\mathrm{H}}} \chi(T) J \,\mathrm{d}T \tag{2.8}$$

where $\chi(T)$ depicts the temperature dependent *Thomson* coefficient. *Thomson* and *Seebeck* coefficient are connected by the second *Kelvin* relation

$$\chi = T \frac{\mathrm{d}\alpha}{\mathrm{d}T} \tag{2.9}$$

as carried out in the following section.

2.1.4 Thermodynamic Relations

As already indicated, the three thermoelectric effects are not independent from each other and thus the according coefficients are related. In the sequel, these relations are discussed on the basis of fundamental thermodynamics [9–11].

While all three effects describe reversible phenomena, further two irreversible processes occur within the structure. First, each electrical current causes the dissipation of *Joule* heat when passing a material with a certain electrical resistance. Second, heat is conducted within the device as described by *Fourier*'s law.

In the following derivations, the device illustrated in Fig. 2.1 is considered as electrically short–circuited for the sake of brevity. Thus, no external electric voltage is induced and no electric power is dissipated. Furthermore, the cold and the hot contact are connected to thermal reservoirs. Energy losses by *Joule* heating are very small and can be safely neglected. Considering all three thermoelectric effects, the application of total energy conservation within the entire device including the reservoirs for a closed loop reads

$$\underbrace{J\alpha_{\mathrm{ab}}\Delta T}_{\text{Seebeck}} = \underbrace{J\pi_{\mathrm{ab}}(T_{\mathrm{H}}) - J\pi_{\mathrm{ab}}(T_{\mathrm{C}})}_{\text{Peltier}} + \underbrace{J\int\limits_{T_{\mathrm{C}}}^{T_{\mathrm{H}}}\chi_{\mathrm{b}}\,\mathrm{d}T - J\int\limits_{T_{\mathrm{C}}}^{T_{\mathrm{H}}}\chi_{\mathrm{a}}\,\mathrm{d}T}_{\text{Thomson}}\,. \tag{2.10}$$

There, the *Seebeck* effect maintains a driving force causing a current running throughout the device. This current itself induces the *Peltier* effect as well as the *Thomson* effect. Introducing the temperature difference ΔT as $T_{\mathrm{H}} - T_{\mathrm{C}}$ and dividing (2.10) by ΔT as well as J results in

$$\alpha_{\mathrm{ab}} = \frac{\pi_{\mathrm{ab}}(T_{\mathrm{C}}+\Delta T) - \pi_{\mathrm{ab}}(T_{\mathrm{C}})}{\Delta T} + \frac{1}{\Delta T}\left(\int\limits_{T_{\mathrm{C}}}^{T_{\mathrm{C}}+\Delta T}\chi_{\mathrm{b}}\,\mathrm{d}T - \int\limits_{T_{\mathrm{C}}}^{T_{\mathrm{C}}+\Delta T}\chi_{\mathrm{a}}\,\mathrm{d}T\right)\,. \tag{2.11}$$

Letting ΔT approach zero, the energy relation between the three effects is obtained

$$\alpha_{\mathrm{ab}} = \frac{\mathrm{d}\pi_{\mathrm{ab}}}{\mathrm{d}T} + \chi_{\mathrm{b}} - \chi_{\mathrm{a}}\,. \tag{2.12}$$

Next, the net change of entropy of the entire structure including the heat reservoirs can be assumed to be zero due to the neglect of irreversible processes. Accordingly, contributions from all three effects cancel

$$\Delta S = -J\frac{\pi_{\mathrm{ab}}(T_{\mathrm{C}}+\Delta T)}{T_{\mathrm{C}}+\Delta T} + J\frac{\pi_{\mathrm{ab}}(T_{\mathrm{C}})}{T_{\mathrm{C}}} - J\int\limits_{T_{\mathrm{C}}}^{T_{\mathrm{H}}}\frac{\chi_{\mathrm{b}}}{T}\,\mathrm{d}T + J\int\limits_{T_{\mathrm{C}}}^{T_{\mathrm{H}}}\frac{\chi_{\mathrm{a}}}{T}\,\mathrm{d}T = 0\,. \tag{2.13}$$

Division of (2.13) by J as well as extending the *Peltier* term by $\Delta T/\Delta T$ results in

$$\left(-\frac{\pi_{\mathrm{ab}}(T_{\mathrm{C}}+\Delta T)}{T_{\mathrm{C}}+\Delta T} + \frac{\pi_{\mathrm{ab}}(T_{\mathrm{C}})}{T_{\mathrm{C}}}\right)\frac{\Delta T}{\Delta T} = \int\limits_{T_{\mathrm{C}}}^{T_{\mathrm{H}}}\frac{\chi_{\mathrm{b}}}{T}\,\mathrm{d}T - \int\limits_{T_{\mathrm{C}}}^{T_{\mathrm{H}}}\frac{\chi_{\mathrm{a}}}{T}\,\mathrm{d}T\,. \tag{2.14}$$

Again letting ΔT approach zero, the relation between *Peltier* and *Thomson* coefficients is obtained as

$$-\frac{\mathrm{d}}{\mathrm{d}T}\left(\frac{\pi_{\mathrm{ab}}}{T}\right) = \frac{\chi_{\mathrm{b}} - \chi_{\mathrm{a}}}{T}\,. \tag{2.15}$$

Expansion of the derivative yields a more convenient formulation

$$\frac{\pi_{\mathrm{ab}}}{T} = \frac{\mathrm{d}\pi_{\mathrm{ab}}}{\mathrm{d}T} + \chi_{\mathrm{b}} - \chi_{\mathrm{a}}\,. \tag{2.16}$$

Inserting (2.12) to (2.16) yields the correlation between *Seebeck* and *Peltier* effect, which has already been observed by *Thomson* and is well known as the first *Kelvin* relation

$$\frac{\pi_{\mathrm{ab}}}{T} = \alpha_{\mathrm{ab}}\,. \tag{2.17}$$

Furthermore, substitution of the *Peltier* term in (2.16) with (2.17) yields the correlation between *Seebeck* and *Thomson* coefficients, which is known as the second *Kelvin* relation

$$T\frac{\mathrm{d}\alpha_{\mathrm{ab}}}{\mathrm{d}T} = \chi_{\mathrm{a}} - \chi_{\mathrm{b}}\,. \tag{2.18}$$

The same result can be obtained from *Onsager*'s reciprocal relations of irreversible thermodynamics [12] which are a cornerstone within the description of linear irreversible processes and are applied in Section 3.5.9 to analyze macroscopic transport models.

2.2 Applications of Thermoelectric Devices

Thermoelectric applications can be generally subdivided by the direction of energy conversion. While the *Peltier* effect is used within thermoelectric cooling devices, the *Seebeck* effect is responsible for the conversion of temperature gradients to an electrical voltage.

The initial configuration of thermoelements as illustrated in Fig. 2.1 is used for temperature measurement applications [13–15], where the conversion efficiency plays an incidental role beside the linearity between generated voltage and temperature difference within a desired measurement range. Typical materials for thermocouples used in temperature measurement applications are alloys of nickel with chromium as well as aluminum and copper, iron, platinum, and rhodium [16]. Due to the considerable temperature range of about −270 °C to 3000 °C covered by available thermoelements, they can be found in measurement applications in almost every process control system in chemical industry.

In spite of the early discovery of the thermoelectric effects almost two centuries ago, a widely spread usage in commercial power conversion applications has not been reached until today due to the low conversion efficiencies. While the most metallic configurations are not suitable because of their low *Seebeck* coefficients, the introduction of semiconductors as thermoelectric materials enabled maximum conversion efficiencies in the range of 5–10 % [17, 18], whereby theoretically maximum values are predicted in the range of 20 % [19–23]. The efficiencies are still very low in absolute terms, but it enables a limited economical usage of thermoelectric generators to niche applications, where their outstanding reliability outweighs the low conversion efficiencies. Furthermore, reported power densities are rather low, which is another limitation for some weight sensitive applications.

However, due to their solid state nature and the lack of moving parts, thermoelectric generators convince by good lifetime, extremely long maintenance intervals, and thus high reliability. While these qualities are beneficial in a series of remote applications, under extreme conditions new applications have even been enabled. In the sequel, the most prominent are briefly summarized [24–26].

Wherever very cheap energy is available, the drawback of low conversion efficiency is relativized. A good example is the application of thermoelectric generators as power sources for measurement stations in oil and natural gas facilities [27]. While power consumption in measurement applications is relatively low, the power demand can be manifold for cathodic protection of pipelines and reach several hundreds watts. On unmanned offshore oil rigs, thermoelectric generators are used as security backup power source in order to establish a defined state in emergency cases [24].

Some further examples are seismic measurement stations for earthquake prediction as well as early remote communication gear, as radio and TV relay stations [24]. Wherever the waste heat can be used for heating, thermoelectric generation of electric energy can be favorable as well. Thus, some research stations and radio communications gear in the arctic and antarctic region are equipped with thermoelectric generators [28].

Thermoelectric active parts in most fossil fueled thermoelectric generators consist of either lead telluride or one of its alloys, or silicon–germanium alloys due to their fitting operational temperature range. While lead telluride can be used at temperatures of up to 900 K, SiGe enables higher temperatures of up to 1300 K. The biggest limitation for fossil–fueled devices is the availability of fuel, and in some cases also air to maintain proper combustion. An approach to overcome these limitations in even more extreme situations is to use radioisotopes as a heat source. In most reported terrestrial applications, strontium–90 has been applied, which has a half life of about 29 years and thus acts as a continuous power source over a long time. However, the need for proper shielding as well as high costs and, last but not least, security issues and the availability of nuclear fuel limits their use to governmental projects. Probably the most prominent application of radioisotope powered thermoelectric generators is as a power source on space vehicles such as satellites and research gear on several missions [29, 30].

2.3 Future Applications

Beside the already established niches, further increase of efficiency and power density as well as the ongoing development of energy costs can open a series of additional applications in economically competitive areas to conventional energy sources. Wherever a lot of waste heat is produced in a considerable temperature range, a good chance exists to establish increased efficiencies by thermoelectric devices [31].

In the automotive sector, it is thinkable to replace the alternator by thermogenerators driven by waste heat at both radiator and exhaust gas system [32, 33]. Depending on the size of the vehicle, an increase of the fuel efficiency of up to 5 % can be achieved with today's technology [34]. Furthermore, the emerge of hybrid vehicles opens a wide application of thermoelectric devices as additional energy source for battery charging [35].

Sufficiently cheap thermoelectric modules could be used to increase the efficiency in stationary industry and power generation facilities beside other measures such as coupling to district heating systems. Solar energy is thinkable as a clean power source for an alternative to caloric power plants. Thermoelectric devices could be used to increase the efficiency of solar cells. Materials having their maximum figure of merit at relatively low temperatures such as bismuth telluride and its alloys could be used for geothermal power sources.

In the cooling sector, *Peltier* modules with sufficiently high efficiencies would be an attractive alternative to conventional thermodynamic machines [36]. Refrigerators would benefit from several advantages of solid state cooling such as silence and long life times as well as the absence of environmentally hazardous coolants. On a much smaller scale, within integrated devices such as power amplifiers and processors, the steady increase of power densities requires sophisticated thermal management both within the device as well as on a packaging level [37–40].

Beside the replacement and improvement of established technologies, thermoelectrics is one of the technologies having the potential to open completely new applications. The lifetime of mobile and integrated devices is mostly limited by their energy sources. Therefore, a replacement of classical batteries by according self–recharging systems is highly desired. Ongoing reduction of the power consumption of VLSI circuits makes them compatible to available natural energy sources incorporated in the environment of usage.

Recently, the term "energy harvesting" has been established based on the idea of energy conversion from even very small ambient sources to electrical energy. It incorporates the exploitation of several present forms of energy by according converters [41, 42]. While mechanical vibrations can be harvested by piezoelectric as well as electrostatic and electromagnetic devices [43, 44], especially wireless compact devices are thinkable to power themselves from ambient radio frequency electromagnetic radiation. Light serves as the energy source converted by solar cells and thermoelectric devices gain potential from ambient temperature differences.

Thereby, the power characteristics with respect to time of each conversion mechanism has to be adapted to the needs of the application. Thermoelectric generators are thinkable to continuously harvest small amounts of energy for charging a battery or capacitor, which itself provides comparable high power over a short time. Especially when different technologies are combined, power management has to be applied. Furthermore, the operating cycles of the application can be adapted to the energy available [45].

Despite of the single technologies possible power densities, the ideal power source varies from application to application. For example, personal radio communication gear, mobile computing devices, health monitoring systems [46], or simple wristwatches [47] could be recharged by a combination of piezoelectric and thermoelectric converters within clothes. While available mechanical energy during walking can be converted by shoe inserts [48, 49], the temperature difference between the human body and its ambiance can serve as the energy source for thermoelectric generators [50, 51].

Another energy harvesting application for thermoelectric devices is the exploitation of natural temperature differences between air and soil [52,53]. Thereby, the soil's thermal capacity causes a delay in temperature evolution and the temperature difference changes its sign between daytime and nighttime. In contrast to photovoltaic devices, there is always a potential for harvesting, even in the absence of sunlight.

The slowly closing gap between the energy consumption of single applications, especially in low power microelectronics, and available devices for providing the energy needed on a regenerative basis is documented by an impressive number of publications. However, there is still a long way to go in order to make thermoelectrics competitive for a wider range of applications by continuous efforts on increasing efficiency and power densities.

'You can know the name of a bird in all the languages of the world, but when you're finished, you'll know absolutely nothing whatever about the bird... So let's look at the bird and see what it's doing — that's what counts.'

Richard Feynman

Chapter 3

Electrical Transport

THE FOLLOWING CHAPTER deals with the description of electrical transport within semiconductors. Starting with an overview of different simulation approaches based on either quantum mechanical or classical principles, the further focus is put on classical transport based on *Boltzmann*'s equation. In the sequel, the two cornerstones of classical device simulation, namely *Poisson*'s equation and *Boltzmann*'s equation are discussed followed by a glimpse on their solution, the distribution function. Furthermore, models for the band structure are introduced and their validity is discussed.

Macroscopic transport models based on *Boltzmann*'s equation are derived by the method of moments, which is a powerful approach to obtain a series of weighted balance and flux equations. Dependent on the number of involved equations, transport models of increasing complexity can be derived. In this work, the highest order moment taken into account is the energy flux equation, which is governed by the third weight in a geometric series of weights based on the carrier momentum.

Within semiconductor device simulation, the simulation domain is subdivided into several subsystems comprising electrons, holes, and the lattice as illustrated in Fig. 3.1. For each the electron and hole subsystem, moment–based equations are derived, while for the lattice, an additional heat–flow equation has to be solved in the non–isothermal case. Energy can be transferred between the single subsystems by scattering. Phonon scattering causes an energy exchange between the carrier subsystems and the lattice. Carrier generation and recombination is described as particle exchange between the electron and hole subsystem.

Introduction of the relaxation time approximation enables an analytical treatment of the scattering term. Dependent on the treatment of the stochastic part of *Boltzmann*'s equation, different terms result in the equations. The two approaches of microscopic and macroscopic relaxation times proposed by *Stratton* and *Bløtekjær* are applied.

Finally, an electrothermal transport model is formulated assuming local thermal equilibrium, which is compatible to an approach based on phenomenological irreversible thermodynamics [54]. This transport model is the chosen for the case studies presented in Chapter 6, since the size of the thermoelectric devices taken into account is far above the critical size where hot carrier effects play a dominant role.

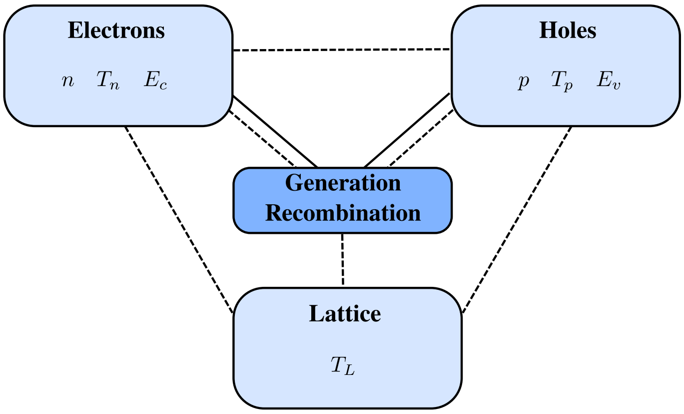

Figure 3.1: Interactions between the subsystems of electrons, holes, and the lattice. While solid lines depict particle exchange, dashed lines denote energy exchange, after [54].

The validity of *Onsager*'s relations, which are a fundamental principle for thermodynamic equilibrium is investigated for several transport models. Furthermore, special attention is devoted to the *Seebeck* coefficient, which is a crucial parameter for thermoelectric applications and enters the transport model as a link between the thermal and the electrical systems.

3.1 A Hierarchy of Simulation Strategies

Gordon Moore, one of the founders of Intel Corporation, predicted an exponential increase in computing power available in the mid 1960s [55]. He stated the transistors on a chip to roughly double every eighteen months. This rule, which has become known as Moore's law, has turned out to be true for the last four decades.

Technology Computer–Aided Design (TCAD) has become crucial to maintain the continuous gain in transistor performance, which itself enables more and more powerful simulation tools for engineering applications. While device design solely based on an experimental basis results in long development cycles and enormous costs, simulation offers a fast and inexpensive way to check and optimize device structures as well as their fabrication processes. With the tremendous progress in mainstream CMOS design as a strong background, TCAD has also reached the development process of novel and — from a CMOS point of view — more exotic devices.

The tools for numerical simulation in semiconductor device modeling can be separated in three categories of hierarchical order as sketched in Fig. 3.2. Accurate device simulation is based on an appropriate description of the underlying materials. Careful measurements of basic physical and chemical material properties are a valuable foundation of several simulation strategies for material description. Pseudopotential methods [56, 57] deliver the band structure as well as its temperature dependence later used in bulk full band Monte Carlo simulations, which themselves calculate parameters like carrier mobility and energy relaxation time for high order transport models. Numerical simulation in material science not only performs parameter extraction for several device simulation strategies, but also enables directed research for a possible synthesis of certain materials with desired parameters. Practical application of first principle methods based

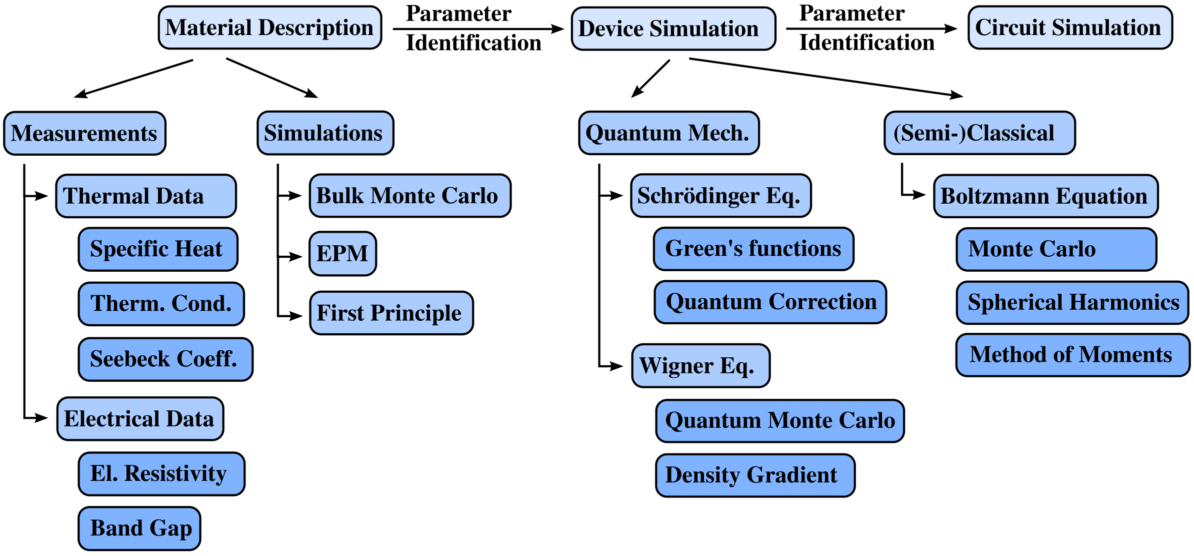

Figure 3.2: Hierarchy of simulation approaches. Physically rigorous simulation approaches as well as measurement data are used to parametrize device simulators, which can be based on either quantum mechanical or semi–classical approaches. Device simulation results itself can be used to develop compact models for circuit simulation.

on density functional theory (DFT) has been made possible in recent years by the ongoing increase of available computing power [58].

Depending on the needs of the device structure to be described, several models of different complexity can be derived. While all approaches have *Poisson*'s equation in common, the transport description can be based on differently sophisticated physical principles. The simulation of devices in the nanometer regime demands quantum–mechanical formulations, which are either based on the *Schrödinger* [59–61] or the *Wigner* equation [62, 63]. Quantum effects can be safely neglected in larger devices, and thus a semi–classical approach based on *Boltzmann*'s equation may be chosen [64]. The *Boltzmann* transport equation can be either solved by Monte Carlo methods [65], by the expansion of the distribution function into its spherical harmonics [66, 67], or by moment–based methods [68, 69]. In contrast to the other approaches, the Monte Carlo method is based on a computationally rather expensive statistical approach. The Full band Monte Carlo method is by now the physically most rigorous approach to solve the *Boltzmann* transport equation, because it relies on the exactly calculated band structure, and is thus frequently used as a reference [70, 71].

Moment–based methods can be carried out to different orders. Depending on the number of equations derived, the drift–diffusion model, energy transport models, or models of even higher order can be achieved. The drift–diffusion model has been TCAD's workhorse for many years due to its outstanding numerical robustness and performance. From physically–based device simulation, empirically derived compact models can be derived for lumped simulation of entire circuits. Their parameters are obtained by parameter extraction from device simulation. Mixed–mode simulation tools combine the approaches of device simulation and compact modeling.

Thereby, device level simulation of one or more devices coupled with a set of devices described by compact models is possible.

3.2 The Basic Equations

In this section, the two cornerstones of semi–classical device simulation are given — *Poisson*'s equation and *Boltzmann*'s equation. While electrostatics is covered by *Poisson*'s equation, *Boltzmann*'s equation describes the propagation of the distribution function within a simulation domain. These two equations are solved in a self consistent manner for example in Monte–Carlo simulators, often used as a reference for higher–order transport models which are derived from the *Boltzmann* transport equation as well.

3.2.1 *Poisson*'s Equation

Poisson's equation is a common constituent to all charge transport models for semiconductor devices and serves as the link between the electrostatic potential and the charge distribution within the device. It reads

$$\nabla_{\boldsymbol{r}} \cdot (\epsilon \nabla_{\boldsymbol{r}} \varphi) = -\mathrm{q}\,(p - n + N_A - N_D) \ , \tag{3.1}$$

where φ denotes the electrostatic potential, ϵ the dielectric permittivity, n and p the electron and hole concentration, respectively, and N_A and N_D the concentration of acceptors and donors. Its derivation is straight–forward from *Gauss*' law and the proper material equation for the quasi stationary case [72]. In order to obtain a complete device description, *Poisson*'s equation has to be solved self–consistently with the transport system in an iterative approach.

3.2.2 *Boltzmann*'s Equation

In this section, *Boltzmann*'s equation is introduced as an important foundation for semi–classical transport description in semiconductor devices. In order to describe the complete device behavior, theoretically every single carrier within the device would have to be described by solving *Newton*'s classical equations of motion

$$\frac{\mathrm{d}\boldsymbol{r}}{\mathrm{d}t} = \boldsymbol{v} \ = \frac{1}{\hbar}\nabla_{\boldsymbol{k}}\mathcal{H}\,, \tag{3.2}$$

$$\hbar\frac{\mathrm{d}\boldsymbol{k}}{\mathrm{d}t} = \boldsymbol{F} = -\nabla_{\boldsymbol{r}}\mathcal{H}\,. \tag{3.3}$$

Within these, a generalized force $\boldsymbol{F}$ with unique direction comprises the electric field as well as other fields causing a driving force to carriers, such as a thermal gradient (*Seebeck*–, *Peltier*–effect) or a magnetic field (*Lorentz*–force). This force is overlaid by forces with random direction describing the microscopic thermal movement.

The *Hamilton* function $\mathcal{H}$ represents the total carrier energy and can be split into two parts: The potential energy $\mathcal{E}_{\mathrm{pot}}$ and the kinetic energy $\mathcal{E}_{\mathrm{kin}}$. The potential energy incorporates the conduction and valence band edge energies $\mathcal{E}_{\mathrm{c,v}}$ for electrons and holes, respectively, $\Delta\mathcal{E}_{\mathrm{c,v}}$ considering band gap narrowing, and the electrostatic potential φ. Thus, $\mathcal{H}$ can be expanded as

$$\mathcal{H} = \underbrace{\mathcal{E}_{\mathrm{c,v}} + \Delta\mathcal{E}_{\mathrm{c,v}} + \mathrm{s}_\nu \mathrm{q}\varphi}_{\mathcal{E}_{\mathrm{pot}}} + \underbrace{\mathcal{E}}_{\mathcal{E}_{\mathrm{kin}}} . \tag{3.4}$$

For the sake of clarity, q denotes the elementary charge and does not incorporate the different sign of the charges of electrons and holes. The different charge of electrons and holes is treated by s_ν, which becomes -1 for electrons and 1 for holes.

Instead of keeping the focus on every single carrier, a statistical description is introduced. Neglecting *Heisenberg*'s uncertainty principle, each carrier is exactly described by its momentum and position, so it takes a certain place within 6 dimensional $(\boldsymbol{r},\boldsymbol{k})$–space. The normalization of all present carriers within the volume under investigation results in the distribution function, which is the solution variable of *Boltzmann*'s equation. It incorporates the carrier density within 6–dimensional $(\boldsymbol{r}, \boldsymbol{k})$–space.

In the sequel, the *Boltzmann* transport equation is derived from phenomenological considerations and its range of validity is discussed. Formally, *Boltzmann*'s equation represents a seven–dimensional integro–differential equation within the phase space $(\boldsymbol{r}, \boldsymbol{k}, t)$. However, it is accessible using a book–keeping background, which is presented in Section 3.2.2.1. Originally formulated for the description of statistical mechanics of gases, it is the cornerstone for the classical description of transport in semiconductors as well. The transport models derived in this thesis later on are based on the *Boltzmann* transport equation.

3.2.2.1 Phenomenological Approach

Since the *Boltzmann* transport equation represents a book–keeping equation for the distribution function, it can be derived from a phenomenological point of view illustrated in Fig. 3.3 for each spatial and momentum dimension. The net increase of carriers within the volume $\Delta r \Delta k$ can only be caused by a net in–flux of carriers in both real and momentum space or net in–scattering. Thus, the change of carriers within the volume $\Delta r \Delta k$ during the time window Δt reads

$$\begin{aligned} \Delta f \Delta r \hbar \Delta k = {} & \left(f(r) - f(r+\Delta r)\right) v \hbar \Delta k \Delta t \\ & + \left(f(\hbar k) - f(\hbar k + \hbar \Delta k)\right) F \Delta r \Delta t \\ & + \mathcal{Q}(f) \Delta r \hbar \Delta k \Delta t - \mathcal{R}(f) \Delta r \hbar \Delta k \Delta t \,, \end{aligned} \tag{3.5}$$

with the velocity in real space v and F as a generic force. Scattering is expressed with the scattering operators $\mathcal{Q}(f)$ and $\mathcal{R}(f)$, whereby the latter comprises inter–band processes and thus represents generation and recombination of free carriers in the semiconductor. Letting Δr, Δk, and Δt become infinitesimal small and rearranging the equation leads to the one–dimensional *Boltzmann* transport equation

$$\partial_t f + v \partial_r f + F \frac{1}{\hbar} \partial_k f = \mathcal{Q}(f) - \mathcal{R}(f) \,. \tag{3.6}$$

Reformulation of (3.6) for three spatial and momentum dimensions yields

$$\partial_t f + \boldsymbol{v} \cdot \nabla_{\boldsymbol{r}} f + \boldsymbol{F} \cdot \frac{1}{\hbar} \nabla_{\boldsymbol{k}} f = \mathcal{Q}(f) - \mathcal{R}(f) \,. \tag{3.7}$$

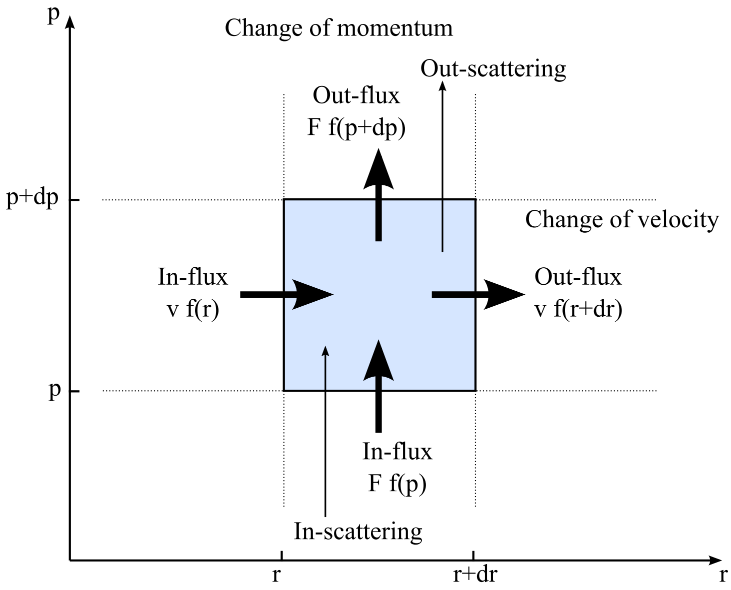

Figure 3.3: Illustration of the book–keeping character of *Boltzmann*'s equation for one $\boldsymbol{r}$– and $\boldsymbol{p}$–dimension. Possible transitions are a spatial flux of carriers, a change of the carrier's momentum due to an external generic force, and scattering processes, after [73].

Inserting Eqs. (3.2) and (3.3) into (3.7) delivers the commonly used form of the *Boltzmann* transport equation

$$\partial_t f + \frac{1}{\hbar}\nabla_{\boldsymbol{k}}\mathcal{H}\cdot\nabla_{\boldsymbol{r}} f - \nabla_{\boldsymbol{r}}\mathcal{H}\cdot\frac{1}{\hbar}\nabla_{\boldsymbol{k}} f = \mathcal{Q}(f) - \mathcal{R}(f)\,. \tag{3.8}$$

The introduction of a formulation using *Poisson* brackets enables a compact and convenient notation incorporating useful identities. The definition of *Poisson* brackets as well as important properties are given in Section A. For the distribution function and the total energy, the *Poisson* bracket's definition (A.1) reads

$$\{f,\mathcal{H}\} = \nabla_{\boldsymbol{r}} f\cdot\frac{1}{\hbar}\nabla_{\boldsymbol{k}}\mathcal{H} - \frac{1}{\hbar}\nabla_{\boldsymbol{k}} f\cdot\nabla_{\boldsymbol{r}}\mathcal{H}\,, \tag{3.9}$$

which enables the formulation of (3.8) in the compact form of

$$\partial_t f + \{f,\mathcal{H}\} = \mathcal{Q}(f) - \mathcal{R}(f)\,. \tag{3.10}$$

The left side of the equation describes the ballistic behavior of the particle influenced by the generic force F. The *Poisson* bracket $\{f,\mathcal{H}\}$ is also often referred to as the drift term of the *Boltzmann* transport equation. The generic force incorporates the sum of all considered driving forces to the particle, namely the electric field, a temperature gradient, as well as a position dependent band structure. The *Lorentz* force $\boldsymbol{v}\times\boldsymbol{B}$ describing the influence of a magnetic field is not taken into account in this work.

Statistical collisions interrupt the ballistic motion of the particles which are described by the collision term at the right side of *Boltzmann*'s equation. The collision term incorporates both in–scattering from $\boldsymbol{p}'$ to $\boldsymbol{p}$ as well as out–scattering from $\boldsymbol{p}$ to $\boldsymbol{p}'$. Thus it can be formulated as [73]

$$\mathcal{Q}(f) = \sum_{\boldsymbol{p}'} f(\boldsymbol{p}')\,(1 - f(\boldsymbol{p}))\,S(\boldsymbol{p}',\boldsymbol{p}) - \sum_{\boldsymbol{p}'} f(\boldsymbol{p})\,\big(1 - f(\boldsymbol{p}')\big)\,S(\boldsymbol{p},\boldsymbol{p}')\,, \tag{3.11}$$

where $f(\boldsymbol{p}')$ denotes the probability for the state at $\boldsymbol{p}'$ to be occupied and $(1 - f(\boldsymbol{p}))$ the probability for the state at $\boldsymbol{p}$ to be available for in–scattering. $S(\boldsymbol{p}',\boldsymbol{p})$ is the transition rate from $\boldsymbol{p}'$ to $\boldsymbol{p}$. The sum is performed over all states available for scattering to and from $\boldsymbol{p}$. Physically speaking, the collision term incorporates the interaction of the carriers with the lattice (phonon scattering), the influence of ionized impurities, as well as additional scattering caused by inhomogeneities in the grid in material alloys and has to be modeled accordingly [65, 74].

An alternative approach for the derivation of the *Boltzmann* transport equation can be found e.g. in [73], which is also useful for solving it with the help of path integrals. The motion of free carriers is influenced by an external electric field and the resulting path through $(\boldsymbol{r},\boldsymbol{k})$–space is described with trajectories following *Newton*'s laws. Scattering events cause the particle to change its momentum, but not its position.

3.2.2.2 Validity

In the derivation of the *Boltzmann* transport equation, several assumptions are inherently incorporated which result in a limited range of validity. These assumptions include the items below:

- By the introduction of the distribution function, the original many–electron problem is replaced by a one–electron problem with an appropriate potential. According to the *Hartree-Fock* approximation [75], the contribution of all surrounding electrons to this potential is approximated by a surrounding charge density. Thus, the short range electron–electron interaction can not be described properly. However, the potential of the surrounding carriers is treated by the electric field self–consistently.
- The *Boltzmann* transport equation is a semi–classical equation and thus not compatible with a quantum mechanical approach, since the carriers are described by *Newton*'s classic equation set of motion. A particle's position and momentum can never be determined with arbitrary accuracy because of *Heisenberg*'s uncertainty relations.
- The collisions are considered to happen instantaneously. The validity of this approximation is in good agreement with the conception of very long free flight times compared to the collision times.

3.3 Band Structure Model

Generally, the full band structure of semiconductors incorporates an anisotropic dispersion relation $\mathcal{E}(\boldsymbol{k})$, which is only accessible by numerical methods. Fig. 3.4 illustrates iso–energy surfaces of the first conduction band of silicon within one octant of the *Brillouin* zone, where the lowest energy minima are located close to the X–points. Around these energy minima valleys

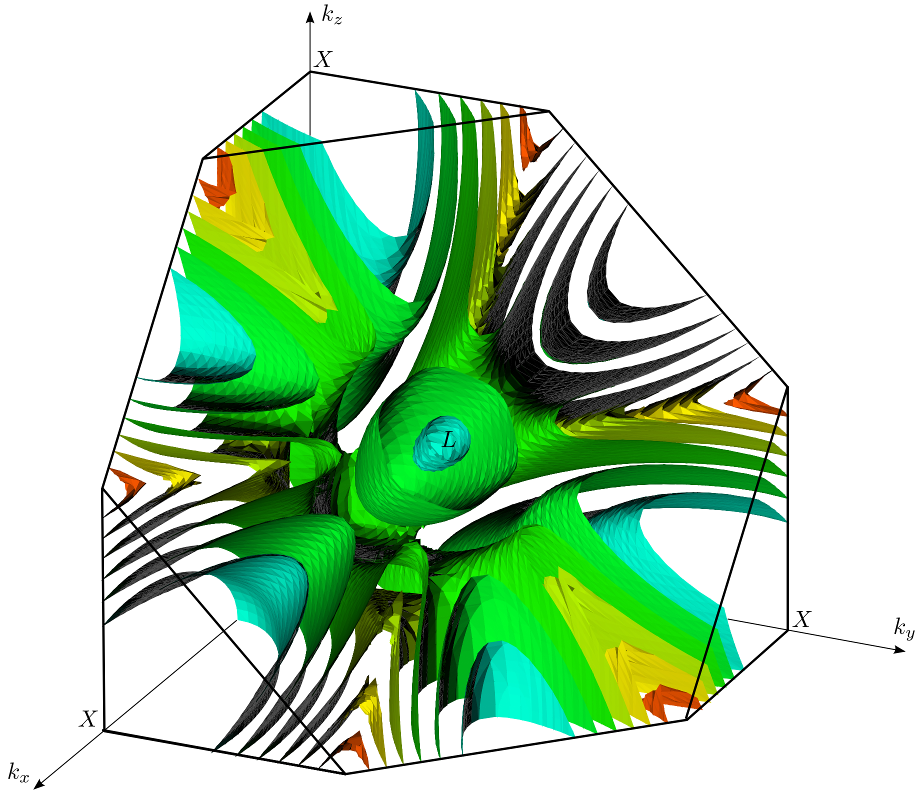

Figure 3.4: Equi–energy surfaces of the full band structure of silicon within one octant of the first *Brillouin* zone.

are formed, whose shape deviates strongly from the conventionally used elliptic approximation with increasing energies. Beside the valleys at the X–points, further valleys are located at the L–points, whose energy minima are higher than that of the X–valleys. However, in order to describe the transport in the semiconductor in a closed analytical way, simplified expressions for the rather complicated full–band structure are commonly introduced. In the following derivations, isotropic bands are assumed, which imply the dispersion relation to depend only on the magnitude of the wave vector $\boldsymbol{k}$. For the sake of convenience, the dispersion relation is separated into its parabolic and non–parabolic contributions [76]

$$\mathcal{E}(k)H_{\mathcal{E}}(\mathcal{E}) = \frac{\hbar^2 k^2}{2m^*} \tag{3.12}$$

with the non–parabolicity function $H_{\mathcal{E}}$ and the isotropic carrier mass m^*. The simplest band structure model is the parabolic one, which is obtained for $H_{\mathcal{E}} = 1$ as

$$\mathcal{E}(k) = \frac{\hbar^2 k^2}{2m^*}\,. \tag{3.13}$$

However, the validity of the parabolic band model is restricted to low carrier energies. In order to address higher energies, the non–parabolicity of the band structure has to be taken into account by appropriate expressions for $H_{\mathcal{E}}$. *Kane* proposed a first–order correction [77] in the form

$$\mathcal{E}(k)\left(1 + \gamma\mathcal{E}(k)\right) = \frac{\hbar^2 k^2}{2m^*}\,, \tag{3.14}$$

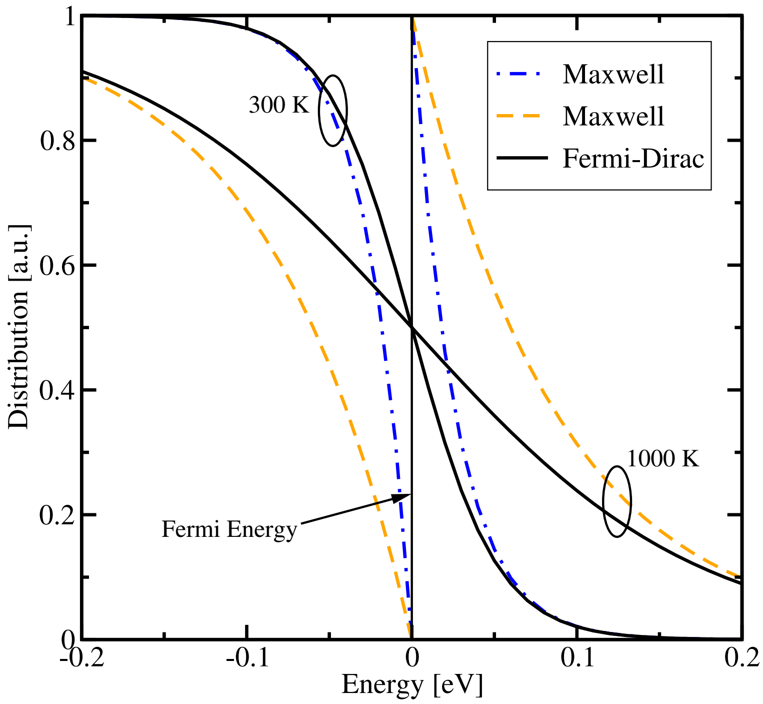

Figure 3.5: *Fermi–Dirac* equilibrium distribution function and *Maxwell–Boltzmann* approximations at 300 K and 1000 K.

whose validity is limited to energies below 1 eV in silicon [73]. In order to accurately describe the dispersion relation for even higher energies, more sophistic models can be applied, such as tabulated data for $H_{\mathcal{E}}$ obtained from numerical band structure calculations. However, the carriers in thermoelectric devices as investigated in this work are not driven far from equilibrium and thus the band structure is described by the parabolic expression (3.13) in the following derivations of transport models.

3.4 The Distribution Function

As the solution variable of the *Boltzmann* transport equation, the distribution function plays an important role for the description of transport within semiconductor devices. The distribution function of electrons and holes in thermal equilibrium is the *Fermi–Dirac* distribution

$$f(\mathcal{E}) = A \frac{1}{1+\exp\dfrac{\mathcal{E}-\mathcal{E}_\mathrm{f}}{k_\mathrm{B}T_\nu}} \,. \tag{3.15}$$

A commonly used approximation to the *Fermi–Dirac* distribution function is the *Maxwell–Boltzmann* distribution

$$f(\mathcal{E}) = A \exp\frac{\mathcal{E}_\mathrm{f}-\mathcal{E}}{k_\mathrm{B}T_\nu} \,. \tag{3.16}$$

From a mathematical point of view, the 1 in the denominator of (3.15) can be neglected, if the second term dominates. This is valid if the difference between the carrier's energy and the *Fermi* level is large compared to $k_\mathrm{B}T_\nu$, which is the case in non–degenerate semiconductors. While the *Fermi–Dirac* distribution incorporates *Pauli*'s exclusion principle, which becomes important at high dopings, the *Maxwell–Boltzmann* distribution neglects this principle. Thus, the *Maxwell–Boltzmann* distribution's validity is limited to the lowly doped case.

Fig. 3.5 illustrates the situation for a semiconductor in equilibrium. Both *Fermi–Dirac* and *Maxwell–Boltzmann* statistics are plotted for 300 K and 1000 K, respectively. While the transition at the *Fermi* level is relatively sharp at lower temperatures, it is extended to a higher energy range at elevated temperatures. For intrinsic and lowly doped semiconductors, the range where the deviation between *Fermi–Dirac* and *Maxwell–Boltzmann* statistics accounts for a non–negligible error is completely covered by the forbidden energy gap. However, the *Fermi* energy is shifted close to the band edge in highly doped samples and thus the range with non–negligible deviations between *Maxwell–Boltzmann* statistics and *Fermi–Dirac* statistics reaches energy levels outside the forbidden gap.

While (3.16) represents the equilibrium case, carrier transport can be incorporated by a displaced *Maxwell*ian, which reads assuming parabolic bands (3.13)

$$f(\boldsymbol{k}) = A \exp\left(-\frac{\hbar^2 \left|\boldsymbol{k}-\boldsymbol{k}_0\right|^2}{2m^* k_\mathrm{B}T_\nu}\right) . \tag{3.17}$$

Here, $\boldsymbol{p}_0 = \hbar\boldsymbol{k}_0$ is the average momentum of the carriers and their average velocity reads $\boldsymbol{v}_0 = \boldsymbol{p}_0/m^*$. Especially in thermoelectric devices, the deterministic shift of the distribution function is very small compared to the stochastic movement due to non–zero temperature. Therefore, the diffusion approximation can be applied, where the displaced *Maxwell*ian (3.17) is expanded to is *Taylor* series and truncated after the first–order term [73]

$$f(\boldsymbol{k}) = A\left(1+\frac{\boldsymbol{p}\cdot\boldsymbol{v}_0}{k_\mathrm{B}T_\nu}\right)\exp\left(-\frac{\mathcal{E}(\boldsymbol{k})}{k_\mathrm{B}T_\nu}\right) . \tag{3.18}$$

For the derivation of electrical transport models in the next sections, *Maxwell–Boltzmann* statistics in the formulation of (3.18) have been assumed for the closure relations due to reasons of mathematical convenience. However, strictly speaking this approximation consequently affects macroscopic quantities, which are assessed in Section 3.5.1.

3.5 Macroscopic Transport Models

Since the direct solution of the *Boltzmann* transport equation is computationally very demanding, it is either solved applying the Monte–Carlo technique or approximated by macroscopic transport models, which are the background for commercial device simulators. The solution variables of macroscopic transport models are macroscopic quantities, which are accessible by measurement in contrast to the distribution function. However, the information of the device state incorporated in the macroscopic quantities is limited, and the access to the full distribution function is limited to approaches dealing directly with *Boltzmann*'s equation, such as the Monte–Carlo method [65]. Thus, data governed by Monte–Carlo simulations is frequently used to judge the validity of macroscopic transport models for a certain device regime [78–80]. Macroscopic quantities represent averages of microscopic quantities in momentum–space. The coherences between microscopic and macroscopic quantities are given in Section 3.5.1.

Basically, macroscopic transport models can be formulated following two approaches. First, in the systematic approach, a set of equations is derived from the *Boltzmann* transport equation applying the method of moments, which is introduced in Section 3.5.2. In mathematical words, *Boltzmann*'s equation, which is a seven–dimensional integro–differential equation is transformed into a series of coupled partial differential equations. Compared to the underlying *Boltzmann* transport equation, information on the distribution function is approximated due to the truncation of the system after a certain number of equations and the closure of the equation system based on information incorporated in the equations governed. Theoretically, an arbitrary number of equations could be derived, but the computational effort increases considerably with the number of equations. By a proper choice of weight functions, these equations hold a physical meaning which is also accessible from a more intuitive point of view.

Second, in the phenomenological approach, the semiconductor equations are formulated following the basic laws of mass and energy conservation as well as the principles of irreversible thermodynamics. In the simplest case, both approaches based on completely different procedures lead to similar results.

In the sequel, a toolkit for the systematic derivation of transport models and a proper nomenclature are given. Three transport models are derived and compared following the systematic approach applying different assumptions on the collision term.

3.5.1 Microscopic and Macroscopic Quantities

While microscopic quantities represent a certain state in $(\boldsymbol{r}, \boldsymbol{k})$–space, their macroscopic counterparts are averages over $\boldsymbol{k}$–space. As a consequence, their dependency restricts to $\boldsymbol{r}$–space. Macroscopic quantities are obtained by the integration of the according microscopic quantity multiplied by the distribution function f. The spin degeneracy is implied by a factor of two, a further factor of $1/(2\pi)$ per degree of freedom results from the transition from discrete states to a continuum distribution function. Thus, a general macroscopic density x reads from its microscopic, scalar–valued counterpart X and the distribution function f

$$\begin{aligned} x(\boldsymbol{r}) &= \frac{2}{(2\pi)^3} \iiint\limits_{-\infty}^{\infty} f(\boldsymbol{r}, \boldsymbol{k}) X(\boldsymbol{r}, \boldsymbol{k}) \ \mathrm{d}k_x \ \mathrm{d}k_y \ \mathrm{d}k_z \\ &= \frac{2}{(2\pi)^3} \iiint\limits_{-\infty}^{\infty} \nu(\boldsymbol{r}) F(\boldsymbol{r}, \boldsymbol{k}) X(\boldsymbol{r}, \boldsymbol{k}) \ \mathrm{d}k_x \ \mathrm{d}k_y \ \mathrm{d}k_z \\ &= \nu(\boldsymbol{r}) \langle X(\boldsymbol{r}, \boldsymbol{k}) \rangle \\ &= \langle\!\langle X(\boldsymbol{r}, \boldsymbol{k}) \rangle\!\rangle \end{aligned} \tag{3.19}$$

with F as the normalized distribution function and ν the carrier density. The short forms $\langle \cdot \rangle$ and $\langle\!\langle \cdot \rangle\!\rangle$ denote the normalized statistic average and the statistic average, respectively. Analogously, macroscopic current densities are defined from vector–valued microscopic quantities $\boldsymbol{X}$ and the distribution function f

$$\begin{aligned} \boldsymbol{j}_x(\boldsymbol{r}) &= \frac{2}{(2\pi)^3} \iiint\limits_{-\infty}^{\infty} f(\boldsymbol{r},\boldsymbol{k})\boldsymbol{X}(\boldsymbol{r},\boldsymbol{k})\ \mathrm{d}k_x\ \mathrm{d}k_y\ \mathrm{d}k_z \\ &= \nu(\boldsymbol{r})\langle \boldsymbol{X}(\boldsymbol{r},\boldsymbol{k})\rangle \\ &= \langle\!\langle \boldsymbol{X}(\boldsymbol{r},\boldsymbol{k})\rangle\!\rangle\,. \end{aligned} \tag{3.20}$$

Macroscopic densities occurring in the following derivations are the carrier density ν and the energy density w. The corresponding fluxes are a particle flux $\boldsymbol{j}_\nu$ and the energy flux $\boldsymbol{j}_\nu^{\mathrm{u}}$, respectively. The formulation used within this work consequently implies the particle flux, which differs from the electric current by the elementary charge. Important microscopic quantities and their macroscopic counterparts are outlined in Table 3.1.

Macroscopic quantity	Symbol	Definition
general macroscopic density	x	$\langle\!\langle X\rangle\!\rangle$
general macroscopic flux	$\boldsymbol{j}_x$	$\langle\!\langle \boldsymbol{X}\rangle\!\rangle$
carrier density	ν	$\langle\!\langle 1\rangle\!\rangle$
carrier flux density	$\boldsymbol{j}_\nu$	$\nu\langle \boldsymbol{v}\rangle$
average energy density	w	$\langle \mathcal{E}\rangle$
energy flux density	$\boldsymbol{j}_\nu^{\mathrm{u}}$	$\langle \boldsymbol{v}\mathcal{E}\rangle$

Table 3.1: Some important macroscopic quantities for transport models with their definition from the microscopic counterparts.

In the following, important averages are given for a heated, displaced *Maxwell*ian (3.17) and parabolic bands (3.13). The carrier concentration evaluates as

$$\begin{aligned} \nu = \langle\!\langle 1\rangle\!\rangle &= \frac{2A}{(2\pi)^3}\int \mathrm{e}^{-\frac{\hbar^2(k-k_0)^2}{2m^* k_\mathrm{B} T_\nu}}\ \mathrm{d}^3\boldsymbol{k} = \frac{2A}{(2\pi)^3}\int \mathrm{e}^{-\frac{\hbar^2 k'^2}{2m^* k_\mathrm{B} T_\nu}}\ \mathrm{d}^3\boldsymbol{k}' \\ &= \frac{2A}{(2\pi)^3} 4\pi \int\limits_0^\infty k'^2 \mathrm{e}^{-\frac{\hbar^2 k'^2}{2m^* k_\mathrm{B} T_\nu}}\ \mathrm{d}k' = \frac{2A}{(2\pi)^3}\left(\frac{2\pi m^* k_\mathrm{B} T_\nu}{\hbar^2}\right)^{\frac{3}{2}} \end{aligned} \tag{3.21}$$

and is used to normalize further averages in the sequel. In order to derive the average energy w, the average of the carrier energy $\langle\!\langle \mathcal{E}\rangle\!\rangle$ has to be evaluated

$$\begin{aligned} w = \frac{1}{\nu}\langle\!\langle \mathcal{E}\rangle\!\rangle &= \frac{1}{\nu}\frac{2A}{(2\pi)^3}\int \mathrm{e}^{-\frac{\hbar^2(k-k_0)^2}{2m^* k_\mathrm{B} T_\nu}}\frac{\hbar^2 k^2}{2m^*}\ \mathrm{d}^3\boldsymbol{k} \\ &= \frac{1}{\nu}\frac{2A}{(2\pi)^3}\int \mathrm{e}^{-\frac{\hbar^2 k'^2}{2m^* k_\mathrm{B} T_\nu}}\frac{\hbar^2 (k'+k_0)^2}{2m^*}\ \mathrm{d}^3\boldsymbol{k}' \\ &= \frac{1}{\nu}\frac{2A}{(2\pi)^3}\int \mathrm{e}^{-\frac{\hbar^2 k'^2}{2m^* k_\mathrm{B} T_\nu}}\left(\frac{\hbar^2 k'^2}{2m^*} + \frac{\hbar^2 2k' k_0}{2m^*} + \frac{\hbar^2 k_0^2}{2m^*}\right)\ \mathrm{d}^3\boldsymbol{k}'\,. \end{aligned} \tag{3.22}$$

The second term within the parenthesis vanishes due to the product of an odd and an even term in the integrand. Furthermore, the transformation to polar coordinates yields

$$\begin{aligned} w &= \frac{1}{\nu}\frac{2A}{(2\pi)^3}4\pi\int\limits_0^\infty k'^2 \mathrm{e}^{-\frac{\hbar^2k'^2}{2m^*k_\mathrm{B}T_\nu}}\frac{\hbar^2k'^2}{2m^*}\,\mathrm{d}k' + \frac{1}{\nu}\frac{2A}{(2\pi)^3}4\pi\int\limits_0^\infty k'^2 \mathrm{e}^{-\frac{\hbar^2k'^2}{2m^*k_\mathrm{B}T_\nu}}\frac{\hbar^2k_0^2}{2m^*}\,\mathrm{d}k' \\ &= \frac{1}{\nu}\left(\frac{3A}{(2\pi)^3}k_\mathrm{B}T_\nu\left(\frac{2\pi m^*k_\mathrm{B}T_\nu}{\hbar^2}\right)^{\frac{3}{2}} + \frac{2A}{(2\pi)^3}\frac{\hbar^2k_0^2}{2m^*}\left(\frac{2\pi m^*k_\mathrm{B}T_\nu}{\hbar^2}\right)^{\frac{3}{2}}\right) \\ &= \frac{3}{2}k_\mathrm{B}T_\nu + \frac{\hbar^2k_0^2}{2m^*}\,. \end{aligned} \tag{3.23}$$

The resulting average energy consists of two parts comprising the thermal energy by random movement and the drift energy corresponding to the average carrier movement. For comparison, the average energy is evaluated within the diffusion approximation, whereby the heated *Maxwell*ian is expressed by its first–order *Taylor* approximation (3.18)

$$\begin{aligned} w &= \frac{1}{\nu}\langle\!\langle\mathcal{E}\rangle\!\rangle = \frac{1}{\nu}\frac{2A}{(2\pi)^3}\int\left(1+\frac{\hbar\boldsymbol{k}\cdot\boldsymbol{v}_0}{k_\mathrm{B}T_\nu}\right)\mathrm{e}^{-\frac{\hbar^2k^2}{2m^*k_\mathrm{B}T_\nu}}\frac{\hbar^2k^2}{2m^*}\,\mathrm{d}^3\boldsymbol{k} \\ &= \frac{1}{\nu}\frac{2A}{(2\pi)^3}4\pi\int\limits_0^\infty k^2\mathrm{e}^{-\frac{\hbar^2k^2}{2m^*k_\mathrm{B}T_\nu}}\frac{\hbar^2k^2}{2m^*}\,\mathrm{d}k = \frac{1}{\nu}\frac{2A}{(2\pi)^3}\frac{3}{2}k_\mathrm{B}T_\nu\left(\frac{2\pi m^*k_\mathrm{B}T_\nu}{\hbar^2}\right)^{\frac{3}{2}} \\ &= \frac{3}{2}k_\mathrm{B}T_\nu\,. \end{aligned} \tag{3.24}$$

In contrast to the full displaced *Maxwell*ian, the first–order approximation leads to a neglection of the drift component in the average energy expression. This result underlines the range of validity of the diffusion approximation. For a slowly drifting, hot carrier gas, the drift term in (3.23) is negligibly small compared to the thermal energy. The formulation of the distribution function approximation (3.18) has been motivated exactly by this assumption.

3.5.2 Method of Moments

The basic idea behind the method of moments is not to solve the *Boltzmann* transport equation coupled with the *Poisson* equation directly, but to derive a set of balance and flux equations for macroscopic quantities based on the moments of the *Boltzmann* transport equation. Theoretically, an arbitrary number of equations can be derived, each containing information from the next–higher equation. As a consequence, the number of variables exceeds the number of equations. In order to obtain a closed equation system, the derivation of moments has to be truncated and a closure relation has to be formulated by a suitably chosen ansatz [81,82] based on the information incorporated in the underlying lower moments equations. Besides several theoretical approaches [83], the closure can be obtained by extraction of the missing next–higher moment from Monte–Carlo simulations [84].

In order to obtain a certain moment equation, the *Boltzmann* transport equation is multiplied by a general weight function and integrated over $\boldsymbol{k}$–space according to equations (3.19) and (3.20). Thereby, the series of weight functions is chosen as the powers of increasing orders of the momentum $\boldsymbol{p}$. Because of this average in $\boldsymbol{k}$–space, information on the distribution of microscopic quantities over the momentum is lost, which is originally incorporated in *Boltzmann*'s equation. However, the information incorporated in the macroscopic equations is sufficient for a wide range of engineering applications.

For scalar–valued weights X, the application of the moment definition to *Boltzmann*'s equation (3.10) leads to the conservation equation for the general weight function X

$$\begin{aligned}\partial_t \frac{2}{(2\pi)^3}\int X(\boldsymbol{r},\boldsymbol{k}) f \, \mathrm{d}^3\boldsymbol{k} + \frac{2}{(2\pi)^3}\int X(\boldsymbol{r},\boldsymbol{k})\{f,\mathcal{H}\}\, \mathrm{d}^3\boldsymbol{k} \\ = \frac{2}{(2\pi)^3}\int X(\boldsymbol{r},\boldsymbol{k})\mathcal{Q}(f)\, \mathrm{d}^3\boldsymbol{k} - \frac{2}{(2\pi)^3}\int X(\boldsymbol{r},\boldsymbol{k})\mathcal{R}(f)\, \mathrm{d}^3\boldsymbol{k}\,.\end{aligned} \tag{3.25}$$

which can be conveniently formulated as

$$\partial_t x + \frac{2}{(2\pi)^3}\int X(\boldsymbol{r},\boldsymbol{k})\{f,\mathcal{H}\}\, \mathrm{d}^3\boldsymbol{k} = \mathcal{Q}(x) - \mathcal{R}(x)\,. \tag{3.26}$$

With the Poisson bracket identities (A.8), (A.10), and (A.11), the second term of the right hand side of equation 3.25 can be expanded as

$$\begin{aligned}\frac{2}{(2\pi)^3}\int X\{f,\mathcal{H}\}\, \mathrm{d}^3\boldsymbol{k} &= \frac{2}{(2\pi)^3}\int \{Xf,\mathcal{H}\} - f\{X,\mathcal{H}\}\, \mathrm{d}^3\boldsymbol{k} \\ &= \frac{2}{(2\pi)^3}\int \left(\nabla_{\boldsymbol{r}}(Xf)\frac{1}{\hbar}\nabla_{\boldsymbol{k}}\mathcal{H} - \frac{1}{\hbar}\nabla_{\boldsymbol{k}}(Xf)\nabla_{\boldsymbol{r}}\mathcal{H}\right) \mathrm{d}^3\boldsymbol{k} - \langle\!\langle \{X,\mathcal{H}\}\rangle\!\rangle \\ &= \frac{2}{(2\pi)^3}\int \left(\nabla_{\boldsymbol{r}}\left(Xf\frac{1}{\hbar}\nabla_{\boldsymbol{k}}\mathcal{H}\right) - Xf\nabla_{\boldsymbol{r}}\frac{1}{\hbar}\nabla_{\boldsymbol{k}}\mathcal{H} - \frac{1}{\hbar}\nabla_{\boldsymbol{k}}(Xf\nabla_{\boldsymbol{r}}\mathcal{H}) + Xf\frac{1}{\hbar}\nabla_{\boldsymbol{k}}\nabla_{\boldsymbol{r}}\mathcal{H}\right) \\ &\quad - \langle\!\langle \{X,\mathcal{H}\}\rangle\!\rangle\,.\end{aligned} \tag{3.27}$$

Transforming the third term using *Gauss*' theorem and assuming f to go stronger to zero than X, this term vanishes [80]. Applying (3.20) to the first term, we can write the general moment equation as

$$\partial_t x + \nabla_{\boldsymbol{r}}\cdot\langle\!\langle X\boldsymbol{v}\rangle\!\rangle - \langle\!\langle \{X,\mathcal{H}\}\rangle\!\rangle = \mathcal{Q}(x) - \mathcal{R}(x)\,. \tag{3.28}$$

Inserting the decomposition of the *Hamilton* function (3.4) into (3.28) and introducing the effective potential $\tilde{\varphi}$, we finally obtain the macroscopic balance equation, which follows from the even, scalar–valued weight functions X

$$\partial_t\langle\!\langle X\rangle\!\rangle + \nabla_{\boldsymbol{r}}\cdot\langle\!\langle X\boldsymbol{v}\rangle\!\rangle - \langle\!\langle \{X,\mathcal{E}\}\rangle\!\rangle + \mathrm{s}_\nu \mathrm{q}\left\langle\!\!\left\langle \frac{1}{\hbar}\nabla_{\boldsymbol{k}}X\right\rangle\!\!\right\rangle\nabla_{\boldsymbol{r}}\tilde{\varphi} = \mathcal{Q}(x) - \mathcal{R}(x)\,. \tag{3.29}$$

Analogously, formulation of the moment equation with a general odd, vector–valued weight function $\boldsymbol{X}$ yields the according macroscopic flux equation

$$\partial_t\langle\!\langle \boldsymbol{X}\rangle\!\rangle + \nabla_{\boldsymbol{r}}\cdot\langle\!\langle \boldsymbol{X}\otimes\boldsymbol{v}\rangle\!\rangle - \langle\!\langle \{\boldsymbol{X},\mathcal{E}\}\rangle\!\rangle + \mathrm{s}_\nu \mathrm{q}\left\langle\!\!\left\langle \frac{1}{\hbar}\nabla_{\boldsymbol{k}}\otimes\boldsymbol{X}\right\rangle\!\!\right\rangle\cdot\nabla_{\boldsymbol{r}}\tilde{\varphi} = \mathcal{Q}(\boldsymbol{j}_x) - \mathcal{R}(\boldsymbol{j}_x)\ . \tag{3.30}$$

Equations (3.29) and (3.30) are the starting point for the derivation of macroscopic transport models carried out in the sequel. For homogeneous materials, $\nabla\tilde{\varphi}$ is equal to the gradient of the electrostatic potential $\nabla\varphi$, while for inhomogeneous samples, the additional gradient of the band edges due to spatially dependent material composition enters $\nabla\tilde{\varphi}$ as well. Throughout the derivation of (3.29) and (3.30), no approximations beside the ones implied in the *Boltzmann* transport equation described in Section 3.2.2 were made.

3.5.3 A Hierarchy of Transport Models

In the following sections, the method of moment is applied to *Boltzmann*'s equation in order to systematically derive a set of equations for the carriers within a semiconductor. Depending on the number of equations involved, different levels of physical complexity can be described with the according models. Furthermore, additional driving forces caused by graded material alloys and hetero–structures can be considered or neglected, dependent on the device under analysis. All models have *Poisson*'s equation in common, describing electrostatics within the device.

The simplest model is the isothermal drift–diffusion model, which is also accessible by a phenomenological approach. It consists of carrier balance equations and current equations for electrons and holes, respectively accounting for carrier drift induced by external driving forces as well as diffusion. The unknowns for the equation system are the electrostatic potential and carrier densities as well as current densities for both electrons and holes.

For the treatment of non–isothermal conditions the lattice temperature has to be included as an additional solution variable. The temperature is addressed by the heat–flow equation, which has to be solved self–consistently with the carrier balance and flux equations. For the non–isothermal drift–diffusion model, the equation series is truncated after the first moment and the equation system is closed by the condition of local thermal equilibrium $\langle\mathcal{E}\rangle_\nu = \langle\mathcal{E}\rangle_\mathrm{L}$. An elaborate discussion of the energy exchange between carriers and lattice is given in Section 3.5.10 and Section 3.5.11 based on a systematic and a phenomenological thermodynamic approach, respectively.

The set of models incorporating equations up to the first moment — the particle current equations — is able to accurately describe the behavior of comparably large structures. Their only parameters are the carrier mobilities, which are easily accessible by measurement. Besides their dependencies on temperature and dopant concentration, the mobilities depend on the shape of the distribution function. However, due to the lack of additional information incorporated in the equation system, they are modeled as field dependent. This approximation incorporates the neglection of non–local effects such as the velocity–overshoot [85], which can be addressed by proper modeling of an energy–dependent mobility. In small devices, non–local effects play an important role and the assumption of local thermal equilibrium breaks down, since carriers gain energy from strong electric fields and carrier temperatures much above the lattice temperatures are possible.

In order to include appropriate description of carriers driven far from equilibrium, the carrier energies as well as the according energy fluxes have to be included as additional solution variables. In order to maintain the additional unknowns, the energy balance equation as well as the energy flux equation for each of the carrier subsystems is included. In terms of the method of moments, the highest–order moment is the third one. This class of transport models is referred to as hydrodynamic transport models [86].

The systematic approach to the formulation of transport models can be continued by the inclusion of further equations obtained by higher moments of the *Boltzmann* transport equation. With each moment, more information on the carrier distribution function is included. A truncation after the fifth moment results in the six moments model including the kurtosis as well as the according flux as additional unknowns [76, 78, 87]. However, the consideration of these high moments is only of importance in devices driven far from equilibrium, such as modern CMOS devices of the deca–nanometer regime used in today's microprocessors and DRAM memories. In this work, transport models including equations up to the third moment are derived in order to accurately reproduce the energy relations within large thermoelectric devices.

3.5.4 Relaxation Time Approximation

In order to obtain an expression for the right hand side of (3.29) that can be handled analytically, a commonly used simplification — the relaxation time approximation is introduced [73]. For small deviations of the distribution function f from its equilibrium state f_0, the collision term can be expressed by [79]

$$\mathcal{Q}(f) = -\frac{f - f_0}{\tau_f} \,. \tag{3.31}$$

Within this formulation, the distribution function f relaxes to its equilibrium state f_0 with the time constant τ_f after removing all driving forces.

The moments of the collision term can be modeled following different strategies. *Bløtekjær* proposed a set of one single relaxation time for each macroscopic moment derived [88], thus the according formulations read

$$\mathcal{Q}(x) \approx -\frac{\langle\langle X \rangle\rangle - \langle\langle X_0 \rangle\rangle}{\tau_x} = \frac{x - x_0}{\tau_x} \tag{3.32}$$

$$\mathcal{Q}(\boldsymbol{j}_x) \approx -\frac{\langle\langle \boldsymbol{X} \rangle\rangle - \langle\langle \boldsymbol{X}_0 \rangle\rangle}{\tau_{j_x}} = \frac{\boldsymbol{j}_x}{\tau_{j_x}} \tag{3.33}$$

for macroscopic balance and flux equations, respectively. In equilibrium, all averages of vector–valued weights vanish, thus $\langle\langle \boldsymbol{X}_0 \rangle\rangle = 0$. The relaxation times τ_x and τ_{j_x} are generally dependent on the distribution function and represent the parameters of the transport model. In order to gain accurate results, they have to be carefully calibrated. However, only the particle flux relaxation time, which is connected to the carrier mobility is accessible by measurement. Models for all other relaxation times can be extracted from Monte–Carlo simulations, which incorporate information on the full distribution function. In order to obtain a closed formulation of the transport model, the relaxation times have to be modeled with respect to quantities available in the macroscopic transport model.

In contrast to the macroscopic relaxation time approximation applied in *Bløtekjær*'s approach, *Stratton*'s ansatz incorporates one microscopic relaxation time τ for the entire transport model that describes the scattering of single carriers. Therefrom, the according formulation for the collision term reads

$$\mathcal{Q}(\boldsymbol{j}_x) = -\left\langle\!\!\left\langle \frac{\boldsymbol{j}_X}{\tau_f} \right\rangle\!\!\right\rangle . \tag{3.34}$$

The weights for the odd moment equations are chosen in a way that the right sides become the fluxes themselves. As a consequence, additional terms in the flux equations appear, which are systematically derived and analyzed in the sequel. The relaxation time τ is often modeled to depend on the energy by a power law

$$\tau_f \approx \tau_0 \left(\frac{\mathcal{E}}{\mathcal{E}_0}\right)^{r_\nu} , \tag{3.35}$$

which enables the analytical treatment of several integrals. Depending on the dominant scattering mechanism, the scattering parameter r_ν takes values between $-1/2$ for acoustic phonon scattering and $3/2$ for ionized impurity scattering. While expression (3.35) is valid with a constant τ_0 for acoustic phonon scattering, τ_0 is slightly energy dependent for ionized impurity scattering [73].

3.5.5 ***Stratton***'s Approach

Stratton proposed to formulate the collision term using one single microscopic relaxation time. Usually, this relaxation time, τ, is modeled to be energy dependent. In order to obtain the fluxes on the right side of the governed flux equations directly, the weights for the derivation are chosen as

$$X = (1, \tau\boldsymbol{p}, \mathcal{E}, \tau\mathcal{E}\boldsymbol{p}) \; . \tag{3.36}$$

During the following derivation, several assumptions and simplifications are sequentially introduced. The assumptions made throughout the derivation of this transport model are as follows:

- Microscopic relaxation time approximation
- Time derivatives are neglected in the flux equations
- Product ansatz for the kinetic energy
- The tensor valued transport parameters are estimated by their traces
- Power–law approximation $\tau = \tau_0 \left(\frac{\mathcal{E}}{\mathcal{E}_0}\right)^{r_\nu}$ for the microscopic relaxation time
- Parabolic band structure
- Linearized heated displaced *Maxwell*ian distribution function for the closure relation
- $\boldsymbol{k}$–independent r_ν

3.5.5.1 Carrier Balance Equation

The derivation of the continuity equation is trivial starting from equation (3.29). Inserting the weight $X = 1$ results in a vanishing *Poisson* bracket because of (A.9) as well as a vanishing field term. Thus, the continuity equation for carriers reads

$$\partial_t \nu + \nabla_{\boldsymbol{r}} \cdot \boldsymbol{j}_\nu = -R \, . \tag{3.37}$$

The systematically derived equation is what can also be expected from a phenomenological point of view: The increase of carriers within a certain volume has to be equal to the influx minus the net recombination rate within this volume.

3.5.5.2 Particle Flux Equation

In the following, the particle flux equation is derived, whereby the starting point is *Boltzmann*'s equation with a general vector–valued weight $\boldsymbol{X}$ in the form of equation (3.30). For the flux equations, the time derivative (first term in (3.30)) can be safely neglected, since the relaxation time is in the order of picoseconds, which ensures quasi–stationary behavior even for today's fastest signals [87]. This means that a transient signal must only change as fast as the carriers are available to follow into a new equilibrium state.

Inserting $\tau\boldsymbol{p}$ as $\boldsymbol{X}$ into (3.30) delivers the particle current equation in its original form which serves as a basis for further derivations

$$\underbrace{\nabla_{\boldsymbol{r}} \cdot \langle\!\langle \tau\boldsymbol{p} \otimes \boldsymbol{v} \rangle\!\rangle}_{\text{(i)}} - \underbrace{\langle\!\langle \{\tau\boldsymbol{p}, \mathcal{E}\} \rangle\!\rangle}_{\text{(ii)}} + \underbrace{\mathrm{s}_\nu \mathrm{q} \left\langle\!\!\left\langle \frac{1}{\hbar}\nabla_{\boldsymbol{k}} \otimes (\tau\boldsymbol{p}) \right\rangle\!\!\right\rangle \cdot \nabla_{\boldsymbol{r}}\tilde{\varphi}}_{\text{(iii)}} = -\langle\!\langle \boldsymbol{p} \rangle\!\rangle \,. \tag{3.38}$$

The single contributions to the left side can be identified as a diffusion term (i) and two drift terms (ii) and (iii), whereby the latter one is caused by external electric fields (iii). In the sequel, these terms are subject to several simplifications caused by assumptions on the distribution function, the band structure, and the relaxation time.

Equation (3.38) contains statistical averages of tensor–valued quantities, which are subject to closer investigation in the following. With the assumption of an almost isotropic distribution function, the non–diagonal elements of the tensors are negligible. For a hot, slowly drifting electron gas, such as discussed in Sections 3.4 and 3.5.1, the influence of the displacement on the averages of even weights, such as energy–like tensors is negligible [84]. Thus, each of the terms can be represented by proper scalar quantities, which are expressed using traces of the corresponding tensor–valued transport parameters. For example, $\boldsymbol{p} \otimes \boldsymbol{v}$ can be estimated using

$$\boldsymbol{p} \otimes \boldsymbol{v} = \begin{pmatrix} p_x v_x & p_x v_y & p_x v_z \\ p_y v_x & p_y v_y & p_y v_z \\ p_z v_x & p_z v_y & p_z v_z \end{pmatrix} \approx \frac{p_x v_x + p_y v_y + p_z v_z}{3}\hat{\mathrm{I}} = \frac{1}{3}\,\mathrm{tr}\,(\boldsymbol{p} \otimes \boldsymbol{v})\hat{\mathrm{I}} \,. \tag{3.39}$$

Monte–Carlo simulations indicate the validity of this approximation. It turned out that for the case sketched above, the non–diagonal elements are about five magnitudes smaller than the diagonal elements. In low field cases, the assumption of isotropy is fulfilled very well for the materials taken into account in this work.

In order to incorporate the band structure in an analytical way, assumptions on the dispersion relation as discussed in Section 3.3 have to be made. In order to obtain a mathematically convenient formulation, a product ansatz for the kinetic energy separating the dependencies on $\boldsymbol{r}$ and $\boldsymbol{k}$ is performed

$$\mathcal{E}(\boldsymbol{r}, \boldsymbol{k}) = \theta^{\mathcal{E}}_{\boldsymbol{r}}(\boldsymbol{r})\theta^{\mathcal{E}}_{\boldsymbol{k}}(\boldsymbol{k}) \,, \tag{3.40}$$

which will be expressed by parabolic bands later on in this derivation. As a direct consequence, the energy's gradients in $\boldsymbol{r}$– and $\boldsymbol{k}$–space read

$$\nabla_{\boldsymbol{r}}\mathcal{E} = \theta^{\mathcal{E}}_{\boldsymbol{k}}\nabla_{\boldsymbol{r}}\theta^{\mathcal{E}}_{\boldsymbol{r}} = \mathcal{E}\nabla_{\boldsymbol{r}} \ln \theta^{\mathcal{E}}_{\boldsymbol{r}} \,, \tag{3.41}$$

$$\frac{1}{\hbar}\nabla_{\boldsymbol{k}}\mathcal{E} = \boldsymbol{v} = \theta^{\mathcal{E}}_{\boldsymbol{r}}\frac{1}{\hbar}\nabla_{\boldsymbol{k}}\theta^{\mathcal{E}}_{\boldsymbol{k}} = \mathcal{E}\frac{1}{\hbar}\nabla_{\boldsymbol{k}} \ln \theta^{\mathcal{E}}_{\boldsymbol{k}} \,. \tag{3.42}$$

It is useful to introduce a non–parabolicity factor $\gamma(\boldsymbol{k})$ which becomes 1 for parabolic bands. Thus, the velocity reads

$$\boldsymbol{v} = \mathcal{E}\frac{1}{\hbar}\nabla_{\boldsymbol{k}} \ln \theta^{\mathcal{E}}_{\boldsymbol{k}} = \mathcal{E}\frac{1}{\hbar}\partial_{\boldsymbol{k}} \ln \theta^{\mathcal{E}}_{\boldsymbol{k}}\frac{\boldsymbol{p}}{p} = \mathcal{E}\gamma\frac{2\boldsymbol{p}}{p^2} \quad \text{with} \quad \gamma = \frac{1}{\hbar}\partial_{\boldsymbol{k}} \ln \theta^{\mathcal{E}}_{\boldsymbol{k}}\frac{p}{2}\,. \tag{3.43}$$

In the following, the three parts of equation (3.38) indicated by the horizontal braces are sequentially treated. Applying Eqs. (3.39) and (3.43) to equation (3.38), part (i), one obtains

$$\nabla_{\boldsymbol{r}} \cdot \left\langle\!\!\left\langle \tau\boldsymbol{p} \otimes \boldsymbol{p}\mathcal{E}\gamma\frac{2}{p^2} \right\rangle\!\!\right\rangle \approx \frac{2}{3}\nabla_{\boldsymbol{r}}\langle\!\langle \tau\mathcal{E}\gamma \rangle\!\rangle\,. \tag{3.44}$$

For the second part of equation (3.38), the *Poisson* bracket has to be expanded using (A.10) as well as the definitions for the *Poisson* bracket, equations (A.1) and (A.6)

$$\begin{aligned}\langle\!\langle \{\tau\boldsymbol{p}, \mathcal{E}\} \rangle\!\rangle &= \langle\!\langle \tau\{\boldsymbol{p}, \mathcal{E}\} + \boldsymbol{p}\{\tau, \mathcal{E}\} \rangle\!\rangle \\ &= \left\langle\!\!\left\langle \tau\left((\nabla_{\boldsymbol{r}} \otimes \boldsymbol{p}) \cdot \boldsymbol{v} - \left(\frac{1}{\hbar}\nabla_{\boldsymbol{k}} \otimes \boldsymbol{p}\right) \cdot \nabla_{\boldsymbol{r}}\mathcal{E} \right) \right\rangle\!\!\right\rangle \\ &\quad + \left\langle\!\!\left\langle \boldsymbol{p}\left((\nabla_{\boldsymbol{r}}\tau) \cdot \boldsymbol{v} - \frac{1}{\hbar}\nabla_{\boldsymbol{k}}\tau \cdot \nabla_{\boldsymbol{r}}\mathcal{E} \right) \right\rangle\!\!\right\rangle\end{aligned} \tag{3.45}$$

The first term vanishes due to the momentum being orthogonal to the space vector, and finally the approximation for tensor valued quantities (3.39) and the application of identity (B.5) leads to

$$\begin{aligned}&\left\langle\!\!\left\langle -\tau\mathcal{E}\nabla_{\boldsymbol{r}} \ln \theta^{\mathcal{E}}_{\boldsymbol{r}} + \boldsymbol{p}\left(\boldsymbol{v} \cdot (\nabla_{\boldsymbol{r}}\tau) - \boldsymbol{p}\frac{1}{\hbar}\nabla_{\boldsymbol{k}}\tau \cdot \nabla_{\boldsymbol{r}}\mathcal{E} \right) \right\rangle\!\!\right\rangle \\ &= -\langle\!\langle \tau\mathcal{E} \rangle\!\rangle\nabla_{\boldsymbol{r}} \ln \theta^{\mathcal{E}}_{\boldsymbol{r}} + \langle\!\langle (\boldsymbol{p} \otimes \boldsymbol{v}) \cdot \nabla_{\boldsymbol{r}}\tau \rangle\!\rangle - \left\langle\!\!\left\langle \boldsymbol{p}\frac{1}{\hbar}\nabla_{\boldsymbol{k}}\tau \cdot \mathcal{E}\nabla_{\boldsymbol{r}} \ln \theta^{\mathcal{E}}_{\boldsymbol{r}} \right\rangle\!\!\right\rangle \\ &= -\langle\!\langle \tau\mathcal{E} \rangle\!\rangle\nabla_{\boldsymbol{r}} \ln \theta^{\mathcal{E}}_{\boldsymbol{r}} + \frac{2}{3}\langle\!\langle \mathcal{E}\gamma\nabla_{\boldsymbol{r}}\tau \rangle\!\rangle - \frac{1}{3}\left\langle\!\!\left\langle \mathcal{E}\boldsymbol{p} \cdot \frac{1}{\hbar}\nabla_{\boldsymbol{k}}\tau \right\rangle\!\!\right\rangle\nabla_{\boldsymbol{r}} \ln \theta^{\mathcal{E}}_{\boldsymbol{r}}\,.\end{aligned} \tag{3.46}$$

Part (iii) of equation (3.38) has to be converted using identity (B.4) before the trace approximation can be performed, which leads to

$$\mathrm{q}\left\langle\!\!\left\langle \frac{1}{\hbar}\nabla_{\boldsymbol{k}} \otimes (\tau\boldsymbol{p}) \right\rangle\!\!\right\rangle \cdot \nabla_{\boldsymbol{r}}\tilde{\varphi} = \mathrm{q}\langle\!\langle \tau \rangle\!\rangle\nabla_{\boldsymbol{r}}\tilde{\varphi} + \mathrm{q}\left\langle\!\!\left\langle \frac{p}{3}\frac{1}{\hbar}\partial_{\boldsymbol{k}}\tau \right\rangle\!\!\right\rangle\nabla_{\boldsymbol{r}}\tilde{\varphi}\,. \tag{3.47}$$

Assembling the terms (i) – (iii) again, the isotropic particle current equation with a product ansatz used on the kinetic energy $\mathcal{E}$ is obtained

$$\begin{aligned}\langle\!\langle \boldsymbol{p} \rangle\!\rangle = &\frac{2}{3}\nabla_{\boldsymbol{r}}\langle\!\langle \tau\mathcal{E}\gamma \rangle\!\rangle + \langle\!\langle \tau\mathcal{E} \rangle\!\rangle\nabla_{\boldsymbol{r}} \ln \theta^{\mathcal{E}}_{\boldsymbol{r}} \\ &- \frac{2}{3}\langle\!\langle \mathcal{E}\gamma\nabla_{\boldsymbol{r}}\tau \rangle\!\rangle + \frac{1}{3}\left\langle\!\!\left\langle \mathcal{E}\boldsymbol{p} \cdot \frac{1}{\hbar}\nabla_{\boldsymbol{k}}\tau \right\rangle\!\!\right\rangle\nabla_{\boldsymbol{r}} \ln \theta^{\mathcal{E}}_{\boldsymbol{r}} \\ &+ \mathrm{s}_\nu\mathrm{q}\langle\!\langle \tau \rangle\!\rangle\nabla_{\boldsymbol{r}}\tilde{\varphi} - \mathrm{q}\left\langle\!\!\left\langle \frac{p}{3}\frac{1}{\hbar}\partial_{\boldsymbol{k}}\tau \right\rangle\!\!\right\rangle\nabla_{\boldsymbol{r}}\tilde{\varphi}\,.\end{aligned} \tag{3.48}$$

In order to obtain a closed formulation, the relaxation time has to be parametrized with macroscopic quantities available in the equation system. Thus, a power–law approximation is introduced as discussed in Section 3.5.4. The according reference energy $\mathcal{E}_0$ refers to the energy in local thermal equilibrium with the lattice and thus incorporates the lattice temperature. τ is expressed as

$$\tau = \tau_0 \left(\frac{\mathcal{E}}{\mathcal{E}_0}\right)^{r_\nu} = \tau_0 \left(\frac{\mathcal{E}}{k_\mathrm{B} T_\mathrm{L}}\right)^{r_\nu} . \tag{3.49}$$

Inserting (3.49) to (3.48) yields

$$\begin{aligned} \langle\!\langle \boldsymbol{p} \rangle\!\rangle = {} & \frac{2}{3}\nabla_{\boldsymbol{r}} \left(\tau_0 \frac{1}{(k_\mathrm{B}T_\mathrm{L})^{r_\nu}} \langle\!\langle \mathcal{E}^{r_\nu+1} \rangle\!\rangle\right) \\ & + \tau_0 \frac{1}{(k_\mathrm{B}T_\mathrm{L})^{r_\nu}} \langle\!\langle \mathcal{E}^{r_\nu+1} \rangle\!\rangle \nabla_{\boldsymbol{r}} \ln \theta_{\boldsymbol{r}}^{\mathcal{E}} - \frac{2}{3}\tau_0 \left\langle\!\!\left\langle \mathcal{E}\gamma\nabla_{\boldsymbol{r}} \left(\frac{\mathcal{E}}{k_\mathrm{B}T_\mathrm{L}}\right)^{r_\nu} \right\rangle\!\!\right\rangle + \left\langle\!\!\left\langle \mathcal{E} \frac{\tau_0}{(k_\mathrm{B}T_\mathrm{L})^{r_\nu}} \boldsymbol{v} \right\rangle\!\!\right\rangle \cdot \nabla_{\boldsymbol{r}} \ln \theta_{\boldsymbol{r}}^{\mathcal{E}} \\ & + \mathrm{s}_\nu \mathrm{q} \tau_0 \frac{1}{(k_\mathrm{B}T_\mathrm{L})^{r_\nu}} \langle\!\langle \mathcal{E}^{r_\nu} \rangle\!\rangle \nabla_{\boldsymbol{r}} \tilde{\varphi} + \mathrm{s}_\nu \mathrm{q} \tau_0 \frac{1}{(k_\mathrm{B}T_\mathrm{L})^{r_\nu}} \left\langle\!\!\left\langle \frac{p}{3}\frac{1}{\hbar} \partial_{\boldsymbol{k}} \mathcal{E}^{r_\nu} \right\rangle\!\!\right\rangle \nabla_{\boldsymbol{r}} \tilde{\varphi} . \end{aligned} \tag{3.50}$$

In order to close the equation system, a heated, displaced *Maxwell*ian in the diffusion approximation (3.18) is assumed. This approximation is justified by the comparably low drift velocities in thermoelectric devices. Furthermore, parabolic bands (3.13) are introduced

$$f = A \left(1 + \frac{\boldsymbol{p}\cdot\boldsymbol{v}_0}{k_\mathrm{B}T_\nu}\right) \mathrm{e}^{-\frac{\mathcal{E}(\boldsymbol{k})}{k_\mathrm{B}T_\nu}} \quad \text{and} \quad \mathcal{E} = \frac{\hbar^2 \boldsymbol{k}^2}{2m^*} . \tag{3.51}$$

With these assumptions, the average in (i) is first transformed to polar coordinates and furthermore to an integral in $\mathcal{E}$–space and the gamma function can be identified. The integral over the odd term of the distribution function

$$f_A = A \frac{\boldsymbol{p}\cdot\boldsymbol{v}_0}{k_\mathrm{B}T_\nu} \mathrm{e}^{-\frac{\mathcal{E}(\boldsymbol{k})}{k_\mathrm{B}T_\nu}} \tag{3.52}$$

vanishes, since the product of an even and an odd function results in an odd function

$$\begin{aligned} \langle\!\langle \mathcal{E}^{r_\nu+1} \rangle\!\rangle & = \iiint\limits_{-\infty}^{\infty} \mathcal{E}^{r_\nu+1} A \left(1 + \frac{\boldsymbol{p}\cdot\boldsymbol{v}_0}{k_\mathrm{B}T_\nu}\right) \mathrm{e}^{-\frac{\mathcal{E}(\boldsymbol{k})}{k_\mathrm{B}T_\nu}} \, \mathrm{d}k_x \, \mathrm{d}k_y \, \mathrm{d}k_z \\ & = 4\pi A \int\limits_0^\infty \mathcal{E}^{r_\nu+1} k^2 \mathrm{e}^{-\frac{\mathcal{E}(k)}{k_\mathrm{B}T_\nu}} \, \mathrm{d}k = && \left| \mathcal{E} = \frac{\hbar^2 k^2}{2m^*} , \quad \frac{\mathrm{d}\mathcal{E}}{\mathrm{d}k} = \frac{\hbar^2 k}{m^*} \right. \\ & = \frac{4\pi\sqrt{2}m^{*\frac{3}{2}}}{\hbar^3} A \int \mathcal{E}^{r_\nu+\frac{3}{2}} \mathrm{e}^{-\frac{\mathcal{E}}{k_\mathrm{B}T_\nu}} \, \mathrm{d}\mathcal{E} = && \left| \Gamma(\zeta) = \int\limits_0^\infty \mathcal{E}^{\zeta-1} \mathrm{e}^{-\mathcal{E}} \, \mathrm{d}\mathcal{E} \right. \\ & = \frac{4\pi\sqrt{2}m^{*\frac{3}{2}}}{\hbar^3} A \left(k_\mathrm{B}T_\nu\right)^{r_\nu+\frac{5}{2}} \Gamma\left(r_\nu + \frac{5}{2}\right) . \end{aligned} \tag{3.53}$$

The integral for the carrier density is derived analogously, and yields

$$\nu = \langle\!\langle 1 \rangle\!\rangle = \frac{2}{3} \frac{4\pi\sqrt{2}m^{*\frac{3}{2}}}{\hbar^3} A \left(k_\mathrm{B}T_\nu\right)^{\frac{3}{2}} \Gamma\left(\frac{3}{2}\right) \tag{3.54}$$

whereby the identity $\zeta\Gamma(\zeta) = \Gamma(\zeta+1)$ has been applied. The carrier concentration is introduced to normalize (3.50). Finally, the carrier mobility is obtained from a coefficient comparison for the homogeneous case as [73]

$$\mu_\nu = \frac{\mathrm{q}}{m^*} \frac{\langle\!\langle \mathcal{E}\tau \rangle\!\rangle}{\langle\!\langle \mathcal{E} \rangle\!\rangle} = \frac{\mathrm{q}\tau_0}{m^*} \left(\frac{T_\nu}{T_\mathrm{L}}\right)^{r_\nu} \frac{\Gamma\left(r_\nu + \frac{5}{2}\right)}{\Gamma\left(\frac{5}{2}\right)} , \tag{3.55}$$

for a heated, displaced *Maxwell*ian. Inserting equations (3.54) and (3.55) to (3.53), part (i) becomes

$$\frac{2}{3}\nabla_{\boldsymbol{r}}\left(\tau_0\frac{1}{k_\mathrm{B}T_\mathrm{L}^{r_\nu}}\frac{3}{2}\nu\left(k_\mathrm{B}T_\nu\right)^{r_\nu+1}\frac{\Gamma\left(r_\nu+\frac{5}{2}\right)}{\Gamma\left(\frac{5}{2}\right)}\right)=\frac{k_\mathrm{B}}{\mathrm{q}}\nabla_{\boldsymbol{r}}\left(\mu_\nu\nu T_\nu m^*\right)\,. \tag{3.56}$$

Parts (ii) and (iii) can be treated as described above. The gradient in the second average has to be expanded resulting in the sum of two expressions, a $\nabla_{\boldsymbol{r}}\ln m^*$ and a $\nabla_{\boldsymbol{r}}T_\mathrm{L}$ term. The average needed for the expressions of part (iii) can be derived analogously to (3.53) and results in

$$\langle\!\langle\mathcal{E}^{r_\nu}\rangle\!\rangle=\frac{3}{2}\left(k_\mathrm{B}T_\nu\right)^{r_\nu}\frac{\Gamma\left(r_\nu+\frac{3}{2}\right)}{\Gamma\left(\frac{5}{2}\right)}\,. \tag{3.57}$$

Assembling the three parts and inserting the definition of the particle flux

$$\boldsymbol{j}_\nu=\langle\!\langle\boldsymbol{v}\rangle\!\rangle=\frac{1}{m^*}\langle\!\langle\boldsymbol{p}\rangle\!\rangle \tag{3.58}$$

results in the final isotropic particle flux equation obtained using a power–law approximation for the microscopic relaxation time, parabolic bands and a heated, displaced *Maxwell*ian

$$\boldsymbol{j}_\nu=-\frac{k_\mathrm{B}}{\mathrm{q}m^*}\nabla_{\boldsymbol{r}}\left(\mu_\nu\nu T_\nu m^*\right)+\frac{3}{2}\mu_\nu\nu\frac{k_\mathrm{B}}{\mathrm{q}}T_\nu\nabla_{\boldsymbol{r}}\ln m^*-r_\nu\mu_\nu\nu\frac{k_\mathrm{B}}{\mathrm{q}}\frac{T_\nu}{T_\mathrm{L}}\nabla_{\boldsymbol{r}}T_\mathrm{L}-\mathrm{s}_\nu\mu_\nu\nu\nabla_{\boldsymbol{r}}\tilde{\varphi}\,. \tag{3.59}$$

An alternative formulation of the current equation is obtained by combining the gradients of the carrier concentration ν and the effective mass m^* to the chemical potential which itself is summed up with the electrostatic potential $\tilde{\varphi}$ to the electrochemical potential Φ_ν. Therefore, the effective density of states is introduced [89], which is proportional to m^* and T

$$N_\mathrm{c,v}=N_0\left(m^*T_\nu\right)^{3/2}\,, \tag{3.60}$$

where N_0 reads for a *Maxwell*ian distribution function

$$N_0=2M_\mathrm{c,v}\left(\frac{k_\mathrm{B}}{2\pi\hbar}\right)^{3/2}\,. \tag{3.61}$$

The chemical potential Φ_ν^c and the electrochemical potential Φ_ν are introduced as

$$\Phi_\nu=\tilde{\varphi}+\mathrm{s}_\nu\Phi_\nu^\mathrm{c}=\tilde{\varphi}+\mathrm{s}_\nu\frac{k_\mathrm{B}T_\nu}{\mathrm{q}}\ln\frac{\nu}{N_\mathrm{c,v}}\,. \tag{3.62}$$

Applying Eqs. (3.60) and (3.62) to the particle current (3.59) yields

$$\begin{aligned}\boldsymbol{j}_\nu=&-\mathrm{s}_\nu\mu_\nu\nu\nabla_{\boldsymbol{r}}\Phi_\nu-\frac{k_\mathrm{B}}{\mathrm{q}}\left(\frac{5}{2}-\ln\frac{\nu}{N_\mathrm{c,v}}\right)\mu_\nu\nu\nabla_{\boldsymbol{r}}T_\nu\\&-\frac{k_\mathrm{B}T_\nu}{\mathrm{q}}\mu_\nu\nu\nabla_{\boldsymbol{r}}\ln m^*-\frac{k_\mathrm{B}T_\nu}{\mathrm{q}}\nu\nabla_{\boldsymbol{r}}\mu_\nu-r_\nu\mu_\nu\nu\frac{k_\mathrm{B}}{\mathrm{q}}\frac{T_\nu}{T_\mathrm{L}}\nabla_{\boldsymbol{r}}T_\mathrm{L}\,.\end{aligned} \tag{3.63}$$

3.5.5.3 Energy Balance Equation

For the weight $X = \mathcal{E}$, the energy balance equation is obtained. Starting from (3.29) with a microscopic relaxation time approximation, one obtains

$$\partial_t w + \nabla_{\boldsymbol{r}} \cdot \boldsymbol{j}_\nu^{\mathrm{u}} - \langle\!\langle \{\mathcal{E},\mathcal{E}\} \rangle\!\rangle + \mathrm{s}_\nu \mathrm{q} \left\langle\!\!\left\langle \frac{1}{\hbar}\nabla_{\boldsymbol{k}}\mathcal{E} \right\rangle\!\!\right\rangle \cdot \nabla_{\boldsymbol{r}}\tilde{\varphi} = -\frac{\langle\!\langle \mathcal{E}\rangle\!\rangle - \langle\!\langle \mathcal{E}_0\rangle\!\rangle}{\tau} + G_\nu^{\mathcal{E}} . \tag{3.64}$$

While the *Poisson* bracket in the second term vanishes according to (A.8), the average in the third term can be identified as the particle current. $G_\nu^{\mathcal{E}}$ represents the net energy generation rate by recombination processes. Assuming *Boltzmann* statistics in the diffusion approximation, the averages on the right side can be expressed as $3/2\nu k_{\mathrm{B}} T_\nu$ and $3/2\nu k_{\mathrm{B}} T_{\mathrm{L}}$, respectively. Thus, the final energy balance equation reads

$$\frac{3}{2} k_{\mathrm{B}} \partial_t T_\nu + \nabla_{\boldsymbol{r}} \cdot \boldsymbol{j}_\nu^{\mathrm{u}} + \mathrm{s}_\nu \mathrm{q} \boldsymbol{j}_\nu \cdot \nabla_{\boldsymbol{r}}\tilde{\varphi} + \frac{3}{2}\nu k_{\mathrm{B}} \frac{T_\nu - T_{\mathrm{L}}}{\tau} - G_\nu^{\mathcal{E}} = 0 . \tag{3.65}$$

Having a closer look at the final result, one can easily recognize the total energy conservation character of this equation. The change of total energy within an infinitesimal small volume is equal to the energy influx minus the energy exchanged with the lattice. In the homogeneous case without external driving forces, the last term ensures the relaxation of the carrier temperature T_ν to T_{L}.

3.5.5.4 Energy Flux Equation

The energy flux equation is obtained analogously to the particle current equation starting from equation (3.30) with the weight $\boldsymbol{X} = \tau\mathcal{E}\boldsymbol{p}$

$$\underbrace{\nabla_{\boldsymbol{r}} \left(\langle\!\langle \tau\mathcal{E}\boldsymbol{p} \otimes \boldsymbol{v} \rangle\!\rangle\right)}_{\text{(i)}} - \underbrace{\langle\!\langle \{\tau\mathcal{E}\boldsymbol{p},\mathcal{E}\} \rangle\!\rangle}_{\text{(ii)}} + \underbrace{\mathrm{s}_\nu \mathrm{q} \left\langle\!\!\left\langle \frac{1}{\hbar}\nabla_{\boldsymbol{k}} \otimes (\tau\mathcal{E}\boldsymbol{p}) \right\rangle\!\!\right\rangle \cdot \nabla_{\boldsymbol{r}}\tilde{\varphi}}_{\text{(iii)}} = -\nu\langle \mathcal{E}\boldsymbol{p}\rangle \tag{3.66}$$

The estimation of all tensor valued quantities with their traces as outlined in (3.39) as well as the expansion of the kinetic energy $\mathcal{E}$ using the product ansatz (3.40) are applied on equation (3.66). Part (i) is straight–forward

$$\nabla_{\boldsymbol{r}} \langle\!\langle \tau\mathcal{E}\boldsymbol{p} \otimes \boldsymbol{v} \rangle\!\rangle = \frac{2}{3}\nabla_{\boldsymbol{r}} \langle\!\langle \tau\mathcal{E}^2\gamma \rangle\!\rangle . \tag{3.67}$$

The *Poisson* bracket in part (ii) has to be expanded using (A.10)

$$\langle\!\langle \{\tau\mathcal{E}\boldsymbol{p},\mathcal{E}\} \rangle\!\rangle = \langle\!\langle \mathcal{E}\{\tau\boldsymbol{p},\mathcal{E}\} + \tau\boldsymbol{p}\{\mathcal{E},\mathcal{E}\} \rangle\!\rangle . \tag{3.68}$$

The second term vanishes because of (A.8) while the first term is treated according to (3.45) and yields

$$-\langle\!\langle \mathcal{E}^2\tau \rangle\!\rangle \nabla_{\boldsymbol{r}} \ln\theta_{\boldsymbol{r}}^{\mathcal{E}} + \frac{2}{3}\langle\!\langle \mathcal{E}^2\gamma\nabla_{\boldsymbol{r}}\tau \rangle\!\rangle - \frac{1}{3}\left\langle\!\!\left\langle \mathcal{E}^2\boldsymbol{p} \cdot \frac{1}{\hbar}\nabla_{\boldsymbol{k}}\tau \right\rangle\!\!\right\rangle \nabla_{\boldsymbol{r}} \ln\theta_{\boldsymbol{r}}^{\mathcal{E}} . \tag{3.69}$$

Application of identity (B.4) to part (iii) and assembly of all three terms results in

$$\begin{aligned}\langle\!\langle \mathcal{E}\boldsymbol{p}\rangle\!\rangle = {}& \frac{2}{3}\nabla_{\boldsymbol{r}}\langle\!\langle \tau\mathcal{E}^2\gamma\rangle\!\rangle \\ & + \langle\!\langle \mathcal{E}^2\tau\rangle\!\rangle\nabla_{\boldsymbol{r}}\ln\theta_{\boldsymbol{r}}^{\mathcal{E}} - \frac{2}{3}\langle\!\langle \mathcal{E}^2\gamma\nabla_{\boldsymbol{r}}\tau\rangle\!\rangle + \frac{1}{3}\left\langle\!\!\left\langle \mathcal{E}^2\boldsymbol{p}\cdot\frac{1}{\hbar}\nabla_{\boldsymbol{k}}\tau\right\rangle\!\!\right\rangle\nabla_{\boldsymbol{r}}\ln\theta_{\boldsymbol{r}}^{\mathcal{E}} \\ & + \mathrm{s}_\nu\mathrm{q}\langle\!\langle \tau\mathcal{E}\rangle\!\rangle\nabla_{\boldsymbol{r}}\tilde{\varphi} - \frac{1}{3}\mathrm{q}\left\langle\!\!\left\langle p\frac{1}{\hbar}\partial_{\boldsymbol{k}}\left(\tau\mathcal{E}\right)\right\rangle\!\!\right\rangle\nabla_{\boldsymbol{r}}\tilde{\varphi}\,.\end{aligned} \tag{3.70}$$

Next, the power–law ansatz is introduced for the relaxation time τ

$$\begin{aligned}\langle\!\langle \mathcal{E}\boldsymbol{p}\rangle\!\rangle = {}& \frac{2}{3}\tau_0\nabla_{\boldsymbol{r}}\left(\left(k_\mathrm{B}T_\mathrm{L}\right)^{-r_\nu}\langle\!\langle \mathcal{E}^{r_\nu+2}\gamma\rangle\!\rangle\right) \\ & + \tau_0\left(k_\mathrm{B}T_\mathrm{L}\right)^{-r_\nu}\langle\!\langle \mathcal{E}^{r_\nu+2}\rangle\!\rangle\nabla_{\boldsymbol{r}}\ln\theta_{\boldsymbol{r}}^{\mathcal{E}} - \frac{2}{3}\tau_0\left\langle\!\!\left\langle \mathcal{E}^2\gamma\nabla_{\boldsymbol{r}}\left(\frac{\mathcal{E}}{k_\mathrm{B}T_\mathrm{L}}\right)^{r_\nu}\right\rangle\!\!\right\rangle \\ & + \frac{1}{3}\tau_0\left(k_\mathrm{B}T_\mathrm{L}\right)^{-r_\nu}\left\langle\!\!\left\langle \mathcal{E}^2\boldsymbol{p}\cdot\frac{1}{\hbar}\nabla_{\boldsymbol{k}}\mathcal{E}^{r_\nu}\right\rangle\!\!\right\rangle\nabla_{\boldsymbol{r}}\ln\theta_{\boldsymbol{r}}^{\mathcal{E}} \\ & + \mathrm{s}_\nu\mathrm{q}\tau_0\left(k_\mathrm{B}T_\mathrm{L}\right)^{-r_\nu}\langle\!\langle \mathcal{E}^{r_\nu+1}\rangle\!\rangle\nabla_{\boldsymbol{r}}\tilde{\varphi} + \mathrm{s}_\nu\frac{1}{3}\mathrm{q}\tau_0\left(k_\mathrm{B}T_\mathrm{L}\right)^{-r_\nu}\left\langle\!\!\left\langle p\frac{1}{\hbar}\partial_{\boldsymbol{k}}\mathcal{E}^{r_\nu+1}\right\rangle\!\!\right\rangle\nabla_{\boldsymbol{r}}\tilde{\varphi}\,.\end{aligned} \tag{3.71}$$

For the next steps, parabolic bands and a heated, displaced *Maxwell*ian (3.51) are assumed. The statistical average in part (i) is carried out similarly to (3.53), normalized using (3.54), and reads

$$\langle\!\langle \mathcal{E}^{r_\nu+2}\rangle\!\rangle = \frac{4\pi\sqrt{2}m^{*\frac{3}{2}}}{\hbar^3}A\left(k_\mathrm{B}T_\nu\right)^{r_\nu+\frac{7}{2}}\Gamma\left(r_\nu+\frac{7}{2}\right)\,. \tag{3.72}$$

Thus, part (i) becomes

$$\nabla_{\boldsymbol{r}}\left(\left(r_\nu+\frac{5}{2}\right)\nu\left(k_\mathrm{B}T_\mathrm{L}\right)^2\mu_\nu\frac{m^*}{\mathrm{q}}\right) \tag{3.73}$$

using the mobility definition (3.55). With the assumption of a $\boldsymbol{k}$–independent r_ν and basic arithmetic operations, the first term of part (ii) is expressed in terms of an effective mass gradient $\nabla_{\boldsymbol{r}}m^*$. The second term is split into a $\nabla_{\boldsymbol{r}}T_\mathrm{L}$ and a $\nabla_{\boldsymbol{r}}m^*$ term, while the $\nabla_{\boldsymbol{r}}m^*$–term cancels with the third term. Thus, part (ii) finally reads

$$-\frac{3}{2}\frac{m^*}{\mathrm{q}}\mu_\nu\nu\left(r_\nu+\frac{5}{2}\right)\left(k_\mathrm{B}T_\nu\right)^2\nabla_{\boldsymbol{r}}\ln m^* + r_\nu\frac{m^*}{\mathrm{q}}\mu_\nu\nu\frac{T_\nu}{T_\mathrm{L}}\left(r_\nu+\frac{5}{2}\right)\left(k_\mathrm{B}T_\nu\right)\nabla_{\boldsymbol{r}}\left(k_\mathrm{B}T_\mathrm{L}\right)\,. \tag{3.74}$$

While the first term of part (iii) is handled straight–forwardly with the statistical average (3.53), the derivative in the second term has to be expressed before processing the statistical average. While the first term contributes with a factor of $\frac{3}{2}$, the second's contribution is $r_\nu+1$. Thus, the sum reads

$$\left(r_\nu+\frac{5}{2}\right)\mu_\nu\nu k_\mathrm{B}T_\nu m^*\nabla_{\boldsymbol{r}}\tilde{\varphi}\,. \tag{3.75}$$

With a definition of the energy flux analogously to (3.58)

$$\boldsymbol{j}_\nu^\mathrm{u} = \langle\!\langle \mathcal{E}\boldsymbol{v}\rangle\!\rangle = \frac{1}{m^*}\langle\!\langle \mathcal{E}\boldsymbol{p}\rangle\!\rangle \tag{3.76}$$

the final energy flux for parabolic bands and a heated, displaced *Maxwell*ian reads

$$\begin{aligned}\boldsymbol{j}_\nu^{\mathrm{u}} = &-\frac{1}{m^*}\nabla_{\boldsymbol{r}}\left(\left(r_\nu+\frac{5}{2}\right)\nu\left(k_{\mathrm{B}}T_\nu\right)^2\mu_\nu\frac{m^*}{\mathrm{q}}\right)\\ &+\frac{3}{2}\frac{1}{\mathrm{q}}\mu_\nu\nu\left(r_\nu+\frac{5}{2}\right)\left(k_{\mathrm{B}}T_\nu\right)^2\nabla_{\boldsymbol{r}}\ln m^* - r_\nu\frac{1}{\mathrm{q}}\mu_\nu\nu\frac{T_\nu}{T_{\mathrm{L}}}\left(r_\nu+\frac{5}{2}\right)\left(k_{\mathrm{B}}T_\nu\right)\nabla_{\boldsymbol{r}}\left(k_{\mathrm{B}}T_{\mathrm{L}}\right)\\ &-\mathrm{s}_\nu\left(r_\nu+\frac{5}{2}\right)\mu_\nu\nu k_{\mathrm{B}}T_\nu\nabla_{\boldsymbol{r}}\tilde{\varphi}\,.\end{aligned}\tag{3.77}$$

Introducing the electrochemical potential as defined in Eqs. (3.60) and (3.62) yields

$$\begin{aligned}\boldsymbol{j}_\nu^{\mathrm{u}} = &-\mathrm{s}_\nu\left(r_\nu+\frac{5}{2}\right)\mu_\nu\nu k_{\mathrm{B}}T_\nu\nabla_{\boldsymbol{r}}\Phi_\nu - \left(r_\nu+\frac{5}{2}\right)\mu_\nu\nu\frac{k_{\mathrm{B}}^2T_\nu}{\mathrm{q}}\left(\frac{7}{2}-\ln\frac{\nu}{N_{\mathrm{c,v}}}\right)\nabla_{\boldsymbol{r}}T_\nu\\ &-\frac{k_{\mathrm{B}}^2}{\mathrm{q}}\mu_\nu\nu T_\nu^2\nabla_{\boldsymbol{r}}r_\nu - \frac{k_{\mathrm{B}}^2}{\mathrm{q}}\left(r_\nu+\frac{5}{2}\right)\nu T_\nu^2\nabla_{\boldsymbol{r}}\mu_\nu - \frac{k_{\mathrm{B}}^2}{\mathrm{q}}\left(r_\nu+\frac{5}{2}\right)\mu_\nu\nu T_\nu^2\nabla_{\boldsymbol{r}}\ln m^*\\ &-r_\nu\frac{k_{\mathrm{B}}^2T_\nu}{\mathrm{q}}\left(r_\nu+\frac{5}{2}\right)\mu_\nu\nu\frac{T_\nu}{T_{\mathrm{L}}}\nabla_{\boldsymbol{r}}T_{\mathrm{L}}\,.\end{aligned}\tag{3.78}$$

3.5.6 *Bløtekjær*'s Approach

In contrast to *Stratton*, *Bløtekjær* originally proposed the concept of macroscopic relaxation times introducing one relaxation time for each moment equation. The set of weight functions used in this derivation is

$$X = \left(1, \boldsymbol{p}, \mathcal{E}, \mathcal{E}\boldsymbol{p}\right)\,, \tag{3.79}$$

which gives the possibility of a direct comparison to the terms obtained throughout the derivation after *Stratton*. The assumptions and simplifications are listed below:

- Macroscopic relaxation time approximation
- Time derivatives are neglected in the flux equations
- Product ansatz for the kinetic energy
- Tensor–valued transport parameters are estimated by their traces
- Parabolic band–structure
- Linearized heated displaced *Maxwell*ian distribution function as closure relation

3.5.6.1 Particle Flux Equation

In the following, the derivation of the particle flux equation is performed analogously to *Stratton*'s approach. The starting point is again the *Boltzmann* transport equation with a general weight $\boldsymbol{X}$ in the form of equation (3.30). Inserting $X=\boldsymbol{p}$ as X yields

$$\underbrace{\nabla_{\boldsymbol{r}}\langle\!\langle\boldsymbol{p}\otimes\boldsymbol{v}\rangle\!\rangle}_{\text{(i)}} - \underbrace{\langle\!\langle\{\boldsymbol{p},\mathcal{E}\}\rangle\!\rangle}_{\text{(ii)}} + \underbrace{\mathrm{s}_\nu\mathrm{q}\left\langle\!\!\left\langle\frac{1}{\hbar}\nabla_{\boldsymbol{k}}\otimes\boldsymbol{p}\right\rangle\!\!\right\rangle\cdot\nabla_{\boldsymbol{r}}\tilde{\varphi}}_{\text{(iii)}} = -\frac{\langle\!\langle\boldsymbol{p}\rangle\!\rangle-\langle\!\langle\boldsymbol{p}_0\rangle\!\rangle}{\tau_{\boldsymbol{j}}}\,. \tag{3.80}$$

Application of the trace approximation of tensor valued expressions (3.39) as well as a product ansatz for the energy as presented in equation (3.40) on term (i) results in

$$\nabla_{\boldsymbol{r}}\langle\!\langle \boldsymbol{p}\otimes\boldsymbol{v}\rangle\!\rangle = \nabla_{\boldsymbol{r}}\left\langle\!\!\left\langle \mathcal{E}\gamma^2\frac{1}{p^2}\boldsymbol{p}\otimes\boldsymbol{p}\right\rangle\!\!\right\rangle = \frac{2}{3}\nabla_{\boldsymbol{r}}\langle\!\langle \mathcal{E}\gamma\rangle\!\rangle\,. \tag{3.81}$$

The *Poisson* bracket within the average in (ii) has to be expanded using (A.6). Furthermore, the inverse product rule (B.3) is used to transform the $\nabla_{\boldsymbol{r}}\otimes\boldsymbol{p}$ – term in the first term. The product ansatz for the energy as well as the trace approximation result in

$$\begin{aligned}\langle\!\langle\{\boldsymbol{p},\mathcal{E}\}\rangle\!\rangle &= \left\langle\!\!\left\langle(\nabla_{\boldsymbol{r}}\otimes\boldsymbol{p})\cdot\boldsymbol{v} - \left(\frac{1}{\hbar}\nabla_{\boldsymbol{k}}\otimes\boldsymbol{p}\right)\cdot\nabla_{\boldsymbol{r}}\mathcal{E}\right\rangle\!\!\right\rangle \\ &= \langle\!\langle\nabla_{\boldsymbol{r}}(\boldsymbol{p}\otimes\boldsymbol{v})\rangle\!\rangle - \langle\!\langle\boldsymbol{p}\,(\nabla_{\boldsymbol{r}}\cdot\boldsymbol{v})\rangle\!\rangle - \langle\!\langle\mathcal{E}\rangle\!\rangle\nabla_{\boldsymbol{r}}\ln\theta_{\boldsymbol{r}}^{\mathcal{E}} \\ &= \left\langle\!\!\left\langle\nabla_{\boldsymbol{r}}\left(\boldsymbol{p}\otimes\boldsymbol{p}\mathcal{E}\gamma\frac{2}{p^2}\right)\right\rangle\!\!\right\rangle - \left\langle\!\!\left\langle\boldsymbol{p}\left(\nabla_{\boldsymbol{r}}\cdot\boldsymbol{p}\mathcal{E}\gamma\frac{2}{p^2}\right)\right\rangle\!\!\right\rangle - \langle\!\langle\mathcal{E}\rangle\!\rangle\nabla_{\boldsymbol{r}}\ln\theta_{\boldsymbol{r}}^{\mathcal{E}} \\ &= -\langle\!\langle\mathcal{E}\rangle\!\rangle\nabla_{\boldsymbol{r}}\ln\theta_{\boldsymbol{r}}^{\mathcal{E}}\,.\end{aligned} \tag{3.82}$$

The third term (iii) can be handled in a straight–forward manner. Assembly of all three terms leads to

$$\frac{2}{3}\nabla_{\boldsymbol{r}}\langle\!\langle\mathcal{E}\gamma\rangle\!\rangle + \langle\!\langle\mathcal{E}\rangle\!\rangle\nabla_{\boldsymbol{r}}\ln\theta_{\boldsymbol{r}}^{\mathcal{E}} + \mathrm{s}_\nu\mathrm{q}\nu\nabla_{\boldsymbol{r}}\tilde{\varphi} = -\frac{\langle\!\langle\boldsymbol{p}\rangle\!\rangle}{\tau_{\boldsymbol{j}}}\,. \tag{3.83}$$

Assuming parabolic bands and a heated, displaced *Maxwell*ian, γ becomes unity and the average reads

$$\langle\!\langle\mathcal{E}\rangle\!\rangle = \frac{4\pi\sqrt{2}m^{*\frac{3}{2}}}{\hbar^3}A\,(k_\mathrm{B}T_\nu)^{\frac{5}{2}}\,\Gamma\left(\frac{5}{2}\right) = \frac{3}{2}\nu k_\mathrm{B}T_\nu \tag{3.84}$$

normalized with the carrier concentration (3.54). Summation over all parts as well as the mobility definition consistent with the homogeneous case

$$\mu_\nu = \frac{\mathrm{q}\tau_{\boldsymbol{j}}}{m^*} \tag{3.85}$$

yields the final form of the particle current equation

$$-\frac{\langle\!\langle\boldsymbol{p}\rangle\!\rangle}{\tau_{\boldsymbol{j}}} = \nabla_{\boldsymbol{r}}(\nu k_\mathrm{B}T_\nu) - \frac{3}{2}\nu k_\mathrm{B}T_\nu\nabla_{\boldsymbol{r}}\ln m^* + \mathrm{s}_\nu\mathrm{q}\nu\nabla_{\boldsymbol{r}}\tilde{\varphi} \tag{3.86}$$

$$\boldsymbol{j}_\nu = -\frac{k_\mathrm{B}}{\mathrm{q}}\mu_\nu\nabla_{\boldsymbol{r}}(\nu T_\nu) + \frac{3}{2}\frac{k_\mathrm{B}}{\mathrm{q}}\mu_\nu\nu T_\nu\nabla_{\boldsymbol{r}}\ln m^* - \mathrm{s}_\nu\mu_\nu\nu\nabla_{\boldsymbol{r}}\tilde{\varphi}\,. \tag{3.87}$$

Rewriting the particle current equation with the electrochemical potential defined in Eqs. (3.60) and (3.62) results in

$$\boldsymbol{j}_\nu = -\mathrm{s}_\nu\mu_\nu\nu\nabla_{\boldsymbol{r}}\Phi_\nu - \mu_\nu\nu\frac{k_\mathrm{B}}{\mathrm{q}}\left(\frac{5}{2} - \ln\frac{\nu}{N_\mathrm{c,v}}\right)\nabla_{\boldsymbol{r}}T_\nu\,. \tag{3.88}$$

3.5.6.2 Energy Flux Equation

With the weight $\boldsymbol{X} = \mathcal{E}\boldsymbol{p}$, one obtains the energy flux equation

$$\underbrace{\nabla_{\boldsymbol{r}}\langle\!\langle \mathcal{E}\boldsymbol{p}\otimes\boldsymbol{v}\rangle\!\rangle}_{\text{(i)}} - \underbrace{\langle\!\langle\{\mathcal{E}\boldsymbol{p},\mathcal{E}\}\rangle\!\rangle}_{\text{(ii)}} + \underbrace{\mathrm{s}_\nu \mathrm{q}\left\langle\!\!\left\langle \frac{1}{\hbar}\nabla_{\boldsymbol{k}}\otimes(\mathcal{E}\boldsymbol{p})\right\rangle\!\!\right\rangle\cdot\nabla_{\boldsymbol{r}}\tilde{\varphi}}_{\text{(iii)}} = -\frac{\langle\!\langle\mathcal{E}\boldsymbol{p}\rangle\!\rangle}{\tau_{\boldsymbol{u}}}\,. \tag{3.89}$$

The first part is straight–forward

$$\nabla_{\boldsymbol{r}}\langle\!\langle \mathcal{E}\boldsymbol{p}\otimes\boldsymbol{v}\rangle\!\rangle = \frac{2}{3}\nabla_{\boldsymbol{r}}\langle\!\langle \mathcal{E}^2\gamma\rangle\!\rangle\,, \tag{3.90}$$

while part (ii) has to be expanded using (A.10). The Poisson bracket $\{\mathcal{E},\mathcal{E}\}$ vanishes because of (A.8) as well as the $\nabla_{\boldsymbol{r}}\otimes\boldsymbol{p}$ – term. Thus, the second part becomes

$$\langle\!\langle\{\mathcal{E}\boldsymbol{p},\mathcal{E}\}\rangle\!\rangle = -\langle\!\langle\mathcal{E}^2\rangle\!\rangle\nabla_{\boldsymbol{r}}\ln\theta_{\boldsymbol{r}}^{\mathcal{E}}\,. \tag{3.91}$$

The derivative in part (iii) has to be expanded using identity (B.6)

$$\mathrm{q}\left\langle\!\!\left\langle \frac{1}{\hbar}\nabla_{\boldsymbol{k}}\otimes(\mathcal{E}\boldsymbol{p})\right\rangle\!\!\right\rangle\cdot\nabla_{\boldsymbol{r}}\tilde{\varphi} = \mathrm{q}\langle\!\langle\mathcal{E}\rangle\!\rangle\nabla_{\boldsymbol{r}}\tilde{\varphi} + \frac{1}{3}\mathrm{q}\left\langle\!\!\left\langle\boldsymbol{p}\frac{1}{\hbar}\partial_{\boldsymbol{k}}\mathcal{E}\right\rangle\!\!\right\rangle\nabla_{\boldsymbol{r}}\tilde{\varphi}\,. \tag{3.92}$$

Thus, the equation becomes

$$\frac{2}{3}\nabla_{\boldsymbol{r}}\langle\!\langle\mathcal{E}^2\gamma\rangle\!\rangle + \langle\!\langle\mathcal{E}^2\rangle\!\rangle\nabla_{\boldsymbol{r}}\ln\theta_{\boldsymbol{r}}^{\mathcal{E}} + \mathrm{s}_\nu\mathrm{q}\langle\!\langle\mathcal{E}\rangle\!\rangle\nabla_{\boldsymbol{r}}\tilde{\varphi} + \mathrm{s}_\nu\frac{1}{3}\mathrm{q}\left\langle\!\!\left\langle\boldsymbol{p}\frac{1}{\hbar}\partial_{\boldsymbol{k}}\mathcal{E}\right\rangle\!\!\right\rangle\nabla_{\boldsymbol{r}}\tilde{\varphi} = -\frac{\langle\!\langle\mathcal{E}\boldsymbol{p}\rangle\!\rangle}{\tau_{\boldsymbol{u}}}\,. \tag{3.93}$$

For parabolic bands and a heated, displaced *Maxwell*ian, the average $\langle\!\langle\mathcal{E}^2\rangle\!\rangle$ becomes

$$\langle\!\langle\mathcal{E}^2\rangle\!\rangle = \frac{4\pi\sqrt{2}m^{*\frac{3}{2}}}{\hbar^3}A\left(k_\mathrm{B}T_\nu\right)^{\frac{7}{2}}\Gamma\left(\frac{7}{2}\right) = \frac{15}{4}\nu\left(k_\mathrm{B}T_\nu\right)^2 \tag{3.94}$$

analogously to (3.53). While the parts (i) and (ii) are straight–forward to handle, the derivative in part (iii) has to be explicitly expressed which finally also leads to the energy average. Finally, the mobility definition (3.85) already used in the particle flux equation is inserted

$$-\frac{\langle\!\langle\mathcal{E}\boldsymbol{p}\rangle\!\rangle}{\tau_{\boldsymbol{u}}} = \frac{5}{2}\nabla_{\boldsymbol{r}}\left(\nu\left(k_\mathrm{B}T_\nu\right)^2\right) - \frac{15}{4}\nu\left(k_\mathrm{B}T_\nu\right)^2\nabla_{\boldsymbol{r}}\ln m^* + \mathrm{s}_\nu\frac{5}{2}\mathrm{q}\nu k_\mathrm{B}T_\nu\nabla_{\boldsymbol{r}}\tilde{\varphi} \tag{3.95}$$

$$\boldsymbol{j}_\nu^\mathrm{u} = -\frac{5}{2}\frac{\mu_\nu^\mathrm{u}}{\mathrm{q}}\nabla_{\boldsymbol{r}}\left(\nu\left(k_\mathrm{B}T_\nu\right)^2\right) + \frac{15}{4}\frac{\mu_\nu^\mathrm{u}}{\mathrm{q}}\nu\left(k_\mathrm{B}T_\nu\right)^2\nabla_{\boldsymbol{r}}\ln m^* - \mathrm{s}_\nu\frac{5}{2}\mu_\nu^\mathrm{u}\nu k_\mathrm{B}T_\nu\nabla_{\boldsymbol{r}}\tilde{\varphi}\,. \tag{3.96}$$

Introducing the electrochemical potential defined in Eqs. (3.60) and (3.62), the energy flux equation becomes

$$\boldsymbol{j}_\nu^\mathrm{u} = -\mathrm{s}_\nu\mu_\nu^\mathrm{u}\nu\frac{5}{2}k_\mathrm{B}T_\nu\nabla_{\boldsymbol{r}}\Phi_\nu - \mu_\nu^\mathrm{u}\nu\frac{5}{2}\frac{k_\mathrm{B}^2T_\nu}{\mathrm{q}}\left(\frac{7}{2} - \ln\frac{\nu}{N_\mathrm{c,v}}\right)\nabla T_\nu\,. \tag{3.97}$$

3.5.7 Non–Diagonal Relaxation Time Ansatz

In the sequel, an alternative ansatz for the scattering operator is introduced. Instead of the commonly used relaxation time approximation, the stochastic part of the moments is modeled using an expansion of the scattering integrals into the odd moments of the distribution function [90, 91]. Thus, the scattering integrals are represented as linear combinations of the fluxes derived. The weight set chosen for this ansatz is the same as in *Bløtekjær*'s approach, so the left side of the *Boltzmann* transport equation can be expressed similarly. Using the deterministic parts of the particle and energy flux equations from Eqs. (3.86) and (3.96)

$$\boldsymbol{F}_0 = -\frac{1}{\mathrm{q}}\nabla_{\boldsymbol{r}}\left(\nu k_\mathrm{B} T_\nu\right) + \frac{3}{2}\frac{k_\mathrm{B}}{\mathrm{q}}\nu T_\nu \nabla_{\boldsymbol{r}} \ln m^* - \mathrm{s}_\nu \nu \nabla_{\boldsymbol{r}} \tilde{\varphi} \tag{3.98}$$

$$\boldsymbol{F}_1 = -\frac{5}{2}\frac{1}{\mathrm{q}}\nabla_{\boldsymbol{r}}\left(\nu \left(k_\mathrm{B} T_\nu\right)^2\right) + \frac{15}{4}\frac{1}{\mathrm{q}}\nu \left(k_\mathrm{B} T_\nu\right)^2 \nabla_{\boldsymbol{r}} \ln m^* - \mathrm{s}_\nu \frac{5}{2}\nu k_\mathrm{B} T_\nu \nabla_{\boldsymbol{r}} \tilde{\varphi}\,, \tag{3.99}$$

the corresponding equations are formally expanded as

$$\boldsymbol{F}_0 = Z_{00}\boldsymbol{j}_\nu + Z_{01}\boldsymbol{j}_\nu^\mathrm{u} \tag{3.100}$$

$$\boldsymbol{F}_1 = Z_{10}\boldsymbol{j}_\nu + Z_{11}\boldsymbol{j}_\nu^\mathrm{u}\,. \tag{3.101}$$

Since the actual quantities of interest are the particle current $\boldsymbol{j}_\nu$ and the energy flux density $\boldsymbol{j}_\nu^\mathrm{u}$, the coupled equations are formulated in order to explicitly express the particle and energy flux, respectively

$$\boldsymbol{j}_\nu = \frac{Z_{11}\boldsymbol{F}_0 - Z_{01}\boldsymbol{F}_1}{Z_{00}Z_{11} - Z_{10}Z_{01}} \tag{3.102}$$

$$\boldsymbol{j}_\nu^\mathrm{u} = \frac{Z_{00}\boldsymbol{F}_1 - Z_{10}\boldsymbol{F}_0}{Z_{00}Z_{11} - Z_{10}Z_{01}}\,. \tag{3.103}$$

The fluxes $\boldsymbol{F}_0$ and $\boldsymbol{F}_1$ Eqs. (3.98) and (3.99) are inserted to (3.102) and thus the particle current equation reads

$$\begin{aligned}\boldsymbol{j}_\nu = &-\frac{Z_{11} - \frac{5}{2}k_\mathrm{B}T_\nu Z_{01}}{Z_{00}Z_{11} - Z_{10}Z_{01}}\frac{1}{\mathrm{q}}\nabla_{\boldsymbol{r}}\left(\nu k_\mathrm{B}T_\nu\right) + \frac{Z_{11} - \frac{5}{2}k_\mathrm{B}T_\nu Z_{01}}{Z_{00}Z_{11} - Z_{10}Z_{01}}\frac{3}{2}\frac{k_\mathrm{B}}{\mathrm{q}}\nu T_\nu \nabla_{\boldsymbol{r}}\ln m^* \\ &-\frac{Z_{11} - \frac{5}{2}k_\mathrm{B}T_\nu Z_{01}}{Z_{00}Z_{11} - Z_{10}Z_{01}}\mathrm{s}_\nu \nu \nabla_{\boldsymbol{r}}\tilde{\varphi} + \frac{Z_{01}}{Z_{00}Z_{11} - Z_{10}Z_{01}}\frac{5}{2}\frac{k_\mathrm{B}^2}{\mathrm{q}}\nu T_\nu \nabla_{\boldsymbol{r}} T_\nu\,.\end{aligned} \tag{3.104}$$

Introducing the electrochemical potential (3.62), the current can be expressed as a linear combination of a $\nabla_{\boldsymbol{r}}\Phi_\nu$ and a $\nabla_{\boldsymbol{r}}T_\nu$ expression

$$\begin{aligned}\boldsymbol{j}_\nu = &-\frac{Z_{11} - \frac{5}{2}k_\mathrm{B}T_\nu Z_{01}}{Z_{00}Z_{11} - Z_{10}Z_{01}}\mathrm{s}_\nu \nu \nabla_{\boldsymbol{r}}\Phi_\nu \\ &-\frac{\left(Z_{11} - \frac{5}{2}k_\mathrm{B}T_\nu Z_{01}\right)\left(\frac{5}{2} - \ln\frac{\nu}{N_{\mathrm{c,v}}}\right) - \frac{5}{2}k_\mathrm{B}T_\nu Z_{01}}{Z_{00}Z_{11} - Z_{10}Z_{01}}\frac{k_\mathrm{B}}{\mathrm{q}}\nu \nabla_{\boldsymbol{r}} T_\nu\,.\end{aligned} \tag{3.105}$$

For the according energy flux equation, which is expressed analogously, the fluxes $\boldsymbol{F}_0$ and $\boldsymbol{F}_1$ Eqs. (3.98) and (3.99) are inserted to (3.103)

$$\begin{aligned}\boldsymbol{j}_\nu^\mathrm{u} = &-\frac{\frac{5}{2}k_\mathrm{B}T_\nu Z_{00} - Z_{10}}{Z_{00}Z_{11} - Z_{10}Z_{01}}\frac{1}{\mathrm{q}}\nabla_{\boldsymbol{r}}\left(\nu k_\mathrm{B}T_\nu\right) + \frac{\frac{5}{2}k_\mathrm{B}T_\nu Z_{00} - Z_{10}}{Z_{00}Z_{11} - Z_{10}Z_{01}}\frac{3}{2}\frac{k_\mathrm{B}}{\mathrm{q}}\nu T_\nu \nabla_{\boldsymbol{r}}\ln m^* \\ &-\frac{\frac{5}{2}k_\mathrm{B}T_\nu Z_{00} - Z_{10}}{Z_{00}Z_{11} - Z_{10}Z_{01}}\mathrm{s}_\nu \nu \nabla_{\boldsymbol{r}}\tilde{\varphi} - \frac{Z_{00}}{Z_{00}Z_{11} - Z_{10}Z_{01}}\frac{5}{2}\frac{k_\mathrm{B}^2}{\mathrm{q}}\nu T_\nu \nabla_{\boldsymbol{r}} T_\nu\,.\end{aligned} \tag{3.106}$$

With the electrochemical potential, it can be rewritten as

$$\begin{aligned}\boldsymbol{j}_\nu^{\mathrm{u}} = &-\frac{\frac{5}{2}k_{\mathrm{B}}T_\nu Z_{00} - Z_{10}}{Z_{00}Z_{11} - Z_{10}Z_{01}}\mathrm{s}_\nu \nu \nabla_{\boldsymbol{r}}\Phi_\nu \\ &- \frac{\left(\frac{5}{2}k_{\mathrm{B}}T_\nu Z_{00} - Z_{10}\right)\left(\frac{5}{2} - \ln\frac{\nu}{N_{\mathrm{c,v}}}\right) + \frac{5}{2}k_{\mathrm{B}}T_\nu Z_{00}}{Z_{00}Z_{11} - Z_{10}Z_{01}}\frac{k_{\mathrm{B}}}{\mathrm{q}}\nu\nabla_{\boldsymbol{r}}T_\nu\,.\end{aligned} \tag{3.107}$$

A coefficient comparison between the particle flux equation (3.105) and the according equation derived using *Bløtekjær*'s concept of macroscopic relaxation times (3.88) enables the identification of several transport parameters

$$\mu_\nu = \frac{Z_{11} - \frac{5}{2}k_{\mathrm{B}}T_\nu Z_{01}}{Z_{00}Z_{11} - Z_{10}Z_{01}}\,, \tag{3.108}$$

$$\mu_\nu^{\mathrm{u}} = \frac{1}{\frac{5}{2}k_{\mathrm{B}}T_\nu}\frac{\frac{5}{2}k_{\mathrm{B}}T_\nu Z_{00} - Z_{10}}{Z_{00}Z_{11} - Z_{10}Z_{01}}\,, \tag{3.109}$$

$$\alpha = -\mathrm{s}_\nu\frac{k_{\mathrm{B}}}{\mathrm{q}}\left(\frac{5}{2} - \ln\frac{\nu}{N_{\mathrm{c,v}}}\right) + \mathrm{s}_\nu\frac{k_{\mathrm{B}}}{\mathrm{q}}\frac{\frac{5}{2}k_{\mathrm{B}}T_\nu Z_{01}}{Z_{11} - \frac{5}{2}k_{\mathrm{B}}T_\nu Z_{01}}\,. \tag{3.110}$$

Analogously to the extended ansatz for the stochastic part of *Boltzmann*'s equation, these transport coefficients can be seen as an extension to the ones derived using *Bløtekjær*'s ansatz. Assuming the cross coefficients Z_{01} and Z_{10} to be zero, the coefficients for *Bløtekjær*'s approach carried out in Section 3.5.6 are obtained. Although the scattering parameters Z_{ij} can be calculated using accurate physical models, this approach results in a very complicated description.

3.5.8 Summary of Equations

In the following, the equations derived applying both *Stratton*'s and *Bløtekjær*'s approach are summarized. While the balance equations, which belong to scalar weights are equivalent for both approaches, the flux equations differ due to the different approaches of relaxation time approximations to the collision term as well as the associated choice of weights. For both *Stratton*'s and *Bløtekjær*'s approach the carrier balance equation and energy balance equation read

$$\partial_t\nu + \nabla_{\boldsymbol{r}}\cdot\boldsymbol{j}_\nu = -R \tag{3.111}$$

$$\partial_t w + \nabla_{\boldsymbol{r}}\cdot\boldsymbol{j}_\nu^{\mathrm{u}} - \mathrm{q}\boldsymbol{j}_\nu\cdot\nabla_{\boldsymbol{r}}\tilde{\varphi} + \frac{3}{2}\nu k_{\mathrm{B}}\frac{T_\nu - T_{\mathrm{L}}}{\tau} - G_\nu^{\mathcal{E}} = 0\,. \tag{3.112}$$

The carrier flux and energy flux equations derived by using *Stratton*'s microscopic relaxation time ansatz are

$$\begin{aligned}\boldsymbol{j}_\nu = &-\frac{k_{\mathrm{B}}}{\mathrm{q}m^*}\nabla_{\boldsymbol{r}}\left(\mu_\nu\nu T_\nu m^*\right) + \frac{3}{2}\mu_\nu\nu\frac{k_{\mathrm{B}}}{\mathrm{q}}T_\nu\nabla_{\boldsymbol{r}}\ln m^* \\ &- r_\nu\mu_\nu\nu\frac{k_{\mathrm{B}}}{\mathrm{q}}\frac{T_\nu}{T_{\mathrm{L}}}\nabla_{\boldsymbol{r}}T_{\mathrm{L}} - \mathrm{s}_\nu\mu_\nu\nu\nabla_{\boldsymbol{r}}\tilde{\varphi}\end{aligned} \tag{3.113}$$

$$\begin{aligned}\boldsymbol{j}_\nu^{\mathrm{u}} = &-\frac{k_{\mathrm{B}}^2}{\mathrm{q}m^*}\nabla_{\boldsymbol{r}}\left(\left(r_\nu + \frac{5}{2}\right)\mu_\nu\nu T_\nu^2 m^*\right) + \left(r_\nu + \frac{5}{2}\right)\frac{3}{2}\mu_\nu\nu\frac{k_{\mathrm{B}}^2}{\mathrm{q}}T_\nu^2\nabla_{\boldsymbol{r}}\ln m^* \\ &- \left(r_\nu + \frac{5}{2}\right)r_\nu\frac{1}{\mathrm{q}}\mu_\nu\nu\frac{T_\nu}{T_{\mathrm{L}}}\left(k_{\mathrm{B}}T_\nu\right)\nabla_{\boldsymbol{r}}\left(k_{\mathrm{B}}T_{\mathrm{L}}\right) - \mathrm{s}_\nu\left(r_\nu + \frac{5}{2}\right)\mu_\nu\nu k_{\mathrm{B}}T_\nu\nabla_{\boldsymbol{r}}\tilde{\varphi}\,.\end{aligned} \tag{3.114}$$

The according formulation with the electrochemical potential introduced reads

$$\begin{aligned}\boldsymbol{j}_\nu &= -\mathrm{s}_\nu \mu_\nu \nu \nabla_{\boldsymbol{r}} \Phi_\nu - \frac{k_\mathrm{B}}{\mathrm{q}} \left(\frac{5}{2} - \ln \frac{\nu}{N_\mathrm{c,v}} \right) \mu_\nu \nu \nabla_{\boldsymbol{r}} T_\nu \qquad (3.115)\\ &\quad - \frac{k_\mathrm{B} T_\nu}{\mathrm{q}} \mu_\nu \nu \nabla_{\boldsymbol{r}} \ln m^* - \frac{k_\mathrm{B} T_\nu}{\mathrm{q}} \nu \nabla_{\boldsymbol{r}} \mu_\nu - r_\nu \mu_\nu \nu \frac{k_\mathrm{B}}{\mathrm{q}} \frac{T_\nu}{T_\mathrm{L}} \nabla_{\boldsymbol{r}} T_\mathrm{L}\\ \boldsymbol{j}_\nu^\mathrm{u} &= -\mathrm{s}_\nu \left(r_\nu + \frac{5}{2} \right) \mu_\nu \nu k_\mathrm{B} T_\nu \nabla_{\boldsymbol{r}} \Phi_\nu - \left(r_\nu + \frac{5}{2} \right) \mu_\nu \nu \frac{k_\mathrm{B}^2 T_\nu}{\mathrm{q}} \left(\frac{7}{2} - \ln \frac{\nu}{N_\mathrm{c,v}} \right) \nabla_{\boldsymbol{r}} T_\nu \qquad (3.116)\\ &\quad - \frac{k_\mathrm{B}^2}{\mathrm{q}} \mu_\nu \nu T_\nu^2 \nabla_{\boldsymbol{r}} r_\nu - \frac{k_\mathrm{B}^2}{\mathrm{q}} \left(r_\nu + \frac{5}{2} \right) \nu T_\nu^2 \nabla_{\boldsymbol{r}} \mu_\nu - \frac{k_\mathrm{B}^2}{\mathrm{q}} \left(r_\nu + \frac{5}{2} \right) \mu_\nu \nu T_\nu^2 \nabla_{\boldsymbol{r}} \ln m^*\\ &\quad - r_\nu \frac{k_\mathrm{B}^2 T_\nu}{\mathrm{q}} \left(r_\nu + \frac{5}{2} \right) \mu_\nu \nu \frac{T_\nu}{T_\mathrm{L}} \nabla_{\boldsymbol{r}} T_\mathrm{L} \,.\end{aligned}$$

In some cases, it is convenient to formulate the energy flux in terms of the particle flux. For *Stratton*'s equations, it is given by

$$\boldsymbol{j}_\nu^\mathrm{u} = \left(\frac{5}{2} + r_\nu \right) k_\mathrm{B} T_\nu \boldsymbol{j}_\nu - \left(\frac{5}{2} + r_\nu \right) \frac{k_\mathrm{B}^2 T_\nu}{\mathrm{q}} \mu_\nu \nu \nabla_{\boldsymbol{r}} T_\nu - \frac{k_\mathrm{B}^2}{\mathrm{q}} \mu_\nu \nu T_\nu^2 \nabla_{\boldsymbol{r}} r_\nu \,. \qquad (3.117)$$

Bløtekjær's concept of macroscopic relaxation times yields for the particle and energy flux equations, respectively

$$\begin{aligned}\boldsymbol{j}_\nu &= -\frac{\mu_\nu}{\mathrm{q}} \nabla_{\boldsymbol{r}} \left(\nu k_\mathrm{B} T_\nu \right) + \frac{3}{2} \frac{\mu_\nu}{\mathrm{q}} \nu k_\mathrm{B} T_\nu \nabla_{\boldsymbol{r}} \ln m^* - \mathrm{s}_\nu \mu_\nu \nu \nabla_{\boldsymbol{r}} \tilde{\varphi} \qquad (3.118)\\ \boldsymbol{j}_\nu^\mathrm{u} &= -\frac{5}{2} \frac{\mu_\nu^\mathrm{u}}{\mathrm{q}} \nabla_{\boldsymbol{r}} \left(\nu \left(k_\mathrm{B} T_\nu \right)^2 \right) + \frac{15}{4} \frac{\mu_\nu^\mathrm{u}}{\mathrm{q}} \nu \left(k_\mathrm{B} T_\nu \right)^2 \nabla_{\boldsymbol{r}} \ln m^* - \mathrm{s}_\nu \frac{5}{2} \mu_\nu^\mathrm{u} \nu k_\mathrm{B} T_\nu \nabla_{\boldsymbol{r}} \tilde{\varphi} \,. \qquad (3.119)\end{aligned}$$

With the electrochemical potential, they are

$$\begin{aligned}\boldsymbol{j}_\nu &= -\mathrm{s}_\nu \mu_\nu \nu \nabla_{\boldsymbol{r}} \Phi_\nu - \mu_\nu \nu \frac{k_\mathrm{B}}{\mathrm{q}} \left(\frac{5}{2} - \ln \frac{\nu}{N_\mathrm{c,v}} \right) \nabla_{\boldsymbol{r}} T_\nu \qquad (3.120)\\ \boldsymbol{j}_\nu^\mathrm{u} &= -\mathrm{s}_\nu \mu_\nu^\mathrm{u} \nu \frac{5}{2} k_\mathrm{B} T_\nu \nabla_{\boldsymbol{r}} \Phi_\nu - \mu_\nu^\mathrm{u} \nu \frac{5}{2} \frac{k_\mathrm{B}^2 T_\nu}{\mathrm{q}} \left(\frac{7}{2} - \ln \frac{\nu}{N_\mathrm{c,v}} \right) \nabla_{\boldsymbol{r}} T_\nu \,. \qquad (3.121)\end{aligned}$$

Formulation of the energy flux in terms of the particle flux yields

$$\boldsymbol{j}_\nu^\mathrm{u} = \frac{\mu_\nu^\mathrm{u}}{\mu_\nu} \frac{5}{2} k_\mathrm{B} T_\nu \boldsymbol{j}_\nu - \mu_\nu^\mathrm{u} \nu \frac{5}{2} \frac{k_\mathrm{B}^2 T_\nu}{\mathrm{q}} \nabla_{\boldsymbol{r}} T_\nu \,. \qquad (3.122)$$

Compared to *Bløtekjær*'s model, *Stratton*'s equations incorporate additional gradients of the mobility and the lattice temperature resulting from the formulation of the microscopic relaxation time in a power–law. The exponent r_ν enters the equations as a further model parameter, which has to be approximated to account for the dominant scattering mechanisms. It depends on both the doping profile and the temperature and can be in the range $[-0.5, 1.5]$ [73]. Generally, both approaches are able to cover the physical background on the same level [92]. However, it has to be kept in mind that the definitions of the mobilities employed in both model equations differ significantly. In the homogeneous case, the mobilities are equal [92,93], but for locally changing driving forces, they diverge. While the mobility in *Bløtekjær*'s equations can be approximated by the energy dependent bulk value, the definition in *Stratton*'s model is always different [86]. Thus, for engineering purposes, transport description based on *Bløtekjær*'s equations is more convenient.

3.5.9 *Onsager* Relations

The relationship between *Seebeck* and *Peltier* coefficient has been identified in the pioneering work by *Kelvin* and formulated in the first *Kelvin* relation. However, *Onsager* formulated an extended theory valid for general systems consisting of several mutually dependent irreversible processes [12]. His theory is based on thermodynamics and the general principle of time symmetry and holds for systems around their equilibrium. Every flux of a certain quantity x_i within a system is given by the linear combination of according driving forces

$$\boldsymbol{j}_{x_i} = \sum_j L_{ij} \xi_j \,, \tag{3.123}$$

while each flux has an assigned driving force defined by the derivative of the system's entropy with respect to the according quantity [94]

$$\xi_j = \partial_{x_j} S \,. \tag{3.124}$$

Following (3.123), the affinities ξ_j describe the deviation from equilibrium, which is characterized by zero currents. In equilibrium, the entropy S reaches a maximum. *Onsager*'s reciprocal relations state the identities of the cross coefficients

$$L_{ij} = L_{ji} \tag{3.125}$$

for vanishing magnetic fields. The cross coefficients L_{ij} are a measure for the coupling of the single transport phenomena within the system. A system with $L_{ij} = 0$ consists of independent irreversible processes, where every driving force only affects its connected flux. A convenient form to identify the according affinities to given fluxes is obtained by considering the time derivative of the entropy

$$\partial_t S = \sum_j \xi_j \nabla_{\boldsymbol{r}} \cdot \boldsymbol{j}_{x_i} \,. \tag{3.126}$$

For the thermoelectric case, the basic relations are given from irreversible thermodynamics [9]. In local thermodynamic equilibrium, the differential total energy is obtained as the sum of products of corresponding internal variable and the differential external variable

$$\mathrm{d}U = T\,\mathrm{d}S - p\,\mathrm{d}V + \mathrm{q}\Phi_\nu^\mathrm{c}\,\mathrm{d}N \tag{3.127}$$

with the number of particles within the system N and the chemical potential Φ_ν^c, which is the difference of the electrochemical and electrostatic potentials. Since the electrostatic potential is connected to the carrier densities as well as doping densities by *Poisson*'s equation, it is not an independent variable in the thermodynamic sense. Neglecting thermal expansion, the dV–term vanishes. Thus, expression of the differential entropy results in

$$\mathrm{d}S = \frac{1}{T}\,\mathrm{d}U - \frac{\mathrm{q}\Phi_\nu^\mathrm{c}}{T}\,\mathrm{d}N \,. \tag{3.128}$$

Introducing the according current densities, the entropy flux becomes

$$\boldsymbol{j}_s = \frac{1}{T}\boldsymbol{j}_u - \frac{\mathrm{q}\Phi_\nu^\mathrm{c}}{T}\boldsymbol{j}_\nu \,. \tag{3.129}$$

Formulating balance equations for the entropy, the total energy, and the particle density, as well as assuming steady state conditions, the change of entropy for the thermoelectric case is obtained as

$$\partial_t S = \nabla_{\boldsymbol{r}} \frac{1}{T} \cdot \boldsymbol{j}_u - \nabla_{\boldsymbol{r}} \frac{\mathrm{q}\Phi_\nu^\mathrm{c}}{T} \boldsymbol{j}_\nu \,. \tag{3.130}$$

According to the definition of heat $\mathrm{d}Q = T\,\mathrm{d}S$, the heat flux equation can be obtained from the energy flux as

$$\boldsymbol{j}_\nu^\mathrm{q} = \boldsymbol{j}_\nu^\mathrm{u} - \mathrm{q}\Phi_\nu^\mathrm{c} \boldsymbol{j}_\nu \,. \tag{3.131}$$

Thus, the change of entropy with respect to the heat flux instead of the total energy flux reads

$$\partial_t S = \nabla_{\boldsymbol{r}} \frac{1}{T} \cdot \boldsymbol{j}_\nu^\mathrm{q} - \frac{1}{T} \nabla_{\boldsymbol{r}} \Phi_\nu^\mathrm{c} \cdot \boldsymbol{j}_\nu \,. \tag{3.132}$$

From (3.130), it follows that if particle current and total energy current are considered as fluxes, the according affinities are $\nabla_{\boldsymbol{r}}(1/T)$ and $\nabla_{\boldsymbol{r}}(\Phi_\nu^\mathrm{c}/T)$. A more convenient choice can be extracted from (3.132), where the affinities $\nabla_{\boldsymbol{r}}(1/T)$ and $(1/T)\nabla_{\boldsymbol{r}}\Phi_\nu^\mathrm{c}$ follow from the particle current and the heat current as chosen fluxes. In the sequel, the combination of particle flux and heat flux has been chosen for the analysis of several transport models derived. The general equations for particle and heat flux with the *Onsager* coefficients L_{ij} read

$$\boldsymbol{j}_\nu = L_{11} \frac{1}{T} \nabla_{\boldsymbol{r}} \mathrm{q}\Phi_\nu^\mathrm{c} + L_{12} \nabla_{\boldsymbol{r}} \left(\frac{1}{T} \right) \tag{3.133}$$

$$\boldsymbol{j}_\nu^\mathrm{q} = L_{21} \frac{1}{T} \nabla_{\boldsymbol{r}} \mathrm{q}\Phi_\nu^\mathrm{c} + L_{22} \nabla_{\boldsymbol{r}} \left(\frac{1}{T} \right) \,. \tag{3.134}$$

The expansion of the temperature derivatives results in a more convenient form which can be used for a direct coefficient comparison with the transport equations obtained previously

$$\boldsymbol{j}_\nu = L_{11} \frac{1}{T} \nabla_{\boldsymbol{r}} \mathrm{q}\Phi_\nu^\mathrm{c} - L_{12} \frac{1}{T^2} \nabla_{\boldsymbol{r}} T \tag{3.135}$$

$$\boldsymbol{j}_\nu^\mathrm{q} = L_{21} \frac{1}{T} \nabla_{\boldsymbol{r}} \mathrm{q}\Phi_\nu^\mathrm{c} - L_{22} \frac{1}{T^2} \nabla_{\boldsymbol{r}} T \,. \tag{3.136}$$

Particle current and heat current obtained by *Bløtekjær*'s approach read

$$\boldsymbol{j}_\nu = -\mathrm{s}_\nu \mu_\nu \nu \nabla_{\boldsymbol{r}} \Phi_\nu - \mu_\nu \nu \frac{k_\mathrm{B}}{\mathrm{q}} \left(\frac{5}{2} - \ln \frac{\nu}{N_\mathrm{c,v}} \right) \nabla_{\boldsymbol{r}} T \tag{3.137}$$

$$\begin{aligned} \boldsymbol{j}_\nu^\mathrm{q} = &-\mathrm{s}_\nu \mu_\nu \nu k_\mathrm{B} T \left(\frac{\mu_\nu^\mathrm{u}}{\mu_\nu} \frac{5}{2} - \ln \frac{\nu}{N_\mathrm{c,v}} \right) \nabla_{\boldsymbol{r}} \Phi_\nu \\ &- \mu_\nu \nu k_\mathrm{B}^2 T \left(\frac{\mu_\nu^\mathrm{u}}{\mu_\nu} \frac{5}{2} \left(\frac{7}{2} - \ln \frac{\nu}{N_\mathrm{c,v}} \right) + \left(\frac{5}{2} - \ln \frac{\nu}{N_\mathrm{c,v}} \right) \ln \frac{\nu}{N_\mathrm{c,v}} \right) \nabla_{\boldsymbol{r}} T \,. \end{aligned} \tag{3.138}$$

A coefficient comparison between (3.135) and (3.137) as well as (3.136) and (3.139) yields the *Onsager* coefficients

$$L_{12} = \mu_\nu \nu \frac{k_\mathrm{B} T^2}{\mathrm{q}} \left(\frac{5}{2} - \ln \frac{\nu}{N_\mathrm{c,v}} \right) \tag{3.139}$$

$$L_{21} = \mu_\nu \nu \frac{k_\mathrm{B} T^2}{\mathrm{q}} \left(\frac{\mu_\nu^\mathrm{u}}{\mu_\nu} \frac{5}{2} - \ln \frac{\nu}{N_\mathrm{c,v}} \right) \,. \tag{3.140}$$

As a consequence of the macroscopic relaxation time approximation, where one relaxation time for every current is introduced, different mobility definitions enter the particle current and heat current. Thus, the model obtained by *Bløtekjær*'s approach does not inherently fulfill *Onsager*'s reciprocity theorem.

Next, the model obtained by *Stratton*'s approach is analyzed. The equations for particle and heat flux are obtained for homogeneous materials as

$$\boldsymbol{j}_\nu = -\mathrm{s}_\nu \mu_\nu \nu \nabla_{\boldsymbol{r}} \Phi_\nu - \frac{k_\mathrm{B}}{\mathrm{q}}\left(\frac{5}{2} + r_\nu - \ln\frac{\nu}{N_\mathrm{c,v}}\right)\mu_\nu \nu \nabla_{\boldsymbol{r}} T \tag{3.141}$$

$$\begin{aligned}\boldsymbol{j}_\nu^\mathrm{q} = &-\mathrm{s}_\nu \mu_\nu \nu k_\mathrm{B} T \left(\frac{5}{2} + r_\nu - \ln\frac{\nu}{N_\mathrm{c,v}}\right) \nabla_{\boldsymbol{r}} \Phi_\nu \\ &- \mu_\nu \nu \frac{k_\mathrm{B}^2 T}{\mathrm{q}} \left(\left(\frac{5}{2} + r_\nu\right)^2 - \left(\ln\frac{\nu}{N_\mathrm{c,v}}\right)^2 + \frac{5}{2} + r_\nu\right) \nabla_{\boldsymbol{r}} T\,.\end{aligned} \tag{3.142}$$

Analogously, the *Onsager* coefficients are identified by a coefficient comparison between (3.135) and (3.141) as well as (3.136) and (3.142) as

$$L_{12} = L_{21} = \mu_\nu \nu \frac{k_\mathrm{B} T^2}{\mathrm{q}} \left(\frac{5}{2} + r_\nu - \ln\frac{\nu}{N_\mathrm{c,v}}\right)\,. \tag{3.143}$$

For the *Stratton* model, *Onsager*'s reciprocity theorem holds due to the application of the microscopic relaxation time approximation, where a single relaxation time enters all fluxes.

Finally, the model derived in Section 3.5.7 is analyzed. In contrast to the other models, the stochastic part is described by a linear combination of all fluxes taken into account. The final particle current and heat current equations are

$$\begin{aligned}\boldsymbol{j}_\nu = &-\frac{Z_{11} - \frac{5}{2}k_\mathrm{B} T Z_{01}}{Z_{00}Z_{11} - Z_{10}Z_{01}} \mathrm{s}_\nu \nu \nabla_{\boldsymbol{r}} \Phi_\nu \\ &- \frac{\left(Z_{11} - \frac{5}{2}k_\mathrm{B} T Z_{01}\right)\left(\frac{5}{2} - \ln\frac{\nu}{N_\mathrm{c,v}}\right) - \frac{5}{2}k_\mathrm{B} T Z_{01}}{Z_{00}Z_{11} - Z_{10}Z_{01}} \frac{k_\mathrm{B}}{\mathrm{q}} \nu \nabla_{\boldsymbol{r}} T\end{aligned} \tag{3.144}$$

$$\begin{aligned}\boldsymbol{j}_\nu^\mathrm{q} = &-\frac{\frac{5}{2}k_\mathrm{B} T Z_{00} - Z_{10} - k_\mathrm{B} T \ln\frac{\nu}{N_\mathrm{c,v}}\left(Z_{11} - \frac{5}{2}k_\mathrm{B} T Z_{01}\right)}{Z_{00}Z_{11} - Z_{10}Z_{01}} \mathrm{s}_\nu \nu \nabla_{\boldsymbol{r}} \Phi_\nu \\ &- \left(\frac{\left(\frac{5}{2}k_\mathrm{B} T Z_{00} - Z_{10}\right)\left(\frac{5}{2} - \ln\frac{\nu}{N_\mathrm{c,v}}\right) + \frac{5}{2}k_\mathrm{B} T Z_{00}}{Z_{00}Z_{11} - Z_{10}Z_{01}}\right. \\ &\left. -k_\mathrm{B} T \ln\frac{\nu}{N_\mathrm{c,v}} \frac{\left(Z_{11} - \frac{5}{2}k_\mathrm{B} T Z_{01}\right)\left(\frac{5}{2} - \ln\frac{\nu}{N_\mathrm{c,v}}\right) - \frac{5}{2}k_\mathrm{B} T Z_{01}}{Z_{00}Z_{11} - Z_{10}Z_{01}}\right) \frac{k_\mathrm{B}}{\mathrm{q}} \nu \nabla_{\boldsymbol{r}} T\,.\end{aligned} \tag{3.145}$$

The *Onsager* coefficients are identified in the usual way by a coefficient comparison between (3.135) and (3.145) as well as (3.136) and (3.146), respectively. Thus, the according *Onsager* coefficients are

$$L_{12} = \frac{\left(Z_{11} - \frac{5}{2}k_\mathrm{B} T Z_{01}\right)\left(\frac{5}{2} - \ln\frac{\nu}{N_\mathrm{c,v}}\right) + \frac{5}{2}k_\mathrm{B} T Z_{01}}{Z_{00}Z_{11} - Z_{10}Z_{01}} \nu T^2\,, \tag{3.146}$$

$$L_{21} = \frac{\frac{5}{2}k_\mathrm{B} T Z_{00} - Z_{10} - k_\mathrm{B} T \ln\frac{\nu}{N_\mathrm{c,v}}\left(Z_{11} - \frac{5}{2}k_\mathrm{B} T Z_{01}\right)}{Z_{00}Z_{11} - Z_{10}Z_{01}} \nu T\,. \tag{3.147}$$

A comparison of the relevant parameters results in the relation

$$Z_{10} + \frac{5}{2} k_\mathrm{B} T Z_{11} - \frac{5}{2} k_\mathrm{B} T Z_{00} - \frac{35}{4} \left(k_\mathrm{B} T\right)^2 Z_{01} = 0\,. \tag{3.148}$$

Briefly summarized, *Stratton*'s equations inherently fulfill the *Onsager* relations, while the *Onsager* conformity of *Bløtekjær*'s equations depends on the choice of the model parameters. This is a consequence of the extended degrees of freedom due to the additional model parameters introduced by the macroscopic relaxation time approximation. For the non–diagonal ansatz, the reciprocity principle is fulfilled, when the model is parametrized obeying the relation (3.148).

3.5.10 Electrothermal Transport Model

For the simulation of thermoelectric devices, it is important to accurately describe the energy relations within the device. In the electrothermal transport model, the contributions of the carrier subsystems and the lattice are combined to one heat–flux equation, whereby a rigorous treatment of the coupling mechanisms between the thermal and the electrical description is achieved.

Since the driving forces within thermoelectric devices are very low compared to modern CMOS devices, the carrier gas can be safely assumed to be in local thermodynamic equilibrium with the lattice. Thus, the inclusion of additional equations accounting for carriers driven far from equilibrium to the constituent equation system are an unnecessary computational overhead. Assuming local thermodynamic equilibrium, the electrothermal transport model can be obtained from the energy transport model as a starting point.

Besides *Poisson*'s equation, the electrothermal transport model incorporates carrier balance equations as well as current equations for both electrons and holes. The energy relations are described by an additional heat–flow equation, which is accessible from both a systematic and a phenomenological point of view.

In the sequel, the electrothermal transport model is governed based on the moment equations derived by *Bløtekjær*'s approach. The calculation with *Stratton*'s equations is similar, and includes additional terms accounting for the scattering parameters r_ν. The energy flux equation derived after *Bløtekjær* (3.122) assuming local thermal equilibrium expressed in terms of the particle flux reads

$$\boldsymbol{j}_\nu^\mathrm{u} = \frac{\mu_\nu^\mathrm{u}}{\mu_\nu} \frac{5}{2} k_\mathrm{B} T \boldsymbol{j}_\nu - \kappa_\nu \nabla_{\boldsymbol{r}} T \tag{3.149}$$

with the thermal conductivity κ_ν of the carrier subsystem obeying a *Wiedemann–Franz* law

$$\kappa_\nu = \frac{5}{2} \frac{k_\mathrm{B}^2}{\mathrm{q}} \mu_\nu^\mathrm{u} \nu T\,. \tag{3.150}$$

In (3.149), the two contributions to the energy flux by a moving carrier gas as well as heat conduction by the carrier gas can be identified. However, in non–degenerate semiconductors, the thermal conductivities of the carrier subsystems can be neglected against the lattice contribution [95]. Insertion of (3.149) into the energy balance equation (3.65) yields

$$\begin{aligned} \partial_t w + \frac{\mu_\nu^\mathrm{u}}{\mu_\nu} \frac{5}{2} k_\mathrm{B} T \nabla \cdot \boldsymbol{j}_\nu + \frac{\mu_\nu^\mathrm{u}}{\mu_\nu} \frac{5}{2} k_\mathrm{B} \boldsymbol{j}_\nu \cdot \nabla_{\boldsymbol{r}} T - \nabla_{\boldsymbol{r}} \cdot \left(\kappa_\nu \nabla_{\boldsymbol{r}} T\right) & \\ + \mathrm{s}_\nu \mathrm{q} \boldsymbol{j}_\nu \cdot \nabla_{\boldsymbol{r}} \tilde{\varphi} - G_\nu^\mathcal{E} = 0\,. & \end{aligned} \tag{3.151}$$

In order to obtain expressions accessible by physical interpretation, a few rearrangements have to be performed on (3.151). First, the gradient of the electrochemical potential has to be substituted by the current relation (3.88)

$$\nabla_{\boldsymbol{r}}\Phi_\nu = -\mathrm{s}_\nu \frac{\boldsymbol{j}_\nu}{\mu_\nu \nu} - \mathrm{s}_\nu \frac{k_\mathrm{B}}{\mathrm{q}}\left(\frac{5}{2} - \ln\frac{\nu}{N_\mathrm{c,v}}\right)\nabla_{\boldsymbol{r}} T \,. \tag{3.152}$$

Furthermore, the *Seebeck* coefficient

$$\alpha_\nu = \mathrm{s}_\nu \frac{k_\mathrm{B}}{\mathrm{q}}\left(\frac{5}{2} - \ln\frac{\nu}{N_\mathrm{c,v}}\right) \,, \tag{3.153}$$

is introduced which is described closer in Section 3.5.12. Inserting (3.152) and (3.153) to (3.151) yields

$$\begin{aligned}\partial_t \frac{3}{2} k_\mathrm{B} T - \nabla_{\boldsymbol{r}} \cdot \left(\kappa_\nu \nabla_{\boldsymbol{r}} T\right) + \mathrm{s}_\nu \mathrm{q} \frac{\mu_\nu^\mathrm{u}}{\mu_\nu} \nabla_{\boldsymbol{r}} \cdot \boldsymbol{j}_\nu \left(\alpha_\nu T + \Phi_\nu - \tilde{\varphi}\right) + \frac{\mu_\nu^\mathrm{u}}{\mu_\nu} \mathrm{q} \mathrm{s}_\nu T \boldsymbol{j}_\nu \cdot \nabla_{\boldsymbol{r}} \alpha_\nu \\ - \frac{\mu_\nu^\mathrm{u}}{\mu_\nu} \mathrm{q} \frac{|\boldsymbol{j}_\nu|^2}{\mu_\nu \nu} + \mathrm{s}_\nu \left(1 - \frac{\mu_\nu^\mathrm{u}}{\mu_\nu}\right) \mathrm{q} \boldsymbol{j}_\nu \cdot \nabla_{\boldsymbol{r}} \tilde{\varphi} - G_\nu^\mathcal{E} = 0 \,.\end{aligned} \tag{3.154}$$

Equation (3.154) denotes the energy balance equation for the electron and hole subsystem, respectively. The lattice contribution incorporates an additional heat flux term, which is the dominant contribution to heat conduction within most moderately doped semiconductors. This heat flux is expressed by a *Fourier* law with the according lattice heat conductivity κ_L. The energy balance equations for the three subsystems read

$$\begin{aligned}\frac{3}{2} k_\mathrm{B} \partial_t T &= \nabla_{\boldsymbol{r}} \cdot \left(\kappa_n \nabla_{\boldsymbol{r}} T\right) + \frac{\mu_n^\mathrm{u}}{\mu_n} \mathrm{q} \frac{|\boldsymbol{j}_n|^2}{\mu_n n} + \frac{\mu_n^\mathrm{u}}{\mu_n} \mathrm{q} \left(\alpha_n T + \Phi_n - \tilde{\varphi}\right) \nabla_{\boldsymbol{r}} \cdot \boldsymbol{j}_n \qquad (3.155) \\ &\quad + \frac{\mu_n^\mathrm{u}}{\mu_n} \mathrm{q} T \boldsymbol{j}_n \cdot \nabla_{\boldsymbol{r}} \alpha_n + \left(1 - \frac{\mu_n^\mathrm{u}}{\mu_n}\right) \mathrm{q} \boldsymbol{j}_n \cdot \nabla_{\boldsymbol{r}} \tilde{\varphi} + G_n^\mathcal{E} \\ \frac{3}{2} k_\mathrm{B} \partial_t T &= \nabla_{\boldsymbol{r}} \cdot \left(\kappa_p \nabla_{\boldsymbol{r}} T\right) + \frac{\mu_p^\mathrm{u}}{\mu_p} \mathrm{q} \frac{|\boldsymbol{j}_p|^2}{\mu_p p} - \frac{\mu_p^\mathrm{u}}{\mu_p} \mathrm{q} \left(\alpha_p T + \Phi_p - \tilde{\varphi}\right) \nabla_{\boldsymbol{r}} \cdot \boldsymbol{j}_p \qquad (3.156) \\ &\quad - \frac{\mu_p^\mathrm{u}}{\mu_p} \mathrm{q} T \boldsymbol{j}_p \cdot \nabla_{\boldsymbol{r}} \alpha_p - \left(1 - \frac{\mu_p^\mathrm{u}}{\mu_p}\right) \mathrm{q} \boldsymbol{j}_p \cdot \nabla_{\boldsymbol{r}} \tilde{\varphi} + G_p^\mathcal{E} \\ c_\mathrm{L} \partial_t T &= \nabla_{\boldsymbol{r}} \cdot \left(\kappa_\mathrm{L} \nabla_{\boldsymbol{r}} T\right) \qquad (3.157)\end{aligned}$$

The final heat–flow equation is governed as the sum of the contributions of all three subsystems. Both specific heat and thermal conductivity are expressed as parameters for the entire semiconductor. Thus, the heat–flow equation reads

$$c_\mathrm{tot} \partial_t T = \nabla_{\boldsymbol{r}} \cdot \left(\kappa_\mathrm{tot} \nabla_{\boldsymbol{r}} T\right) + H \tag{3.158}$$

with the heat source term

$$
\begin{aligned}
H = {} & \frac{\mu_n^{\mathrm{u}}}{\mu_n}\mathrm{q}\frac{|\boldsymbol{j}_n|^2}{\mu_n n} + \frac{\mu_p^{\mathrm{u}}}{\mu_p}\mathrm{q}\frac{|\boldsymbol{j}_p|^2}{\mu_p p} \\
& + \mathcal{E}_{\mathrm{g}} R \\
& + \frac{\mu_n^{\mathrm{u}}}{\mu_n}\mathrm{q}\left(\alpha_n T + \Phi_n - \tilde{\varphi}\right)\nabla_{\boldsymbol{r}}\cdot\boldsymbol{j}_n \\
& - \frac{\mu_p^{\mathrm{u}}}{\mu_p}\mathrm{q}\left(\alpha_p T + \Phi_p - \tilde{\varphi}\right)\nabla_{\boldsymbol{r}}\cdot\boldsymbol{j}_p \\
& + \mathrm{q}T\left(\frac{\mu_n^{\mathrm{u}}}{\mu_n}\boldsymbol{j}_n\cdot\nabla_{\boldsymbol{r}}\alpha_n - \frac{\mu_p^{\mathrm{u}}}{\mu_p}\boldsymbol{j}_p\cdot\nabla_{\boldsymbol{r}}\alpha_p\right) \\
& + \mathrm{q}\left(\left(1 - \frac{\mu_n^{\mathrm{u}}}{\mu_n}\right)\boldsymbol{j}_n - \left(1 - \frac{\mu_p^{\mathrm{u}}}{\mu_p}\right)\boldsymbol{j}_p\right)\nabla_{\boldsymbol{r}}\tilde{\varphi}\,.
\end{aligned}
\tag{3.159}
$$

For the stationary case, the divergence terms of the electron and hole currents can be expressed by the net recombination rate due to the vanishing $\partial_t\nu$–term in the carrier balance equation (3.37). For this special case, the heat source term becomes

$$
\begin{aligned}
H = {} & \frac{\mu_n^{\mathrm{u}}}{\mu_n}\mathrm{q}\frac{|\boldsymbol{j}_n|^2}{\mu_n n} + \frac{\mu_p^{\mathrm{u}}}{\mu_p}\mathrm{q}\frac{|\boldsymbol{j}_p|^2}{\mu_p p} \\
& + \mathrm{q}\left(\frac{\mu_n^{\mathrm{u}}}{\mu_n}\left(\alpha_n T + \Phi_n - \tilde{\varphi}\right) - \frac{\mu_p^{\mathrm{u}}}{\mu_p}\left(\alpha_p T + \Phi_p - \tilde{\varphi}\right) - \mathcal{E}_{\mathrm{g}}\right) G \\
& + \mathrm{q}T\left(\frac{\mu_n^{\mathrm{u}}}{\mu_n}\boldsymbol{j}_n\cdot\nabla_{\boldsymbol{r}}\alpha_n - \frac{\mu_p^{\mathrm{u}}}{\mu_p}\boldsymbol{j}_p\cdot\nabla_{\boldsymbol{r}}\alpha_p\right) \\
& + \mathrm{q}\left(\left(1 - \frac{\mu_n^{\mathrm{u}}}{\mu_n}\right)\boldsymbol{j}_n - \left(1 - \frac{\mu_p^{\mathrm{u}}}{\mu_p}\right)\boldsymbol{j}_p\right)\nabla_{\boldsymbol{r}}\tilde{\varphi}\,.
\end{aligned}
\tag{3.160}
$$

An often used, but not fully justifiable assumption is that the mobility ratios equal unity for each electrons and holes [86]. Therefore, the heat source term reduces to

$$
\begin{aligned}
H = {} & \mathrm{q}\frac{|\boldsymbol{j}_n|^2}{\mu_n n} + \mathrm{q}\frac{|\boldsymbol{j}_p|^2}{\mu_p p} \\
& + \mathrm{q}\left(T\left(\alpha_n - \alpha_p\right) + \Phi_n - \Phi_p - \mathcal{E}_{\mathrm{g}}\right) G \\
& + \mathrm{q}T\left(\boldsymbol{j}_n\cdot\nabla_{\boldsymbol{r}}\alpha_n - \boldsymbol{j}_p\cdot\nabla_{\boldsymbol{r}}\alpha_p\right)\,.
\end{aligned}
\tag{3.161}
$$

The contributions to equation (3.161) are the *Joule* heat losses due to current flow throughout the structure, the recombination heat, which is transferred to the lattice due to carrier recombination, and the *Thomson* heat. This expression is compatible to an approach based on considerations of phenomenological irreversible thermodynamics, which is summarized in the following section.

3.5.11 Phenomenological Approach

Besides the systematic approach carried out in the preceding sections, the thermoelectric behavior of semiconductors can also be explained by an approach based on phenomenological irreversible thermodynamics [54, 96].

For the non–isothermal case, besides the gradient of the electrochemical potential a temperature gradient yields an additional driving force which is known as the *Seebeck* effect in the particle current relations

$$\boldsymbol{j}_n = \mu_n n \left(\nabla_{\boldsymbol{r}}\Phi_n + \alpha_n \nabla_{\boldsymbol{r}} T\right) \tag{3.162}$$

$$\boldsymbol{j}_p = -\mu_p p \left(\nabla_{\boldsymbol{r}}\Phi_p + \alpha_p \nabla_{\boldsymbol{r}} T\right) \,, \tag{3.163}$$

which are similar to the systematically derived equations. The corresponding heat fluxes are identified as

$$\boldsymbol{j}^{\mathrm{q}}_n = \mathrm{q}\alpha_n T \boldsymbol{j}_n - \kappa_n \nabla_{\boldsymbol{r}} T \tag{3.164}$$

$$\boldsymbol{j}^{\mathrm{q}}_p = \mathrm{q}\alpha_p T \boldsymbol{j}_p - \kappa_p \nabla_{\boldsymbol{r}} T \tag{3.165}$$

by the application of *Onsager*’s reciprocity theorem. The total energy flux of all three subsystems is written as

$$\boldsymbol{j}^{\mathrm{u}}_{\mathrm{tot}} = -\kappa_{\mathrm{L}} \nabla_{\boldsymbol{r}} T + \boldsymbol{j}^{\mathrm{q}}_n - \mathrm{q}\Phi_n \boldsymbol{j}_n + \boldsymbol{j}^{\mathrm{q}}_p + \mathrm{q}\Phi_\nu \boldsymbol{j}_p \,. \tag{3.166}$$

The differential energy densities of electrons and holes are derived using *Maxwell*’s relations [9] as

$$\mathrm{d}u_n = c_n \mathrm{d}T + \mathrm{q}\left(T\left(\partial_T \Phi_n\right)_{n,p} - \Phi_n\right) \tag{3.167}$$

$$\mathrm{d}u_p = c_p \mathrm{d}T + \mathrm{q}\left(T\left(\partial_T \Phi_p\right)_{n,p} - \Phi_p\right) \,. \tag{3.168}$$

Inserting the accumulated differential energy densities for the electron, hole, and lattice subsystems into the energy balance equation

$$\partial_t u_{\mathrm{tot}} + \nabla_{\boldsymbol{r}} \cdot \boldsymbol{j}^{\mathrm{u}}_{\mathrm{tot}} = 0 \tag{3.169}$$

yields the heat conduction equation

$$c_{\mathrm{tot}} \partial_t T = \nabla_{\boldsymbol{r}} \cdot \left(\kappa_{\mathrm{tot}} \nabla_{\boldsymbol{r}} T\right) + H \tag{3.170}$$

accounting for the conservation of total energy with the heat source term

$$\begin{aligned} H = {} & \mathrm{q}\frac{|\boldsymbol{j}_n|^2}{\mu_n n} + \mathrm{q}\frac{|\boldsymbol{j}_p|^2}{\mu_p p} \\ & + \mathrm{q}\left(T\left(\partial_T \Phi_n\right)_{n,p} - \Phi_n - T\left(\partial_T \Phi_p\right)_{n,p} + \Phi_p\right) G \\ & + \mathrm{q}T\left(\left(\partial_T \Phi_n\right)_{n,p} - \alpha_n\right) \nabla_{\boldsymbol{r}} \cdot \boldsymbol{j}_n - \mathrm{q}T\left(\left(\partial_T \Phi_p\right)_{n,p} + \alpha_p\right) \nabla_{\boldsymbol{r}} \cdot \boldsymbol{j}_p \\ & + \mathrm{q}T\left(\boldsymbol{j}_n \cdot \nabla_{\boldsymbol{r}} \alpha_n - \boldsymbol{j}_p \cdot \nabla_{\boldsymbol{r}} \alpha_p\right) \,. \end{aligned} \tag{3.171}$$

With the electrochemical potential (3.88) and the *Seebeck* coefficient (3.153) for *Maxwell–Boltzmann* statistics, the heat–source term can be rewritten to

$$\begin{aligned} H = {} & \mathrm{q}\frac{|\boldsymbol{j}_n|^2}{\mu_n n} + \mathrm{q}\frac{|\boldsymbol{j}_p|^2}{\mu_p p} \\ & + \left(\frac{5}{2} k_{\mathrm{B}} T\right) R \\ & + \mathrm{q}\left(\alpha_n T + \Phi_n - \tilde{\varphi}\right) \nabla_{\boldsymbol{r}} \cdot \boldsymbol{j}_n - \mathrm{q}\left(\alpha_p T + \Phi_p - \tilde{\varphi}\right) \nabla_{\boldsymbol{r}} \cdot \boldsymbol{j}_p \\ & + \mathrm{q}T\left(\boldsymbol{j}_n \cdot \nabla_{\boldsymbol{r}} \alpha_n - \boldsymbol{j}_p \cdot \nabla_{\boldsymbol{r}} \alpha_p\right) \,, \end{aligned} \tag{3.172}$$

which can be finally simplified for the static case because of the vanishing $\partial_t \nu$–term in (3.37) to

$$\begin{aligned} H = {} & \mathrm{q}\frac{|\boldsymbol{j}_n|^2}{\mu_n n} + \mathrm{q}\frac{|\boldsymbol{j}_p|^2}{\mu_p p} \\ & + \mathrm{q}\left(T\left(\alpha_n - \alpha_p\right) + \Phi_n - \Phi_p - \mathcal{E}_\mathrm{g}\right) G \\ & + \mathrm{q}T\left(\boldsymbol{j}_n \cdot \nabla_{\boldsymbol{r}}\alpha_n - \boldsymbol{j}_p \cdot \nabla_{\boldsymbol{r}}\alpha_p\right) . \end{aligned} \tag{3.173}$$

The final result is equal to the heat–source term of the systematically derived heat–flow equation in Section 3.5.10 under several simplifying assumptions, when the electrochemical potential as well as the *Seebeck* coefficient are expressed by the corresponding relations for *Maxwell–Boltzmann* statistics.

3.5.12 *Seebeck* Coefficient

While the *Seebeck* coefficient has been treated on a phenomenological basis in Section 2.1.1, the identification of its inclusion in the semiconductor current equations is the topic of this section.

Assuming a block of homogeneous material, a thermoelectric voltage can be measured between the two ends of the solid in the case of a non–zero temperature gradient. The *Seebeck* coefficient is defined as the ratio of the resulting voltage and the temperature difference. Expressed in "internal" quantities, the negative gradient of the electrochemical potential is equal to the temperature gradient times the *Seebeck* coefficient

$$-\nabla_{\boldsymbol{r}}\Phi_\nu = \alpha_\nu \nabla_{\boldsymbol{r}} T\,. \tag{3.174}$$

This relation is limited to thermoelectric devices in the open circuit case, which is characterized by zero current. The current equation (3.88) derived after *Bløtekjær* in the formulation incorporating the electrochemical potential reads

$$\boldsymbol{j}_\nu = -\mathrm{s}_\nu \mu_\nu \nu \nabla_{\boldsymbol{r}}\Phi_\nu - \mu_\nu \nu \frac{k_\mathrm{B}}{\mathrm{q}}\left(\frac{5}{2} - \ln\frac{\nu}{N_\mathrm{c,v}}\right)\nabla_{\boldsymbol{r}} T \doteq 0\,, \tag{3.175}$$

whereby the carrier gas is assumed to be in local thermal equilibrium with the lattice. Thus, the carrier temperature is equal to the lattice temperature, which is expressed by a single temperature in the current relations

$$T_\nu = T_\mathrm{L} = T\,. \tag{3.176}$$

An identification of the *Seebeck* coefficient in (3.175) with its definition after (3.174) results in

$$\alpha_\nu = \mathrm{s}_\nu \frac{k_\mathrm{B}}{\mathrm{q}}\left(\frac{5}{2} - \ln\frac{\nu}{N_\mathrm{c,v}}\right) . \tag{3.177}$$

Finally, the current equations for electrons and holes read

$$\boldsymbol{j}_n = \mu_n n \nabla_{\boldsymbol{r}}\Phi_n - \mu_n n \frac{k_\mathrm{B}}{\mathrm{q}}\left(\frac{5}{2} - \ln\frac{n}{N_\mathrm{c}}\right)\nabla_{\boldsymbol{r}} T = \mu_n n\left(\nabla_{\boldsymbol{r}}\Phi_n + \alpha_n \nabla_{\boldsymbol{r}} T\right) , \tag{3.178}$$

$$\boldsymbol{j}_p = -\mu_p p \nabla_{\boldsymbol{r}}\Phi_p - \mu_p p \frac{k_\mathrm{B}}{\mathrm{q}}\left(\frac{5}{2} - \ln\frac{p}{N_\mathrm{v}}\right)\nabla_{\boldsymbol{r}} T = -\mu_p p\left(\nabla_{\boldsymbol{r}}\Phi_p + \alpha_p \nabla_{\boldsymbol{r}} T\right) \tag{3.179}$$

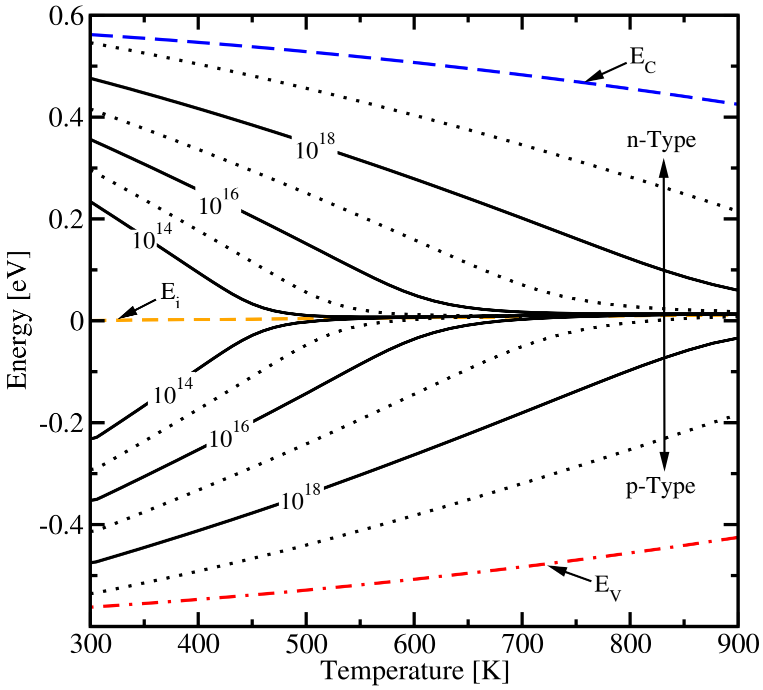

Figure 3.6: Doping dependent *Fermi* energy with respect to temperature.

with the modeled *Seebeck* coefficients

$$\alpha_n = -\frac{k_\mathrm{B}}{\mathrm{q}} \left(\frac{5}{2} - \ln \frac{n}{N_\mathrm{c}} \right) , \tag{3.180}$$

$$\alpha_p = \frac{k_\mathrm{B}}{\mathrm{q}} \left(\frac{5}{2} - \ln \frac{p}{N_\mathrm{v}} \right) . \tag{3.181}$$

In literature, they are also often referred to as thermoelectric forces. The different sign of the *Seebeck* coefficients is the basis for thermoelectric devices consisting of two legs with opposite doping. Their construction with the legs parallel in a thermal sense and electrically serial yields a constructive interference of both leg's contributions.

Stratton's equations can be treated analogously to *Bløtekjær*'s approach. They yield additional r_ν summands within the brackets due to the formulation of the microscopic relaxation time in a power–law ansatz, which refer to the dependence of the *Seebeck* coefficients on different dominant scattering mechanisms, which are expressed explicitly in this case. Thus, the *Seebeck* coefficients within *Stratton*'s framework for electrons and holes are modeled as

$$\alpha_n = -\frac{k_\mathrm{B}}{\mathrm{q}} \left(\frac{5}{2} + r_n - \ln \frac{n}{N_\mathrm{c}} \right) , \tag{3.182}$$

$$\alpha_p = \frac{k_\mathrm{B}}{\mathrm{q}} \left(\frac{5}{2} + r_p - \ln \frac{p}{N_\mathrm{v}} \right) . \tag{3.183}$$

The modeled *Seebeck* coefficients incorporate several physical mechanisms causing an additional driving force to carriers by a temperature gradient. In order to clarify the situation, the expressions for the *Seebeck* coefficients in n– and p–type semiconductors (3.180) and (3.181) are rewritten in terms of the energy levels in the semiconductor. Therefore, the carrier concentrations are expressed by *Maxwell* statistics

$$n = N_\mathrm{c} \exp\left(\frac{\mathcal{E}_\mathrm{f} - \mathcal{E}_\mathrm{c}}{k_\mathrm{B} T}\right) \tag{3.184}$$

$$p = N_\mathrm{v} \exp\left(\frac{\mathcal{E}_\mathrm{v} - \mathcal{E}_\mathrm{f}}{k_\mathrm{B} T}\right) \tag{3.185}$$

is inserted and yields

$$\alpha_n = -\frac{k_\mathrm{B}}{\mathrm{q}}\left(\frac{5}{2} - \frac{\mathcal{E}_\mathrm{f} - \mathcal{E}_\mathrm{c}}{k_\mathrm{B} T}\right) \tag{3.186}$$

$$\alpha_p = \frac{k_\mathrm{B}}{\mathrm{q}}\left(\frac{5}{2} - \frac{\mathcal{E}_\mathrm{v} - \mathcal{E}_\mathrm{f}}{k_\mathrm{B} T}\right) . \tag{3.187}$$

Several temperature dependencies within (3.186) and (3.187) are analyzed in the sequel. First, the temperature dependence of the *Fermi* level itself causes a gradient along a thermoelectric device and thus a driving force to the carriers. Furthermore, in semiconductors the temperature dependent band–gap enters into the position of the band edges and thus also contributes to the driving force. Within *Stratton*'s formulation, the scattering parameter r is influenced by the dominance of the single scattering mechanisms. Due to the temperature dependence of single carrier scattering mechanisms, r changes as well and thus has an influence on the *Seebeck* coefficients.

Fig. 3.6 illustrates the temperature dependent energy relations for doped silicon. The band–gap $\mathcal{E}_\mathrm{c} - \mathcal{E}_\mathrm{v}$ decreases with increasing temperature. Furthermore, the intrinsic *Fermi* level for undoped samples moves towards the conduction or valence band edge for n–doped and p–doped samples, respectively. With increasing temperatures, the *Fermi* level for doped samples converges against the intrinsic level of undoped samples again.

Both the models incorporated in *Bløtekjær*'s as well as *Stratton*'s equations have been derived assuming *Maxwell–Boltzmann* statistics. However, in order to account for high doping concentrations, *Fermi–Dirac* statistics have to be considered. Furthermore, the phonon system has been assumed to be in equilibrium, which act as scattering centers for carriers. However, this is not the case in thermoelectric devices, where strong temperature gradients cause a phonon movement throughout the structure. Due to this phonon net movement driven by a temperature gradient from the hot to the cold end, the carriers gain additional momentum. This term caused by the net movement of the phonons is referred to as the phonon–drag effect [97–100] and can be modeled as additional driving force for the carriers within the expressions for the *Seebeck*–coefficients [101–103]. Since *Boltzmann*'s equation does not incorporate a net movement of the phonon gas itself, but relies on thermal equilibrium, this effect is not incorporated in the derivation carried out in the last sections. A theoretical approach including the phonon–drag effect as well can be found in [104]. In silicon, the phonon–drag plays a role in the temperature range between 10 K and 500 K [102].

In order to account for the deviation between *Maxwell–Boltzmann* and *Fermi–Dirac* statistics in the degenerate case as well as for the phonon–drag effect, the correction terms ζ_n and ζ_p are introduced, which are generally both dependent on the temperature as well as the dopant concentration. Therefore, the models for the *Seebeck* coefficients of electrons and holes are

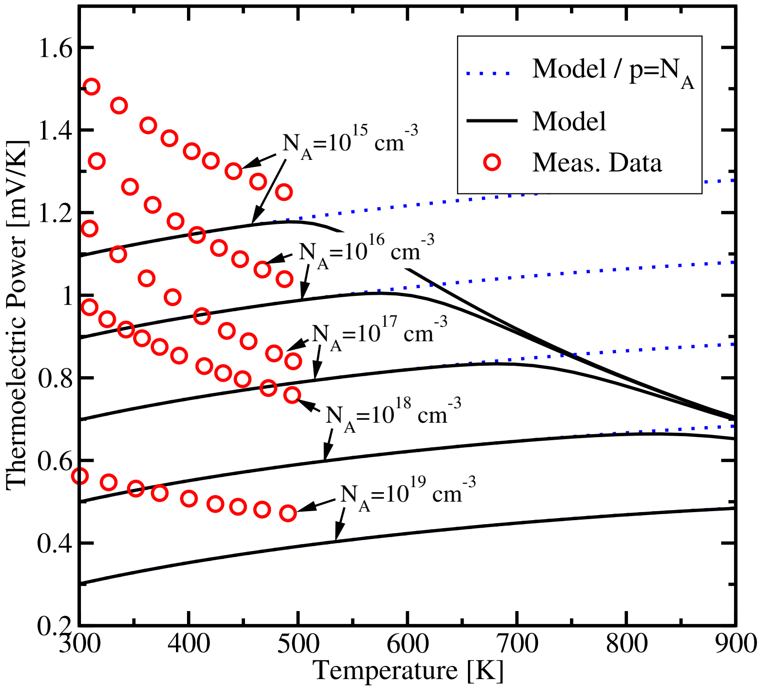

Figure 3.7: *Seebeck* coefficients for differently doped p–type silicon samples. Solid lines depict the theoretical models, whereby the decrease for elevated temperatures results from the increased hole concentration in the intrinsic range.

expressed as

$$\alpha_n = -\frac{k_\mathrm{B}}{\mathrm{q}}\left(\frac{5}{2} - \ln\frac{n}{N_\mathrm{c}} + \zeta_n\right) , \tag{3.188}$$

$$\alpha_p = \frac{k_\mathrm{B}}{\mathrm{q}}\left(\frac{5}{2} - \ln\frac{p}{N_\mathrm{v}} + \zeta_p\right) . \tag{3.189}$$

The *Seebeck* coefficients for p–type and n–type silicon are analyzed in Figures 3.7 and 3.8. Solid lines depict analytical model data based on (3.180) and (3.181), which have been obtained by a post processing step after self–consistent simulations of a thermoelectric device. Thus, the carrier concentrations increase at certain temperatures from the doping concentrations to the intrinsic values. Constant carrier concentrations at the doping level are illustrated by dotted lines and are the asymptotes in the lower temperature regime. Measurement data has been taken from [105], which is based on original data from [97]. However, there is some uncertainty in the temperature range between 350 K and 500 K, since in this range data has been obtained by extrapolation following a $1/T$–law [106]. In contrast to the analytical expressions, measurement values also incorporate the phonon–drag contribution, which is not relevant in the higher temperature range.

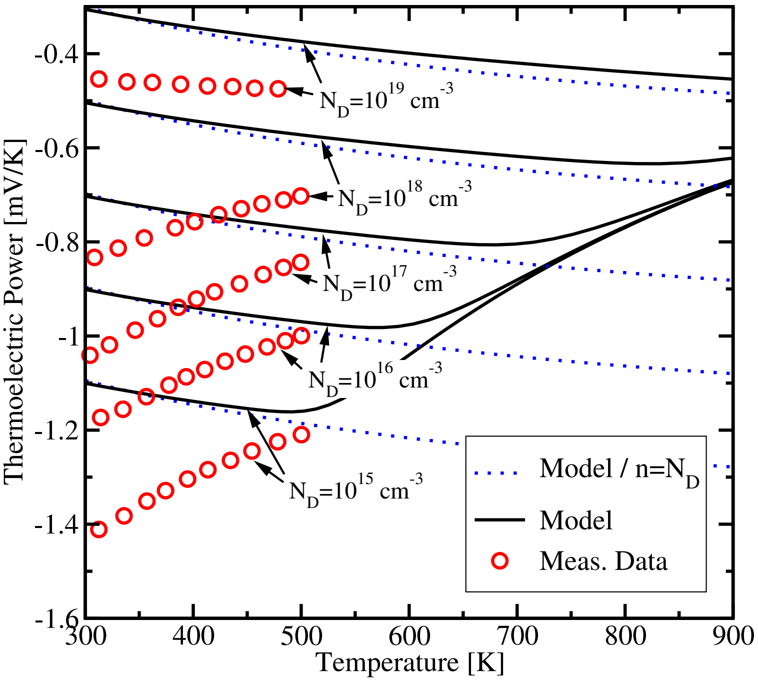

Figure 3.8: *Seebeck* coefficients for differently doped n–type silicon samples.

'Hell must be isothermal; for otherwise the resident engineers and physical chemists (of which there must be some) could set up a heat engine to run a refrigerator to cool off a portion of their surroundings to any desired temperature.'

Henry A. Ben

Chapter 4

Materials for Thermoelectric Devices

MATERIAL RESEARCH AND ENGINEERING is one of the cornerstones of efficient thermoelectric devices. This chapter first gives an overview on characteristic material properties as well as their dependence on temperature and carrier concentration. A good thermoelectric material is identified by high *Seebeck* coefficients and good electric transport properties, while thermal transport is held on the short side [107].

Usually, these material properties are subject to a pronounced temperature dependence, leading to the definition of ideal thermal operation conditions for a certain material. Furthermore, the influence of the doping on several relevant parameters is investigated and an approximation for the ideal material doping is given.

In the following, technologically important thermoelectric materials are introduced and their operational range is outlined. On the example of silicon–germanium, the important feature of lowered thermal conductivity within semiconductor alloys compared to their pure constituents is illustrated. Furthermore, SiGe plays an important role in modeling and simulation due to its elaborate available physical description driven by mainstream microelectronics. On the temperature scale, SiGe is located at relatively high operational values. In contrast to some other materials, it is available for both p- and n-doped samples.

Lead telluride (PbTe) is an interesting candidate for the intermediate temperature range with a maximum operating temperature of about 900 K. Beside its application in thermoelectrics, it is also used for optical devices in the infrared wavelength regime. Its material description is carried out for device modeling in detail in Chapter 5. In addition to doping by foreign atoms, the material type can be adjusted by deviation of its stoichiometric composition. Beside pure lead telluride, several ternary alloys exist, which are subject to ongoing research. Generally, lead telluride is applicable for both n-type and p-type samples. However, in contrast to n-type samples, p-type samples suffer under low stability under high temperatures, difficult bonding, as well as poorer mechanical properties depending on their dopants [108]. Thus, the p-doped leg is often replaced by alloys consisting of silver antimony telluride and germanium telluride, often referred to as TAGS.

The lower end of the temperature scale is covered by bismuth telluride. Due to its good thermoelectric properties at room temperature, devices made of bismuth telluride are often used for cooling applications. As in lead telluride, the material type and number of access carriers can be adjusted by a deviation of stoichiometry.

Besides these “classical” thermoelectric materials, which are well established in several generation and cooling applications, ongoing research focuses on novel materials [109–111] as well as nanostructures [112–120] especially designed for thermoelectric needs.

4.1 Characterization of Materials

The overall performance of a thermoelectric generator is rated by characteristic numbers as its efficiency, total power output, and power density. However, these numbers, especially the efficiency, is limited by several parameters. Besides the geometrical impact, material parameters such as the *Seebeck* coefficient as well as thermal and electrical conductivities have a strong influence on both transport of carriers and phonons and thus the overall device behavior. In the sequel, the thermoelectric figure of merit, which embraces the material parameters affecting the device behavior, as well as its influence on the device efficiency are discussed.

According to *Ioffe* [7], the maximum conversion efficiency η_{max} of a thermoelectric generator at matched load condition $R_{\mathrm{i}} = R_{\mathrm{L}}$ is given by the product of the ideal reversible thermodynamic process' efficiency and a factor describing the energy losses within the device due to Joule heating and non-ideal thermal conductivity [11]

$$\eta_{\mathrm{max}} = \frac{T_{\mathrm{H}} - T_{\mathrm{C}}}{T_{\mathrm{H}}} \frac{M - 1}{M + T_{\mathrm{C}}/T_{\mathrm{H}}} \tag{4.1}$$

where T_{H} and T_{C} denote the temperatures of the heated and the cooled end of the device, respectively and

$$M = \sqrt{1 + \frac{1}{2} Z \left(T_{\mathrm{C}} + T_{\mathrm{H}}\right)}\,. \tag{4.2}$$

The averaged thermoelectric figure of merit for both legs of the device, indicated by numerical subscripts, with matched geometry

$$Z = \frac{\left(\alpha_1 - \alpha_2\right)^2}{\left(\sqrt{\kappa_1/\sigma_1} + \sqrt{\kappa_2/\sigma_2}\right)^2}\,. \tag{4.3}$$

This figure of merit incorporates all relevant material parameters, which are the *Seebeck* coefficient α, thermal conductivity κ, and electric conductivity σ. Due to the strong dependence on both temperature and the concentration of free carriers of these single parameters, the figure of merit exhibits according dependencies as well, which means that each material has its own optimum range of operation. However, in practical devices, both legs have similar material properties, and the bulk figure of merit for a certain material is conveniently defined as

$$Z = \frac{\alpha^2 \sigma}{\kappa}\,. \tag{4.4}$$

From a microscopic point of view, the figure of merit is influenced by both charge and heat transport as well as the coupling of these two within a semiconductor. Thus, the figure of merit follows from the band structure, lattice dynamics, and scattering mechanisms of charge carriers.

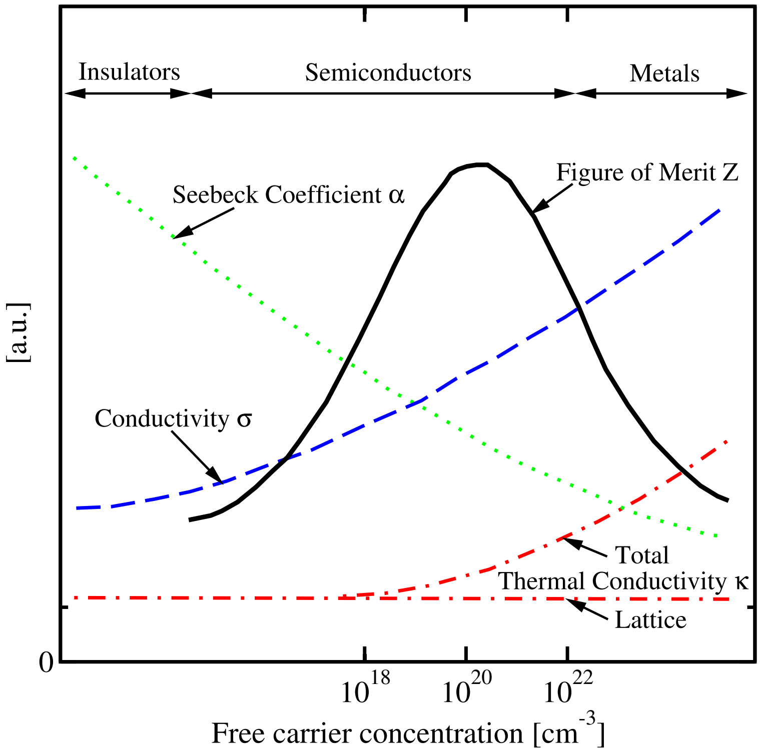

Figure 4.1: *Seebeck* coefficient, conductivity, thermal conductivity, and figure of merit with respect to free carrier concentration, after [121].

An ideal thermoelectric material is not only assured by a high figure of merit, but also by the temperature range, where these high values are achieved. In practical situations, each material has its ideal operation temperature range, thus the choice of the material is strongly affected by the intended use.

The free carrier concentration which is influenced by the doping in semiconductors, has a strong influence on the figure of merit. Fig. 4.1 illustrates the dependence of several material parameters on the concentration of free carriers. While increasing carrier concentrations have generally a detrimental effect on the *Seebeck* coefficient, the electric conductivity σ increases due to the increased number of available carriers. On the other hand, the electric part of the thermal conductivity κ_ν becomes non-negligible at high values of the carrier concentration and the dominant thermal conductivity mechanism on the transition to metals. Both insulators and metals show superior conditions for single parameters, but accordingly poor conditions for others. Metals are characterized by generally low values of the *Seebeck* coefficient and comparably high thermal conductivities, which cannot be compensated by their low electric resistances. On the other hand, insulators have comparably high *Seebeck* coefficients, which cannot outperform the very low electric conductivities. Semiconductors are positioned in the competition region of the single parameters, and thus the resulting thermoelectric figure of merit has its maximum. This maximum is supported by still moderate *Seebeck* coefficients and already good electrical conductivities and limited by elevated electrical thermal conductivity in the region of high carrier concentrations. Within semiconductors, the optimum carrier concentration can be accurately controlled by proper doping concentrations.

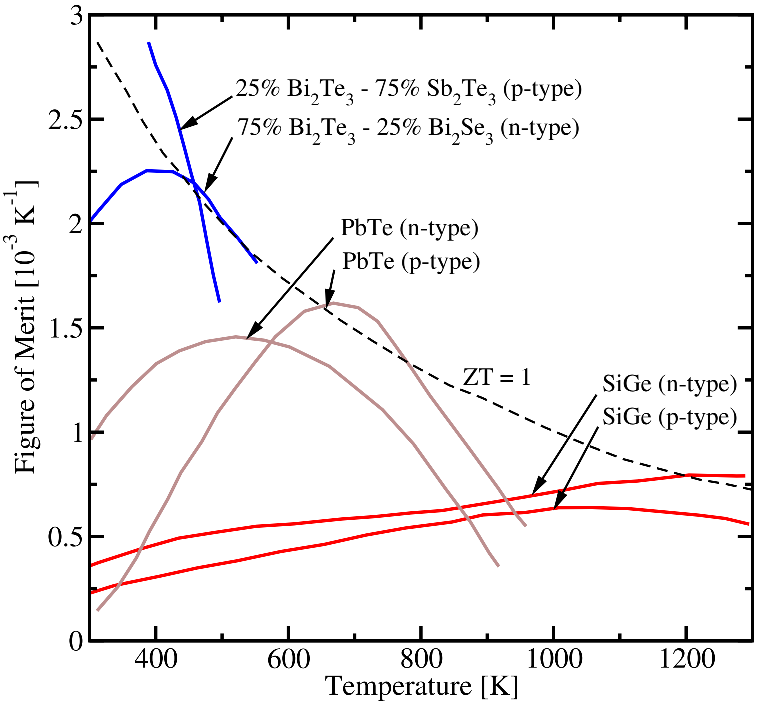

Figure 4.2: Thermoelectric figure of merit vs. temperature for several materials used for thermoelectric devices, after [121].

Temperature dependent figure of merit data for materials commonly used in thermoelectric devices are collected in Fig. 4.2. While bismuth telluride and several ternary alloys area good choice for low temperature thermoelectrics, silicon and silicon-germanium alloys are suitable for higher temperatures. Lead telluride covers the intermediate range between bismuth telluride and silicon-germanium. For even higher temperatures, wide band gap materials such as silicon carbide and boron carbide have to be considered. The dashed line depicts the product of the figure of merit and temperature to be one. Maximum figure of merit values for several materials do not outperform this line by far which results in an accordingly limited conversion efficiency.

4.2 Optimization of Device Performance

In the previous section, the suitability of several materials to certain temperature ranges as well as the basic material properties responsible the maximum device performance have been carried out. In the following, correlations between several parameters are highlighted and furthermore strategies to improve device efficiency and performance are evolved on the basis of these material parameters.

From the definition of the figure of merit (4.4), it is obvious that the thermal conductivity has to be lowered while maintaining high values of electric conductivity and *Seebeck* coefficient in order to achieve high Z values. Since several parameters strongly depend on the carrier concentration as illustrated in Fig. 4.1, it is an interesting task to determine the ideal carrier concentration for a certain material and a certain temperature [122]. For non-degenerated materials, the *Seebeck* coefficient is given by

$$\alpha_\nu = \mp \frac{k_\mathrm{B}}{\mathrm{q}} \left(\frac{5}{2} + r_\nu - \ln \frac{\nu}{N_\mathrm{c,v}} \right) \tag{4.5}$$

where the carrier concentration is denoted by ν, the scattering parameter r_ν, and the effective density of states for the conduction and valence bands $N_\mathrm{c,v}$, respectively. The sign is negative for electrons and positive for holes. This expression ignores the phonon-drag effect, whose impact is normally pronounced in relatively low temperature ranges. Furthermore, the carrier concentration enters the expression for the electric conductivity

$$\sigma_\nu = \mathrm{q}\nu\mu_\nu \tag{4.6}$$

as well as the electric component of the thermal conductivity. The latter is expressed introducing the *Lorentz* number L_0 by

$$\kappa_\nu = L_0 \left(\frac{k_\mathrm{B}}{\mathrm{q}} \right)^2 \sigma T \,. \tag{4.7}$$

Inserting (4.5), (4.6), and (4.7) into equation (4.4) and after some rearrangement, one obtains

$$Z = \left(\frac{5}{2} + r_\nu - \ln \frac{\nu}{N_\mathrm{c,v}} \right)^2 \left(\frac{\kappa_\mathrm{L}}{\left(k_\mathrm{B}/\mathrm{q}\right)^2 \mathrm{q}\nu\mu_\nu} + L_0 T \right)^{-1} \,. \tag{4.8}$$

Setting the derivative with respect to ν of the figure of merit to zero, the equation for the optimum carrier concentration is obtained as [123]

$$\ln \frac{\nu}{N_\mathrm{c,v}} + 2 \left(\frac{5}{2} + r_\nu \right) \frac{k_\mathrm{B}^2}{\mathrm{q}} \frac{\mu_\nu}{\kappa_\mathrm{L}} T\nu = \frac{1}{2} + r_\nu \tag{4.9}$$

assuming that the *Lorentz* number does not depend on the carrier concentration. Ignoring the carrier contribution in the expression for the thermal conductivity, which holds true for low to moderately doped semiconductors, the optimum carrier concentration is given dependent on the scattering parameter [122] as

$$\nu_\mathrm{opt} = N_\mathrm{c,v} \exp \left(\frac{1}{2} + r_\nu \right) \,. \tag{4.10}$$

This result has to be handled carefully, since the scattering parameter itself is doping dependent. While for relatively low impurity concentration, scattering by phonons is dominant and thus $r_\nu = -1/2$, high doping concentrations increase scattering by ionized impurities and shift r_ν to a value of 3/2. However, relatively high doping concentrations are necessary to obtain good thermoelectric performance [122].

The maximum efficiency for a thermoelectric generator made of $\mathrm{Si}_{0.7}\mathrm{Ge}_{0.3}$ has been derived to be 12.1 % in [19]. Furthermore, a reduction of the lattice thermal conductivity without side effects on the electric properties has been calculated to result in a total efficiency of 23.3 %, which is far from today's practically realized generators.

Optimization of the figure of merit by influencing the carrier concentration is quite limited due to the interdependency of *Seebeck* coefficient and electric conductivity as well as the electric part of the thermal conductivity due to their common dependence on the carrier concentration. In contrast to this, the lattice thermal conductivity incorporates potential to increase the figure of merit independently of the carrier concentration. The key to obtain elevated figures of merit are low lattice thermal conductivities in order to keep the heat flux throughout the device low. In terms of microscopic processes, it is favorable to achieve higher phonon scattering rates while not affecting the carrier ones.

In semiconductor alloys, additional scattering is introduced by the internal lattice disorder. This mechanism is especially pronounced in alloys with a rather large difference between the single masses of the components. For example, the thermal conductivity of SiGe with a germanium content of only 10 % is lower by a factor of 6 compared to pure silicon [95]. At the same time, the electrical properties show only minor changes.

Furthermore, the introduction of sintered materials causes increased scattering of phonons at the grain boundaries resulting in accordingly limited phonon mean free paths. The preparation as well as the influence of different grain sizes on the thermal conductivity of lead tin telluride are reported in [124–128]. Similar results are collected for SiGe in [129]. Grain sizes have to be in a range where the electrical conductivity is not significantly affected by additional scattering. Thus, promising combinations seem to be carefully designed sintered semiconductor alloys.

A continuation of this concept is incorporated in the idea of low–dimensional structures as well as directed search for novel materials with accordingly low thermal conductivities. Recent research focuses on both nanostructures [112–120] as well as emerging materials such as clathrates [109, 110], where their large molecular structure ensures low thermal conductivities. In nanostructures, thermal conductivity is held low by affecting phonon transport with low–dimensional structures. In a certain geometrical range, the electrical properties are almost not affected compared to bulk materials, while thermal conductivity is decreased by various size effects.

4.3 Silicon–Germanium

This section gives a brief summary of application examples as well as material properties of silicon–germanium alloys. SiGe thermogenerators have been successfully used in a couple of applications. Probably the most fascinating of them are thermoelements powered by radioisotopes (RTGs), which proved to be a reliable power source on several space missions as well as in remote weather stations [11]. The material has been chosen due to its high reliability as well as high operating temperatures in order to match the conditions provided by the nuclear fuel.

Furthermore, the SiGe material system serves as an ideal basis for simulation studies for thermoelectric device optimization due to its well known material parameters from main stream microelectronics. Especially the introduction of strain techniques to commercially available devices [130–132] caused major research efforts on the properties as well as processability of Si/SiGe devices. Due to the widely available data and models, only the most important material data are briefly summarized in the sequel. Detailed analysis and material characterization of SiGe alloys with its emphasis on physical modeling for device simulation can be found in [133]. Besides this, a review on the validity of several models at high temperatures with a focus on mobility modeling has been carried out in [134].

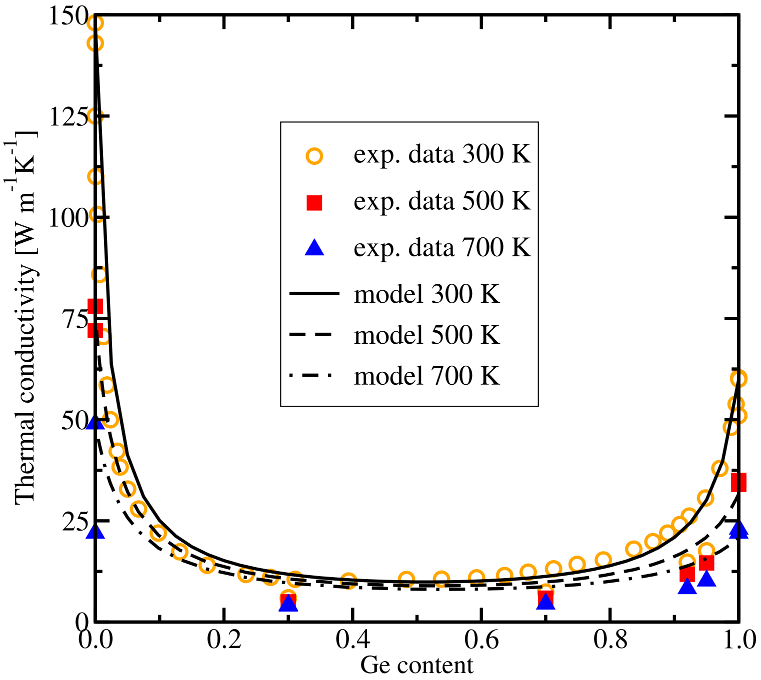

Figure 4.3: Thermal conductivity of silicon–germanium alloys with respect to material composition for different temperatures.

Compared to the corresponding pure materials, SiGe alloys are interesting candidates for thermoelectric applications due to the different influence of the material composition on thermal conductivity and mobility. Theoretical calculations on the maximum figure of merit have been carried out in [19, 135]. While in [135], a two-band model has been used, the second conduction band has been considered in [19] resulting in a wider temperature range covered by the model.

The lattice thermal conductivity for SiGe decreases significantly with increasing germanium content of up to 50 %. Above 50 %, the trend reverses to finally approach the value of pure germanium. This characteristics is caused by the important role of alloy disorder scattering of phonons due to the large mass difference of silicon and germanium as well as the random distribution of the constituents in the alloy [136]. Fig. 4.3 illustrates the material composition dependence of SiGe thermal conductivity for 300 K, 500 K, and 700 K. Several measurement data found in literature are in good agreement to the model [95, 106, 137–141]. Accordingly, lower values in sintered samples are reported in [142] due to additional phonon scattering at grain boundaries. Constantly low sensitivity of the thermal conductivity on the material composition over a wide range of germanium contents results in a good figure of merit for sintered composites, as often used in thermoelectric applications. This is beneficial especially in inhomogeneous samples, where clusters normally cause relatively large local deviations of the material parameters.

Material composition dependent mobilities for n-type silicon–germanium samples are illustrated in Fig. 4.4. The symbols depict data obtained by Monte Carlo simulations, while the lines show data obtained by the according models [143]. In contrast to the thermal conductivity, the mobility decreases more slowly with increasing Ge content resulting in a range with good figures of merit.

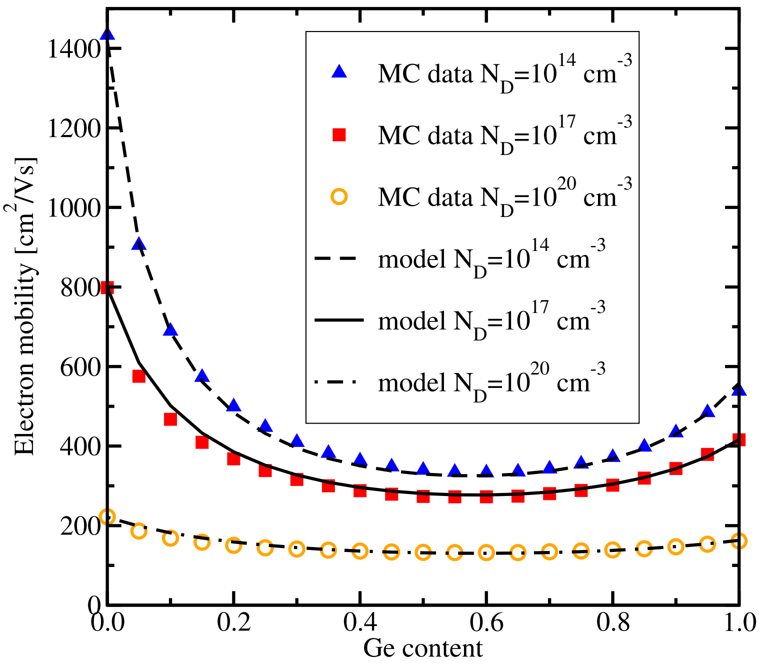

Figure 4.4: Electron mobility vs. material composition for silicon–germanium alloys for different at room temperature.

Several measurements of the *Seebeck* coefficient for both pure silicon and germanium as well as several alloys can be found in literature [97, 98, 106, 144, 145]. At the lower temperature range, the coefficients are elevated by the phonon-drag effect [146–149] in pure silicon, which is not the case in SiGe alloys due to the short phonon mean free paths [19]. Interestingly, the electronic contribution does not change noticeably for different material compositions, thus modeling of the *Seebeck* coefficients for SiGe samples can be reduced to the electronic contribution.

In spite of their outstanding reliability, some attention has to be paid on degradation of SiGe thermoelectric generators [150] causing a reduction of the figure of merit over the device lifetime. At high temperature conditions, sublimation can cause both thermal and electrical shortcuts due to deposition in the surrounding. Under extreme conditions, erosion occurs and may cause device failures by open circuits or mechanical damage. A coating of silicon nitride reduces temperature dependent loss rates by sublimation by a factor of approximately 10 [150]. Furthermore, accordingly high doping concentrations, which are favored in order to achieve high figures of merit, tend to build up local accumulations. Such accumulations cause a reduction of the free carrier concentration and thus increase the electric resistivity resulting in worse figures of merit. Boron-doped p-type samples are less sensitive to this effect than n-type samples doped with phosphorus due to the comparably lower diffusion rates of the dopants.

4.4 Lead Telluride and its Alloys

Lead telluride (PbTe) as well as lead tin telluride ($\mathrm{Pb}_{1-x}\mathrm{Sn}_x\mathrm{Te}$) have their operational temperature ranges between those of bismuth telluride and silicon–germanium. Although the maximum figure of merit is slightly lower than that of bismuth telluride, lead telluride extents the temperature range covered for thermoelectric applications with comparable good efficiencies. Electrical properties can be controlled by variations of the material composition through changing the stoichiometric ratio. While excess usage of lead results in an n-type semiconductor, a shift to more tellurium gives a p-type semiconductor. However, the maximum carrier concentration achievable by this mechanism is in the order of $10^{18}\,\mathrm{cm}^3$, which is lower than the ideal doping for thermoelectric applications [11]. Higher carrier concentrations can be achieved by doping. While PbI_2, $PbBr_2$, or Ge_2Te_3 are used as extra donors, Na_2Te or K_2Te are applied for elevating acceptor concentrations.

Both PbTe and $Pb_{1-x}Sn_xTe$ can be manufactured as single crystals as well as sintered materials. Sintered samples are usually fabricated at temperatures around 1000 K [151] and are distinguished from single crystals by their lower thermal and electrical conductivities due to additional scattering at grain boundaries.

A comprehensive elaboration of the physical properties of lead telluride and lead tin telluride as well as according models for application within device simulation is given in Chapter 5.

4.5 Bismuth Telluride and its Alloys

Due to its good thermoelectric figure of merit at room temperature, bismuth telluride (Bi_2Te_3) as well as some related ternary alloys are often used for cooling applications in commercial *Peltier* elements. Commonly applied ternary alloys consist of bismuth telluride with either bismuth selenide (Bi_2Se_3) or antimony telluride (Sb_2Te_3) [152]. Their common crystal structure is hexagonal [153], although some authors also describe the unit cell as rhombohedral [154], which is not a discrepancy. The hexagonal description outlines the layered structure of the material, and its unit cell has the lattice constants $a = 4.38\,\text{Å}$ and $c = 30.36\,\text{Å}$ at 77 K [155]. Furthermore, the corresponding linear thermal expansion coefficients are $14.4 \times 10^{-6}\,\mathrm{K}^{-1}$ and $21.3 \times 10^{-6}\,\mathrm{K}^{-1}$ [156, 157]. According to [158], Bi_2Te_3 has a mass density of $7.86\,\mathrm{g/cm}^{-3}$ and a melting point of 858 K which limits the temperature range for thermoelectric applications.

A change of the free carrier concentration can, similarly to lead telluride, either be performed by changing the material composition or with extra dopants. In contrast to lead telluride, stoichiometric bismuth telluride is of p-type with a free carrier concentration of approximately $10^{19}\,\mathrm{cm}^{-3}$. A shift to excess tellurium leads to an n-type material.

Bismuth telluride is a narrow gap semiconductor with an indirect band gap of 160 meV at 300 K. As most semiconductors, the temperature dependence of its band–gap is negative with a value of $-1.5 \times 10^{-4}\,\mathrm{eV/K}$ [159–161]. According to pseudopotential band structure calculations [162], both the highest valence band and lowest conduction band have six valleys. Beside these two bands, each a second conduction and valence band with energy separations of 30 meV and 20 meV, respectively are proposed in [163, 164]. Due to the low density of states, the population of higher energy levels is relatively high. Thus, the large non-parabolicity of the band structure becomes important [165]. Recently, experimental work has been accomplished with first principle calculations [166, 167], which serves as a basis for further performance optimization, such as the introduction of low–dimensional structures [168].

Reduction of the thermal conductivity is one important possibility to increase the figure of merit. Within ternary alloys, the lattice thermal conductivity depends on the additional phonon

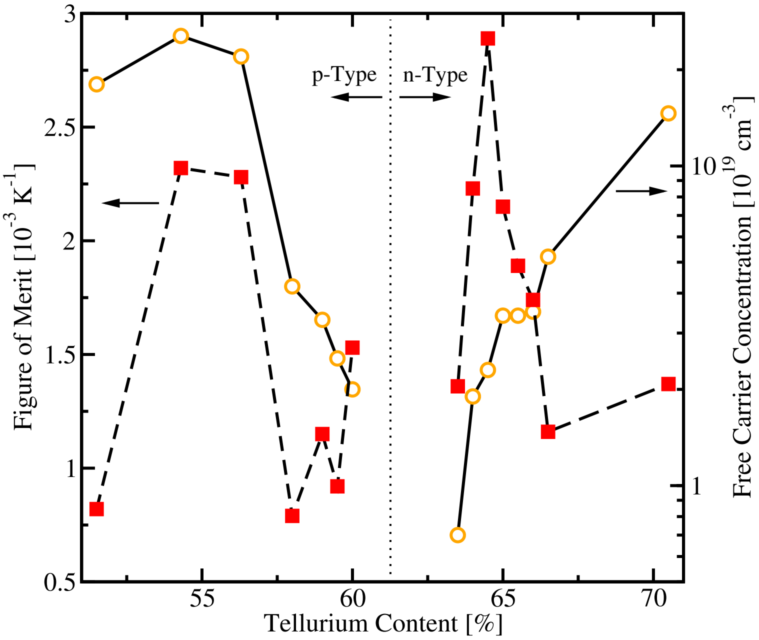

Figure 4.5: Free carrier concentration as well as figure of merit with respect to material composition for Bi_2Te_3, after [175].

scattering introduced by alloy disordering. The lowest values are achieved at the highest lattice disorder, for bismuth antimony telluride, this is achieved in $(Bi_{0.5}Sb_{0.5})_2Te_3$ [169]. However, the according maximum figure of merit is obtained at higher antimony content due to the contra-productive evolution of the electrical conductivity and the carrier contribution to the total thermal conductivity [170, 171]. In sintered samples, the lattice thermal conductivity is reduced by additional grain boundary scattering [172]. The influence of several dopants on the thermal conductivity is examined in [173]. Specific heat as well as the influence of dopants has been studied in [163, 174].

While pioneering work has focused on pure bismuth telluride [176], the electrical properties for many ternary alloys have been investigated extensively later on [177–181]. Additional doping of bismuth antimony telluride with lead telluride causes a more favorable ratio of electrical and thermal conductivity and thus results in an elevated figure of merit [182].

Since the figure of merit reaches its maximum in a narrow temperature range of about 50 K, the overall device performance of a thermoelectric generator is lower than the theoretical maximum. An approach to overcome this fact is the introduction of graded or segmented materials along the temperature gradient in order to match the optimum material properties to the given thermal conditions [183].

Several mechanical, optical, and transport parameters show a strong anisotropy. While anisotropy ratios of 4–6 and 2–2.5 are reported for the electrical resistivity and the thermal conductivity, respectively [169, 184, 185], the *Seebeck* coefficient is rather isotropic with a deviation of about 10 % between the according extrema. Both p-type and n-type samples have *Seebeck* coefficients between 100 μV/K and 250 μV/K which depend on the material composition [175, 186]. The maximum figure of merit can be observed parallel to the cleavage plains and outperforms the

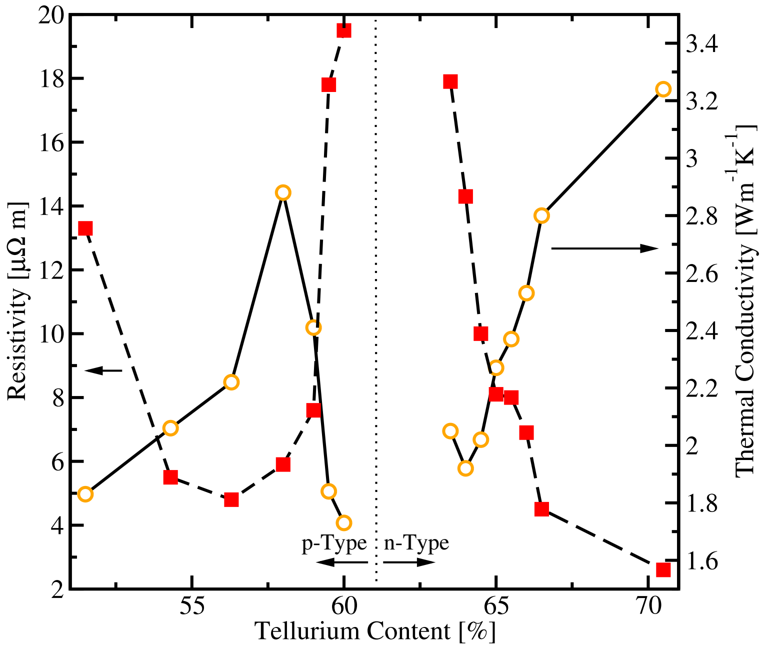

Figure 4.6: Resistivity as well as thermal conductivity with respect to material composition for Bi_2Te_3, after [175].

normal direction by a factor of 2. Figures 4.5 and 4.6 depict thermoelectrically relevant data of bismuth telluride alloys with respect to the material composition at room temperature. Transport properties have been measured parallel to the cleavage plains [175] since this direction is the most favorable for thermoelectric applications.

Thermal conductivity values shown in Fig. 4.6 change due to the influence of the material composition on phonon scattering as well as an additional carrier contribution at elevated free carrier concentrations. Electrical resistivity is mainly influenced by the free carrier concentration and the rate of ionized impurity scattering. The resulting figure of merit has a reported maximum for n-type materials at a tellurium content of 64.5 %. Due to the high sensitivity of the figure of merit to the material composition, an exact stoichiometric control during fabrication is necessary. For p-type material, the maximum figure of merit is lower than that of n-type material.

'The sciences do not try to explain, they hardly even try to interpret, they mainly make models. By a model is meant a mathematical construct which, with the addition of certain verbal interpretations, describes observed phenomena. The justification of such a mathematical construct is solely and precisely that it is expected to work.'

Johann von Neumann

Chapter 5

Physical Modeling of PbTe and PbSnTe

THE FOCUS OF THIS CHAPTER is put on the characterization of physical material properties of lead telluride as well as lead–tin telluride. Material parameters are collected from literature, where parameters needed for both device simulation as well as Monte Carlo simulations are considered. While the formulation of appropriate models for lead telluride is in the foreground, the consideration of lead–tin telluride opens interesting insights to properties of this material class. Models available in the literature are carefully compared and extended by own formulations based on collected measurement data. In the sequel, physical quantities and according models are introduced for the groups of lattice properties, thermal properties, band structure, carrier mobility, as well as generation and recombination.

5.1 Lattice Properties

Both lead telluride and tin telluride are polar semiconductors [187] and crystallize in the rock-salt (NaCl) structure [188]. The melting temperatures for PbTe and SnTe are 1197 K and 1078 K, respectively [189]. At high pressures, PbTe recrystallizes in an orthorhombic structure [190], as transists SnTe to at temperatures lower than 100 K [191].

5.1.1 Lattice Constant, Thermal Expansion, and Mass Density

Lattice constants for both PbTe and SnTe crystallized in the rock salt structure at 300 K are collected in Table 5.1. Their temperature dependence is expressed by the thermal expansion coefficient, which is rather large compared to other semiconductors. For lead telluride, values of $1.98 \times 10^{-5}\,\mathrm{K}^{-1}$ [192] and $2.04 \times 10^{-5}\,\mathrm{K}^{-1}$ [193] were reported, while the values are significantly smaller at very low temperatures [192]. A good approximation for the thermal expansion coefficient for PbTe and SnTe above 250 K is $2 \times 10^{-5}\,\mathrm{K}^{-1}$ [191]. Reported mass densities for PbTe and SnTe at room temperature are collected in Table 5.2.

PbTe		SnTe	
a [Å]	Ref.	a [Å]	Ref.
6.462	[194]	6.327	[188]
6.443	[190]	6.303	[190]

Table 5.1: Lattice constants for PbTe and SnTe in the rock-salt crystal structure at 300 K.

The mass density for alloys can be interpolated linearly between the ones of the constituents

$$\rho^{\mathrm{AB}} = (1-x)\rho^{\mathrm{A}} + x\rho^{\mathrm{B}} \tag{5.1}$$

with $1-x$ and x as the PbTe and SnTe content, respectively.

PbTe		SnTe	
ρ [kgm^{-3}]	Ref.	ρ [kgm^{-3}]	Ref.
8160	[188]	6410	[195]
8219	[196]	6383	[196]
8241	[193]	6454	[197]

Table 5.2: Mass densities for PbTe and SnTe at 300 K.

5.1.2 Dielectric Constant

The dielectric constant, also called permittivity ϵ describes the relation between electric displacement and field strength. For the general case it is a tensor dependent on the frequency and external influences like magnetic fields. In isotropic materials, this tensor reduces to a scalar. The permittivity is usually given as the product of the dimensionless relative permittivity ϵ_{r} and the vacuum permittivity ϵ_0.

Special interest is devoted to the static dielectric constant ϵ_{s} and the high frequency dielectric constant ϵ_∞. While the static dielectric constant enters *Poisson*'s equation as well as the models for several scattering mechanisms, both constants are employed in the description of polar optical scattering.

The static dielectric constant of lead telluride is unusually high and is dependent on temperature as illustrated in Fig. 5.1. Experimental data are mostly available for the low temperature range [198–200]. Values for room temperature and higher are given in [194, 200] but are not sufficient to give us a clear picture of the dependence of $\epsilon(T)$ in that range. The low temperature data from *Nishi* [198], *Tennant* [200], and *Dashevsky* [201] can be modeled by a simple power–law

$$\epsilon_{\mathrm{s}} = 412 \left(\frac{T_{\mathrm{L}}}{300\,\mathrm{K}}\right)^{-0.6} . \tag{5.2}$$

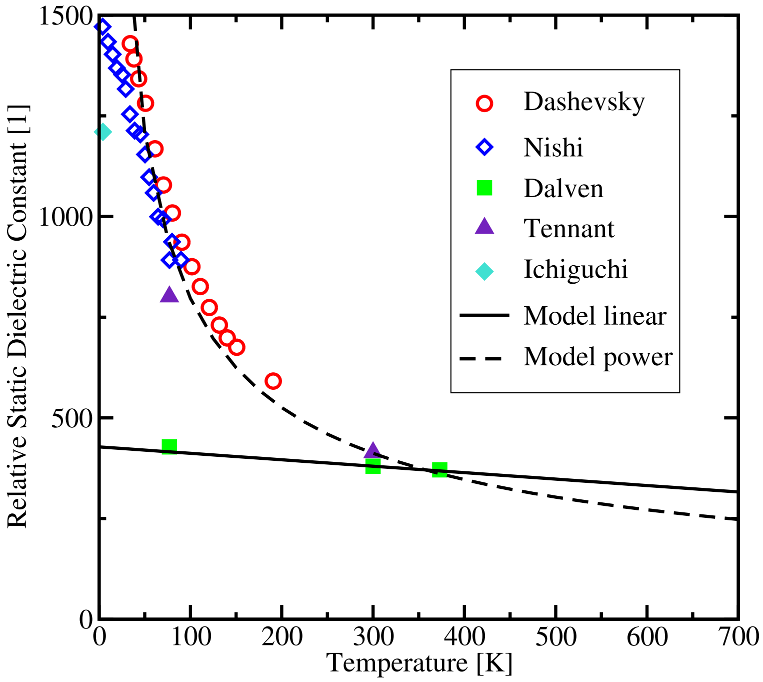

Figure 5.1: Relative static dielectric constant ϵ_s for PbTe with respect to the temperature.

However, data from *Dalven* [194] suggest a linear dependence, modeled by

$$\epsilon_\mathrm{s} = 428 - 48 \left(\frac{T_\mathrm{L}}{300\,\mathrm{K}} \right) . \tag{5.3}$$

An expression for $\epsilon_\mathrm{s}(x)$ in $\mathrm{Pb}_{1-x}\mathrm{Sn}_x\mathrm{Te}$ in the range $x < 0.35$ is given in [202]. Furthermore, experimental data for the low temperature range are provided by *Nishi* in [198].

The high–frequency dielectric constant is about 11 times lower than the static dielectric constant [194, 203].

$$\epsilon_\infty = 38 - 5 \left(\frac{T_\mathrm{L}}{300\,\mathrm{K}} \right) . \tag{5.4}$$

The linear models (5.3) and (5.4) are applied for the Monte–Carlo simulations presented in Section 5.4 for the high–temperature range.

5.1.3 Elastic Moduli and Sound Velocities

Beside the mechanical relevance of the elastic moduli, they are related to the sound velocities dependent on their direction relative to the crystallographic axes. Average values of the sound velocities enter several scattering models applied in Monte Carlo simulations [204]. In literature, data on both elastic moduli as well as sound velocities in specified directions are commonly given. In order to allow a comprehensive comparison, available data are collected in Tables 5.3 and 5.4, where the missing values are calculated using the according relations [205]

$$v_{\mathrm{sl},[100]} = \sqrt{\frac{c_{11}}{\rho}}\,, \tag{5.5}$$

$$v_{\mathrm{st},[100]} = \sqrt{\frac{c_{44}}{\rho}}\,, \tag{5.6}$$

$$v_{\mathrm{sl},[111]} = \sqrt{\frac{c_{11}+2c_{12}+4c_{44}}{3\rho}}\,. \tag{5.7}$$

A comprehensive disquisition on the coherence between sound velocities and second order elastic moduli in different directions is given in [205]. Throughout the calculations, a mass density of $\rho = 8241\,\mathrm{kg\,m^{-3}}$ [193] has been used.

Measurement data and corresponding quantities of lead telluride at room temperature are collected in Table 5.3, where measurement data [188, 193, 196] are summarized and extended by recently presented results of first-principle approaches [206].

c_{11} [GPa]	c_{12} [GPa]	c_{44} [GPa]	PbTe Data	Refs.	$v_{\mathrm{sl},[100]}$ [m/s]	$v_{\mathrm{st},[100]}$ [m/s]	$v_{\mathrm{sl},[111]}$ [m/s]
105.3	7.0	13.22	exp.	[196]	3575	1267	2639
108.0	7.7	13.43	exp.	[193]	3620	1277	2677
107.2	7.68	13.00	exp.	[193]	3607	1256	2657
104.0	4.37	13.00	exp.	[188]	3552	1256	2581
107.4	7.8	12.90	calc.	[207]	3610	1251	2657
115.7	4.2	14.3	calc. GGA	[206]	3747	1317	2708

Table 5.3: Summary of elastic constants and corresponding sound velocities for PbTe.

The temperature dependence of the elastic constants and sound velocities has been investigated by Houston [193] for the low temperature range between 4.2 K and 300 K.

Based on data presented in Tables 5.3 and 5.4, analytical expressions for the second–order elastic moduli of lead telluride have been derived using polynomial ansatzes of second and first order, respectively. The according expressions read

$$c_{11} = 126.9 - 14.5\left(\frac{T_\mathrm{L}}{300\,\mathrm{K}}\right) - 3.9\left(\frac{T_\mathrm{L}}{300\,\mathrm{K}}\right)^2, \tag{5.8}$$

$$c_{12} = 2.86 + 4.74\left(\frac{T_\mathrm{L}}{300\,\mathrm{K}}\right), \tag{5.9}$$

$$c_{44} = 15.0 - 1.55\left(\frac{T_\mathrm{L}}{300\,\mathrm{K}}\right). \tag{5.10}$$

T_L [K]	c_{11} [GPa]	c_{12} [GPa]	c_{44} [GPa]	$v_{\mathrm{sl},[100]}$ [m/s]	$v_{\mathrm{st},[100]}$ [m/s]	$v_{\mathrm{sl},[111]}$ [m/s]
0	126.05	4.28	14.91	3911	1345	2803
10	125.8	4.38	14.89	3907	1344	2802
20	125.41	4.41	14.86	3901	1343	2799
30	124.96	4.47	14.84	3894	1342	2796
50	124.06	4.48	14.75	3880	1338	2787
100	121.39	4.76	14.49	3838	1326	2764
150	118.5	5.23	14.23	3792	1314	2742
200	115.09	6.04	13.97	3737	1302	2721
250	111.78	6.73	13.71	3683	1290	2699
303.2	107.99	7.65	13.44	3620	1277	2676

Table 5.4: Temperature dependence of elastic constants and corresponding sound velocities.

Corresponding expressions for the temperature dependence of the average longitudinal and transversal sound velocities have been determined by applying *Ridley*'s formalism [208] as

$$v_\mathrm{sl} = 3297 - 170\left(\frac{T_\mathrm{L}}{300\,\mathrm{K}}\right) - 37.2\left(\frac{T_\mathrm{L}}{300\,\mathrm{K}}\right)^2, \tag{5.11}$$

$$v_\mathrm{st} = 2016 - 121\left(\frac{T_\mathrm{L}}{300\,\mathrm{K}}\right) - 44.8\left(\frac{T_\mathrm{L}}{300\,\mathrm{K}}\right)^2. \tag{5.12}$$

5.2 Thermal Properties

Besides the temperature dependence of several electrical material parameters, the non-isothermal behavior of semiconductor devices is mainly described by its thermal properties. While specific heat capacity and thermal conductivity enter the heat-flux equation within the non-isothermal drift-diffusion model, the thermoelectric powers directly enter the current relations for electrons and holes, respectively.

5.2.1 Specific Heat Capacity

The specific heat capacity c_L enters the heat flux equation as a time independent model parameter and is defined as the energy per mass needed to increase the temperature of a specimen by one Kelvin. It is modeled by [209]

$$c_\mathrm{L}(T_\mathrm{L}) = c_{\mathrm{L},300} + c_1 \frac{(T_\mathrm{L}/300\,\mathrm{K})^{\alpha_c} - 1}{(T_\mathrm{L}/300\,\mathrm{K})^{\alpha_c} + c_1/c_{\mathrm{L},300}}, \tag{5.13}$$

where $c_{\mathrm{L},300}$ is the specific heat capacity at $T_\mathrm{L} = 300\,\mathrm{K}$. Fig. 5.2 shows the temperature dependence of the specific heat capacities for PbTe and SnTe, respectively. Measurement data have

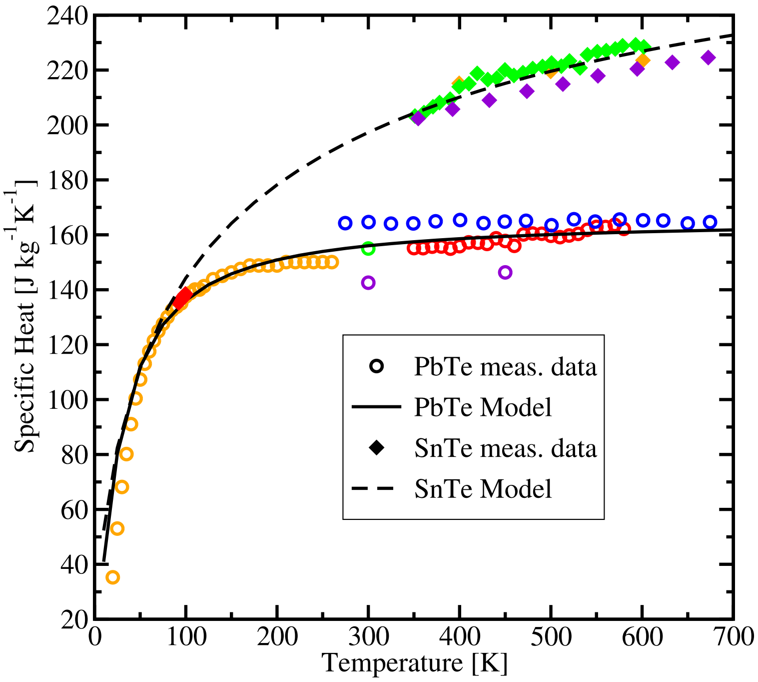

Figure 5.2: Temperature dependence of the specific heat capacity of lead telluride and tin telluride including measurement data and model parameter sets.

been obtained from [121, 174, 210–212] for lead telluride and from [213, 214] for tin telluride, where the latter is a review of several collected papers. For the ternary alloys $\mathrm{Pb}_{1-x}\mathrm{Sn}_x\mathrm{Te}$, the resulting specific heat capacity is expressed as a linear interpolation between the values for the according pure materials

$$c_{\mathrm{L}}^{\mathrm{AB}} = (1-x)c_{\mathrm{L}}^{\mathrm{A}} + xc_{\mathrm{L}}^{\mathrm{B}}\,, \tag{5.14}$$

where A stands for lead telluride, B for tin telluride and x denotes the according atomistic content.

	PbTe	SnTe
$c_{\mathrm{L},300}$	156 J/kgK	197.3 J/kgK
c_1	9.5 J/kgK	115 J/kgK
α_c	1.15	0.63

Table 5.5: Parameters for the specific heat capacity models for PbTe and SnTe.

5.2.2 Thermal Conductivity

The thermal conductivity κ parametrizes the flux term in the heat flux equation and depicts the energy flux per area and temperature difference transported within a homogeneous material. Measurement of the thermal conductivity is conventionally based on gathering the temperature difference caused by a steady heat flow, but also more sophisticated approaches like the 3ω-method can be applied in special cases [215]. The total thermal conductivity in semiconductors consists of the lattice and the electronic contribution, which is connected to the electrical conductivity by a *Wiedemann-Franz* law. While the lattice thermal conductivity, which is the dominant mechanism over a wide range of carrier concentrations in silicon, germanium, and several III-V semiconductors, is commonly modeled as a temperature dependent power law [133], the electron or hole contribution in n- and p-type materials gains weight in heavily doped samples. In the intrinsic range, both electrons and holes contribute to the thermal conductivity, which is referred to as the bipolar contribution. In lead telluride, these additional contributions to the thermal conductivity caused by the carrier gas play already a significant role at technically relevant carrier concentrations [121]. Based on the theoretical considerations presented in [125], the thermal conductivity dependence on the temperature and the electron concentration can be modeled as

$$\kappa = \kappa_{300} \left(\frac{T_\mathrm{L}}{300\,\mathrm{K}} \right)^{\alpha_\kappa} \left(1 + \left(\frac{n}{n_\mathrm{ref}} \right)^{\beta_\kappa} \right) . \tag{5.15}$$

The according parameters are collected in Table 5.6.

Parameter	Value
κ_{300}	$1.5486\,\mathrm{W/Km}$
α_κ	-1.3122
n_ref	$4.55 \times 10^{18}\,\mathrm{cm}^{-3}$
β_κ	0.651

Table 5.6: Parameter values for the lead telluride thermal conductivity model incorporating the carrier contribution.

In Fig. 5.3, the agreement between *Bhandari*'s data [125] and the model is illustrated. Several measurement data available in literature [216–219] show a general decrease of the thermal conductivity for increasing temperatures with an alleviated or even reverse trend at higher temperatures caused by the increased electronic contribution due to additionally available free carriers.

The heat flux between two points with temperatures T_1 and T_2 is calculated by the integral

$$\int_{T_1}^{T_2} \kappa(T,n)\mathrm{d}T = \frac{\kappa_{300}}{\alpha_\kappa + 1} \left(\left(\frac{T_2}{300\,\mathrm{K}} \right)^{\alpha_\kappa + 1} - \left(\frac{T_1}{300\,\mathrm{K}} \right)^{\alpha_\kappa + 1} \right) \left(1 + \left(\frac{n}{n_\mathrm{ref}} \right)^{\beta_\kappa} \right) \tag{5.16}$$

assuming the carrier concentration to be constant throughout the discretization box.

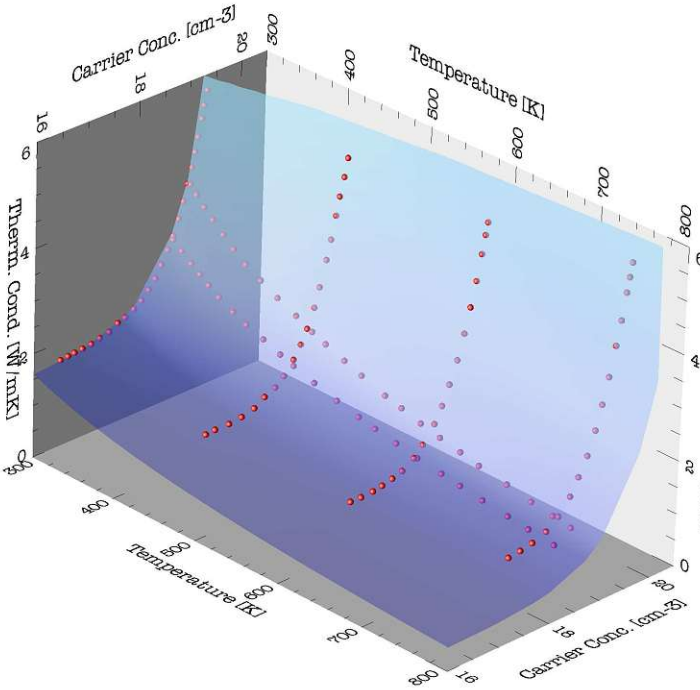

Figure 5.3: Dependence of the thermal conductivity of lead telluride on the lattice temperature and carrier concentration. While red glyphs depict *Bhandari*'s data [125], the surface denotes the modeled thermal conductivity.

In $\mathrm{Pb}_{1-x}\mathrm{Sn}_x\mathrm{Te}$, alloy scattering enters as an additional mechanism and thus the thermal conductivity is drastically reduced compared to pure PbTe and SnTe. Fig. 5.4 depicts the variation of the thermal conductivity with respect to the material composition at 300 K. Measurement data have been collected from [220–222], where the latter two comprise investigations of sintered samples which explains the lower thermal conductivity values. The lattice component has been theoretically investigated by molecular–dynamics studies in [223] and by subtracting the electronic contribution

$$\kappa_\nu = L\sigma T \tag{5.17}$$

derived from the electron conductivity σ, the *Lorentz* number L and the temperature [220]. The model for the material composition dependent thermal conductivity in alloys reads [133]

$$\kappa_{300} = \left(\frac{1-x}{\kappa_{300}^{\mathrm{A}}} + \frac{x}{\kappa_{300}^{\mathrm{B}}} + \frac{(1-x)x}{C_\kappa}\right)^{-1}, \tag{5.18}$$

$$\alpha_\kappa^{\mathrm{AB}} = (1-x)\alpha_\kappa^{\mathrm{A}} + x\alpha_\kappa^{\mathrm{B}}, \tag{5.19}$$

where x and $1-x$ denote the SnTe and PbTe content, respectively. $\kappa_{300}^{\mathrm{A}}$ is the thermal conductivity for PbTe at room temperature, $\kappa_{300}^{\mathrm{B}}$ analogously for SnTe, and C_κ the bowing factor accounting for the alloy scattering reduction of the thermal conductivity. The exponents describing the temperature dependence are interpolated linearly between the values for the pure material constituents. The additional electronic contribution can be estimated by

$$\kappa_{\mathrm{tot},300} = \kappa_{\mathrm{L},300} + A_0 + A_1 x^2 \tag{5.20}$$

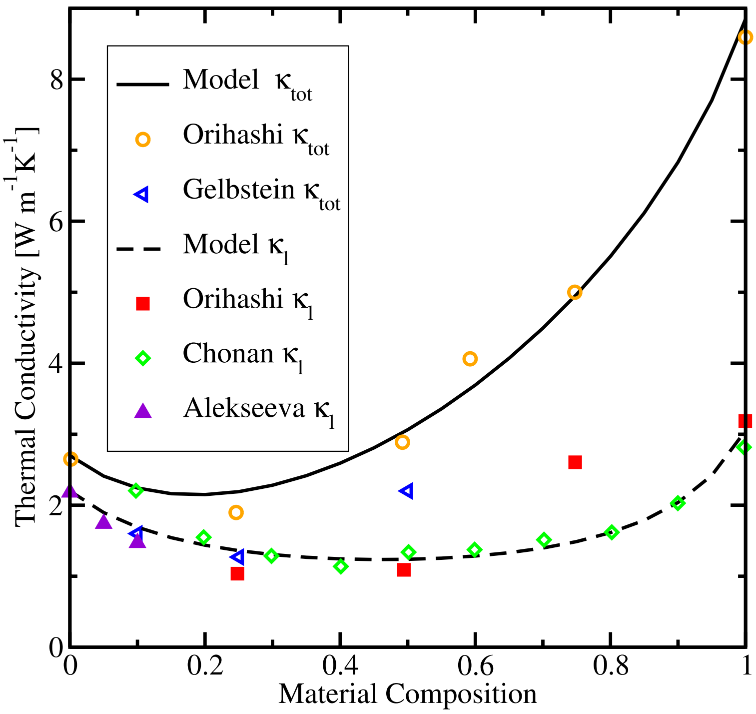

Figure 5.4: Material composition dependent lattice and total thermal conductivity of $Pb_{1-x}Sn_xTe$ at 300K including measurement data and model parameter sets.

for $Pb_{1-x}Sn_xTe$ based on the data published in [220]. According values for the temperature exponents α^{A} and α^{B} have been identified for the lattice thermal conductivity based on data published in [222] and [224]. The parameters for the material composition dependent thermal conductivity model are collected in Table 5.7.

Parameter	Value
κ_{300}^{A}	2.2 W/Km
κ_{300}^{B}	3.05 W/Km
C_{κ}	0.6
α_{κ}^{A}	−1.06
α_{κ}^{B}	−0.27
A_0	0.5 W/Km
A_1	5.3 W/Km

Table 5.7: Parameter values for the material composition dependent PbSnTe thermal conductivity models.

A decrease of the thermal conductivity compared to single crystals due to grain boundary scattering in sintered materials has been reported in [124,126,225] to be as high as 4 − 6% in pure

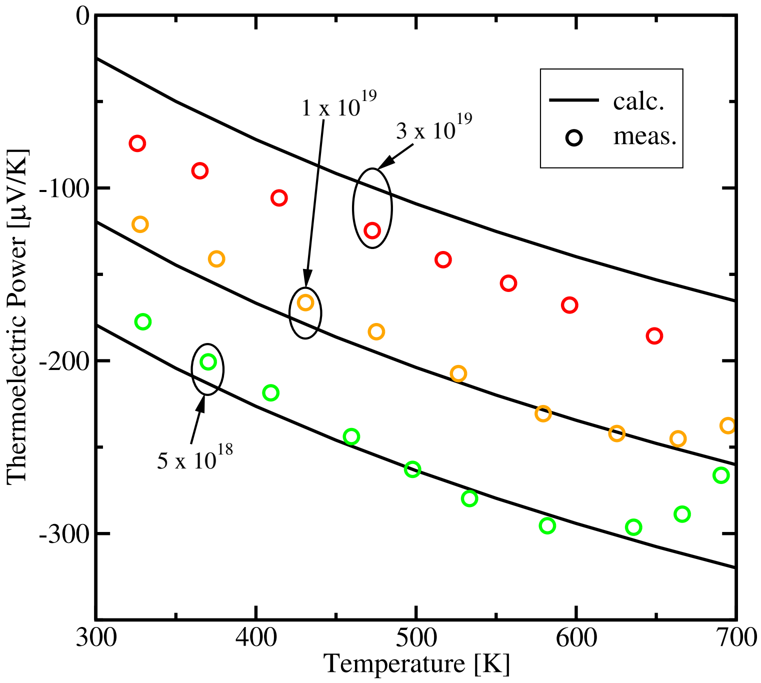

Figure 5.5: Temperature dependence of the thermoelectric power in n–PbTe for different dopings. The lines depict calculated values while the symbols show according measurement data from [228].

lead telluride and $11-13\%$ in disordered lead telluride alloys. However, a drastic decrease of the thermal conductivity is reported in [128] for grain sizes in the range of $0.7-4\,\mu$m. Furthermore, the influence of the grain size within sintered $\mathrm{Pb}_{1-x}\mathrm{Sn}_x\mathrm{Te}$ is investigated in [127] for hot and cold pressed materials. Recent work has dealt with the dependence of the thermal conductivity on the pressure during fabrication using high temperature and high pressure processes [226,227].

5.2.3 Thermoelectric Powers

The thermoelectric powers, or *Seebeck* coefficients for electrons and holes depict the ratio between a temperature gradient and the resulting driving forces on the carriers as presented in Section 3.5.12. They show dependencies on both temperature and carrier concentration. A comparison between measurement data for n–type lead telluride [228] and the theoretical models of the *Seebeck* coefficient is illustrated in Fig. 5.5. Values for the effective densities of states N_c and N_v incorporated in the theoretical models are given in Section 5.3.2.

In contrast to silicon, additional gain on the thermoelectric power by phonon-drag is limited to very low temperatures. Thus, good agreement between theoretical and measured data is achieved. At high temperatures, the measured values drop to lower values due to the additionally available free holes in the intrinsic range, as indicated in Figures 5.5 and 5.6.

Measurement data illustrated by circles in Fig. 5.6 have been taken from [229]. Different concentrations of free carriers have been obtained by deviation from the stoichiometric equilibrium between Pb and Te. The good agreement between theoretical curves and measurement data

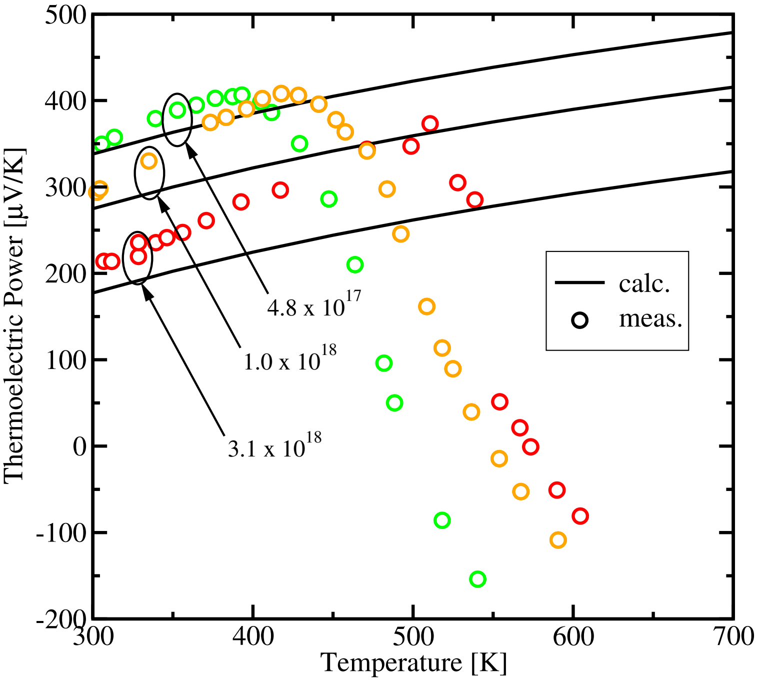

Figure 5.6: Temperature dependence of the thermoelectric power in p-PbTe for different dopings. The lines depict calculated values while the symbols show according measurement data from [229].

in the low temperature range indicates that additional phonon-drag is absent in the indicated temperature range. For temperatures above 400 K, carriers start to populate the second valence band, thus the averaged effective mass of both valleys must be taken into account [230]. With further increasing temperatures, the intrinsic range is reached, where the total thermoelectric power even changes its sign due to the additional contribution of electrons. A comparable behavior is reported for silicon in [97].

Considerably larger values for thermoelectric powers have been measured for sintered samples, where a strong dependence on the grain size has been reported [128, 228]. Values for thermoelectric powers double if the grain size is reduced from 4 μm down to 0.7 μm. Further investigations of several alloys can be found in [218, 231].

5.3 Band Structure

Lead telluride crystallizes in the NaCl structure with face-centered cubic unit cells [232]. The resulting *Brillouin* zone with its first octant as well as its irreducible wedge and high symmetry points are illustrated in Fig. 5.7. The band structure of lead telluride and its alloys has been investigated extensively both theoretically and by experiments. The principle position and alignment of the valleys as well as the band gap have been obtained by several measurement techniques, like investigations on the optical absorption, recombination spectra, reflectivity, as well as magneto- and piezoresistivity [233–237]. Parameters for models based on the $\mathrm{k}\cdot\mathrm{p}$-theory have been obtained for lead chalcogenides in [238–240]. Theoretical band structure calculations

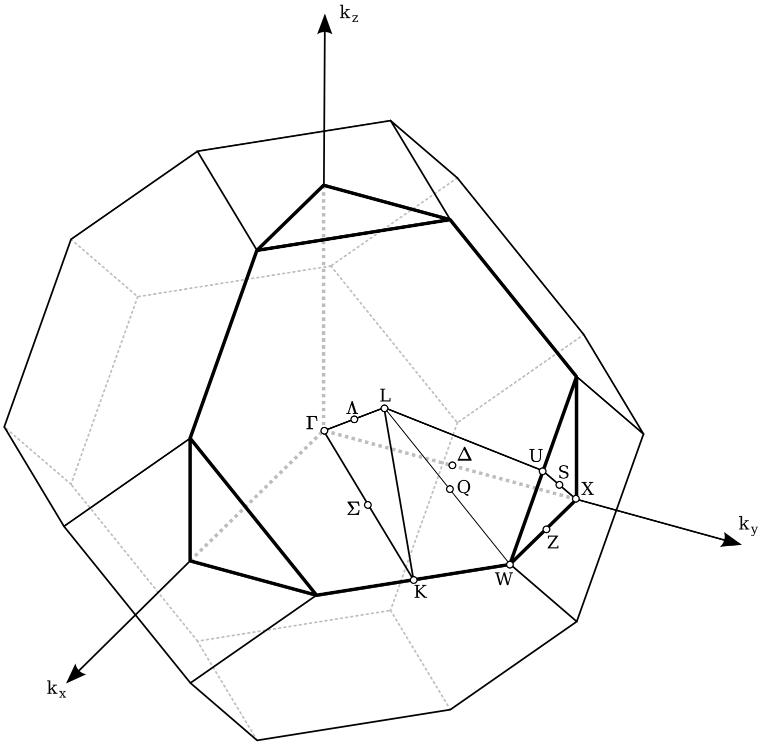

Figure 5.7: *Brillouin* zone, its first octant, and irreducible wedge with high symmetry points and lines for a face centered cubic lattice.

have been performed applying the augmented plane–wave method [241]. The results of relativistic orthogonalized plane–wave calculations are published in [242], while Johnson generally pointed out the importance of relativistic effects within band structure calculations on lead telluride [243]. Extensive calculations based on the empirical pseudopotential method, extended by non-local effects and spin-orbit coupling have been performed in [244–248] and the temperature dependent band-structure has been investigated in [249–251].

Lead telluride is a direct semiconductor where the conduction band minima and valence band maxima are located at the L point of the *Brillouin* zone. The valleys are both heavily anisotropic and non-parabolic. The major alignment is in [111] direction with the band minima located exactly at the L point, thus the valleys have a multiplicity of 4. Furthermore, a second valence band with band minima at Σ exists with an alignment of the valleys in [100] direction [252, 253]. In PbSnTe, a band inversion occurs, meaning that the highest valence band and the lowest conduction band change their roles throughout a variation of the alloy composition between PbTe and SnTe [254]. This band inversion model has been supported by several measurements [255, 256]. However, there is still some uncertainty about the band parameters within the band inversion zone [257].

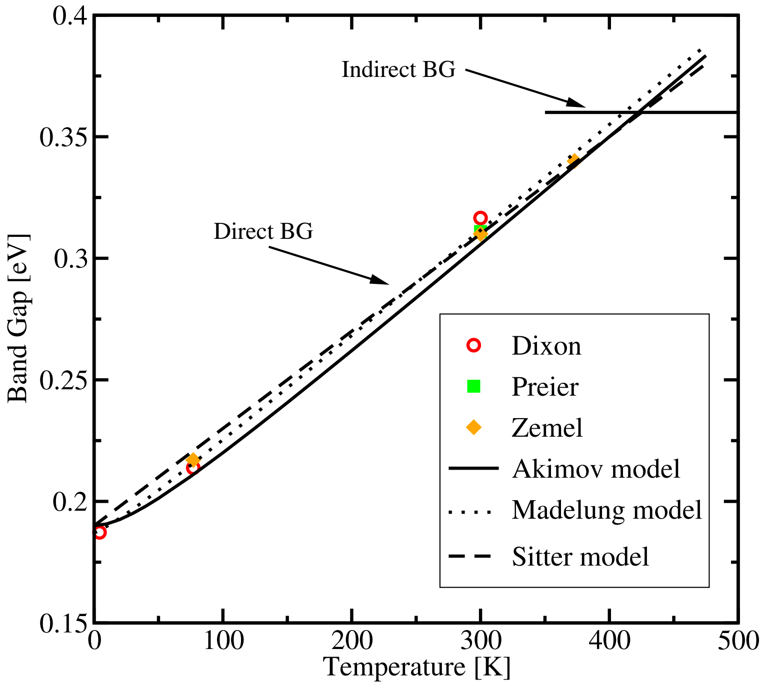

Figure 5.8: Temperature dependence of and transition between direct and indirect band gaps in lead telluride.

5.3.1 Band Gap

At room temperature, the band-gap is defined by the direct distance between the valleys at the L-point of the *Brillouin* zone. In contrast to many other semiconductors, the temperature dependence of this band gap is positive, meaning that with increasing temperatures the direct band gap at the L-point also increases. Beside the valence band maximum at the L point, there exists another one close to Σ resulting in an additional indirect band gap separated by 0.14 eV at 0 K [258]. Reported measurement values differ only slightly, where the 0 K band gap is given as 0.19 eV [194]. The gradient describing the temperature dependence in a linear fit is reported to be $4 \times 10^{-4}\,\mathrm{K}^{-1}$ [234, 253], $4.1 \times 10^{-4}\,\mathrm{K}^{-1}$ [259], and $4.2 \times 10^{-4}\,\mathrm{K}^{-1}$ [194]. There is a transition between the direct and the indirect band gap at about 420 K depending on the chosen temperature dependence of the direct band gap. The indirect band gap has a value of 0.36 eV which is reported to be temperature independent [191, 253].

Several models found in literature have been compared to collected measurement data [199, 255, 260, 261], as illustrated in Fig. 5.8. While the ansatz proposed by *Grisar* [260] delivers

$$\mathcal{E}_\mathrm{g}(T)/\mathrm{meV} = 171.5 + \left(12.8^2 + 0.19(T+20)^2\right)^{1/2}\,, \tag{5.21}$$

Sitter [253] proposed a simple linear fit

$$\mathcal{E}_\mathrm{g}(T)/\mathrm{eV} = 0.19 + 4 \times 10^{-4}\,T\,. \tag{5.22}$$

The parameters for *Varshni*'s model [262], which is widely used in semiconductor device simulation, have been identified in [202]. Thus, the expression for the band gap for the *Varshni* model

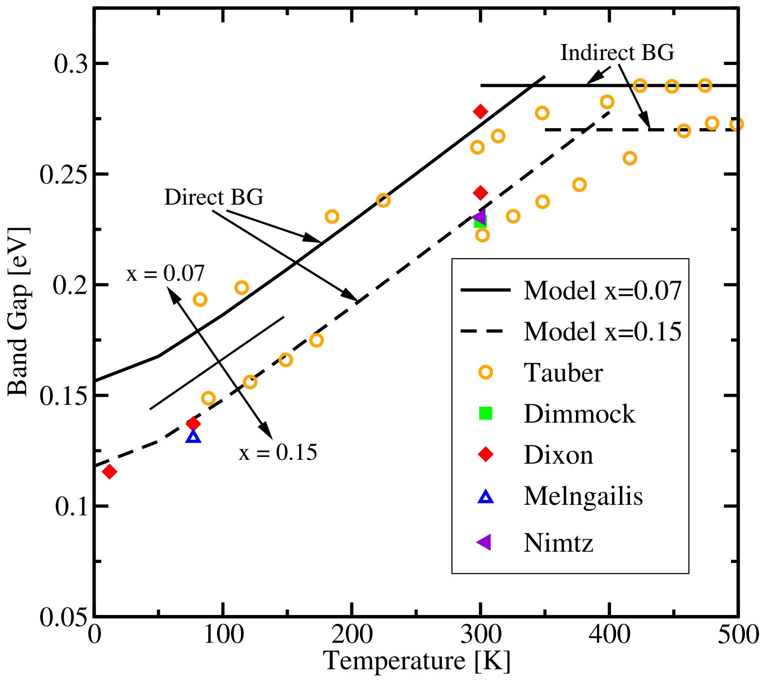

Figure 5.9: Temperature dependence of and transition between direct and indirect band gaps in lead tin telluride at tin contents of 0.07 and 0.15.

reads

$$\mathcal{E}_\mathrm{g}(T)/\mathrm{eV} = 0.19 + \frac{4.5 \times 10^{-4} T^2}{T + 50}\,. \tag{5.23}$$

In PbSnTe, the crossover between the highest valence band and the lowest conduction band throughout a variation of the alloy composition between PbTe and SnTe strongly affects the band gap. This results in decreasing band gap values with increasing SnTe content for PbTe-rich samples, followed by a zero band-gap zone, and finally approaching the SnTe value for lower temperatures. The SnTe content for which the zero band-gap situation occurs shifts to higher contents with increasing temperature [256]. The temperature dependence of the band gap in tin telluride was subject of intense discussion. While generally a slight negative temperature coefficient is suggested, the temperature coefficient's sign is reported to change for higher carrier concentrations [188]. However, for technologically relevant PbTe-rich samples, this is not the case. The band gap models valid for this range are formulated by an extension of the according PbTe models by a material composition dependent expression. Thus, *Varshni*'s extended model reads

$$\mathcal{E}_\mathrm{g}(T)/\mathrm{eV} = 0.19 - 0.48x + \frac{4.5 \times 10^{-4} T^2}{T + 50}\,. \tag{5.24}$$

An extension to *Grisar*'s model is obtained analogously as

$$\mathcal{E}_\mathrm{g}(T)/\mathrm{meV} = 171.5 - 535x + \left(12.8^2 + 0.19(T + 20)^2\right)^{1/2}\,. \tag{5.25}$$

Fig. 5.9 illustrates the situation for different material compositions. The direct band gap is shifted to lower values with increasing SnTe content until the band inversion occurs. Additionally, the indirect band gap decreases due to a shift of the second valence band. The values identified for $x = 0.07$ and $x = 0.15$ are $0.29\,\mathrm{eV}$ and $0.27\,\mathrm{eV}$, respectively. Measurement data published in [188, 199, 254, 255, 263–265] have been used to identify the parameters.

5.3.2 Effective Masses, Density of States, Intrinsic Carrier Density

While the effective masses for each the first conduction and valence band of lead telluride have been studied quite well in literature, only very uncertain information is available for the second valence band. Both the valence and the conduction band feature a strong anisotropy with material composition dependent values of $10 - 14$ [188, 260]. Values based on both measurements as well as band structure calculations of the low temperature effective mass for the first conduction and valence band, respectively are collected in Table 5.8.

Electrons		Holes		
m_l	m_t	m_l	m_t	Ref.
0.24	0.024	0.31	0.022	meas. [194]
0.238	0.031	0.426	0.034	calc. [241]
0.274	0.043			meas. [266]
		0.165	0.030	meas. [267]
0.24	0.022			meas. [199]
0.23	0.022			calc. [199]

Table 5.8: Low temperature effective masses for the first conduction and valence band in lead telluride.

The temperature dependence of the effective masses is commonly expressed by quadratic polynomials [268]. According coefficients have been identified based on temperature dependent data in [188]. Expressions for the longitudinal and transversal effective masses for each the first conduction and valence bands in pure lead telluride read

$$m^*_{\mathrm{c,l}} = 0.25 + 0.11\left(\frac{T_\mathrm{L}}{300\,\mathrm{K}}\right) - 0.011\left(\frac{T_\mathrm{L}}{300\,\mathrm{K}}\right)^2 , \tag{5.26}$$

$$m^*_{\mathrm{c,t}} = 0.024 + 0.0112\left(\frac{T_\mathrm{L}}{300\,\mathrm{K}}\right) - 0.0013\left(\frac{T_\mathrm{L}}{300\,\mathrm{K}}\right)^2 , \tag{5.27}$$

$$m^*_{\mathrm{v,l}} = 0.286 + 0.142\left(\frac{T_\mathrm{L}}{300\,\mathrm{K}}\right) - 0.007\left(\frac{T_\mathrm{L}}{300\,\mathrm{K}}\right)^2 , \tag{5.28}$$

$$m^*_{\mathrm{v,t}} = 0.025 + 0.012\left(\frac{T_\mathrm{L}}{300\,\mathrm{K}}\right) - 0.0012\left(\frac{T_\mathrm{L}}{300\,\mathrm{K}}\right)^2 . \tag{5.29}$$

The according temperature dependencies of the density-of-states masses derived by

$$m^* = \left(m^{*2}_\mathrm{t}\, m^*_\mathrm{l}\right)^{1/3} , \tag{5.30}$$

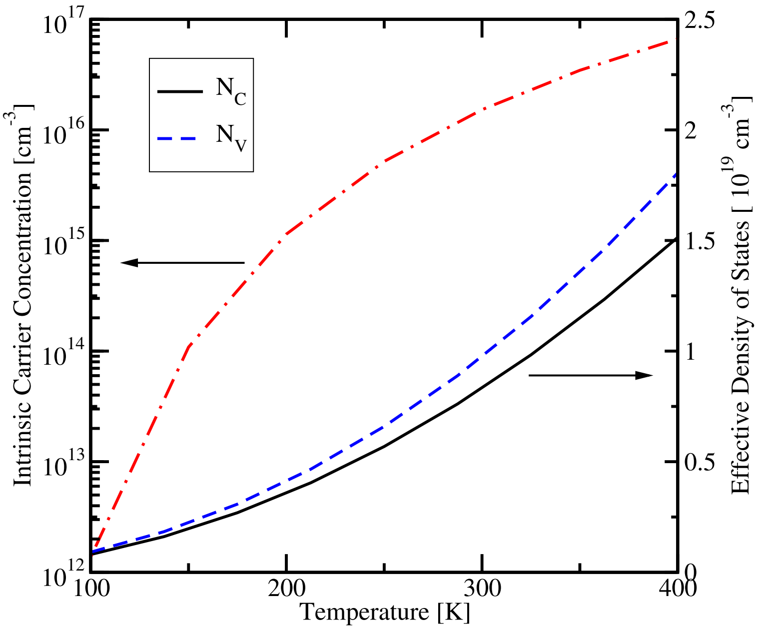

Figure 5.10: Temperature dependence of the effective density of states as well as the intrinsic carrier concentration in lead telluride.

have been identified as

$$m_{\mathrm{c}}^{*} = 0.052 + 0.024 \left(\frac{T_{\mathrm{L}}}{300\,\mathrm{K}}\right) - 0.0027 \left(\frac{T_{\mathrm{L}}}{300\,\mathrm{K}}\right)^{2} , \tag{5.31}$$

$$m_{\mathrm{v}}^{*} = 0.056 + 0.027 \left(\frac{T_{\mathrm{L}}}{300\,\mathrm{K}}\right) - 0.0023 \left(\frac{T_{\mathrm{L}}}{300\,\mathrm{K}}\right)^{2} . \tag{5.32}$$

Since the extrema of both the first conduction and valence band are located at the L point, the number of equivalent valleys within the *Brillouin* zone $M_{\mathrm{c,v}}$ is 4. Thus, the effective density of states including spin-degeneracy can be expressed by [269]

$$N_{\mathrm{c,v}} = 2M_{\mathrm{c,v}} \left(\frac{2\pi m_{\mathrm{c,v}}^{*} k_{\mathrm{B}} T_{\mathrm{L}}}{\mathrm{h}^{2}}\right)^{3/2} , \tag{5.33}$$

and the intrinsic carrier concentration is derived as

$$n_{\mathrm{i}} = \sqrt{N_{\mathrm{c}} N_{\mathrm{v}}} \exp\left(-\frac{\mathcal{E}_{\mathrm{g}}}{2 k_{\mathrm{B}} T_{\mathrm{L}}}\right) . \tag{5.34}$$

Expressions for the material composition and temperature dependent effective masses have been given by *Preier* [260] and *Akimov* [202]. While both give expressions with respect to the temperature and material composition dependent band gap, the latter does not differ between the valence and conduction band and provides a constant anisotropy ratio between the transversal and longitudinal effective masses. His expressions for the relative carrier masses read

$$m_{\mathrm{t}}^{*}(x,T) = 0.16\,\mathcal{E}_{\mathrm{g}}(x,T) \tag{5.35}$$

$$m_{\mathrm{l}}^{*}(x,T) = 10.5\, m_{\mathrm{t}}^{*}(x,T) . \tag{5.36}$$

Preier differs between the according values of the valence and conduction band and implies a material composition dependent anisotropy ratio

$$m^*_{\mathrm{c,t}} = \left(30.58\frac{\mathcal{E}_{\mathrm{g}}(0,0)}{\mathcal{E}_{\mathrm{g}}(x,T)} + 14.29\right)^{-1}, \tag{5.37}$$

$$m^*_{\mathrm{v,t}} = \left(30.58\frac{\mathcal{E}_{\mathrm{g}}(0,0)}{\mathcal{E}_{\mathrm{g}}(x,T)} + 10.00\right)^{-1}, \tag{5.38}$$

$$m^*_{\mathrm{c,l}} = \left(\frac{30.58}{10.25+6.56x}\frac{\mathcal{E}_{\mathrm{g}}(0,0)}{\mathcal{E}_{\mathrm{g}}(x,T)} + 2.42\right)^{-1}, \tag{5.39}$$

$$m^*_{\mathrm{v,l}} = \left(\frac{30.58}{10.25+6.56x}\frac{\mathcal{E}_{\mathrm{g}}(0,0)}{\mathcal{E}_{\mathrm{g}}(x,T)} + 1.52\right)^{-1}. \tag{5.40}$$

5.4 Carrier Mobility

Lead telluride attracts attention due to its extraordinarily high carrier mobilities at low temperatures. Values of $800,000\,\mathrm{cm^2/Vs}$ and $256,000\,\mathrm{cm^2/Vs}$ have been reported for electrons and holes, respectively at 4.2 K, which reduce to $1,900\,\mathrm{cm^2/Vs}$ and $900\,\mathrm{cm^2/Vs}$ at room temperature [270]. The mobilities for electrons and holes, μ_n and μ_p are limited by carrier scattering within the semiconductor. The electron mobility model is based on experimental and Monte–Carlo simulation data [271], while the hole mobility model relies on collected measurement data.

The Monte–Carlo technique serves as a powerful link between measurement data and models for device simulation in hierarchical device simulation [79]. Macroscopic average quantities such as carrier mobility and energy relaxation times are derived from the microscopic behavior of single electrons with statistical methods. Bulk Monte-Carlo simulations have been carried out using the Vienna Monte Carlo simulator (VMC) [204] applying a single particle Monte Carlo technique. For the analysis, the two lowest conduction band valleys at L and W points, respectively are incorporated. Several relevant stochastic mechanisms are considered, which are phonon scattering in the acoustic and optical branch, polar optical phonon scattering, optical deformation potential scattering, L-L intravalley scattering, and scattering by ionized impurities. The band structure is described by a non-parabolic approximation of the valleys using *Kane*'s formula [77]

$$\gamma(\mathcal{E}(k)) = \mathcal{E}(1+\alpha\mathcal{E}) = \frac{\hbar^2k^2}{2m^*}. \tag{5.41}$$

Compared to widely used materials such as silicon or germanium, the material parameters of lead telluride show higher uncertainties, especially at higher temperatures. The influences of the according single material parameters on the mobility are assessed and some parameters are adjusted in an iterative process to account for available measurement data for certain doping and temperature values. This calibrated set of models finally serves as a basis for the extraction of bulk mobility data in order to further calibrate the according mobility models in the device simulator MINIMOS-NT [268].

Only a few Monte-Carlo simulations are currently documented in literature for lead telluride. The negative differential mobility at "high-field" conditions in lead telluride has been investigated in [272] at 77 K. This work has been extended to selected lead-tin telluride alloys

quantity	symbol	value	unit
valley separation energy	$\Delta\mathcal{E}_{\mathrm{WL}}$	$0.15 + 0.04\left(\frac{T_\mathrm{L}}{300\,\mathrm{K}}\right)$	eV
effective masses	$m^*_{\mathrm{L,l}}$	$0.25 + 0.11\left(\frac{T_\mathrm{L}}{300\,\mathrm{K}}\right) - 0.011\left(\frac{T_\mathrm{L}}{300\,\mathrm{K}}\right)^2$	
	$m^*_{\mathrm{L,t}}$	$0.024 + 0.0112\left(\frac{T_\mathrm{L}}{300\,\mathrm{K}}\right) - 0.0013\left(\frac{T_\mathrm{L}}{300\,\mathrm{K}}\right)^2$	
	$m^*_{\mathrm{W,l}}$	0.5	
	$m^*_{\mathrm{W,t}}$	0.5	
sound velocities	v_{sl}	$3297 - 170\left(\frac{T_\mathrm{L}}{300\,\mathrm{K}}\right) - 37.2\left(\frac{T_\mathrm{L}}{300\,\mathrm{K}}\right)^2$	m/s
	v_{st}	$2016 - 121\left(\frac{T_\mathrm{L}}{300\,\mathrm{K}}\right) - 44.8\left(\frac{T_\mathrm{L}}{300\,\mathrm{K}}\right)^2$	m/s
lattice constant	a	6.462	Å
mass density	ρ	8241	$\mathrm{kg/m^3}$
non–parabolicity constants	α_L	3	1/eV
	α_W	3	1/eV
relative permittivities	ϵ_s	$428 - 48\left(\frac{T_\mathrm{L}}{300\,\mathrm{K}}\right)$	
	ϵ_∞	$38 - 5\left(\frac{T_\mathrm{L}}{300\,\mathrm{K}}\right)$	
acoustical deformation potential	$\mathcal{E}_{\mathrm{ADP}}$	10	eV
optical phonon energy	$\hbar\omega_{\mathrm{LO}}$	13.6	meV
intervalley phonon energy	$\hbar\omega_{\mathrm{ij}}$	10.5	meV
intervalley coupling constant	D_{ij}	1.6×10^8	eV/cm
ODP coupling constant	D_o	1.2×10^9	eV/cm

Table 5.9: Parameters for several scattering models incorporated in Monte-Carlo simulations.

in [273]. A comprehensive investigation including both measurements and Monte-Carlo simulation results for the hot-electron behavior in lead telluride as well as lead-tin telluride alloys is presented in [274]. However, all these studies are limited to a temperature of 77 K and focus on the influence of the W-valley. In recent work, *Palankovski* et al. [275] provided results for the electron mobility as a function of temperature up to 500 K, carrier concentration, and electric field.

In contrast to semiconductors with wider band gaps such as silicon, the temperature dependence of several parameters becomes more pronounced. Thus, these parameters are modeled accordingly by introducing temperature dependent expressions. Model parameters applied in the simulations are collected in Table 5.9. Due to the low driving forces far below saturation effects within thermoelectric applications, mobility model parameters are obtained for the low–field case. Low–field mobilities for electrons and holes are modeled by a two-stage model [268]. The temperature dependent mobilities for intrinsic and low doped samples, where lattice scattering is the dominant scattering mechanism, are expressed by a power law

$$\mu^\mathrm{L}_\nu = \mu^\mathrm{L}_{\nu,300}\left(\frac{T_\mathrm{L}}{300\,\mathrm{K}}\right)^{\gamma_{0,\nu}} . \qquad (5.42)$$

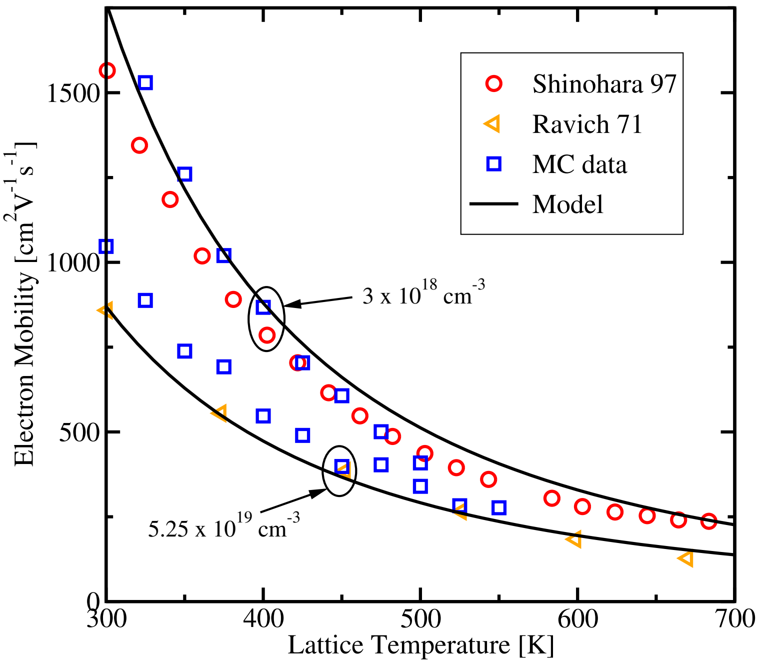

Figure 5.11: Temperature dependence of the electron mobility in lead telluride for different dopings.

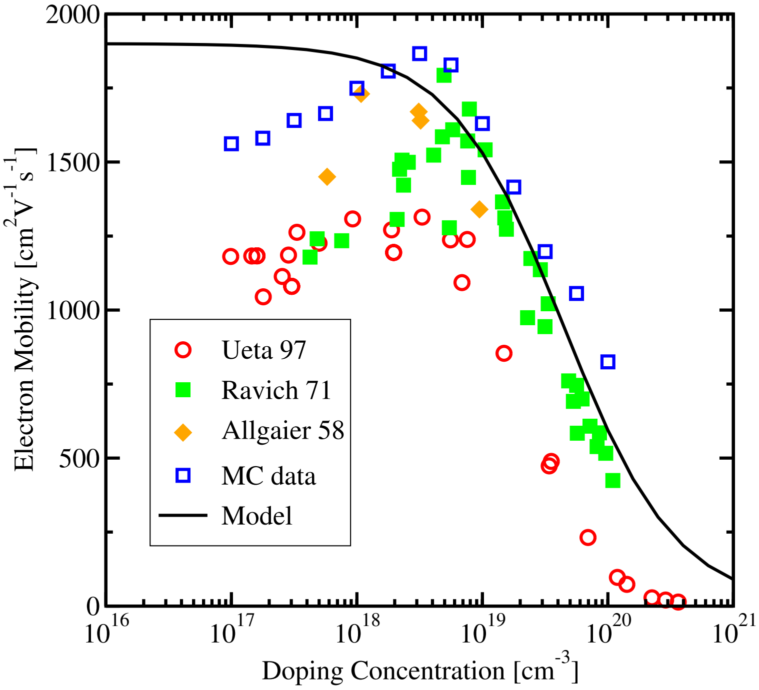

Figure 5.12: Doping dependent electron mobility degradation in lead telluride at room temperature.

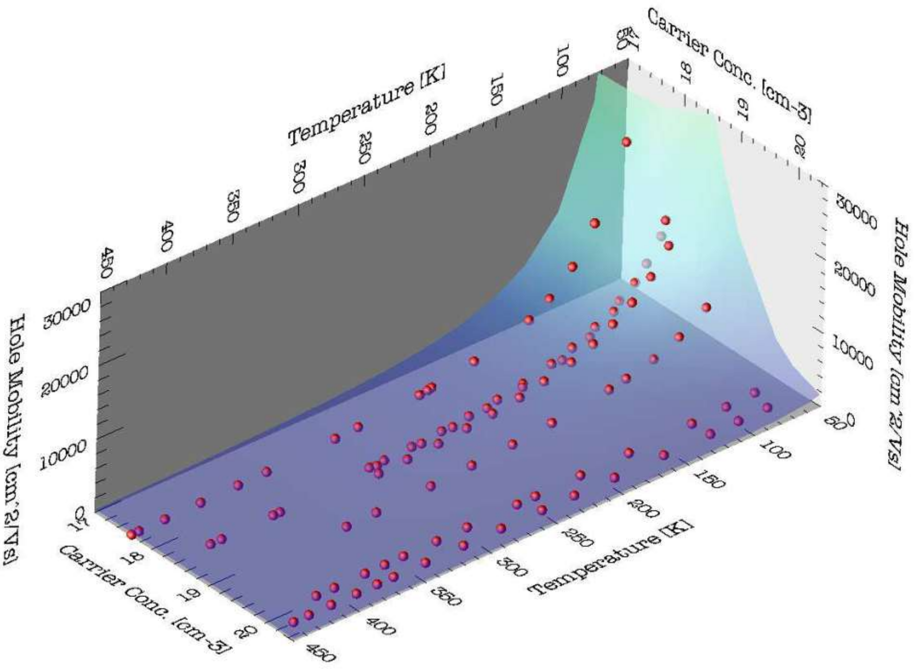

Figure 5.13: Temperature and doping dependent hole mobility in lead telluride.

Doping dependent mobility degradation due to ionized impurity scattering is introduced using a simplified *Caughey-Thomas* equation [276]

$$\mu_\nu^{\mathrm{LI}} = \frac{\mu_\nu^{\mathrm{L}}}{1 + \left(\frac{N_{\mathrm{tot}}}{N_\nu^{\mathrm{ref}}}\right)^{\alpha_\nu}} \, , \tag{5.43}$$

where μ_ν^{L} depicts the temperature dependent mobilities for undoped samples (5.42) and N_{tot} stands for the total impurity concentration. The mobility degradation with increasing impurity concentration is determined by N_ν^{ref} and α_ν. While N_ν^{ref} depicts the impurity concentration, where the according mobility becomes $\mu_\nu^{\mathrm{L}}/2$

$$N_\nu^{\mathrm{ref}} = N_{\nu,300}^{\mathrm{ref}} \left(\frac{T_{\mathrm{L}}}{300\,\mathrm{K}}\right)^{\gamma_{1,\nu}} \, , \tag{5.44}$$

the exponent α_ν models the gradient of the mobility degradation with increasing impurity concentration

$$\alpha_\nu = \alpha_{\nu,300} \left(\frac{T_{\mathrm{L}}}{300\,\mathrm{K}}\right)^{\gamma_{2,\nu}} \, . \tag{5.45}$$

The parameters for lead telluride are collected in Table 5.10 for electrons and holes, respectively. The validity of the model for electrons is illustrated in Figures 5.11 and 5.12. Fig. 5.11 depicts the temperature dependent electron mobility for doping concentrations of $3 \times 10^{18}\,\mathrm{cm}^{-3}$ and $5.25 \times 10^{19}\,\mathrm{cm}^{-3}$, respectively. The temperature dependence follows a power law, where the

	Electrons	Holes
$\mu^{\mathrm{L}}_{\nu,300}$	$1900\,\mathrm{cm}^2/\mathrm{Vs}$	$900\,\mathrm{cm}^2/\mathrm{Vs}$
$\gamma_{0,\nu}$	-2.4	-2.45
$N^{\mathrm{ref}}_{\nu,300}$	$4.4\times10^{19}\,\mathrm{cm}^{-3}$	$8.2\times10^{19}\,\mathrm{cm}^{-3}$
$\gamma_{1,\nu}$	0.56	2.05
$\alpha_{\nu,300}$	0.96	1.38
$\gamma_{2,\nu}$	-0.32	0.3

Table 5.10: Parameters for lead telluride mobility models.

exponent's value of -2.4 for low doped samples reduces for higher dopings. Fig. 5.12 illustrates the mobility degradation with increasing dopant concentrations at room temperature. *Ueta*'s data are based on epitaxial layers grown on BaF_2 and are thus somewhat lower than bulk values due to additional surface scattering and lattice mismatch. An overview of hole mobility data is given in Fig. 5.13, where measurement data from [194, 270, 277–281] has been used as a basis for the hole mobility model.

5.5 Generation and Recombination

Generation and recombination has been studied extensively for the lead chalcogenides because of its applications as photodetectors and lasers in the infrared range [282–286]. In lead telluride, radiative transitions dominate the generation/recombination behavior due to the direct band gap within pure single crystals. Furthermore, defects generate states within the band gap and thus have a strong influence on generation and recombination rates [287, 288] which can be described by the *Shockley-Read-Hall* model [289]. For high carrier concentrations, the *Auger* process becomes highly competitive with direct recombination [290]. Furthermore, a temperature dependence of the intrinsic recombination rates analogously to *Shockley-Read-Hall* recombination is suggested due to the strong temperature dependence of the band gap as well as the effective masses. An overview of the mechanisms involved in lead telluride as well as modeling parameters are given in the sequel.

5.5.1 Direct Recombination

Direct recombination is an important transition in semiconductors with a direct band gap like lead telluride. Recombination goes hand in hand with radiative emission, while carrier generation is used within photodetectors for selective frequencies matching the band gap. For lead telluride, the sensitive frequency region is the infrared range. Due to the strong band gap dependence on material composition in lead tin telluride, the corresponding wavelength can be adjusted. The according generation/recombination rate depends on the carrier concentration and is modeled as

$$R^{\mathrm{RAD}} = C^{\mathrm{RAD}}\left(np - n_{\mathrm{i}}^2\right)\,, \tag{5.46}$$

where C^{RAD} denotes a proportionality factor. Calculated radiative carrier lifetimes of $0.6\,\mu\mathrm{s}$ are reported in [291] for lead telluride comparable to $0.8\,\mu\mathrm{s}$ in [292].

5.5.2 Shockley-Read-Hall Recombination

Trap-assisted generation and recombination is modeled using the *Shockley-Read-Hall* model [289]. The rate dependence on the carrier concentration is described by the expression

$$R^{\mathrm{SRH}} = \frac{np - n_{\mathrm{i}}^2}{\tau_p(n+n_1) + \tau_n(p+p_1)}\,, \tag{5.47}$$

where τ_n and τ_p depict the generation/recombination lifetimes for electrons and holes, respectively. The auxiliary variables n_1 and p_1 are defined as

$$n_1 = N_{\mathrm{c}}(T_{\mathrm{L}}) \exp\left(\frac{\mathcal{E}_{\mathrm{T}} - \mathcal{E}_{\mathrm{c}}}{k_{\mathrm{B}}T_{\mathrm{L}}}\right)\,, \tag{5.48}$$

$$p_1 = N_{\mathrm{v}}(T_{\mathrm{L}}) \exp\left(\frac{\mathcal{E}_{\mathrm{v}} - \mathcal{E}_{\mathrm{T}}}{k_{\mathrm{B}}T_{\mathrm{L}}}\right)\,. \tag{5.49}$$

There, the effective densities of states for electrons and holes are denoted by N_{c} and N_{v} and the conduction and valence band edges by $\mathcal{E}_{\mathrm{c}}$ and $\mathcal{E}_{\mathrm{v}}$, respectively. The most effective generation/recombination centers are those with an energy $\mathcal{E}_{\mathrm{T}}$ close to the mid of the band-gap. The generation/recombination lifetimes τ_n and τ_p at room temperature can be expressed as

$$\tau_{n,300} = \frac{1}{\sigma_{\mathrm{T},n} N_{\mathrm{T}} v_{n,300}} \tag{5.50}$$

$$\tau_{p,300} = \frac{1}{\sigma_{\mathrm{T},p} N_{\mathrm{T}} v_{p,300}}\,, \tag{5.51}$$

where they are dependent on the trap concentration N_{T} as well as the trap capture cross sections $\sigma_{\mathrm{T},n}$ and $\sigma_{\mathrm{T},p}$ for electrons and holes, respectively. The thermal velocities for electrons and holes are expressed as

$$v_\nu = \sqrt{\frac{3k_{\mathrm{B}}T_{\mathrm{L}}}{m^*_{\mathrm{c,v}}}} \tag{5.52}$$

in order to formulate the generation/recombination lifetimes dependent on the trap concentration N_{T} as well as the trap capture cross sections $\sigma_{\mathrm{T},n}$ and $\sigma_{\mathrm{T},p}$ for electrons and holes, respectively. Furthermore, the temperature dependence of the generation/recombination lifetimes is described by the empirical power law

$$\tau_n = \left(\frac{300\,\mathrm{K}}{T_{\mathrm{L}}}\right)^{3/2} \tau_{n,300}\,, \tag{5.53}$$

$$\tau_p = \left(\frac{300\,\mathrm{K}}{T_{\mathrm{L}}}\right)^{3/2} \tau_{p,300}\,. \tag{5.54}$$

Additionally, doping dependent generation/recombination lifetimes can be introduced using the *Scharfetter* relation

$$\tau_n(N_\mathrm{tot}) = \tau_{n,\mathrm{min}} \frac{\tau_{n,\mathrm{max}} - \tau_{n,\mathrm{min}}}{1 + \left(\frac{N_\mathrm{tot}}{N_{\mathrm{ref},n}}\right)^{\gamma_n}} , \tag{5.55}$$

$$\tau_p(N_\mathrm{tot}) = \tau_{p,\mathrm{min}} \frac{\tau_{p,\mathrm{max}} - \tau_{p,\mathrm{min}}}{1 + \left(\frac{N_\mathrm{tot}}{N_{\mathrm{ref},p}}\right)^{\gamma_p}} , \tag{5.56}$$

which can be used to calibrate the model to experimental data. Since the lifetimes strongly depend on the process technology as well as material quality, the parameters have to be determined from sample to sample. While in single crystals relatively long lifetimes can be expected, grain boundaries within sintered samples have a reducing effect.

5.5.3 *Auger* Recombination

Auger recombination is a process with three particles involved. In this mechanism, the energy set free by the recombination of an electron-hole pair is absorbed by a third carrier which is thus raised to a higher energy. In a second step, this carrier falls back to its initial state and thus transfers its excess energy to the lattice. *Auger* recombination becomes important for high carrier concentrations. It is modeled as the triple concentration product [268]

$$R^\mathrm{AU} = \left(C_n^\mathrm{AU} n + C_p^\mathrm{AU} p\right)\left(np - n_\mathrm{i}^2\right) \tag{5.57}$$

introducing the *Auger* coefficients C_n^AU and C_p^AU. In [293], the importance of *Auger* recombination in highly excited lead telluride has been discussed for thin films. Furthermore, the coefficients were determined by photo-conductivity measurements as $5 \times 10^{-28}\,\mathrm{cm^6 s^{-1}}$. In contrast to temperature dependent values as suggested for several semiconductors in [73] constant values over a wide temperature range have been observed in [294]. The coefficients for $\mathrm{Pb_{1-x}Sn_xTe}$ have been determined both theoretically and by measurement in [290]. For pure lead telluride, the theoretical value of $4.5 \times 10^{-28}\,\mathrm{cm^6/s}$ corresponds quite well with the measured value of $3.8 \times 10^{-28}\,\mathrm{cm^6/s}$ at 300 K. With a tin telluride content of $x = 0.17$, the according values for room temperature shift to $4.3 \times 10^{-27}\,\mathrm{cm^6/s}$ and $4.5 \times 10^{-27}\,\mathrm{cm^6/s}$.

'For it is with the same imperialism that present-day simulators try to make the real, all the real, coincide with their simulation models.'

Jean Baudrillard

Chapter 6

Case Studies

THERMOELECTRIC DEVICES are interesting candidates for a series of applications due to their capability of direct conversion of heat into electric energy. For a rigorous study, general device structures have to be considered, which demands the application of a general-purpose device simulator. For the following investigations, the device simulator MINIMOS-NT [268] has been applied. As a part of this work, the transport model has been revised and mechanisms for the visualization of thermoelectrically relevant quantities have been implemented.

In the sequel, the device behavior of two classes of devices is analyzed. First, the general behavior of classical thermoelectric devices is investigated with special attention payed to the influence of geometrical parameters as well as thermal environment and device parameters. The influence of material composition in alloys is illustrated for the example of silicon–germanium devices. Based on mixed-mode simulation [295], non-ideal thermal conditions are considered by an analog electric compact model.

For the simulation of lead telluride based devices, the model database has been extended by an according material class and model parameters. Furthermore, a set of models has been implemented in MINIMOS-NT in order to accurately account for the physical properties, such as the band gap and the doping dependent electric contribution to the thermal conductivity, as described in detail in Chapter 5. On the basis of a lead telluride device, an optimization strategy for stacked devices is discussed.

As a second thermoelectric structure, pn-junctions under a temperature gradient are rigorously investigated. In contrast to classical devices, carrier generation plays an important role within this structure. In order to sketch some possibilities for device optimization, the influence of several device parameters on its performance is investigated. Particularly, graded material alloys are investigated as a possibility to engineer the temperature profile within the device. Furthermore, the influence of additional traps on thermal carrier generation and thus the device performance is investigated and geometrical variations in order to improve transport within the device are considered. The complex interaction of several mechanisms are presented in an elaborate case study.

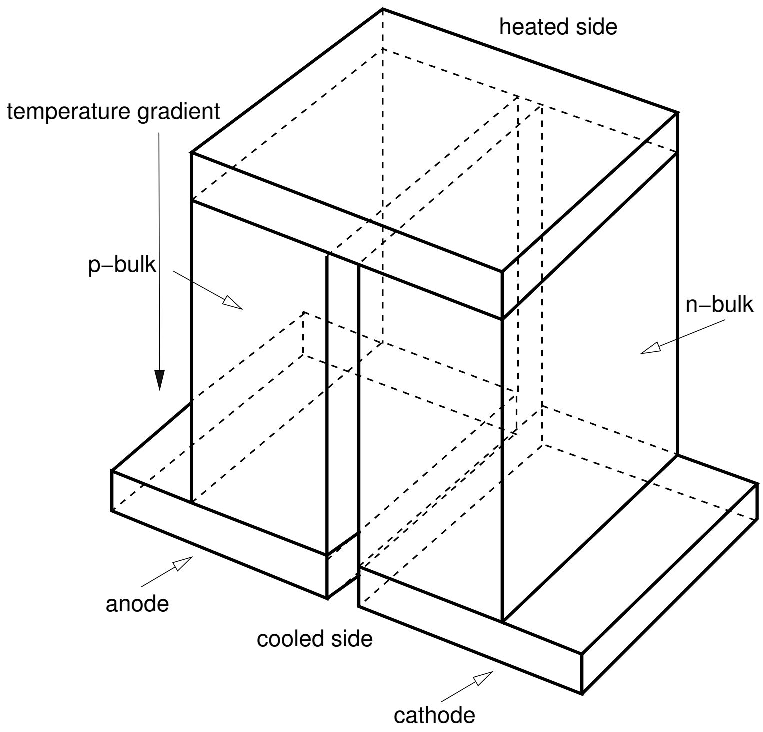

Figure 6.1: Principle configuration of a classical thermoelectric device.

6.1 Ideal Classical Thermoelectric Generators

The first type of thermoelectric generators, which is also the one usually used in commercial energy conversion applications, has inherited its principle assembly from early thermocouples and temperature sensors. It consists of two semiconducting legs, where one is made of p-type and the other of n-type material. In practical devices, the p-type leg is designed with a larger cross section than the n-type one due to the lower hole mobility. While the two legs are thermally parallel, they are electrically connected in series by a contact at the heated end of the devices. Due to the different signs of *Seebeck* coefficients in differently doped materials, the total voltage of the device is the sum of the single contributions of each leg.

In practical applications, thermoelectric modules are constructed of several single thermoelements, as sketched in Fig. 6.1. There, a possibility to adapt to thermal and electrical specifications is the different connection of single elements to modules in both an electrical as well as a thermal sense. While electrically parallel connection of single elements increases the total current, a serial configuration is applied to enhance the output voltage. The same principle works for the thermal configuration. Multiple single elements on the same level increase the heat flux throughout the entire module in order to exploit relatively “strong” temperature reservoirs at temperature differences matching one single stage. Environments with higher temperature differences are often treated with modules consisting of multiple stages. There, the temperature difference is subdivided to a thermally serial configuration within stacked modules. Since every material has an ideal thermal operating point, as outlined in Chapter 4, it is often beneficial to combine stages built of different semiconductors.

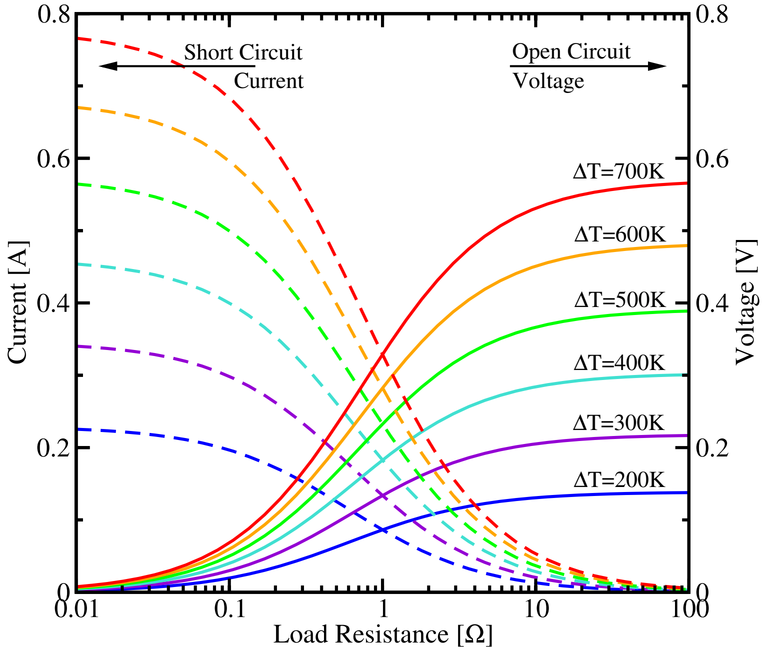

Figure 6.2: Voltage and current with respect to the load resistance.

In the sequel, the basic behavior of single thermoelements is discussed on the basis of simulation results. In order to analyze the internal behavior of a single thermoelectric device, the focus is put on the thermoelectrically active device itself first. In this idealized perspective of thermoelectric generators, thermal contact resistances as well as characteristics of heat sources and sinks are neglected. This means that the thermoelectrically active legs capitalize from the entire thermal potential, which is provided by ideally stiff temperature sources. Furthermore, electric contact resistances are neglected as well. Such a treatment is beneficial in order to identify the maximum conversion potential of a thermoelectric device, which will be reduced by parasitic external effects in practical situations. Furthermore, it enables an analysis of the internal mechanisms, which governs valuable insights for device optimization and further development.

In Fig. 6.2, the current and voltage behavior of a single thermocouple with respect to a load resistance is illustrated for different temperature differences. The device assumed has a leg length of 20 mm and a cross section of $5 \times 1\,\mathrm{mm}^2$. Both legs are made of silicon and have according doping concentrations of $1 \times 10^{19}\,\mathrm{cm}^{-3}$. The electric contacts are considered as ideal conductors, which is a safe assumption for conventional device geometries. For example copper features an electrical conductivity of $59.6 \times 10^6\,\mathrm{S/m}$, which is about three orders of magnitude above the conductivity of accordingly doped silicon.

With a constant temperature difference maintained along the device, a simulated ohmic load resistance is swept over four decades. For low resistances, the behavior converges against short circuit conditions. While the voltage drops to zero, an accordingly high current is driven by the temperature gradient. For accordingly high resistances, the driven current goes to zero, while the voltage approaches its open circuit value. Within considerable ranges, both current and voltage increase with increasing temperature differences. This behavior is limited by strongly decreasing *Seebeck* coefficients at high temperatures, as presented in Figures 3.7 and 3.8.

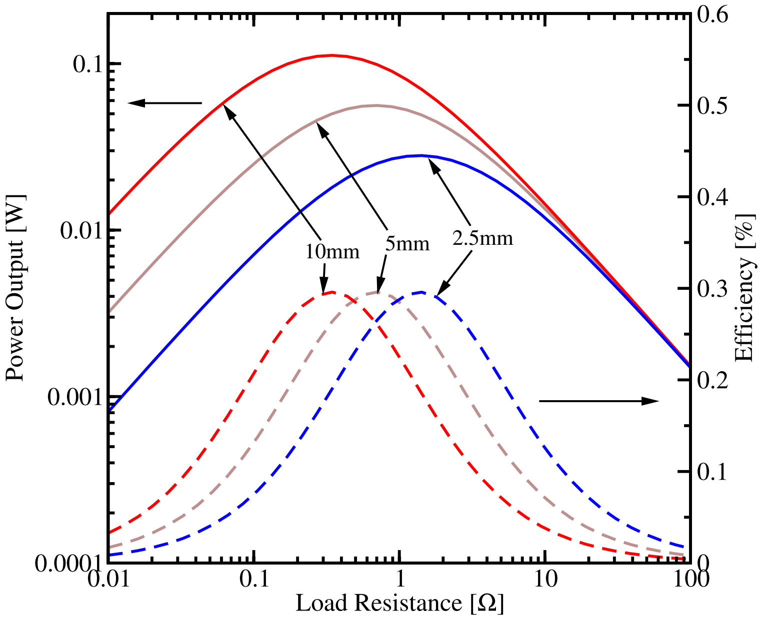

Figure 6.3: Electric power output as well as conversion efficiency vs. load resistance for different leg thicknesses.

The electrical power output is obtained as the product of contact voltage U_c and driven current I, where the contact voltage can be obtained as the directed integral along both legs as

$$P_\mathrm{el} = U_\mathrm{c} I = \left(\int\limits_{x_0}^{x_1} \alpha_p(T(x)) \partial_x T \,\mathrm{d}x - \int\limits_{x_0}^{x_1} \alpha_n(T(x)) \partial_x T \,\mathrm{d}x \right) I \,. \tag{6.1}$$

Due to the different signs of the *Seebeck* coefficients α_p and α_n, the contributions of the legs add constructively to the total voltage. Furthermore, the according current is specified by the driving voltage as well as the sum of internal and external resistances.

The thermoelectric conversion efficiency is defined by the energy balance within the device as the ratio of generated electrical power and incoming heat-flux throughout the heated thermal contact

$$\eta = \frac{P_\mathrm{el}}{J^\mathrm{q}_\mathrm{hot}} \,. \tag{6.2}$$

Fig. 6.3 illustrates the corresponding electric powers and thermoelectric conversion efficiencies at a temperature difference of 500 K above room temperature. The optimum power and efficiency are achieved at matched load conditions, where the external load resistance is equal to the internal resistance $R_\mathrm{l} = R_\mathrm{i}$. A modification of the device geometry results in changed internal resistances. For lower leg thicknesses, the internal resistance increases, thus the total power output decreases and the optimum operating point is shifted to higher load resistances as well. However, due to the lower cross section of the legs, the thermal resistance is increased as well and thus the heat flux throughout the device is reduced resulting in a constant efficiency. For higher leg thicknesses, the quantities change accordingly to the other direction. The resulting power density of the device is constant as well.

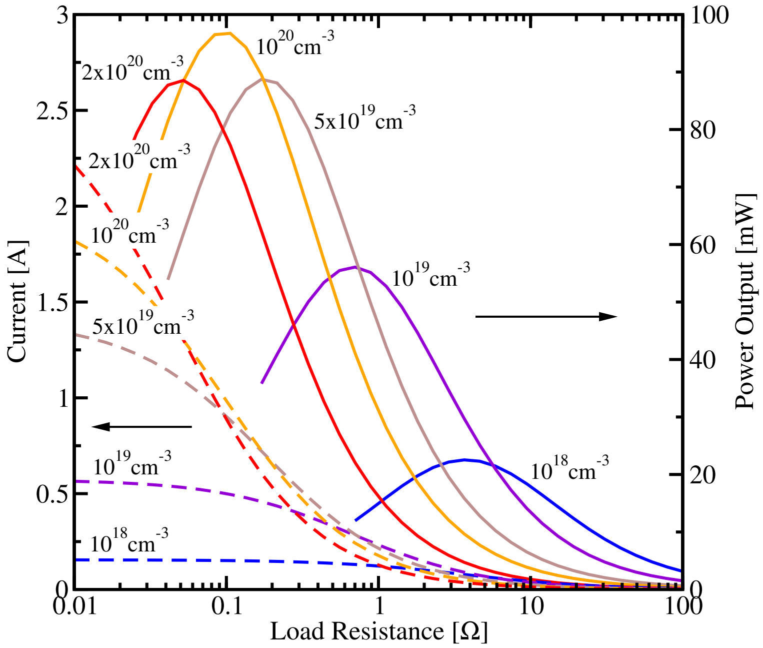

Figure 6.4: Electric current as well as power output vs. load resistance for differently doped devices.

Within the idealized treatment of thermoelectric devices, the same considerations are valid for changes of the leg length, as long as the temperature at the thermal contacts can be assumed to be constant. However, in real world devices, especially in miniaturized elements, this is not the case due to the influence of parasitic external thermal resistances, as demonstrated later on. Since geometrical modifications affect both the thermal as well as the electrical circuit, the conversion efficiency and power density are not affected over a wide range. Mathematically speaking, a principle approach to performance improvement is to change the parameters of only one of the electrical and thermal subsystems as well as their coupling mechanisms. For the thermal part, it is beneficial to reduce the heat flux as much as possible while not affecting the electric conductivity. For the electric part, for example modification of the doping concentrations results in a change of the electrical conductivity. However, the *Seebeck* coefficient is affected reversely and thus, an optimum doping concentration can be identified.

Figures 6.4 and 6.5 point out the influence of different doping concentrations on the device performance. The contact voltage decreases with increasing doping due to the detrimental effect of large carrier concentrations on the *Seebeck* coefficient. For comparison, see also Figures 3.7 and 3.8. The current follows driving voltage and internal resistance. While the driving voltage is reduced at higher doping concentrations, the conductivity is noticeably increased. This results in an increased current as well, as presented in Fig. 6.4. For the power output, a trade–off between the doping's influences on current and voltage occurs. Thus, an optimum carrier concentration exists, which is about $10^{20}\,\mathrm{cm}^{-3}$ in the presented example. Since the carrier contribution to the thermal conductivity is only of subsidiary significance, the heat flux throughout the device is only increased at very high carrier concentrations. This results in an optimum efficiency at a doping concentration close to the one for the optimum power output. Fig. 6.6 illustrates the temperature dependence of the electric power output. The strongly increasing power output saturates at high temperatures depending on the doping concentration.

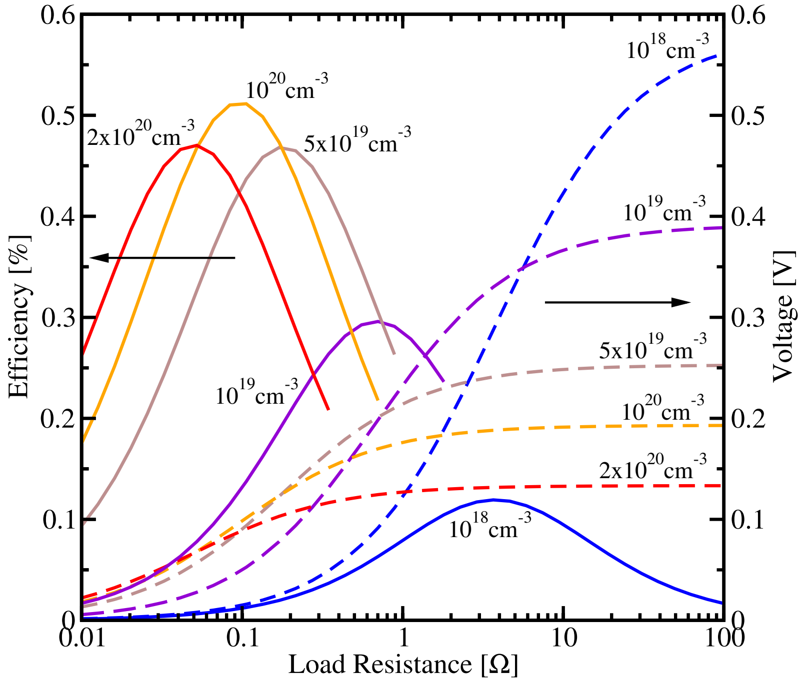

Figure 6.5: Voltage as well as conversion efficiency vs. load resistance for differently doped devices.

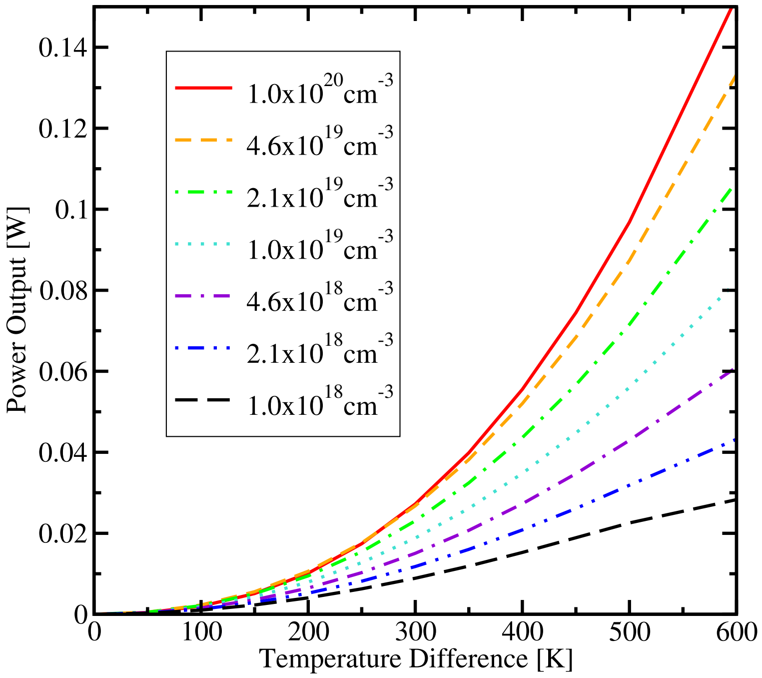

Figure 6.6: Electric power output vs. temperature for differently doped devices.

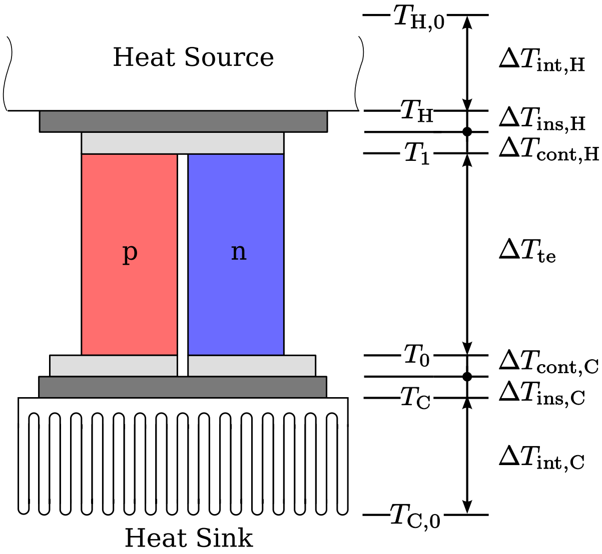

Figure 6.7: Temperature distribution for a non-ideal thermoelectric generator.

6.2 Non-Ideal Devices and Thermal Environment

In real-world thermoelectric devices, several thermal and electrical losses outside the thermoelectrically active parts occur. Furthermore, heat source and sink are not ideally rigid as well, meaning that their temperature changes with their thermal load, which is the heat flux traversing the thermoelectric device. Beside the internal thermal resistances of several subparts, thermal contact resistances occur.

The thermal relations can be described using an electrical analogon, where the temperature takes the same place as the electrical potential [296]. Furthermore, the heat flux corresponds to the electrical current and the thermal conductivity takes the place of the electrical conductivity. A thermal network is formulated similarly to an electric circuit, and consequently can be treated with the same toolkit as an electric circuit. The basic relation is the analogon to *Ohm*'s law, connecting the temperature drop along a structure with its thermal resistance and the traversing heat flux.

The thermal relations within a thermoelectric generator as well as its environment are sketched in Fig. 6.7. A corresponding circuit using the electrical analogon is shown in Fig. 6.8.

A thermoelectric device is connected to a heat source and a heat sink throughout electrically insulating layers. The heat source's "contact" temperature available for the device is given in terms of its off-load temperature, the internal thermal resistance, and the load heat flux as

$$T_\mathrm{H} = T_{\mathrm{H},0} - \Delta T_{\mathrm{int,H}} = T_{\mathrm{H},0} - J^\mathrm{q}_\mathrm{hot} R^\mathrm{th}_{\mathrm{int,H}} \,. \tag{6.3}$$

Subtracting the temperature drop throughout the electrical insulation at the heated end $\Delta T_{\mathrm{ins,H}}$ from the heat source temperature T_H, the temperature at the hot side thermal contact of the thermoelectric generator is obtained. The electric contact further slightly reduces the tempera-

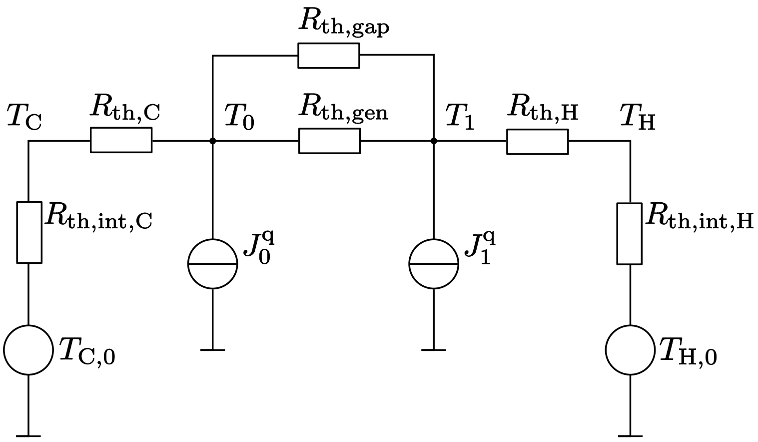

Figure 6.8: Thermal equivalent network of a thermoelectric device accounting for non-ideal thermal environment.

ture to the one at the hotter end of the thermoelectrically active legs. It is considered that the temperature drops include both the ones caused by internal and thermal contact resistances.

The same considerations work for the cooled end of the assembly starting at the non-ideal heat sink. The lower temperature at the active legs is obtained by adding the temperature drops along the electrical insulation to the heat sink's temperature under thermal load conditions T_{C}. The resulting temperature difference available for thermoelectric conversion is reduced from the idealized value of $T_{\mathrm{H}} - T_{\mathrm{C}}$ to $T_1 - T_0$.

Depending on the geometrical relations as well as the kind of insulation medium between the legs, a more or less pronounced parasitic heat flux parallel to the legs can occur. This heat flux contributes to the thermal load of heat source and sink, but not to the thermoelectric conversion process and thus has a detrimental effect on the conversion efficiency by reducing the temperature difference available for thermoelectric exploitation. However, the gaps between the legs are minimized in order to gain a best possible spatial utilization and normally, the thermal conductivity of the legs is by far larger than that of the gaps. Thus, this heat flux parallel to the legs can be neglected safely.

In the following example, all external thermal resistances as well as the non-ideal behavior of the heat source are treated as a lumped thermal resistance between the heat source and the heated end of the thermoelectric generator. Furthermore, the cooled end is assumed to be ideally connected to a heat sink held constantly at 300 K.

The assembly works as a temperature divider between the lumped external thermal resistance and the thermoelectrically active generator itself. Thus, at a certain heat flux, the temperature drop at the legs is reduced to

$$\Delta T_{\mathrm{te}} = (T_{\mathrm{H}} - T_{\mathrm{C}}) \frac{R_{\mathrm{th,TEG}}}{R_{\mathrm{th,TEG}} + R_{\mathrm{th,ext}}}\,, \tag{6.4}$$

where $R_{\mathrm{th,TEG}}$ denotes the thermal resistance of the thermoelectric generator and $R_{\mathrm{th,ext}}$ is the serial external thermal resistance.

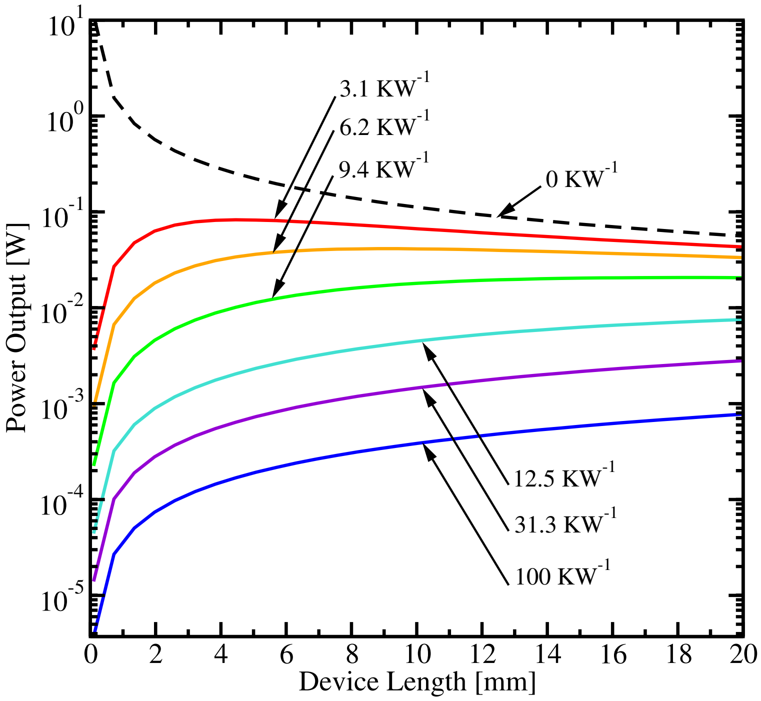

Figure 6.9: Electric power output with respect to the device leg length.

Fig. 6.9 illustrates the influence of the thermal relations to the power output of the thermoelectric generator. At a certain external thermal resistance, longer devices benefit from their increased thermal resistance and thus increased temperature drop. On the other hand side, higher thermal losses decrease the available thermal potential for the thermoelectrically active parts and thus reduce the power output. For relatively low external thermal resistances, the power output first increases with decreasing device length due to the elevated heat flux throughout the structure. However, below a certain length, the detrimental effect of the reduction of the device's temperature drop exceeds the increase of heat flux resulting in strongly decreasing power outputs. This behavior vanishes in the border case of ideal thermal conditions, as indicated by the dashed line. The behavior of the power density is shown in Fig. 6.10.

The according conversion efficiencies are presented in Fig. 6.11. For ideal thermal environment conditions, the conversion efficiency is constant over a wide region, since a change of the device length affects both the heat flux and the power output via the according internal resistances. For increasing external thermal resistances, the conversion efficiency reduces remarkably. In contrast to the power output, the initial increase with decreasing leg length can not be identified for the efficiency since the advantage at the electric power side is compensated by an increased heat flux, which also enters the efficiency.

In any case, a reduction of the external thermal resistance is beneficial for the device performance, as pointed out in Fig. 6.12. Especially for very short devices, the negative influence on power output at already relatively low thermal resistances is pronounced.

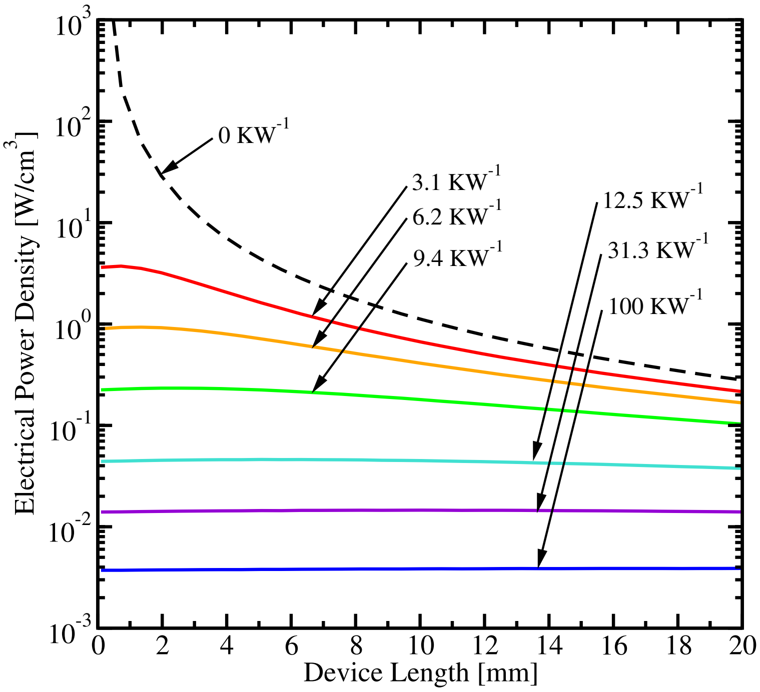

Figure 6.10: Electric power density with respect to the device leg length.

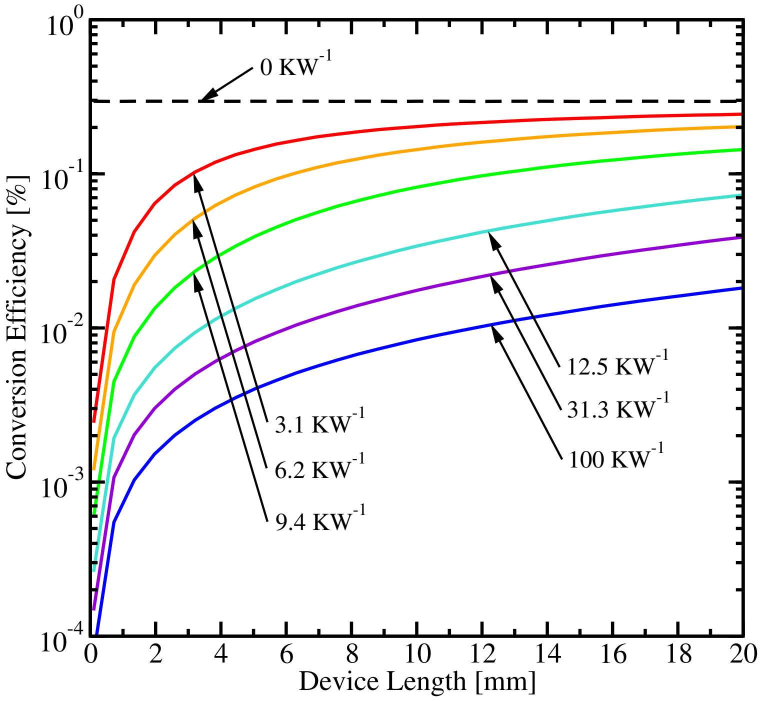

Figure 6.11: Conversion efficiency with respect to the device leg length.

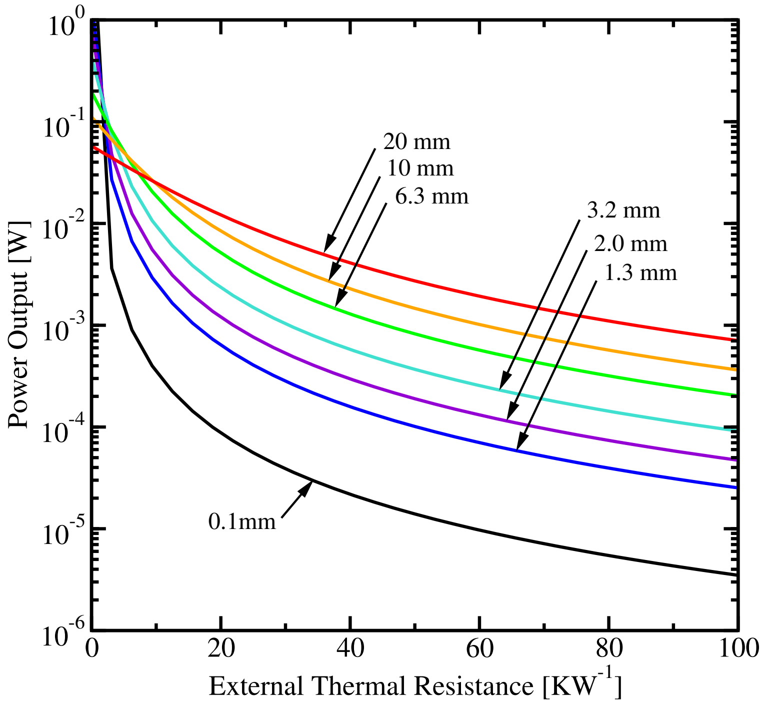

Figure 6.12: Electric power output with respect to the external thermal resistance.

6.3 Reduced Thermal Conductivity by Alloys

In the sequel, the influence of material alloys on thermoelectric device characteristics is discussed on the example of silicon–germanium. As demonstrated in Section 4.3, elevated phonon scattering rates in SiGe alloys lead to a remarkably reduced thermal conductivity compared to pure silicon. However, the electric properties are affected as well. The trade-off between the advantage of lowered thermal conductivity and the drawback of decreased mobility as well yields a more or less pronounced improvement of conversion efficiency.

Simulation studies have been carried out for a thermoelectric generator with a leg length of 20 mm and a cross section of $5 \times 1\,\mathrm{mm}^2$. The dopings for both p– and n–type legs are held constant at $10^{19}\,\mathrm{cm}^{-3}$. Furthermore, the temperature difference considered is 600 K above room temperature.

Both decreased *Seebeck* voltages as well as reduced mobilities with increasing germanium content over a wide range (compare Fig. 4.4) result in a drop of currents with increasing germanium contents. The according electric power output also takes its highest value at pure silicon, as indicated in Fig. 6.13. The lower mobilities result not only in a reduction of the absolute maximum of the power output, but also on a shift to higher resistances.

However, the impact of the material composition on the thermal conductivity and thus the heat flux traversing the device outweighs the influence on the electrical properties, as presented in Fig. 6.14. The heat flux reduces to a minimum at about 50 % Ge which is one magnitude lower than the one of pure silicon. The resulting maximum of the conversion efficiency is predicted for about 30 % germanium content, where an optimum relation between thermal and electrical

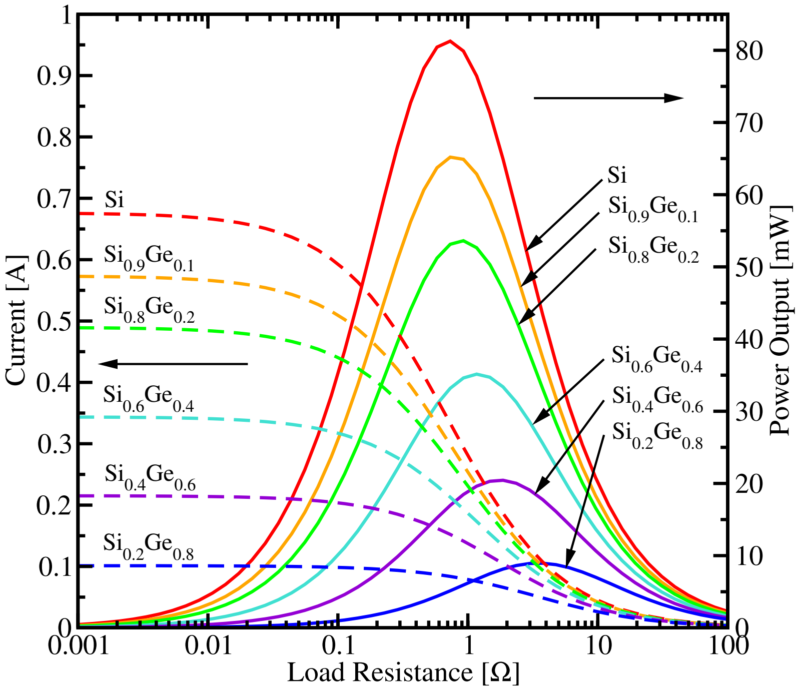

Figure 6.13: Current as well as electric power output with respect to the load resistance.

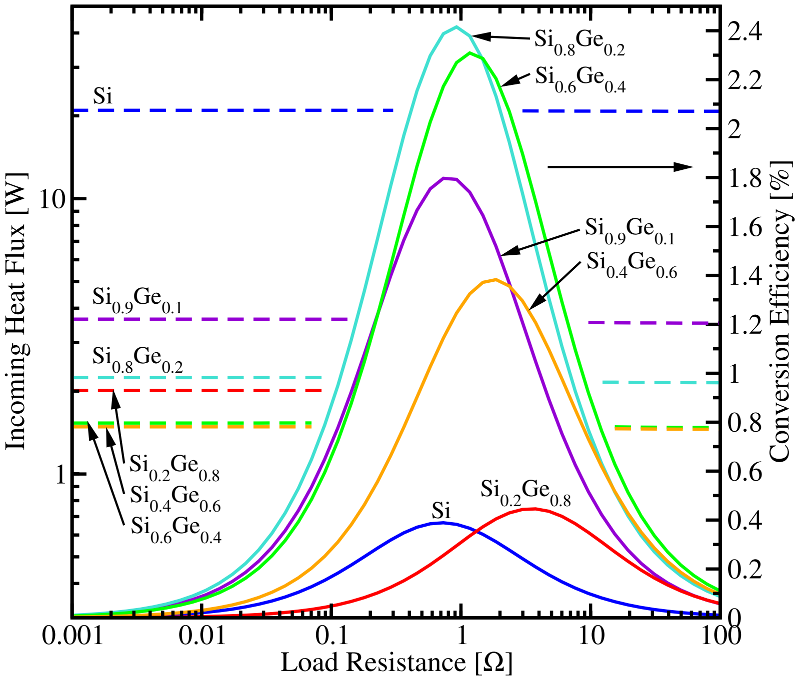

Figure 6.14: Thermal heat flux as well as conversion efficiency with respect to the load resistance.

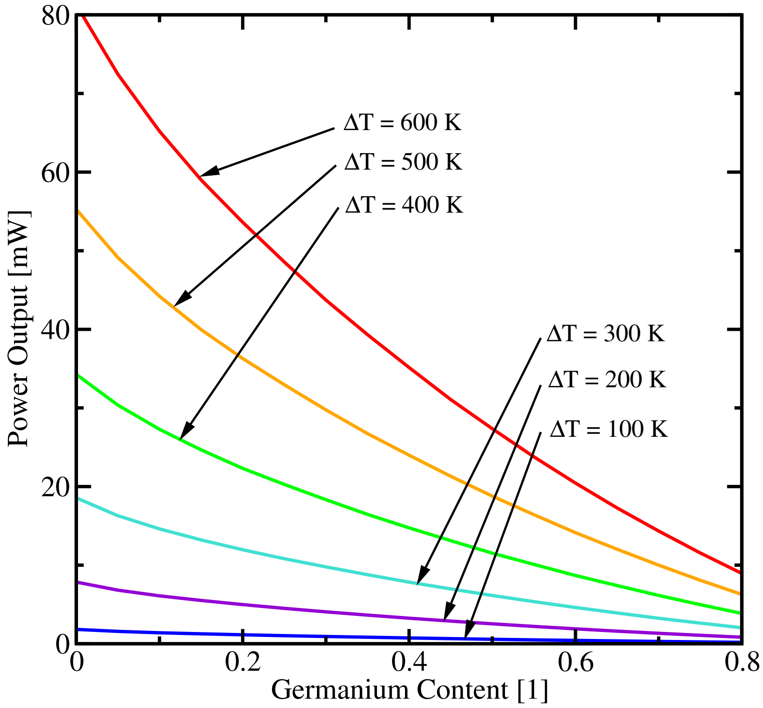

Figure 6.15: Electric power output with respect to the material composition in SiGe alloys for several temperatures.

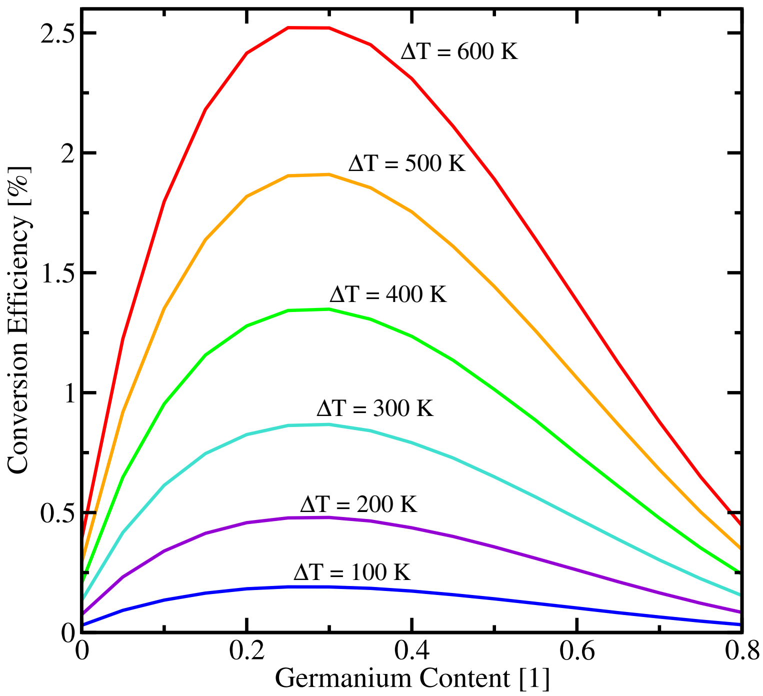

Figure 6.16: Conversion efficiency with respect to the material composition in SiGe alloys for several temperatures.

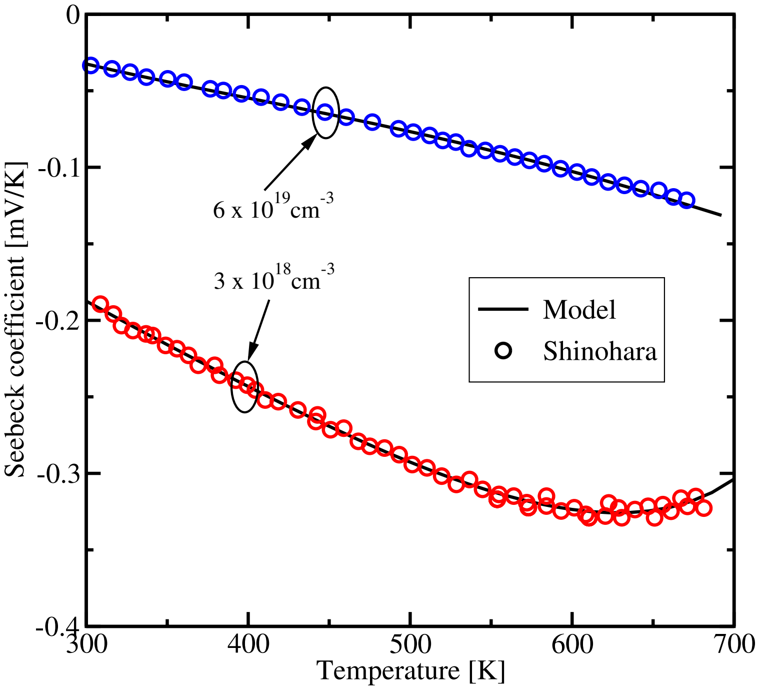

Figure 6.17: Temperature dependent *Seebeck* coefficients for a lead telluride n-type device.

properties occurs. For higher germanium contents, the thermal conductivity still decreases slightly, but cannot outweigh the worse mobility and *Seebeck* voltages anymore. Fig. 6.15 outlines the dependence of the power output on the material composition at matched load conditions for different temperature differences. The according behavior of the conversion efficiency is presented in Fig. 6.16. While the power output steadily decreases with increasing germanium content, the conversion efficiency has its maximum at about 30 % germanium.

6.4 Stacked Lead Telluride Thermoelectric Devices

Due to the temperature dependence of several material parameters, every material configuration has its maximum conversion efficiency in a specified temperature range. Thermoelectric generators built from one single block of homogeneous materials suffer from the spatial limitation of matched thermal conditions which follows from the temperature gradient throughout the device. A possibility to overcome this limitation is the introduction of stacked thermoelectric devices. There, the material parameters are locally adapted in order to match the required temperature range.

This concept is discussed for the example of an n-type lead telluride leg, as experimentally carried out in [297]. Two ingots of lead telluride with a quadratic cross section of 3.45 mm side length and lengths of 2.78 mm and 4.35 mm build the basis for the analysis. The ingots are doped with PbI_2, where the shorter sample has an impurity concentration of $3 \times 10^{18}\,\mathrm{cm}^{-3}$ and the longer one $6 \times 10^{19}\,\mathrm{cm}^{-3}$.

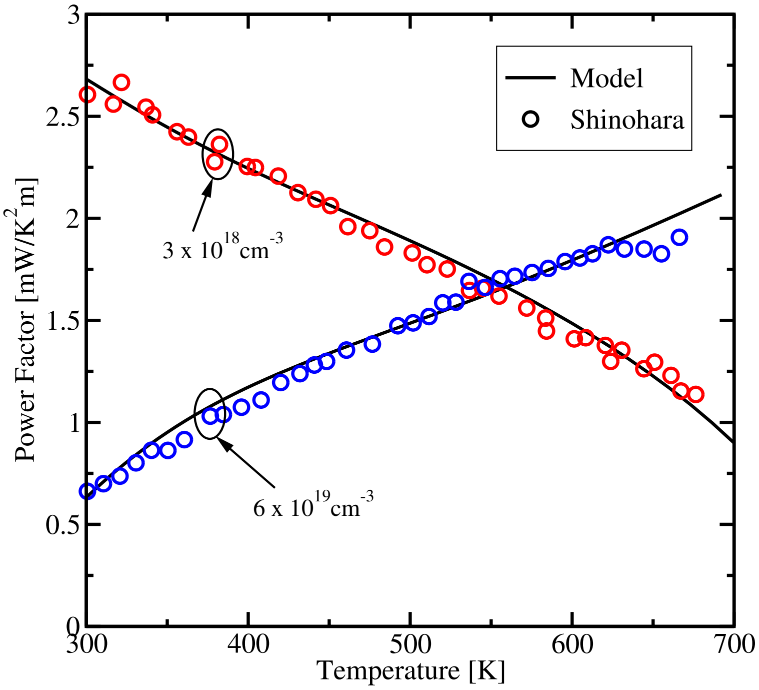

Figure 6.18: Temperature dependent power factor for a lead telluride n-type device.

In order to ensure accurate simulation results, the parameter models have been calibrated to measurement data. While good agreement between resistivity data given in [297] and the mobility model presented in Section 5.4 is obtained, experimental data on the *Seebeck* coefficient has to be treated carefully, since the second conduction band gives a contribution to carrier transport for elevated energies. In the simulations, a two–band model has been applied, where the *Seebeck* coefficient has been calibrated to measurement data from [297] following equation (3.188). Fig. 6.17 demonstrates the calibration of the model to the measured *Seebeck* coefficients. Furthermore, the power factor $\alpha^2\sigma$ as the electric part of the thermoelectric figure of merit Z incorporates both the *Seebeck* coefficient as well as the electric conductivity and thus the carrier mobility. Besides the models for the *Seebeck* coefficients and the effective mass, Fig. 6.18 illustrates the conformance of the mobility model.

The basic principle behind stacked thermoelectric devices can be recognized in Fig. 6.18 as well. A lower *Seebeck* coefficient limits the power factor of the higher doped ingot in spite of its relatively high conductivity. For the lower doped ingot, the higher *Seebeck* coefficient dominates over the lower conductivity at lower temperatures. Thus, at lower temperatures, the lowly doped ingot outperforms the higher doped one, which is reversed at temperatures above about 550 K for the considered dopant concentrations of $3 \times 10^{18}\,\text{cm}^{-3}$ and $6 \times 10^{19}\,\text{cm}^{-3}$, respectively.

Fig. 6.19 illustrates the maximum specific power output at matched load conditions of both the single higher doped ingot and the stacked combination of both ingots as illustrated in the inlay. Since the power output depends on the device length, the specific power outputs are used for comparison. The stacked module outperforms the single ingot over the entire temperature range, where the curve for the single ingot represents the total generated power.

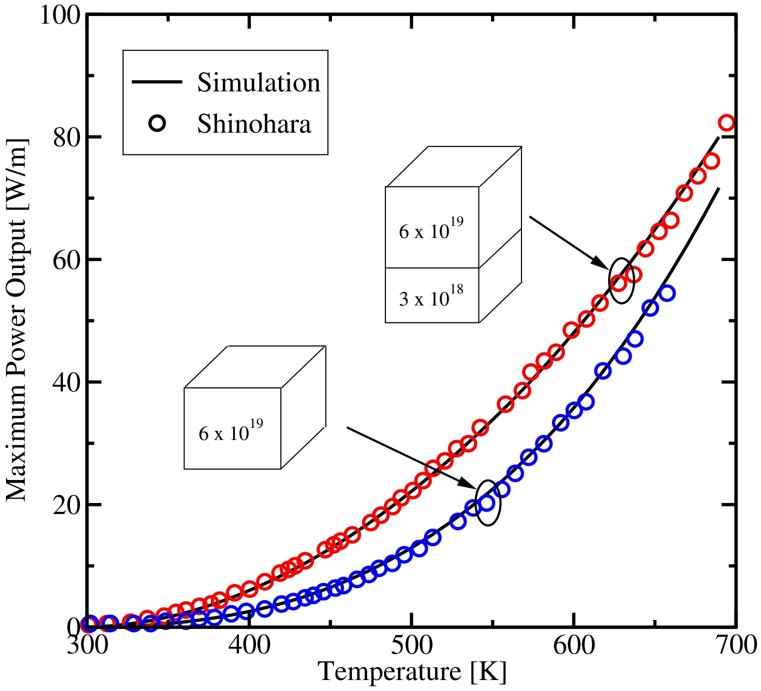

Figure 6.19: Electric power output with respect to temperature difference for a lead telluride n-type device.

The beneficial effect of stacking is further amplified by the relation of the thermal conductivities. In the higher doped ingot, the carrier contribution of the thermal conductivity plays a significant role, as also predicted in Fig. 5.3. As illustrated in Fig. 6.22, the temperature distribution shifts to elevated temperatures in the higher doped ingot and a steeper gradient in the lower doped one. Following Fig. 6.18, ideal power output is obtained with the interface between the two ingots at a temperature of about 550 K. This can been applied as a design rule for the length ratio of the two parts.

The adaption of a stacked thermoelectric generator to given thermal boundary conditions within a desired range of temperatures is illustrated in Figures 6.20 and 6.21. In Fig. 6.20, the influence of the temperature at the heated end as well as the stack assembly on the electrical power output is analyzed. There, the temperature at the cooled end is kept constant at 300 K. For this analysis, the overall length of the entire stacked thermogenerator is 7.13 mm and the length ratio of the two differently doped ingots is varied. For decreasing temperatures at the heated end, the optimum length of the highly doped ingot located at the heated end decreases. This is obvious, since the highly doped sample outperforms the lowly doped one only at elevated temperatures, as shown in Fig. 6.18. Thus, the optimum length ratio maintains the crossover temperature of 550 K at the ingot interface. In Fig. 6.21, the interface temperature is plotted with respect to the temperature of the heated end and the ingot length ratio. The red line depicts the optimum interface temperature, whose parameters are congruent with these of the optimum power output.

While the maximum power output directly depends on the thermoelectric power factor, the conversion efficiency is additionally affected by the heat flux throughout the device.

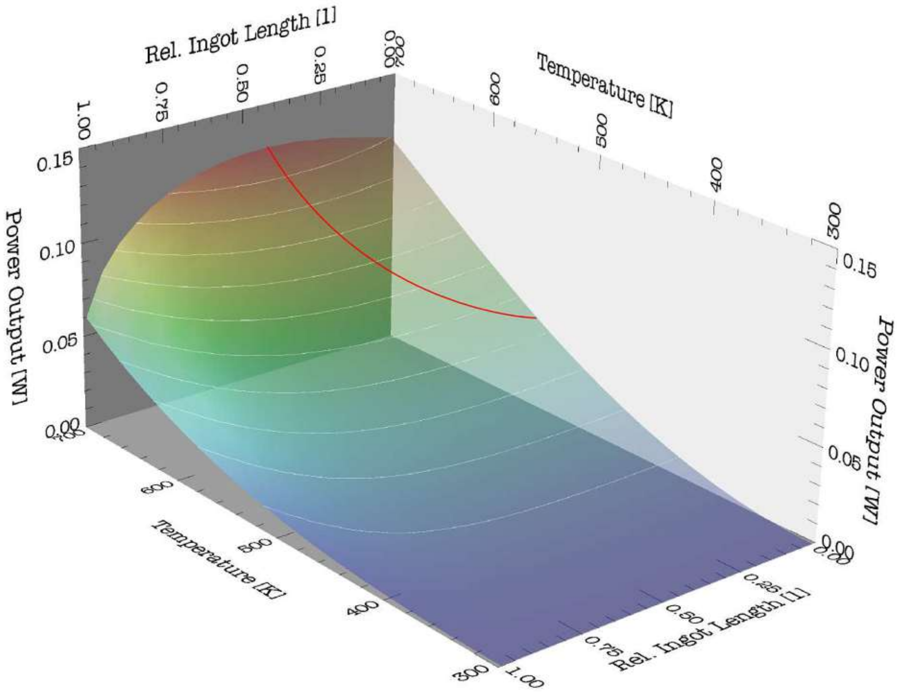

Figure 6.20: Power output with respect to the temperature at the heated end and the ingot length ratio for a stacked lead telluride device.

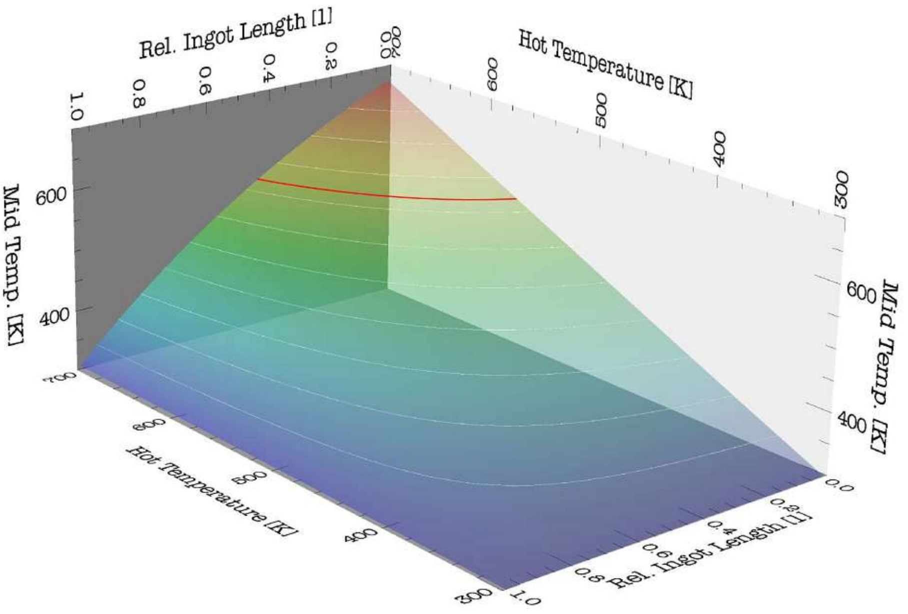

Figure 6.21: Temperature at the ingot interface with respect to the heated end's temperature and the ingot length ratio for a stacked lead telluride device.

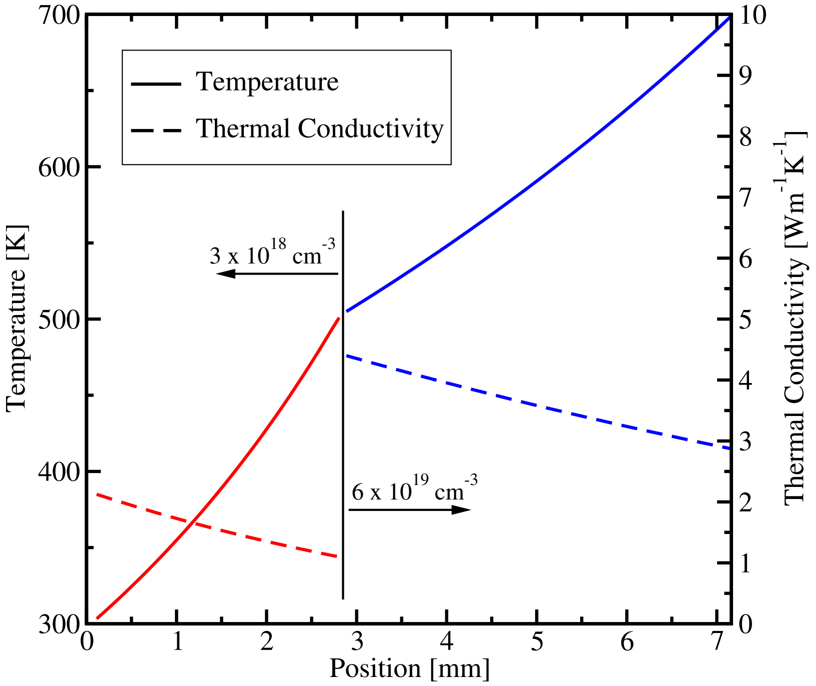

Figure 6.22: Spatial distribution of thermal conductivity as well as temperature within a stacked lead telluride device.

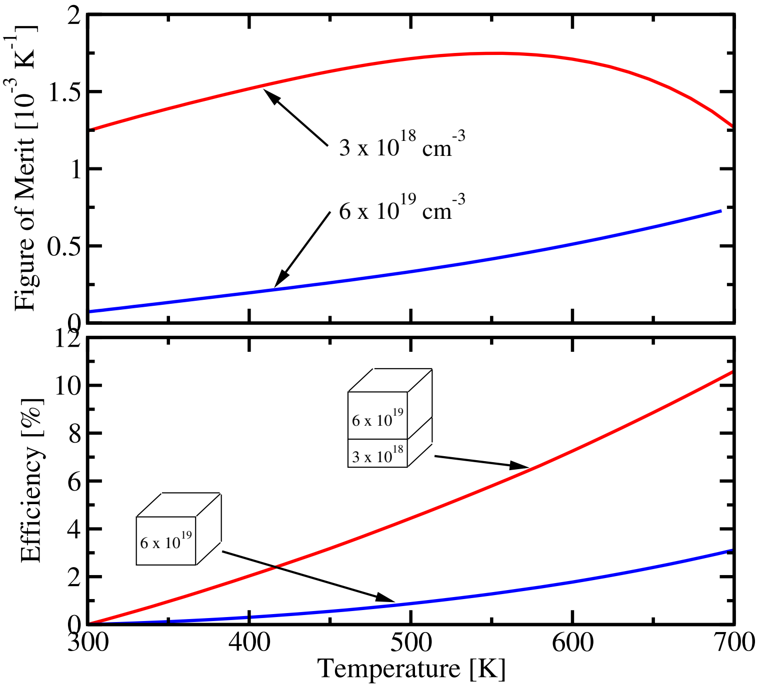

Figure 6.23: Temperature dependent thermoelectric figure of merit for the lowly and highly doped ingots as well as conversion efficiencies for the stacked device and the highly–doped ingot with respect to the heated end's temperature.

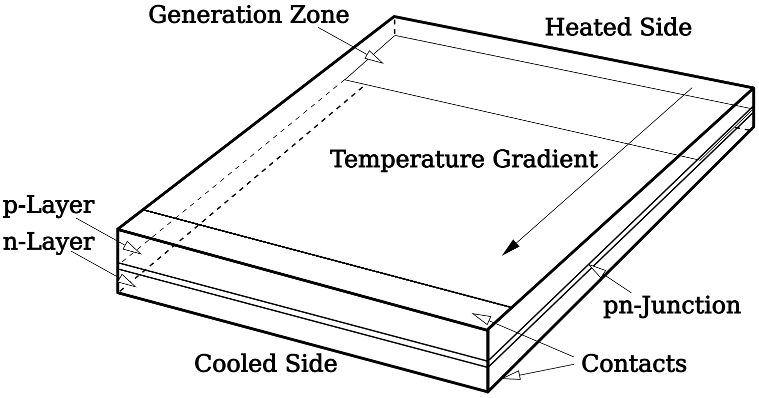

Figure 6.24: Principle configuration of a large area pn-junction thermoelectric generator.

The corresponding material parameter — the thermoelectric figure of merit — therefore incorporates the thermal conductivity. As indicated in Fig. 6.23, the figure of merit of the highly doped ingot is outperformed by the lower doped one throughout the entire temperature range due to the high electric contribution to the thermal conductivity. Thus, the effect of the heat flux on the efficiency is dominant and the efficiencies decrease with increasing length of the highly doped ingot.

Thermoelectric generators consisting of two differently doped legs benefit from the stacking concept as well. Besides the adaption of local doping, as presented for the example of the n–type lead telluride leg, the legs can consist of different materials in order to match the local thermal environment [32]. There, the materials are chosen from several classical thermoelectric materials, such as bismuth telluride, lead telluride, and SiGe, as well as novel materials such as clathrates [110, 183, 298].

6.5 Pn–Junctions as Thermoelectric Devices

As an alternative to classical thermoelectric devices, a structure incorporating a large area pn-junction [299] is investigated in this section. The principle design of a large area pn-junction thermoelectric generator is shown in Fig. 6.24. Both electrical contacts are at the cooled end of the structure and a temperature gradient is applied along the pn-junction. In contrast to conventional thermoelectric devices, the thermal generation of electron-hole pairs is explicitly used within large area pn-junction generators.

The underlying physical functionality is based on the temperature influence on the device's electrostatics. A temperature gradient within the structure leads to the generation of an electrical current, which is caused by the effect of the temperature on the electrostatic potential of a pn-junction. Basically, the higher temperature T_1 leads to a smaller energy step ΔE_1 from the

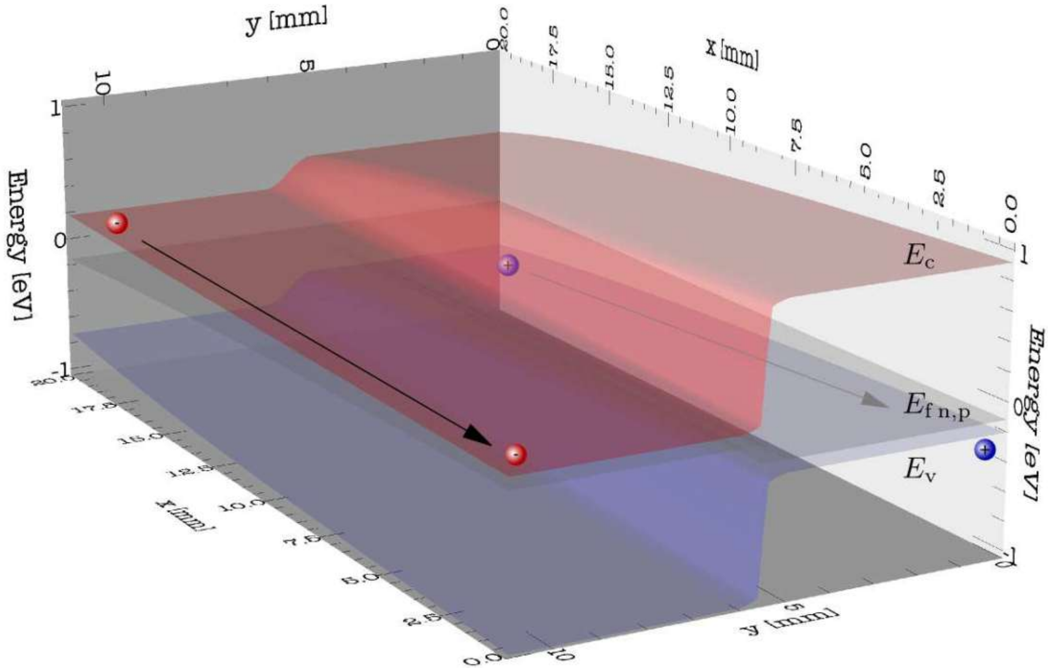

Figure 6.25: Energy relations in large area pn-junction thermoelectric generators.

potential of the n- to the p-layer compared to the step ΔE_0 at the lower temperature T_0. By having a temperature gradient in a large area pn-junction, both conditions occur neighboring to each other with the result that carriers at different potentials come into contact and thus experience a driving force to the colder region. The relations are illustrated in Fig. 6.25.

Because both types of carriers, electrons and holes, are moving in the same direction (ambipolar drift and diffusion), away from the pn-junction at the higher temperature T_1, this region becomes depleted and the local thermal equilibrium is disturbed. The generation-recombination balance is shifted to higher generation to compensate the off-drifting carriers.

At the part of the structure with the lower temperature T_0, the opposite effect takes place. The incoming carriers enhance the recombination, which results in a circular electrical current within the large area pn-junction from the hot region with enhanced generation to the cold side with increased recombination. Using selective contacts to both the n- and p-type layers, this circular current can be diverted to an external load and a power source is established, a thermoelectric element.

The internal functionality of the device can best be illustrated for significant limiting cases. A structure with a length of 20 mm and a total thickness of 2.4 mm is investigated as an example. The p- and n-layer are symmetrically doped with a maximum concentration of $10^{20}\,\mathrm{cm}^{-3}$ and separated by a 0.4 mm thick intrinsic layer. Electric contacts are applied at the cooled end of the structure.

For an open circuit, no current can flow to the outside. This situation is illustrated in Figures 6.26 and 6.27. Carrier generation takes place at the heated end of the device with peaks at the borders of the intrinsic layers, where carriers are extracted to the conducting layers.

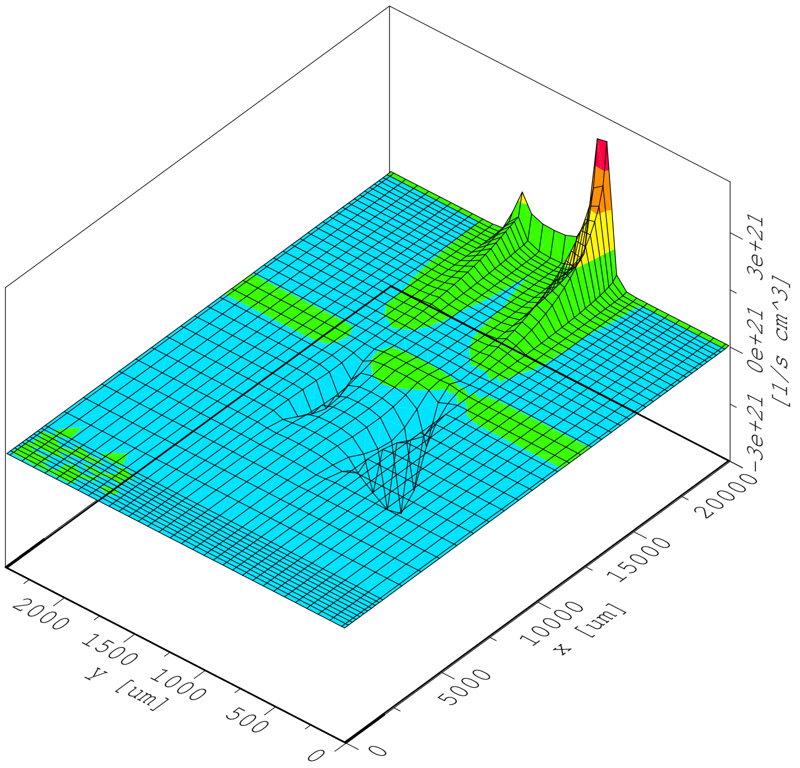

Figure 6.26: Local generation rate at open circuit conditions.

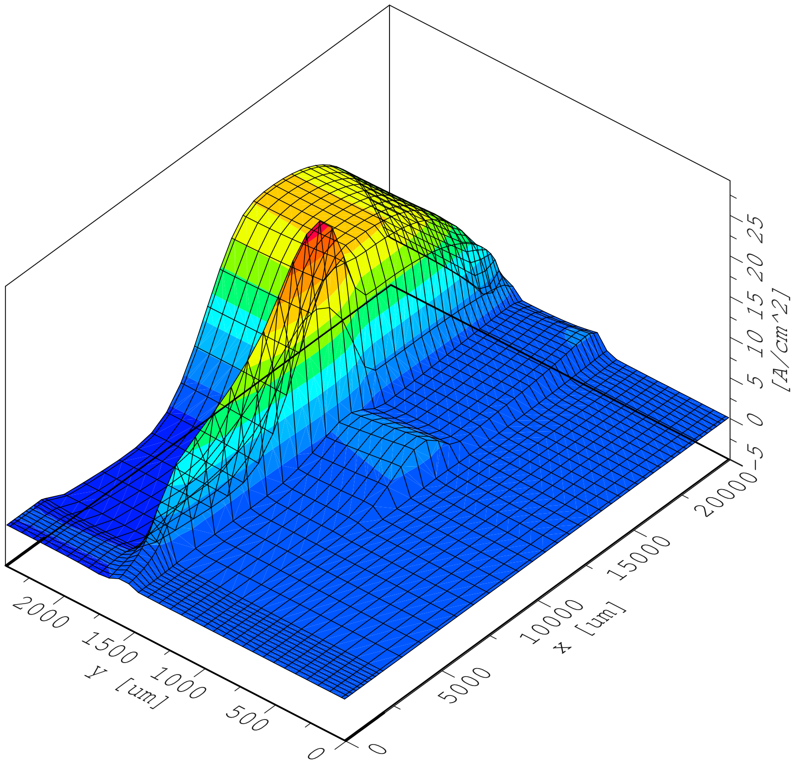

Figure 6.27: Electron current density at open circuit conditions.

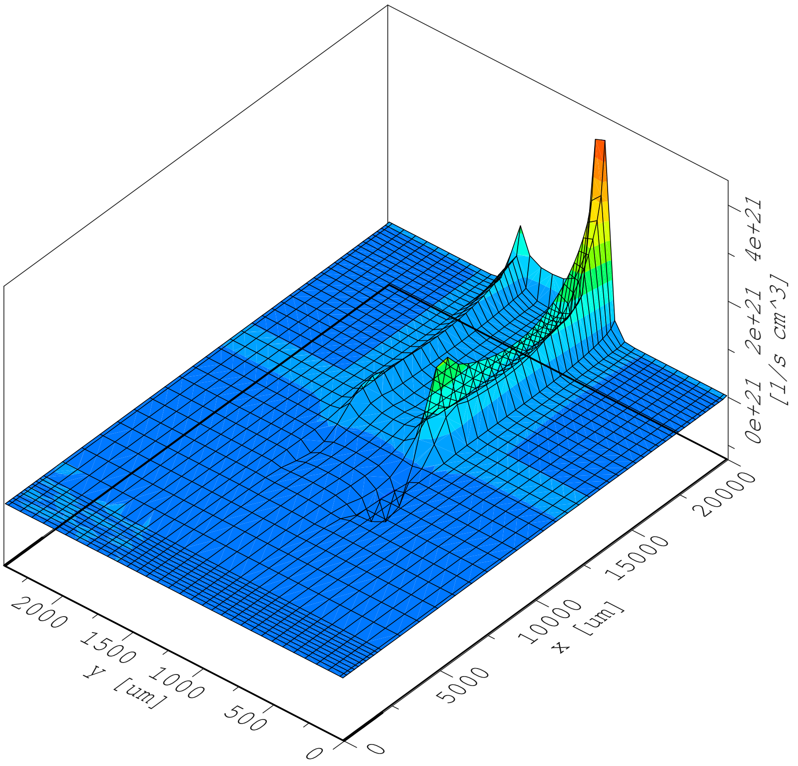

Figure 6.28: Local generation rate at short circuit conditions.

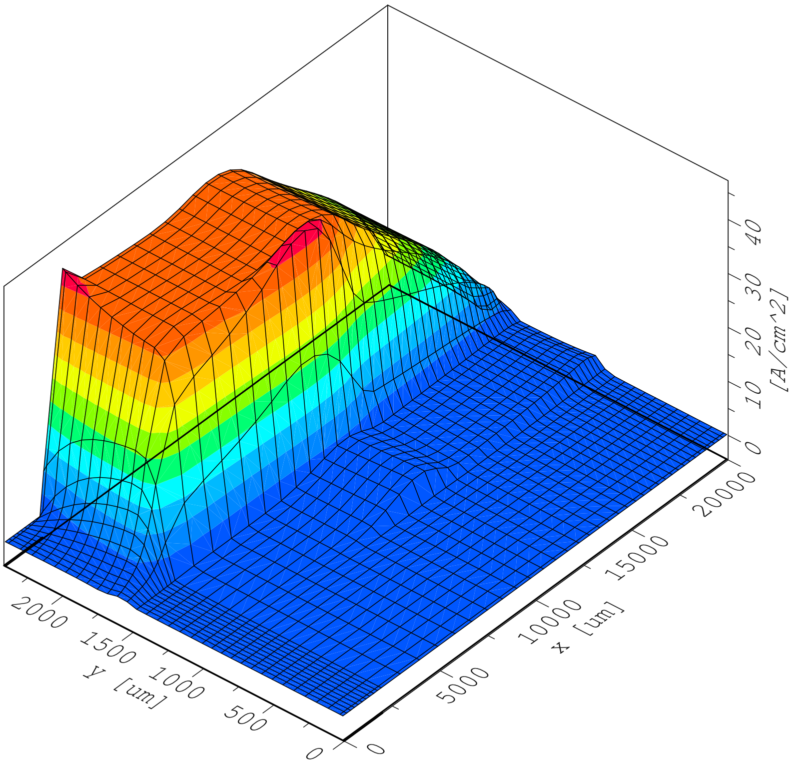

Figure 6.29: Electron current density at short circuit conditions.

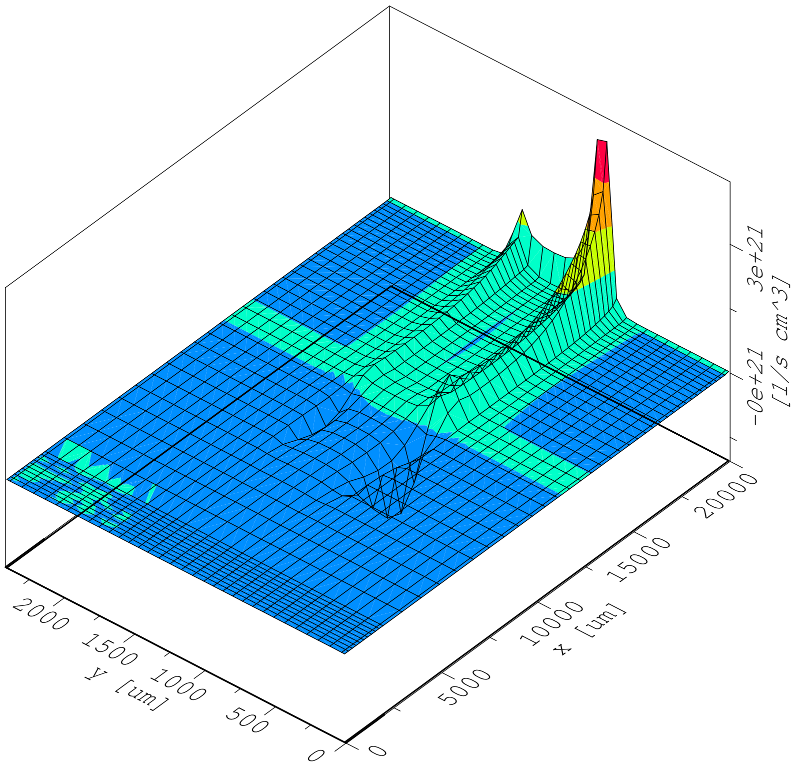

Figure 6.30: Local generation rate at matched load conditions.

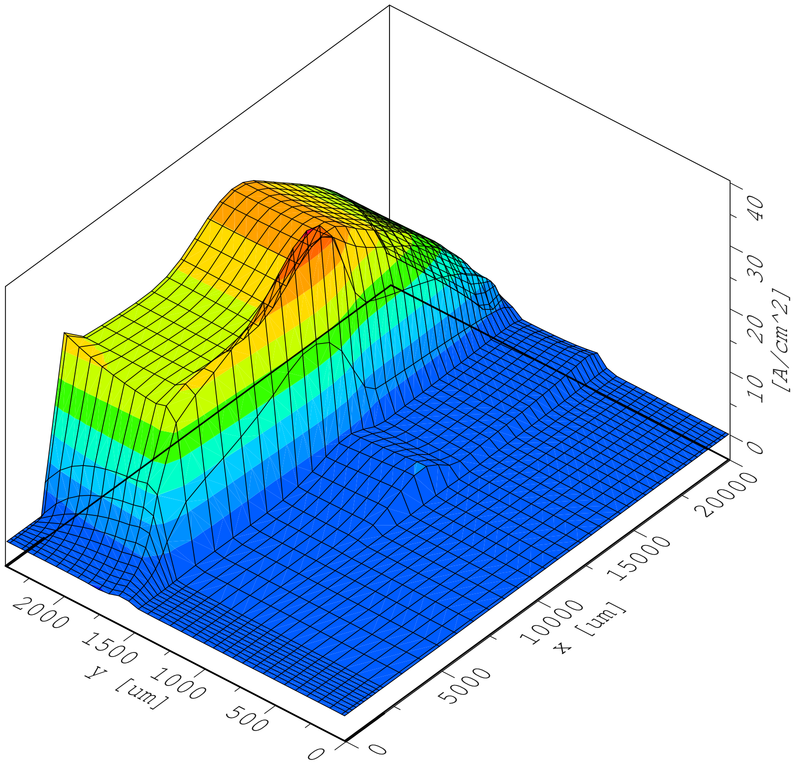

Figure 6.31: Electron current density at matched load conditions.

The generated carriers are accelerated and accumulate to a current starting from the hot thermal contact to the competition region of the device, where the temperature starts to be too low for further carrier generation. Contrary to the heated end, recombination takes place and the current density is reduced again until zero. The total generation of carriers is exactly compensated by recombination throughout the entire structure. The other extreme is represented by a short circuit of the electric contacts as demonstrated in Figures 6.28 and 6.29. Beyond the generation zone, almost the entire current density reaches the electric contacts while recombination is reduced to a minimum. This yields even higher generation rates and the device state adjusts to an accordingly high electric current density.

At matched load conditions, which is shown in Figures 6.30 and 6.31, generation and current density adjust to an equilibrium between the two cases presented above. The existence of recombination indicates that the device is not fully optimized at this stage.

6.5.1 Temperature Control by Graded Material Alloys

As pointed out in the preceding section, carrier generation plays a dominant role for the device characteristics of pn-junction thermoelectric generators. Since the carrier generation is strongly influenced by the lattice temperature, the zone of high generation rates is limited to the hottest parts of the device.

In order to increase the total generation rate, it is beneficial to maintain high temperatures in relatively large parts of the device. In devices consisting of one pure material, the temperature distribution along the pn-junction is concave due to the decrease of the thermal conductivity with increasing temperatures. This results in a steep temperature gradient at the heated end and thus in low areas of high temperature, there limiting carrier generation.

Engineering of the spatial distribution of thermal conductivity is a possibility to increase the area of high temperatures. The introduction of graded material alloys is one way to achieve exactly this. As pointed out in Fig. 4.3, the thermal conductivity drastically increases in SiGe alloys with increasing germanium content up to about 50 %. A material profile with higher germanium contents at the cooled side of the device yields locally lower thermal conductivities and thus shifts the temperature drop to the cooler end. The behavior can be compared to a potential divider in the electric analogon model.

Fig. 6.32 clarifies the situation on the example of a large area pn-junction device. The temperature distribution given in a) results from the assumed spatial distribution of germanium content displayed in b). The concave temperature curve corresponds to pure silicon, whereas an increasing germanium content shifts the temperature distribution more and more to a plateau with a steep gradient at the cooler end. The according spatial distribution of carrier generation rates is presented in c). An enlargement of the area where generation takes place can be identified at already relatively low germanium content. At higher germanium contents, the influence on the temperature profile saturates and the local generation rate is elevated according to the higher temperatures available.

However, besides the high total carrier generation rates, the carriers have to be efficiently transported to the contacts as well. Both doping and geometrical dimensions of the transport layers have to be designed accordingly to avoid recombination at the best. There, geometrically oversized transport layers also increase the heat flux while the electric properties are not further

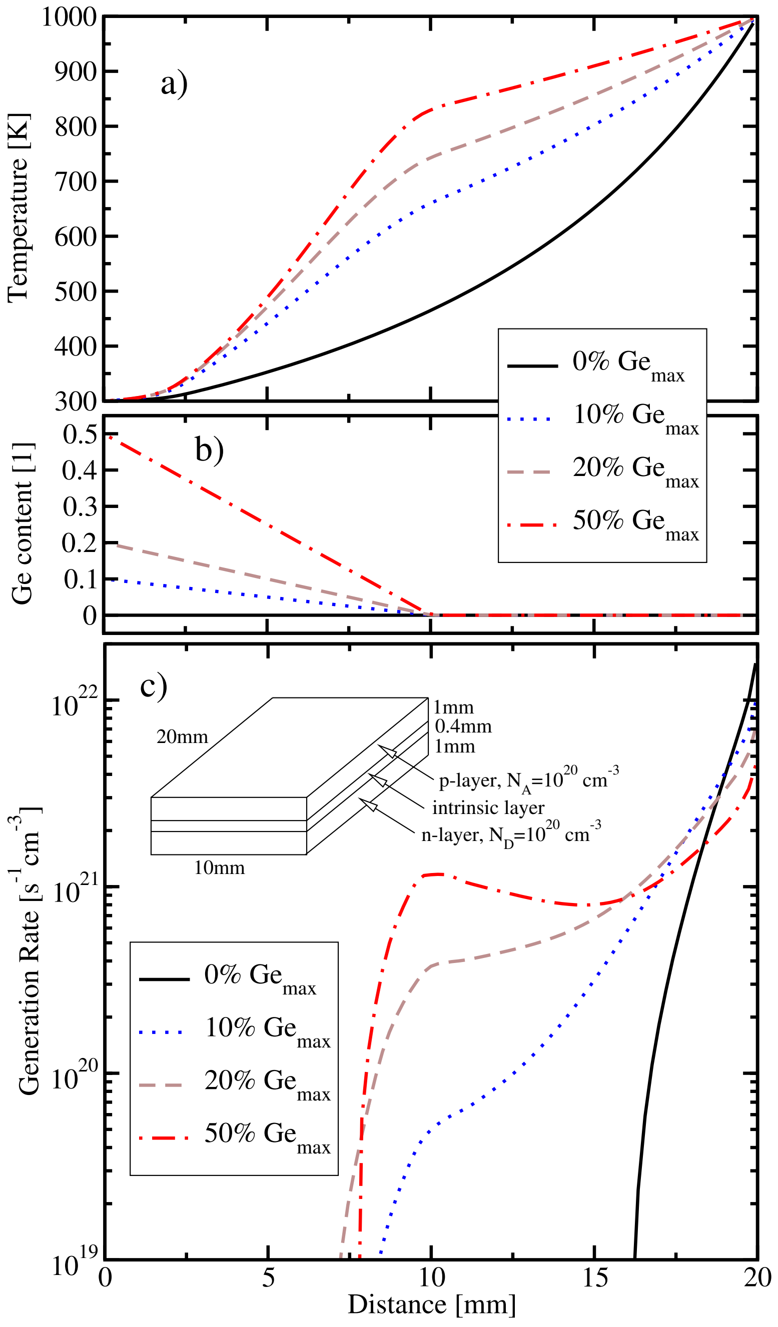

Figure 6.32: a) Temperature distribution along the pn-junction caused by the thermal conductivities of different Ge–profiles as shown in b). The generation rate shown in c) is exponentially dependent on the temperature, thus the material composition is used to increase the generation rate.

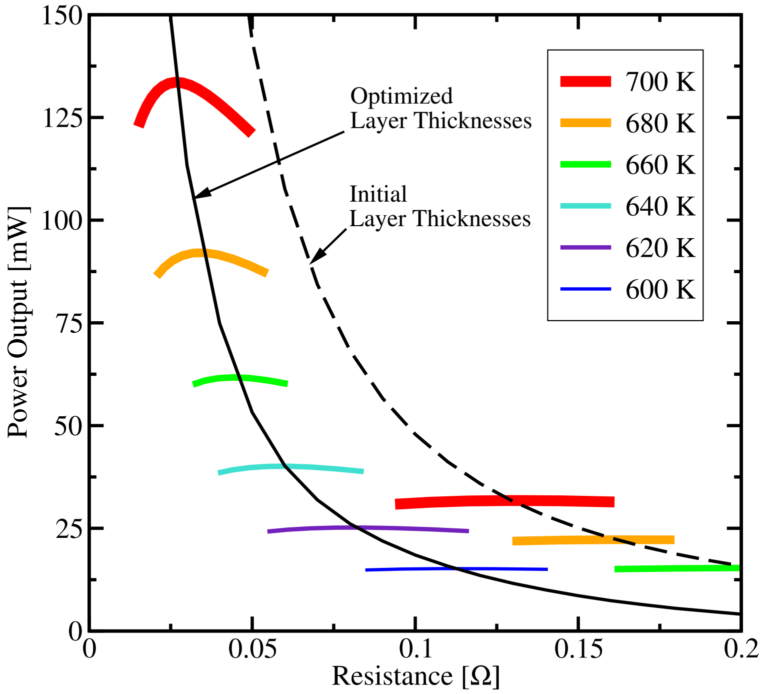

Figure 6.33: Power output for pn-junction thermoelectric generators vs. load resistance for several temperature differences and two layer thicknesses.

improved, which results in a decreasing efficiency. Careful analysis of the interrelation of several effects within the device is a basis for efficient device optimization.

The relation of transport layer thicknesses, available temperature difference, and power output is outlined in Fig. 6.33. The dashed line depicts the maximum power output curve for an initially considered device geometry, while the solid line identifies optimized relations with thicker transport layers. Due to the lower internal resistance, the optimum power output curve shifts to lower load resistances as well. Furthermore, the temperature scale along the maximum power output curve shifts to higher values, thus the same thermal environment yields a noticeably improved power output.

The power output dependence on both n- and p-layer thicknesses is illustrated in Fig. 6.34. For too thin layers, carrier transport is the limiting factor to power output due to increased carrier recombination within the relatively cold zones of the device. The optimum is indicated at an asymmetric device with an accordingly thicker p-layer because of the lower hole mobility.

6.5.2 Generation Enhancement by Additional Traps

Due to the temperature dependence of the generation rate, it is beneficial to maintain large areas of high temperature, as pointed out in the last section. However, carrier generation can be further improved by the introduction of traps in the forbidden energy gap.

According to the Shockley-Read-Hall formalism [289], thermal generation is affected by local temperature as well as the amount and energy level of present traps. For trap energy levels

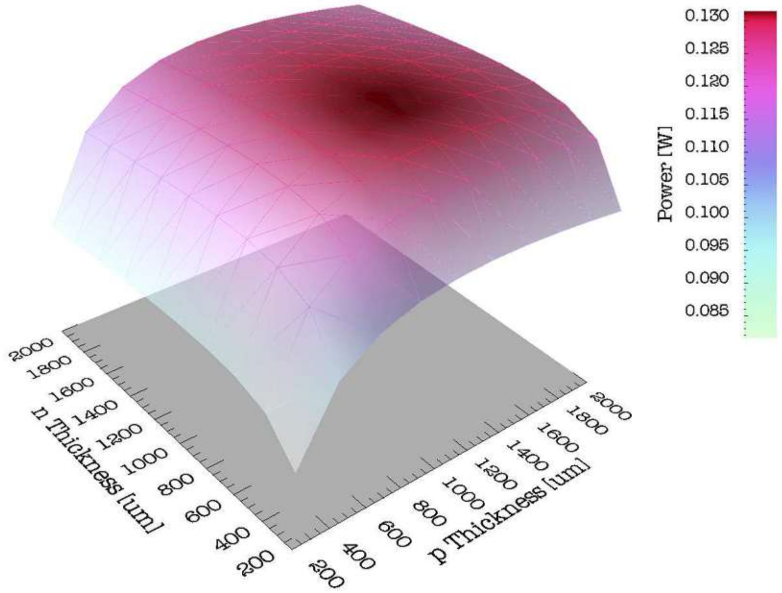

Figure 6.34: Influence of the layer thicknesses on the power output of a pn-junction thermoelectric generator.

at the mid band gap, the thermal generation reaches its maximum. For silicon, gold can be used as additional dopant in the generation region of the device to introduce deep levels close to mid band gap [300]. Since the impurity state can absorb differences in momentum between the carriers, this generation process is the dominant one in silicon and other indirect semiconductors. To some extent, the device performance of a pn-junction thermoelectric generator at a certain temperature can be shifted to lower temperatures by adaption of the additional trap density and distribution.

As an example, a thin film thermoelectric generator based on silicon is investigated. The device consists of a p-doped substrate with a dopant concentration of $10^{19}\,\mathrm{cm}^{-3}$ and an n-doped layer with a dopant concentration of $10^{20}\,\mathrm{cm}^{-3}$, resulting in a pn–junction, which is located at a depth of $2.5\,\mu\mathrm{m}$. In order to increase the power output, gold has been implanted as additional generation centers at the hotter end of the device. The device considered is 30 mm long and has a width of 20 mm.

Fig. 6.35 illustrates the power output of the device at different thermal conditions. The dashed line represents the variation of the maximum power output with temperature. For higher temperatures, carrier generation is more pronounced and thus the power output increases significantly, while at the same time, the inner resistance reduces. The temperature scale along the dashed line has been calibrated by the external thermal resistances as well as the exact trap density within the device. A maximum power output of $19\,\mu\mathrm{W}$ has been measured for a hot end temperature of 535 K, while a temperature of 596 K increases the output to a maximum of $115\,\mu\mathrm{W}$. The dotted line depicts the simulated power output of the similar structure without additional traps. For this device configuration, a maximum power output of $91\,\mu\mathrm{W}$ is predicted.

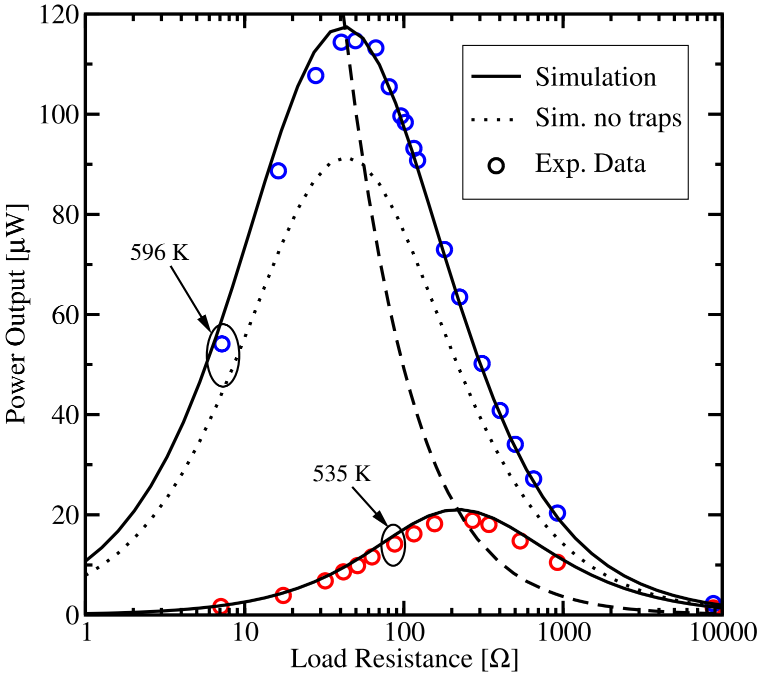

Figure 6.35: Power output of a thin film thermoelectric generator at different hot end temperatures.

6.5.3 Optimization of Device Characteristics

A combination of graded material alloys and suitable trap profiles is a promising approach for optimized devices. In the sequel, a simulation study on different configurations of Si/SiGe structures with spatial variable germanium content are investigated and compared to corresponding structures with constant germanium content throughout the entire device. Furthermore, the influence of additionally introduced traps is demonstrated. The structures under investigation differ in the material composition profile as illustrated in Fig. 6.36, Fig. 6.37, and Fig. 6.38, where the according temperature profiles for increasing germanium content can be found as well. Each of the three structures, which differ in different lengths of their SiGe parts, is analyzed for varied germanium contents and with or without additional traps. Increasing lengths of the SiGe part are indicated by increasing numbers in their designation. The considered trap profiles are adapted to the material profiles, thus a constant trap distribution of $10^{17}\,\mathrm{cm}^{-3}$ is considered within the silicon segment of the devices.

In the sequel, the influence of germanium content, material composition profile, and additional trap states on electric and thermal device behavior is investigated. Fig. 6.39 depicts the heat flux throughout the structures with respect to the germanium content within the SiGe part. The decreasing thermal conductivity with increasing germanium content of silicon–rich SiGe alloys, as illustrated in Fig. 4.3, leads to decreasing heat fluxes as well. The material composition's influence is diminished by longer silicon segments.

Fig. 6.40 illustrates the power output of several structures under investigation. For the homogeneous device, which is depicted by the dotted line, the power output decreases continuously with increasing germanium content due to the detrimental effect of increasing germanium content on the carrier mobility. For the staged structures, two effects can be noticed, whose dominance depend on the germanium content. First, the elevated germanium content results in a shift of the temperature distribution, as indicated in Fig. 6.36, Fig. 6.37, and Fig. 6.38. Thus, the conductive part of the pn-junction is enlarged, which results in higher power output. For further increased germanium content, the decreased mobility becomes the limiting factor, which results in declining power output. Structure 3 (Fig. 6.38) exhibits the highest sensitivity on the germanium content, which decreases with decreasing SiGe segment length.

Fig. 6.41 visualizes the conversion efficiency. The pure silicon structures show the lowest efficiency of about 0.4% because of the very high heat flux. For the staged samples, the efficiency is influenced by the temperature distribution, the conductivity relations, as well as the overall thermal conductivity. For all structures, additional traps increase the power output over the entire range. Since their effect on the thermal conductivity is negligible, the increased power directly leads to increased efficiencies as well. For Structure 3, the maximum efficiency is elevated from 2.0 % to 2.75 %.

In Fig. 6.39, Fig. 6.40, and Fig. 6.41, it can be seen that devices with different material partitioning feature comparable conversion efficiencies while the heat conductivity and power output vary about a factor of two. This behavior can be used to adjust the power and heat flux density to given boundary conditions while maintaining the same geometry of the generator or to reduce costs by changing the geometry but not the conversion efficiency. The large amount of design parameters allows a good adjustment of large area pn-junction thermoelectric generators to specific thermal and geometrical environments.

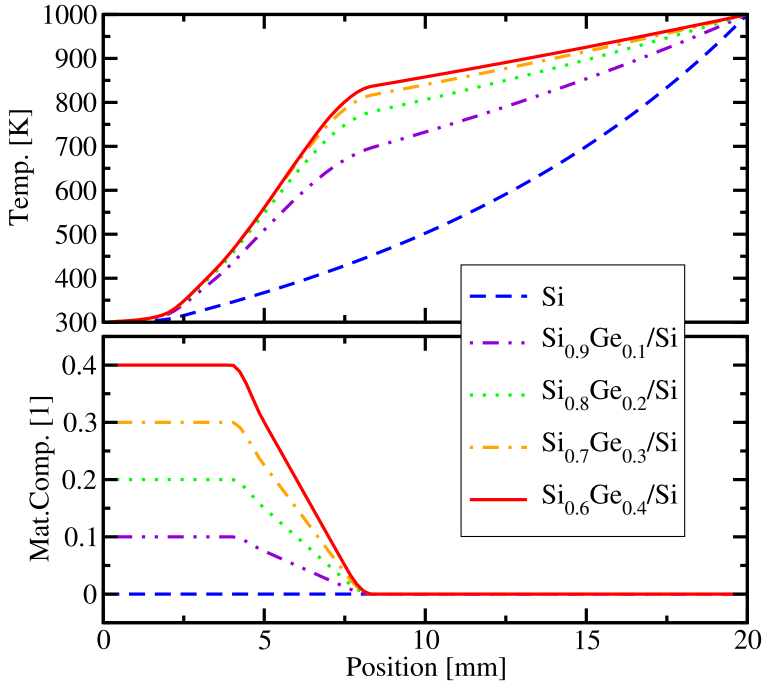

Figure 6.36: Spatial distribution of material composition and temperature for a Ge length of 6 mm (Structure 1).

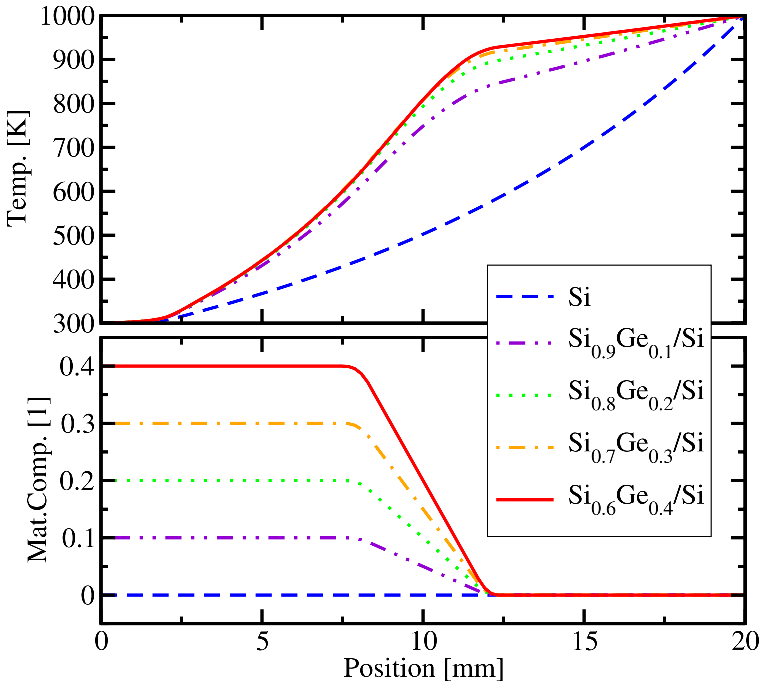

Figure 6.37: Spatial distribution of material composition and temperature for a Ge length of 10 mm (Structure 2).

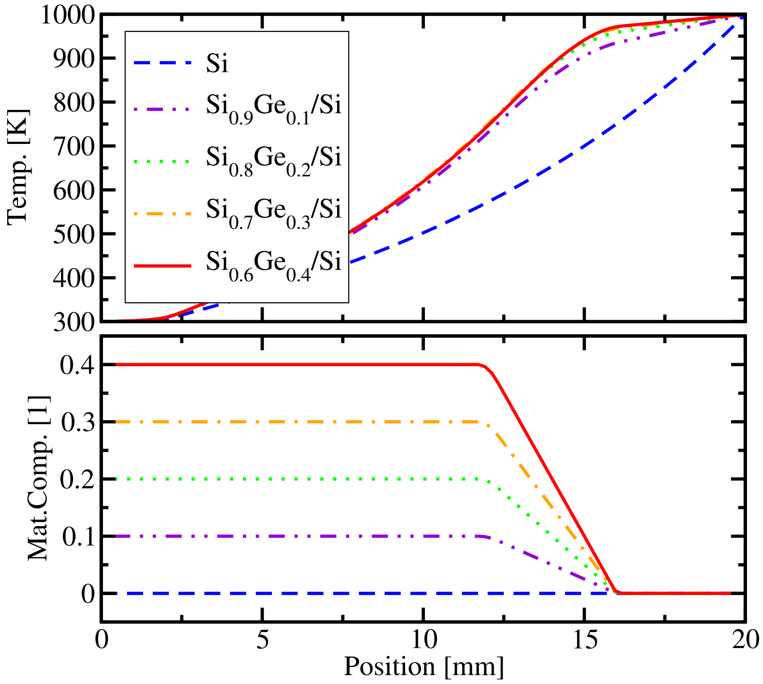

Figure 6.38: Spatial distribution of material composition and temperature for a Ge length of 13 mm (Structure 3).

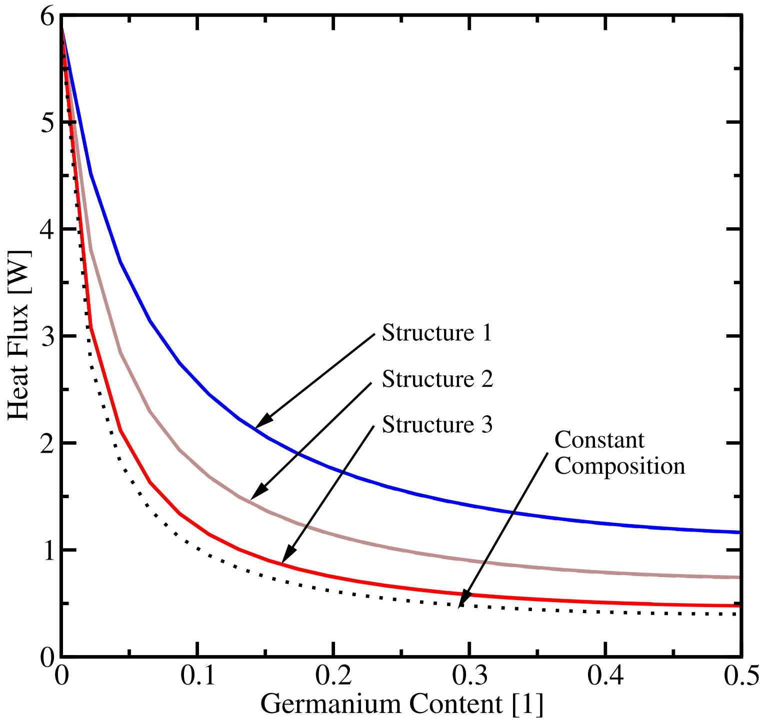

Figure 6.39: Heat flux vs. germanium content for different material composition profiles.

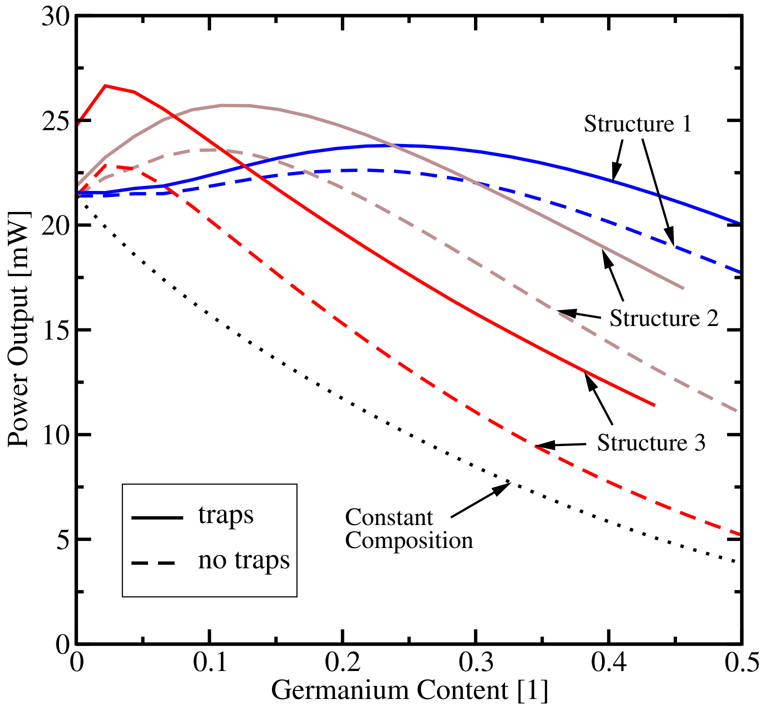

Figure 6.40: Electric power output vs. germanium content for different material composition profiles.

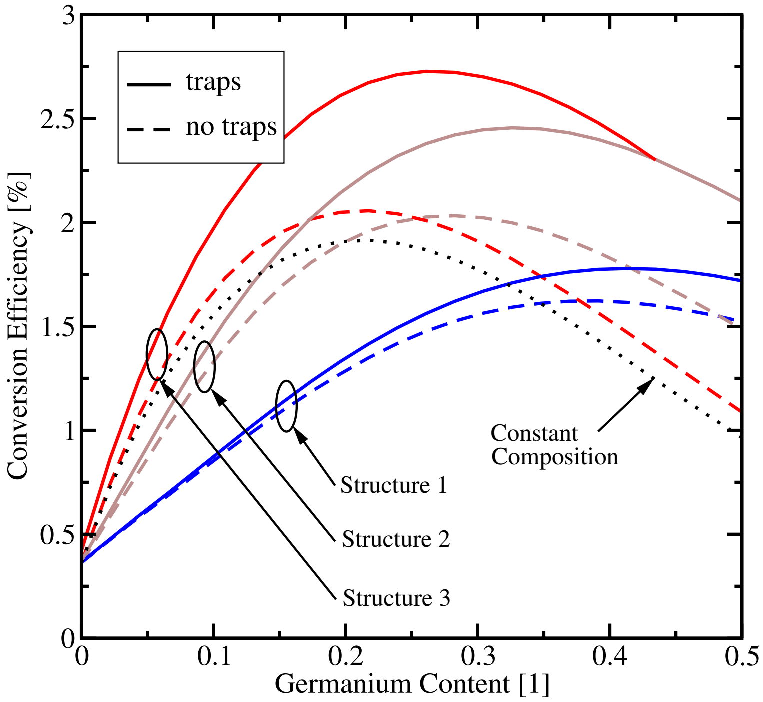

Figure 6.41: Conversion efficiency vs. germanium content for different material composition profiles.

'When you know a thing, to hold that you know it;
and when you do not know a thing, to allow that you
do not know it - this is knowledge.'
Confucius

Chapter 7

Summary and Conclusions

THE PERFORMANCE of thermoelectric materials and devices strongly depends on the thermal environment as well as given geometric constraints. In order to exhaust the available thermal energy at the best, thermoelectric generators have to be optimized for each given situation. Thereby, the design of custom devices for given environments depends on a physically based simulation framework. In mainstream microelectronics, Technology Computer Aided Design (TCAD) has been successfully applied for years to maintain the development of semiconductor devices. Besides its role in process development and device optimization, insights to the internal behavior of devices improve the physical understanding of internal quantities. This work implies a fruitful extension to the field of semiconductor device simulation of thermoelectric devices.

A transport model suitable for thermoelectric devices has been systematically derived by the method of moments, which is compatible to an approach based on phenomenological irreversible thermodynamics. Thereby, special attention has been paid to the *Seebeck* coefficient by a comparison of measurement data with the theoretical formulation.

In addition to the Silicon–Germanium material system which is used for high temperature thermoelectric applications, lead telluride plays an important role for the intermediate temperature range. The material database of MINIMOS-NT has been extended by all relevant models and parameters for lead telluride in order to enable predictive simulation of such devices.

The behavior of both classical thermoelectric devices and novel structures incorporating a large scale pn-junction has been investigated with MINIMOS-NT. Thereby the influence of geometry, material composition, and forced carrier generation on the device performance has been assessed. Non-ideal thermal environments have been discussed and considered using mixed-mode simulations. While the number of possible device variations of conventional thermoelectric devices is relatively small, the numerous design parameters of the novel structures allows good adaption to given environments.

Appendix A

Poisson Brackets Formulation

The Poisson bracket represents an important and convenient operator within *Hamilton*ian mechanics. It allows not only a compact treatment of the *Boltzmann* transport equation and its moments as carried in Chapter 3, but has some useful identities applied throughout the derivation of several transport models. Its basic definition for two scalars reads

$$\{a, b\} = \nabla_{\boldsymbol{r}} a \cdot \frac{1}{\hbar} \nabla_{\boldsymbol{k}} b - \frac{1}{\hbar} \nabla_{\boldsymbol{k}} a \cdot \nabla_{\boldsymbol{r}} b \,, \tag{A.1}$$

whereas the *Poisson* bracket for a vector valued quantity and a scalar has to be handled more carefully. This case can be extrapolated by having a closer look on its single components. Considering a vector $\boldsymbol{a}$ with its components a_x, a_y, and a_z, and using *Einstein*'s summation convention

$$\boldsymbol{a} = \sum_{m=\mathrm{x}}^{\mathrm{z}} a_m \mathbf{e}_m \qquad = a_m \,, \tag{A.2}$$

$$\nabla \cdot \boldsymbol{a} = \sum_{m=\mathrm{x}}^{\mathrm{z}} \partial_m a_m \qquad = \partial_m a_m \,, \tag{A.3}$$

$$\nabla \otimes \boldsymbol{a} = \sum_{m=\mathrm{x}}^{\mathrm{z}} \sum_{n=\mathrm{x}}^{\mathrm{z}} \partial_n b_m = \partial_n b_m \tag{A.4}$$

one can write

$$\begin{aligned} \{a_m, b\} &= \nabla_{\boldsymbol{r}} a_m \cdot \frac{1}{\hbar} \nabla_{\boldsymbol{k}} b - \frac{1}{\hbar} \nabla_{\boldsymbol{k}} a_m \cdot \nabla_{\boldsymbol{r}} b \\ &= \partial_m a_n \frac{1}{\hbar} \partial_n^{\boldsymbol{k}} b - \frac{1}{\hbar} \partial_n^{\boldsymbol{k}} a_m \partial_m b \end{aligned} \tag{A.5}$$

$$\{\boldsymbol{a}, b\} = \nabla_{\boldsymbol{r}} \otimes \boldsymbol{a} \cdot \frac{1}{\hbar} \nabla_{\boldsymbol{k}} b - \frac{1}{\hbar} \nabla_{\boldsymbol{k}} \otimes \boldsymbol{a} \cdot \nabla_{\boldsymbol{r}} b \,. \tag{A.6}$$

With these definitions, the subsequent identities can be carried out. As a consequence of its definition, the Poisson bracket is anti–commutative, meaning that

$$\{a, b\} = -\{b, a\} \,. \tag{A.7}$$

Moreover, the Poisson bracket of a variable with itself vanishes

$$\{a, a\} = 0\,, \tag{A.8}$$

which is important for the special case of $\{\mathcal{E}, \mathcal{E}\}$ in the following derivations. The *Poisson* bracket of every scalar or vector and a constant C vanishes

$$\{C, a\} = 0\,, \tag{A.9}$$

which is especially useful for $C = 1$ during the derivation of the balance equations. Furthermore, the Poisson bracket of a product can be expressed as

$$\{ab, c\} = a\{b, c\} + b\{a, c\} \tag{A.10}$$

which can be easily verified using the product rule. The Poisson bracket is bi-linear, thus two sums can be expanded like

$$\begin{aligned} \{a + b, c + d\} &= \{a, c + d\} + \{b, c + d\} \\ &= \{a, c\} + \{b, c\} + \{a, d\} + \{b, d\}\,. \end{aligned} \tag{A.11}$$

Appendix B

Useful Identities

Several identities from tensor and vector analysis used throughout the derivation of transport models in this work are listed below.

$$\boldsymbol{a}\cdot\nabla b = \nabla\cdot(b\boldsymbol{a}\otimes\boldsymbol{c}) - b\nabla\cdot(\boldsymbol{a}\otimes\boldsymbol{c}) \tag{B.1}$$

$$\boldsymbol{a}\cdot\nabla b = \nabla\cdot(\boldsymbol{a}b) + \boldsymbol{b}\cdot(\nabla\otimes\boldsymbol{a}) \tag{B.2}$$

$$\nabla\cdot(\boldsymbol{b}\otimes\boldsymbol{a}) = \boldsymbol{a}\,(\nabla\cdot\boldsymbol{b}) + \boldsymbol{b}\,(\nabla\otimes\boldsymbol{a}) \tag{B.3}$$

$$\frac{1}{\hbar}\nabla_{\boldsymbol{k}}\otimes\boldsymbol{p}h(p) = h(p)\hat{\mathrm{I}} + (\boldsymbol{p}\otimes\boldsymbol{p})\,\frac{1}{p}\partial_p h \tag{B.4}$$

$$\boldsymbol{a}\,(\boldsymbol{b}\cdot\boldsymbol{c}) = \boldsymbol{c}\cdot(\boldsymbol{b}\otimes\boldsymbol{a}) \tag{B.5}$$

$$\frac{1}{\hbar}\nabla_{\boldsymbol{k}}\otimes\boldsymbol{u}h(p) = h(p)\frac{1}{\hbar}\nabla_{\boldsymbol{k}}\otimes\boldsymbol{u} + \boldsymbol{u}\otimes\frac{1}{\hbar}\nabla_{\boldsymbol{k}}h(p) \tag{B.6}$$

$$\boldsymbol{a}\nabla_{\boldsymbol{r}}\cdot\boldsymbol{b}(r) = \nabla_{\boldsymbol{r}}\cdot(\boldsymbol{b}(r)\otimes\boldsymbol{a})\,,\,\nabla_{\boldsymbol{r}}\cdot\boldsymbol{a}\equiv 0 \tag{B.7}$$

Bibliography

[1] T. Seebeck, “Magnetische Polarisation der Metalle und Erze durch Temperatur-Differenz,” *Abhandlungen der Deutschen Akademie der Wissenschaften zu Berlin*, pp. 265–373, 1823.

[2] J. Peltier, “Nouvelles Experiences sur la Caloriecete des Courans Electrique,” *Ann. Chim.*, vol. LVI, pp. 371–387, 1834.

[3] D. Rowe, ed., *CRC Handbook of Thermoelectrics*. CRC Press, Inc., 1994.

[4] W. Thomson, “On a Mechanical Theory of Thermoelectric Currents,” *Proceedings of the Royal Society of Edinburgh*, pp. 91–98, 1851.

[5] E. Altenkirch, “Über den Nutzeffekt der Thermosäule,” *Physikalische Zeitschrift*, vol. 10, pp. 560–580, 1909.

[6] E. Altenkirch, “Elektrothermische Kälteerzeugung und reversible elektrische Heizung,” *Physikalische Zeitschrift*, vol. 12, pp. 920–924, 1911.

[7] A. Ioffe, *Semiconductor Thermoelements and Thermoelectric Cooling*. Infosearch, London, 1957.

[8] A. Ioffe, “The Revival of Thermoelectricity,” *Scientific American*, vol. 199, pp. 31–37, 1958.

[9] H. Callen, *Thermodynamics*. John Wiley & Sons, 1966.

[10] D. Pollock, *CRC Handbook of Thermoelectrics*, ch. Thermoelectric Phenomena, pp. 7–17. CRC Press, Inc., 1994.

[11] C. Wood, “Materials for Thermoelectric Energy Conversion,” *Rep. Prog. Phys.*, vol. 51, pp. 459–539, 1988.

[12] L. Onsager, “Reciprocal Relations in Irreversible Processes I,” *Physical Review*, vol. 37, pp. 405–426, 1931.

[13] J. Leigh, *Temperature Measurement and Control*. Institution of Electrical Engineers, 1988.

[14] T. McGee, *Principles and Methods of Temperature Measurement.* Wiley Interscience, 1988.

[15] R. Bentley, *Handbook of Temperature Measurement.* Springer, 1998.

[16] P. Childs, J. Greenwood, and C. Long, "Review of Temperature Measurement," *Review of Scientific Instruments*, vol. 71, no. 8, pp. 2959–2978, 2000.

[17] G. Min and D. Rowe, "Recent Concepts in Thermoelectric Power Generation," in *Thermoelectrics, 2002., Twentyfirst International Conference on*, 2002.

[18] D. Rowe and G. Min, "Design Theory of Thermoelectric Modules for Electrical Powergeneration," *IEE Proc.-Sci. Meas. Technol.*, vol. 143, no. 6, pp. 351–356, 1996.

[19] G. Slack and M. Hussain, "The Maximum Possible Conversion Efficiency of Silicon-Germanium Thermoelectric Generators," *J.Appl.Phys.*, vol. 70, no. 5, pp. 2694–2718, 1991.

[20] G. Snyder and T. Ursell, "Thermoelectric Efficiency and Compatibility," *Physical Review Letters*, vol. 91, no. 14, pp. 148301–1–14301–4, 2003.

[21] D. Rowe and V. Shukla, "The Effect of Phonon-Grain Boundary Scattering on the Lattice Thermal Conductivity and Thermoelectric Conversion Efficiency of Heavily Doped Fine-Grained, Hot-Pressed Silicon Germanium Alloy," *J.Appl.Phys.*, vol. 52, no. 12, pp. 7421–7426, 1981.

[22] T. Caillat, J.-P. Fleurial, G. Snyder, A. Zoltan, D. Zoltan, and A. Borshchevsky, "Development of a High Efficiency Thermoelectric Unicouple for Powergeneration Applications," in *Thermoelectrics, 1999. Eighteenth International Conference on*, 1999.

[23] J.-P. Fleurial, A. Borshchevsky, T. Caillat, and R. Ewell, "New Materials and Devices for Thermoelectric Applications," in *Energy Conversion Engineering Conference, 1997. IECEC-97. Proceedings of the 32nd*, 1997.

[24] W. Hall, *CRC Handbook of Thermoelectrics*, ch. Terrestrial Applications of Thermoelectric Generators, pp. 503–513. CRC Press, Inc., 1994.

[25] S. Riffat and X. Ma, "Thermoelectrics: A Review of Present and Potential Applications," *Applied Thermal Engineering*, vol. 23, no. 8, pp. 913–935, 2003.

[26] G. Bennett, *CRC Handbook of Thermoelectrics*, ch. Space Applications, pp. 515–537. CRC Press, Inc., 1994.

[27] J. Bass and R. Farley, "Examples of Power from Waste Heat for Gas Fields," in *Thermoelectrics, 1997. Proceedings ICT '97. XVI International Conference on*, pp. 547–550, 1997.

[28] O. Saka, N. Sato, and S. Uchida, "Development of Unmanned Magnetometer Stations for Use in Antarctica," *Antarctic Science*, vol. 2, no. 4, pp. 355–361, 1990.

[29] A. Pustovalov, "Nuclear Thermoelectric Power Units in Russia, USA and European Space Agency Research Programs," in *Thermoelectrics, 1997. Proceedings ICT '97. XVI International Conference on*, pp. 559–562, 1997.

[30] F. de Winter, G. Stapfer, and E. Medina, "The Design of a Nuclear Power Supply with a 50 Year Life Expectancy: The JPL Voyager's SiGe MHW RTG," *IEEE Aerospace and Electronic Systems Magazine*, vol. 15, no. 4, pp. 5–12, 2000.

[31] B. LaSage, G. Meszaros, and T. Nystrom, "On the Suitability of Low Cost PbTe Devices for High Grade Waste Heat Power Generation Applications," in *Thermoelectrics, 1998. Proceedings ICT 98. XVII International Conference on*, pp. 426–428, May 24-28, 1998.

[32] K. Matsubara, "Development of a High Efficient Thermoelectric Stack for a Waste Exhaust Heat Recovery of Vehicles," in *Thermoelectrics, 2002. Proceedings ICT '02. Twenty-First International Conference on*, pp. 418–423, 25-29 Aug. 2002.

[33] J. Haidar and J. Ghojel, "Waste Heat Recovery from the Exhaust of Low-Power Diesel Engine using Thermoelectric Generators," in *Thermoelectrics, 2001. Proceedings ICT 2001. XX International Conference on*, 2001.

[34] J. Yang, "Potential Applications of Thermoelectric Waste Heat Recovery in the Automotive Industry," in *Thermoelectrics, 2005. ICT 2005. 24th International Conference on*, 2005.

[35] Z. Zhang, J. Wu, and G. Si, "Novel High-Intensity Thermoelectric Generator and its Application on Hybrid Electric Vehicle," *Key Engineering Materials*, vol. 336, pp. 892–895, 2007.

[36] K. Uemura, *CRC Handbook of Thermoelectrics*, ch. Commercial Peltier Modules, pp. 621–631. CRC Press, Inc., 1994.

[37] J. Vandersande and J.-P. Fleurial, "Thermal Management of Power Electronics using Thermoelectric Coolers," in *Thermoelectrics, 1996., Fifteenth International Conference on*, 1996.

[38] S. Garimella, Y. Joshi, A. Bar-Cohen, R. Mahajan, K. Toh, V. Carey, M. Baelmans, J. Lohan, B. Sammakia, and F. Andros, "Thermal Challenges in Next Generation Electronic Systems - Summary of Panel Presentations and Discussions," *IEEE Transactions on Components and Packaging Technologies*, vol. 25, no. 4, pp. 569–575, 2002.

[39] K. Yazawa, G. Solbrekken, and A. Bar-Cohen, "Thermoelectric-Powered Convective Cooling of Microprocessors," *IEEE Transactions on Advanced Packaging*, vol. 28, no. 2, pp. 231–239, 2005.

[40] G. Solbrekken, K. Yazawa, and A. Bar-Cohen, "Thermal Management of Portable Electronic Equipment using Thermoelectric Energy Conversion," in *Thermal and Thermomechanical Phenomena in Electronic Systems, 2004. ITHERM '04. The Ninth Intersociety Conference on*, 2004.

[41] B. Sorenson, *Renewable Energy: It's Physics, Engineering, Use, Environmental Impacts, Economy and Planning Aspects*. Elsevier, 2004.

[42] J. Paradiso and T. Starner, "Energy Scavenging for Mobile and Wireless Electronics," *Pervasive Computing*, vol. 4, no. 1, pp. 18–27, 2005.

[43] S. Roundy, D. Steingart, L. Frechette, P. Wright, and J. Rabaey, “Power Sources for Wireless Sensor Networks,” *Lecture Notes in Computer Science*, vol. 2920/2004, pp. 1–17, 2004.

[44] S. Roundy, P. Wright, and J. Rabaey, “A Study of Low Level Vibrations as a Power Source for Wireless Sensor Nodes,” *Computer Communications*, vol. 26, no. 11, pp. 1131–1144, 2003.

[45] J. Hsu, S. Zahedi, A. Kansal, M. Srivastava, and V. Raghunathan, “Adaptive Duty Cycling for Energy Harvesting Systems,” in *Proceedings of the 2006 International Symposium on Low Power Electronics and Design*, 2006.

[46] F. Axisa, A. Dittmar, and G. Delhomme, “Smart Clothes for the Monitoring in Real Time and Conditions of Physiological, Emotional and Sensorial Reactions of Human,” in *Engineering in Medicine and Biology Society, 2003. Proceedings of the 25th Annual International Conference of the IEEE*, 2003.

[47] M. Kishi, H. Nemoto, T. Hamao, M. Yamamoto, S. Sudou, M. Mandai, and S. Yamamoto, “Micro Thermoelectric Modules and their Application to Wristwatches as an Energy Source,” in *Thermoelectrics, 1999. Eighteenth International Conference on*, 1999.

[48] N. Shenck and J. Paradiso, “Energy Scavenging with Shoe-Mounted Piezoelectrics,” *IEEE Micro*, vol. 21, no. 3, pp. 30–42, 2001.

[49] T. Starner, “Human-Powered Wearable Computing,” *IBM Systems Journal*, vol. 35, no. 3–4, pp. 618–629, 1996.

[50] M. Stordeur and I. Stark, “Low Power Thermoelectric Generator – Self-Sufficient Energy Supply for Micro Systems,” in *Thermoelectrics, 1997. Proceedings ICT ’97. XVI International Conference on*, pp. 575–577, 1997.

[51] H. Böttner, “Thermoelectric Micro Devices: Current State, Recent Developments and Future Aspects for Technological Progress and Applications,” in *Thermoelectrics, 2002. Proceedings ICT ’02. Twenty-First International Conference on*, 2002.

[52] E. Lawrence and G. Snyder, “A Study of Heat Sink Performance in Air and Soil for Use in a Thermoelectric Energy Harvesting Device,” in *Thermoelectrics, 2002. Proceedings ICT ’02. Twenty-First International Conference on*, pp. 446–449, 2002.

[53] J. Stevens, “Optimal Placement Depth for Air–Ground Heat Transfer Systems,” *Appl. Therm. Engin.*, vol. 24, no. 2–3, pp. 149–157, 2004.

[54] G. Wachutka, “Rigorous Thermodynamic Treatment of Heat Generation and Conduction in Semiconductor Device Modeling,” *Computer-Aided Design of Integrated Circuits and Systems, IEEE Transactions on*, vol. 9, pp. 1141–1149, Nov. 1990.

[55] G. Moore, “Cramming More Components onto Integrated Circuits,” *Electronics*, vol. 38, no. 8, pp. 114–117, 1965.

[56] M. Cohen and T. Bergstresser, “Band Structures and Pseudopotential Form Factors for Fourteen Semiconductors of the Diamond and Zinc-Blende Structures,” *Physical Review*, vol. 141, no. 2, pp. 789–796, 1966.

[57] M. Cohen and V. Heine, "The Fitting of Pseudopotentials to Experimental Data and Their Subsequent Application," *Solid State Phys.*, vol. 24, pp. 37–248, 1970.

[58] R. Martin, *Electronic Structure: Basic Theory and Practical Methods*. Cambridge University Press, 2004.

[59] E. Schrödinger, "Quantisierung als Eigenwertproblem," *Annalen der Physik*, vol. 79, pp. 361–376, 1926.

[60] S. Datta, "Nanoscale Device Modeling: The Green's Function Method," *Superlattices and Microstructures*, vol. 28, no. 4, pp. 253–259, 2000.

[61] A. Pacelli, "Self-Consistent Solution of the Schrödinger Equation in Semiconductor Devices by Implicit Iteration," *IEEE Trans.Electron Devices*, vol. 44, no. 7, pp. 1169–1171, 1997.

[62] H. Kosina and M. Nedjalkov, *Handbook of Theoretical and Computational Nanotechnology*, vol. 10, ch. Wigner Function Based Device Modeling, pp. 731–763. Los Angeles: American Scientific Publishers, 2006.

[63] D. Querlioz, J. Saint-Martin, and V. N. Do, "A Study of Quantum Transport in End-of-Roadmap DG-MOSFETs Using a Fully Self-Consistent Wigner Monte Carlo Approach," vol. 5, no. 6, pp. 737–744, 2006.

[64] A. Abramo, L. Baudry, R. Brunetti, R. Castagne, M. Charef, F. Dessenne, P. Dollfus, R. Dutton, W. L. Engl, R. Fauquembergue, C. Fiegna, M. V. Fischetti, S. Galdin, N. Goldsman, M. Hackel, C. Hamaguchi, K. Hess, K. Hennacy, P. Hesto, J. M. Higman, T. Iizuka, C. Jungemann, Y. Kamakura, H. Kosina, T. Kunikiyo, S. E. Laux, H. Lin, C. Maziar, H. Mizuno, H. J. Peifer, S. Ramaswamy, N. Sano, P. G. Scrobohaci, S. Selberherr, M. Takenaka, T.-W. Tang, K. Taniguchi, J. L. Thobel, R. Thoma, K. Tomizawa, M. Tomizawa, T. Vogelsang, S.-L. Wang, X. Wang, C.-S. Yao, P. D. Yoder, and A. Yoshii, "A Comparison of Numerical Solutions of the Boltzmann Transport Equation for High-Energy Electron Transport Silicon," *IEEE Trans.Electron Devices*, vol. 41, no. 9, pp. 1646–1654, 1994.

[65] C. Jacoboni and L. Reggiani, "The Monte Carlo Method for the Solution of Charge Transport in Semiconductors with Applications to Covalent Materials," *Rev. Modern Physics*, vol. 55, no. 3, pp. 645–705, 1983.

[66] M. Abramowitz and I. Stegun, *Handbook of Mathematical Functions*. Dover, 1972.

[67] C. Jungemann, A. Pham, B. Meinerzhagen, C. Ringhofer, and M. Bollhöfer, "Stable Discretization of the Boltzmann Equation Based on Spherical Harmonics, Box Integration, and a Maximum Entropy Dissipation Principle," *J.Appl.Phys.*, vol. 100, pp. 24502–1–24502–13, 2006.

[68] R. Stratton, "Diffusion of Hot and Cold Electrons in Semiconductor Barriers," *Physical Review*, vol. 126, no. 6, pp. 2002–2014, 1962.

[69] K. Blotekjaer, "Transport Equations for Electrons in Two-Valley Semiconductors," *IEEE Trans.Electron Devices*, vol. ED-17, pp. 38–47, Jan. 1970.

[70] C. Jungemann and B. Meinerzhagen, *Hierarchical Device Simulation. The Monte Carlo Perspective.* Springer, 2003.

[71] S. E. Laux, M. V. Fischetti, and D. J. Frank, "Monte Carlo Analysis of Semiconductor Devices: The DAMOCLES Program," *IBM J.Res.Dev.*, vol. 34, no. 4, pp. 466–494, 1990.

[72] A. Prechtl, *Vorlesungen über Theoretische Elektrotechnik, Zweiter Teil: Elektrodynamik.* Institut für Grundlagen und Theorie der Elektrotechnik, TU Wien, 1998.

[73] M. Lundstrom, *Fundamentals of Carrier Transport.* Cambridge University Press, 2000.

[74] J. Singh, *Physics of Semiconductors and their Heterostructures.* McGraw-Hill, 1993.

[75] W. Ludwig, *Festkörperphysik.* Akademische Verlagsgesellschaft Wiesbaden, 1978.

[76] T. Grasser, "Non-Parabolic Macroscopic Transport Models for Semiconductor Device Simulation," *Physica A*, vol. 349, no. 1/2, pp. 221–258, 2005.

[77] E. Kane, "Band structure of Indium Antimonide," *J. Phys. Chem. Solids*, vol. 1, no. 4, pp. 249–261, 1957.

[78] T. Grasser, R. Kosik, C. Jungemann, H. Kosina, and S. Selberherr, "Nonparabolic Macroscopic Transport Models for Device Simulation Based on Bulk Monte Carlo Data," *J.Appl.Phys.*, vol. 97, no. 9, pp. 093710–1 – 093710–12, 2005.

[79] C. Jungemann and B. Meinerzhagen, *Hierarchical Device Simulation.* Springer, 2003.

[80] B. Neinhüs, *Hierarchische Bauelementsimulationen von Si/SiGe Hochfrequenztransistoren.* PhD thesis, Universität Bremen, 2002.

[81] T. Grasser, "Closure Relations for Macroscopic Transport Models in Semiconductor Device Simulation," in *Recent Research Developments in Applied Physics Vol. 7 - 2004 Part II*, pp. 423–446, S.G. Pandalai; Transworld Research Network, 2004.

[82] R. Kosik, T. Grasser, R. Entner, and K. Dragosits, "On the Highest Order Moment Closure Problem," in *Proceedings IEEE International Spring Seminar on Electronics Technology 27th ISSE 2004*, pp. 118–120, IEEE, 2004.

[83] R. Kosik, *Numerical Challanges on the Road to NanoTCAD.* Dissertation, TU Wien, 2004.

[84] R. Thoma, A. Emunds, B. Meinerzhagen, H.-J. Peifer, and W. Engl, "Hydrodynamic Equations for Semiconductors with Nonparabolic Band Structure," *Electron Devices, IEEE Transactions on*, vol. 38, pp. 1343–1353, June 1991.

[85] T. Grasser, H. Kosina, and S. Selberherr, "Investigation of Spurious Velocity Overshoot Using Monte Carlo Data," *Appl.Phys.Lett.*, vol. 79, no. 12, pp. 1900–1902, 2001.

[86] T. Grasser, T. Tang, H. Kosina, and S. Selberherr, "A Review of Hydrodynamic and Energy-Transport Models for Semiconductor Device Simulation," *Proceedings of the IEEE*, vol. 91, pp. 251–274, Feb 2003.

[87] T. Grasser, H. Kosina, M. Gritsch, and S. Selberherr, "Using Six Moments of Boltzmann's Transport Equation for Device Simulation," *J.Appl.Phys.*, vol. 90, no. 5, pp. 2389–2396, 2001.

[88] K. Blotekjaer, "Transport Equations for Electrons in Two-Valley Semiconductors," *IEEE Trans.Electron Devices*, vol. ED-17, pp. 38–47, Jan. 1970.

[89] K. Seeger, *Semiconductor Physics*. Springer Wien - New York, 1973.

[90] W. Hänsch, *The Drift Diffusion Equation and its Application in MOSFET Modeling*. Wien, New York: Springer, 1991.

[91] T. Grasser, H. Kosina, and S. Selberherr, "On the Validity of the Relaxation Time Approximation for Macroscopic Transport Models," in *Simulation of Semiconductor Processes and Devices 2004*, pp. 109–112, Springer, 2004.

[92] T.-W. Tang and H. Gan, "Two Formulations of Semiconductor Transport Equations Based on Spherical Harmonic Expansion of the Boltzmann Transport Equation," *IEEE Trans.Electron Devices*, vol. 47, pp. 1726–1732, 2000.

[93] H. Gan and T.-W. Tang, "A New Method for Extracting Carrier Mobility from Monte Carlo Device Simulation," *IEEE Trans.Electron Devices*, vol. 48, pp. 399–401, 2001.

[94] H. Callen, "The Application of Onsager's Reciprocal Relations to Thermoelectric, Thermomagnetic, and Galvanomagnetic Effects," *Physical Review*, vol. 73, no. 11, pp. 1349–1358, 1948.

[95] P. Maycock, "Thermal Conductivity of Silicon, Germanium, III-V Compounds and III-V Alloys," *Solid-State Electron.*, vol. 10, pp. 161–168, 1967.

[96] G. Wachutka, "Unified Framework for Thermal, Electrical, Magnetic, And Optical Semiconductor Device Modeling," *COMPEL*, vol. 10, no. 4, pp. 311–321, 1989.

[97] T. Geballe and G. Hull, "Seebeck Effect in Silicon," *Physical Review*, vol. 98, no. 4, pp. 940–947, 1955.

[98] T. Geballe and G. Hull, "Seebeck Effect in Germanium," *Physical Review*, vol. 94, no. 5, pp. 1134–1140, 1954.

[99] A. Miele, R. Fletcher, E. Zaremba, Y. Feng, C. Foxon, and J. Harris, "Phonon-Drag Thermopower and Weak Localization," *Physical Review B*, vol. 58, no. 19, pp. 13181–13190, 1998.

[100] I. Weinberg, "Phonon-Drag Thermopower in Cu-Al and Cu-Si Alloys," *Physical Review*, vol. 139, no. 3A, pp. 838–843, 1965.

[101] A. van Herwaarden, "The Seebeck Effect in Silicon ICs," *Sensors and Actuators*, vol. 6, pp. 245–254, 1984.

[102] A. van Herwaarden and P. Sarro, "Thermal Sensors Based on the Seebeck Effect," *Sensors and Actuators*, vol. 10, pp. 321–346, 1986.

[103] A. van Herwaarden, D. van Duyn, B. van Oudheusden, and P. Sarro, "Integrated Thermopile Sensors," *Sensors and Actuators*, vol. A21, pp. 621–630, 1989.

[104] M. Wu, N. Horing, and H. Cui, "Phonon-Drag Effects on Thermoelectric Power," *Physical Review B*, vol. 54, no. 8, pp. 5438–5443, 1996.

[105] K. Kells, *General Electrothermal Semiconductor Device Simulation.* Hartung-Gorre, Konstanz, 1994.

[106] W. Fulkerson, J. Moore, R. Williams, R. Graves, and D. McElroy, "Thermal Conductivity, Electrical Resistivity, and Seebeck Coefficient of Silicon from 100 to 1300 K," *Physical Review*, vol. 167, no. 3, pp. 765–782, 1968.

[107] G. Nolas, J. Sharp, and J. Goldsmid, *Thermoelectrics: Basic Principles and New Materials Developments.* Springer, 2001.

[108] E. Skrabek and D. Trimmer, *CRC Handbook of Thermoelectrics*, ch. Properties of the General TAGS System, pp. 267–285. CRC Press, Inc., 1994.

[109] A. Bentien, M. Christensen, J. Bryan, A. Sanchez, S. Paschen, F. Steglich, G. Stucky, and B. Iversen, "Thermal Conductivity of Thermoelectric Clathrates," *Physical Review B*, vol. 69, pp. 45207–1–45107–5, 2004.

[110] G. Nolas, J. Cohn, G. Slack, and S. Schujman, "Semiconducting Ge Clathrates: Promising Candidates for Thermoelectric Applications," *Appl.Phys.Lett.*, vol. 73, no. 2, pp. 178–180, 1998.

[111] A. Bentien, S. Johnsen, G. Madsen, B. Iversen, and F. Steglich, "Colossal Seebeck Coefficient in Strongly Correlated Semiconductor $FeSb_2$," *Europhys. Lett.*, vol. 80, pp. 17008–1–17008–5, 2007.

[112] G. Chen, T. Zeng, T. Borca-Tasciuc, and D. Song, "Phonon Engineering in Nanostructures for Solid-State Energy Conversion," *Materials Science and Engineering*, vol. A292, pp. 155–161, 2000.

[113] G. Chen, A. Narayanaswamy, and C. Dames, "Engineering Nanoscale Phonon and Photon Transport for Direct Energy Conversion," *Superlattices and Microstructures*, vol. 35, pp. 161–172, 2004.

[114] A. Khitun, J. Liu, and K. Wang, "Thermal Conductivity of Si/Ge Quantum Dot Superlattices," in *Nanotechnology, 2004. 4th IEEE Conference on*, pp. 20–22, 16-19 Aug. 2004.

[115] W. Kim, S. Singer, A. Majumdar, J. Zide, A. Gossard, and A. Shakouri, "Role of Nanostructures in Reducing Thermal Conductivity Below Alloy Limit in Crystalline Solids," in *Thermoelectrics, 2005. ICT 2005. 24th International Conference on*, pp. 9–12, 19-23 June 2005.

[116] D. Li, Y. Wu, R. Fan, P. Yang, and A. Majumdar, "Thermal Conductivity of Si/SiGe Superlattice Nanowires," *Appl.Phys.Lett.*, vol. 83, no. 15, pp. 3186–3188, 2003.

[117] N. Mingo, "Thermoelectric Figure of Merit and Maximum Power Factor in III-V Semiconductor Nanowires," *Appl.Phys.Lett.*, vol. 84, no. 14, pp. 2652–2654, 2004.

[118] J. Zhou, *Thermal and Thermoelectric Transport Measurements of One-Dimensional Nanostructures.* PhD thesis, University of Texas at Austin, 2005.

[119] R. Yang and G. Chen, "Thermal Conductivity Modeling of Periodic Two-Dimensional Nanocomposites," *Physical Review B*, vol. 69, pp. 195316–1–195316–10, 2004.

[120] R. Yang and G. Chen, "Nanostructured Thermoelectric Materials: From Superlattices to Nanocomposites," *Materials Integration*, vol. 18, pp. 1–12, 2006.

[121] Z. Dughaish, "Lead Telluride as a Thermoelectric Material for Thermoelectric Power Generation," *Physica B*, vol. 322, pp. 205–223, 2002.

[122] C. Bhandari and D. Rowe, *CRC Handbook of Thermoelectrics*, ch. Optimization of Carrier Concentration, pp. 43–53. CRC Press, Inc., 1994.

[123] H. Goldsmid, *Applications of Thermoelectricity*. Methuen Monograph, London, 1960.

[124] C. Bhandari and D. Rowe, "The Effect of Phonon-Grain Boundary Scattering, Doping and Alloying on the Lattice Thermal Conductivity of Lead Telluride," *J.Phys.D: Appl.Phys.*, vol. 16, pp. L75–L77, 1983.

[125] C. Bhandari and D. Rowe, "High-Temperature Thermal Transport in Heavily Doped Small-Grain-Size Lead Telluride," *Appl.Phys.A*, vol. 37, pp. 175–178, 1985.

[126] D. Rowe and C. Bhandari, "Lattice Thermal Conductivity of Small Grain Size PbSnTe and PbGeTe Thermoelectric Material," *Appl.Phys.Lett.*, vol. 47, no. 3, pp. 255–257, 1985.

[127] D. Rowe and M. Clee, "Preparation of High-Density Small Grain Size Compacts of Lead Tin Telluride," *Journal of Materials Science: Materials in Electronics*, vol. 1, pp. 129–132, 1990.

[128] K. Kishimoto and T. Koyanagi, "Preparation of Sintered Degenerate N-Type PbTe with a Small Grain Size and its Thermoelectric Properties," *J.Appl.Phys.*, vol. 92, no. 5, pp. 2544–2549, 2002.

[129] C. Bhandari and D. Rowe, "Silicon-Germanium Alloys as High Temperature Thermoelectric Materials," *Contemp. Phys.*, vol. 21, pp. 219–242, 1980.

[130] Z.-Y. Cheng, M. Currie, C. Leitz, G. Taraschi, E. Fitzgerald, J. Hoyt, and D. Antoniadas., "Electron Mobility Enhancement in Strained-Si n-MOSFETs Fabricated on SiGe-On-Insulator (SGOI) Substrates," *IEEE Electron Device Lett.*, vol. 22, pp. 321–323, 2001.

[131] M. Sadaka, A.-Y. Thean, A. Barr, D. Tekleab, S. Kalpat, T. White, T. Nguyen, R. Mora, P. Beckage, D. Jawarani, S. Zollner, M. Kottke, R. Liu, M. Canonico, Q.-H. Xie, X.-D. Wang, S. Parsons, D. Eades, M. Zavala, B.-Y. Nguyen, C. Mazure, and J. Mogab, "Fabrication and Operation of Sub-50 nm Strained-Si on $\mathrm{Si}_{1-x}\mathrm{Ge}_x$ Insulator (SGOI) CMOSFETs," in *SOI Conference, 2004. Proceedings. 2004 IEEE International*, pp. 209–211, 4-7 Oct. 2004.

[132] F. Andrieu, T. Ernst, O. Faynot, O. Rozeau, Y. Bogumilowicz, J. Hartmann, L. Brevard, A. Toffoli, D. Lafond, and B. Ghyselen, "Performance and Physics of Sub-50 nm Strained Si on $\mathrm{Si}_{1-x}\mathrm{Ge}_x$ On Insulator (SGOI) nMOSFETs.," *Solid-State Electron.*, vol. 50, pp. 566–572, 2006.

[133] V. Palankovski, *Simulation of Heterojunction Bipolar Transistors.* Dissertation, Technische Universität Wien, 2000. http://www.iue.tuwien.ac.at/phd/palankovski.

[134] A. Schenk, “Re-Examination of Physical Models in the Temperature Range 300K – 700K,” tech. rep., ETH Zürich, 1999.

[135] C. Vining, “A Model for the High-Temperature Transport Properties of Heavily Doped N-Type Silicon-Germanium Alloys,” *J.Appl.Phys.*, vol. 69, no. 1, pp. 331–341, 1991.

[136] C. Bhandari, *CRC Handbook of Thermoelectrics*, ch. Minimizing the Thermal Conductivity, pp. 55–65. CRC Press, Inc., 1994.

[137] C. Glassbrenner and G. Slack, “Thermal Conductivity of Silicon and Germanium from 3K to the Melting Point,” *Physical Review*, vol. 134, no. 4A, pp. 1058–1069, 1964.

[138] M. Steele and F. Rosi, “Thermal Conductivity and Thermoelectric Power of Germanium-Silicon Alloys,” *J.Appl.Phys.*, vol. 29, no. 11, pp. 1517–1520, 1958.

[139] I. Yonenaga, T. Goto, X. Tang, and S. Yamaguchi, “Thermal and Electrical Properties of Czochralski Grown Germanium-Silicon Alloys,” in *Thermoelectrics, 1999. Proceedings ICT 99. XVIII International Conference on*, 1999.

[140] B. Abeles, D. Beers, G. Cody, and J. Dismukes, “Thermal Conductivity of Ge-Si Alloys at High Temperatures,” *Physical Review*, vol. 125, no. 1, pp. 44–46, 1962.

[141] B. Abeles, “Lattice Thermal Conductivity of Disordered Semiconductor Alloys at High Temperatures,” *Physical Review*, vol. 131, no. 5, pp. 1906–1911, 1963.

[142] H. Meddins and J. Parrott, “The Thermal and Thermoelectric Properties of Sintered Germanium-Silicon Alloys,” *J.Phys.C:Solid State Phys.*, vol. 9, pp. 1263–1276, 1976.

[143] V. Palankovski, G. Röhrer, T. Grasser, S. Smirnov, H. Kosina, and S. Selberherr, “Rigorous Modeling Approach to Numerical Simulation of SiGe HBTs,” *Applied Surface Science*, vol. 224, no. 1–4, pp. 361–364, 2004.

[144] A. Amith, “Seebeck Coefficient in N-Type Germanium-Silicon Alloys: ”Competition Region”,” *Physical Review*, vol. 139, no. 5A, pp. 1624–1627, 1965.

[145] D. Rowe, “Electrical Properties of Hot-Pressed Germanium-Silicon-Boron Alloys,” *J. Phys. D: Appl. Phys.*, vol. 8, pp. 1092–1103, 1975.

[146] M. Brinson and W. Dunstant, “Thermal Conductivity and Thermoelectric Power of Heavily Doped N-Type Silicon,” *J.Phys.C:Solid State Phys.*, vol. 3, no. 3, pp. 483–491, 1970.

[147] K. Hubner and W. Shockley, “Transmitted Phonon Drag Measurements in Silicon,” *Physical Review Letters*, vol. 4, no. 10, pp. 504–505, 1960.

[148] R. Trczinski, E. Gmelin, and H. Queisser, “Quenched Phonon Drag in Silicon Microcontacts,” *Physical Review Letters*, vol. 56, no. 10, pp. 1086–1089, 1986.

[149] L. Weber and E. Gmelin, “Transport Properties of Silicon,” *Appl.Phys.A*, vol. 53, pp. 136–140, 1991.

[150] C. Vining, *CRC Handbook of Thermoelectrics*, ch. Silicon Germanium, pp. 329–337. CRC Press, Inc., 1994.

[151] V. Fano, *CRC Handbook of Thermoelectrics*, ch. Lead Telluride and Its Alloys, pp. 257–266. CRC Press, Inc., 1994.

[152] Z. Ding, S. Huang, D. Marcus, and R. Kaner, "Modification of Bismuth Telluride for Improving Thermoelectric Properties," in *Thermoelectrics, 1999. Eighteenth International Conference on*, pp. 721–724, 29 Aug.-2 Sept. 1999.

[153] W. Kullmann, J. Geurts, W. Richter, N. Lehner, H. Rauh, U. Steigenberger, G. Eichhorn, and R. Geick, "Effect of Hydrostatic and Uniaxial Pressure on Structural Properties and Raman Active Lattice Vibrations in Bi_2Te_3," *Phys.stat.sol.(b)*, vol. 125, pp. 131–138, 1984.

[154] L. Caywood and G. Miller, "Anisotropy of the Constant-Energy Surfaces in N-Type Bi_2Te_3 and Bi_2Se_3 from Galvanomagnetic Coefficients," *Physical Review B*, vol. 2, no. 8, pp. 3209–3220, 1970.

[155] J. Jenkins, J. Rayne, and R. Ure, "Elastic Moduli and Phonon Poperties of Bi_2Te_3," *Physical Review B*, vol. 5, no. 8, pp. 3171–3184, 1972.

[156] J. Barnes, J. Rayne, and R. Ure, "Lattice Expansion of Bi_2Te_3 from 4.2K to 600K," *Phys.Lett.*, vol. 46A, pp. 317–318, 1974.

[157] E. Marchenkov and V. Shipul, "Thermal Expansion of Semionductor Materials," *Journal of Engineering Physics and Thermophysics*, vol. 66, no. 5, pp. 547–551, 1994.

[158] J. Drabble, *Progress in Semiconductors*, vol. 7. John Wiley & Sons, Inc., New York, 1963.

[159] T. Harman, B. Paris, S. Miller, and H. Goering, "Preparation and Some Physical Properties of Bi_2Te_3, Sb_2Te_3, and As_2Te_3," *J. Phys. Chem. Solids*, vol. 2, pp. 181–190, 1957.

[160] R. Sehr and L. Testardi, "The Optical Properties of P-Type $Bi_2Te_3Sb_2Te_3$ Alloys Between 2-15 Microns," *J. Phys. Chem. Solids*, vol. 23, pp. 1219–1224, 1962.

[161] E. Muller, W. Heiliger, P. Reinshaus, and H. Submann, "Determination of the Thermal Band Gap from the Change of the Seebeck-Coefficient at the pn-Transition in $(Bi_{0.5}Sb_{0.5})_2Te_3$," in *Thermoelectrics, 1996., Fifteenth International Conference on*, pp. 412–416, 26-29 March 1996.

[162] R. Togei and G. Miller, *Phys. Semimetals and Narrow Gap Semiconductors.* Pergamon Press, Oxford, 1971.

[163] G. Shoemake, J. Rayne, and R. Ure, "Specific Heat of N- and P-Type Bi_2Te_3 from 1.4 to 90 K," *Physical Review*, vol. 185, no. 3, pp. 1046–1056, 1969.

[164] H. Köhler, "Non-Parabolicity of the Highest Valence Band of Bi_2Te_3 from Shubnikov-de Haas Effect," *Phys.stat.sol.(b)*, vol. 74, pp. 591–600, 1976.

[165] C. Bhandari and V. Agrawal, "Thermal and Electrical Transport in Bismuth Telluride," *Indian Journal of Pure and Applied Physics*, vol. 28, pp. 448–451, 1990.

[166] T. Scheidemantel, C. Ambrosch-Draxl, T. Thonhauser, J. Badding, and J. Sofo, "Transport Coefficients from First-Principles Calculations," *Physical Review B*, vol. 68, pp. 125210–1–125210–6, 2003.

[167] S. Lee and P. von Allmen, "Tight-Binding Modeling of Thermoelectric Properties of Bismuth Telluride," *Appl.Phys.Lett.*, vol. 88, pp. 22107–1–22107–3, 2006.

[168] M. Singh and C. Bhandari, "Thermoelectric Properties of Bismuth Telluride Quantum Wires," *Solid-State Comm.*, vol. 127, pp. 649–654, 2003.

[169] H. Scherrer and S. Scherrer, *CRC Handbook of Thermoelectrics*, ch. Bismulth Telluride, Antimony Telluride, and Their Solid Solutions, pp. 211–237. CRC Press, Inc., 1994.

[170] H. Goldsmid, "The Thermal Conductivity of Bismuth Telluride," *Proc. Phys. Soc. B*, vol. 69, pp. 203–209, 1956.

[171] H. Goldsmid, "Heat Conduction in Bismuth Telluride," *Proc. Phys. Soc.*, vol. 72, pp. 17–26, 1958.

[172] S. Sugihara, S. Tomita, K. Asakawa, and H. Suda, "High Performance Properties of Sintered Bi–Based Thermoelectric Material," in *Thermoelectrics, 1996., Fifteenth International Conference on*, pp. 46–51, 26-29 March 1996.

[173] M. Zhitinskaya, S. Nemov, T. Svechnikova, L. Lukyanova, P. Konstantinov, and V. Kutasov, "Thermal Conductivity of Bi_2Te_3: Sn and the Effect of Codoping by Pb and I Atoms," *Physics of the Solid State*, vol. 45, no. 7, pp. 1251–1253, 2003.

[174] M. Wohlrab, "Die Spezifische Wärme von Bi_2Te_3, CdTe, PbTe und SnTe (Halbleitereigenschaften von Telluriden. VI)," *Ann.Phys.*, vol. 472, pp. 89–90, 1966.

[175] J. Fleurial, L. Gailliard, R. Triboulet, H. Scherrer, and S. Scherrer, "Thermal Properties of High Quality Single Crystals of Bismuth Telluride-Part I: Experimental Characterization," *J. Phys. Chem. Solids*, vol. 49, pp. 1237–1247, 1988.

[176] C. Satterthwaite and R. Ure, "Electrical and Thermal Properties of Bi_2Te_3," *Physical Review*, vol. 108, no. 5, pp. 1164–1170, 1957.

[177] D. Hyun, J. Hwang, T. Oh, J. Shim, and N. Kolomoets, "Electrical Properties of the 85% Bi_2Te_3 - 15% Bi_2Se_3 Thermoelectric Material Doped with SbI_3 And CuBr," *J. Phys. Chem. Solids*, vol. 59, no. 6–7, pp. 1039–1044, 1998.

[178] H.-W. Jeon, H.-P. Ha, D.-B. Hyun, and J.-D. Shim, "Electrical and Thermoelectrical Properties of Undoped Bi_2/Te_3-Sb_2Te_3 and Bi_2Te_3-Sb_2Te_3-Sb_2Se_3 Single Crystals," *J. Phys. Chem. Solids*, vol. 52, no. 4, pp. 579–585, 1991.

[179] V. Kutasov, L. Lukyanova, P. Konstantinov, and G. Alekseeva, "Charge Carrier Mobility in $Bi_2Te_3 - xSe_x$ Solid Solution with Excess of Te," in *Thermoelectrics, 1996., Fifteenth International Conference on*, pp. 42–45, 26-29 March 1996.

[180] O. Yamashita, S. Tomiyoshi, and K. Makita, "Bismuth Telluride Compounds with High Thermoelectric Figures of Merit," *J.Appl.Phys.*, vol. 93, no. 1, pp. 368–374, 2003.

[181] O. Yamashita and S. Tomiyoshi, "High Performance N-Type Bismuth Telluride with Highly Stable Thermoelectric Figure of Merit," *J.Appl.Phys.*, vol. 95, no. 11, pp. 6277–6283, 2004.

[182] D. Kusano and Y. Hori, "Effects of PbTe Doping on the Thermoelectric Properties of $(Bi_2Te_3)_0.2(Sb_2Te_3)_0.8$," in *Thermoelectrics, 2002. Proceedings ICT '02. Twenty-First International Conference on*, pp. 13–16, 25-29 Aug. 2002.

[183] V. Kuznetsov, L. Kuznetsova, A. Kaliazin, and D. Rowe, "High Performance Functionally Graded and Segmented Bi_2Te_3-Based Materials for Thermoelectric Power Generation," *J. Mat. Sci.*, vol. 37, pp. 2893–2897, 2002.

[184] J. Dennis, "Anisotropy of Thermoelectric Power in Bismuth Telluride," Tech. Rep. 377, Massachusetts Institute of Technology, January 1961.

[185] H. Goldsmid, "Recent Studies of Bismuth Telluride and its Alloys," *J.Appl.Phys.*, vol. 32, no. 10, pp. 2198–2002, 1961.

[186] L. Ainsworth, "Single Crystal Bismuth Telluride," *Proc. Phys. Soc. B*, vol. 69, pp. 606–612, 1956.

[187] P. M. Nikolic, *Some Optical Properties of Lead-Tin-Chalcogenide Alloys.* No. 355, Universiteta u Beogradu, 1971.

[188] G. Nimtz and B. Schlicht, *Narrow-Gap Lead Salts.* Springer, Berlin, 1983.

[189] J. Steininger, "Thermodynamics and Calculation of the Liquidus-Solidus Gap in Homogenous, Monotonic Alloy Systems," *J.Appl.Phys.*, vol. 41, no. 6, pp. 2713–2724, 1970.

[190] A. Mariano and K. Chopra, "Polymorphism in Some IV-VI Compounds Induced by High Pressure and Thin-Film Epitaxial Growth," *Appl.Phys.Lett.*, vol. 10, no. 10, pp. 282–284, 1967.

[191] O. Madelung, *Semiconductors: Data Handbook.* Springer, 2004.

[192] S. Novikova and N. Abrikosov, "Investigation of the Thermal Expansion of Lead Chalcogenides," *Soviet Phys. Solid State*, vol. 5, no. 7, pp. 1397–1398, 1964.

[193] B. Houston, R. Strakna, and H. Belson, "Elastic Constants, Thermal Expansion, and Debye Temperature of Lead Telluride," *J.Appl.Phys.*, vol. 39, no. 8, pp. 3913–3916, 1968.

[194] R. Dalven, "A Review of the Semiconductor Properties of PbTe, PbSe, PbS, and PbO," *Infrared Physics*, vol. 9, pp. 141–184, 1969.

[195] T. Seddon, S. Gupta, and G. Saunders, "Hole Contribution to the Elastic Constants of SnTe," *Solid-State Comm.*, vol. 20, pp. 69–72, 1976.

[196] A. Miller, G. Saunders, and Y. Yogurtcu, "Pressure Dependences of the Elastic Constants of PbTe, SnTe, and $Ge_{0.08}Sn_{0.92}Te$," *J.Phys.C:Solid State Phys.*, vol. 14, pp. 1569–1584, 1981.

[197] T. Harman and I. Melngailis, "Narrow-Gap Semiconductors," *Appl. Solid State Science*, vol. 4, p. 1, 1974.

[198] S. Nishi, H. Kawamura, and K. Murase, “Study of Lattice Instability by mm-Wave Magnetoplasma Reflection in PbTe-SnTe Compound Semiconductors,” *Phys.stat.sol.(b)*, vol. 97, pp. 581–590, 1980.

[199] T. Ichiguchi and K. Murase, “Study of Electron and Lattice Properties in (Pb,Sn,Ge)Te by Intra-Band Magneto-Optics,” in *Proc. Oji Int. Seminar, Hakone, Japan; Solid State Sci.*, pp. 249–252, 1981.

[200] W. Tennant, “Index Matching Far-Infrared Method for Measuring the Static Dielectric Constant of PbTe,” *Solid-State Comm.*, vol. 20, pp. 613–616, 1976.

[201] Z. Dashevsky, V. Kasiyan, E. Mogilko, A.Butenko, R. Kahatabi, S. Genikov, V.Sandomirsky, and Y.Schlesinger, *High-Temperature PbTe Diodes.* online available at arXiv.org, 2007.

[202] B. Akimov, A. Dmitriev, D. Khokhlov, and L. Ryabova, “Carrier Transport and Non-Equilibrium Phenomena in Doped PbTe and Related Materials,” *Phys.stat.sol.(a)*, vol. 137, no. 9, pp. 9–55, 1993.

[203] J. Lowney and S. Senturia, “Optical Dielectric Constant of $\mathrm{Pb}_{1-x}\mathrm{Sn}_x\mathrm{Te}$ in the Narrow-Gap Region,” *J.Appl.Phys.*, vol. 47, p. 1773, 1976.

[204] H. Kosina, T. Grasser, G. Karlowatz, C. Kopf, M. Nedjalkov, S. Selberherr, S. Smirnov, E. Ungersboeck, L. Wang, and W. Wessner, *VMC 2.0 User’s Guide.* Institute for Microelectronics, TU Wien, 2002.

[205] W. Mason, *Physical Acoustics and the Properties of Solids.* Princeton, N.J.: D. Van Nostrand Co., Inc., 1958.

[206] M. Lach-Hab, D. Papaconstantopoulos, and M. Mehl, “Electronic Structure Calculations of Lead Chalcogenides PbS, PbSe, PbTe,” *J. of Phys. and Chem.*, vol. 63, pp. 833–841, 2002.

[207] W. Cochran, R. Cowley, G. Dolling, and M. Elcombe, “The Crystal Dynamics of Lead Telluride,” *Proc. Roy. Soc.*, vol. 293, pp. 433–451, 1966.

[208] B. Ridley, *Quantum Processes in Semiconductors.* Oxford University Press, 3rd ed., 1993.

[209] V. Palankovski and R. Quay, *Analysis and Simulation of Heterostructure Devices.* Springer, Wien–New York, 2004.

[210] D. Parkinson and J. Quarrington, “The Molar Heats of Lead Sulphide, Selenide, and Telluride in the Temperature Range 20K to 260K,” *Proc. Phys. Soc.*, vol. 67, no. 7A, pp. 569–579, 1954.

[211] A. Pashinkin, V. Zlomanov, and A. Malkova, “On the Heat Capacity of Lead Selenide and Telluride,” *Inorganic Materials*, vol. 30, no. 9, pp. 1118–1120, 1994.

[212] E. Rogacheva, N. Sinelnik, and I. Krivulkin, “Concentration Anomaly of Heat Capacity in PbTe Based Solid Solutions,” *Semiconductor Phys., Quantum Electronics and Optoelectronics*, vol. 5, no. 4, pp. 368–372, 2002.

[213] I. Hatta and K. Kobayashi, "A Mean-Field Behavior of the Specific Heat at the Phase Transition of SnTe with a Low Carrier Concentration," *Solid-State Comm.*, vol. 22, no. 12, pp. 775–777, 1977.

[214] A. Pashinkin, A. Malkova, and M. Mikhailova, "Standard Enthalpy and Heat Capacity of Solid Tin Telluride," *Russian J. Physical Chemistry*, vol. 80, no. 8, pp. 1342–1343, 2006.

[215] D. Cahill, "Thermal Conductivity Measurement From 30 to 750K: The 3ω Method," *Rev. Sci. Instrum.*, vol. 61, no. 2, pp. 802–806, 1990.

[216] A. El-Sharkawy, A. A. El-Azm, M. Kenawy, A. Hillal, and H. Abu-Basha, "Thermophysical Properties of Polycristalline PbS, PbSe, and PbTe in the Temperature Range 300 - 700K," *Int. J. Thermophys.*, vol. 4, no. 3, pp. 261–269, 1983.

[217] Y. Gelbstein, Z. Dashevsky, and M. Dariel, "Design, Synthesis and Characterization of Graded N-Type PbTe," in *Thermoelectrics, 2002. Proceedings ICT '02. Twenty-First International Conference on*, pp. 9–12, 25-29 Aug. 2002.

[218] P. Zhu, Y. Imai, Y. Isoda, Y. Shinohara, X. Jia, and G. Zou, "Enhanced Thermoelectric Properties of PbTe Alloyed with Sb_2Te_3," *J.Phys.:Condensed Matter*, vol. 17, pp. 7319–7326, 2005.

[219] T. Su, P. Zhu, H. Ma, G. Ren, L. Chen, W. Guo, Y. Iami, and X. Jia, "Electrical Transport and High Thermoelectric Properties of PbTe Doped with Bi2Te3 Prepared by HPHT," *Solid-State Comm.*, vol. 138, pp. 580–584, 2006.

[220] M. Orihashi, Y. Noda, L. Chen, and T. Hirai, "Effect of Composition on the Electrical Properties and Thermal Conductivity of $Pb_{1-x}Sn_xTe$," *J. Japan Inst. Metals, Special Issue on Thermoelectric Energy Conversion Materials*, vol. 63, no. 11, pp. 1423–1428, 1999.

[221] Y. Gelbstein, Z. Dashevsky, and M. Dariel, "Powder Metallurgical Processing of Functionally Graded P-$Pb_{1-x}Sn_xTe$ Materials for Thermoelectric Applications," *Physica B*, vol. 391, pp. 256–265, 2007.

[222] G. Alekseeva, B. Efimova, and Y. Logachev, "Thermal Conductivity (80-300K) of Pseudobinary Solid Solutions Based on N-Type PbTe," *Sov. Phys. Semicond.*, vol. 9, no. 1, pp. 83–84, 1975.

[223] T. Chonan and S. Katayama, "Molecular-Dynamics Simulation of Lattice Thermal Conductivity in $Pb_{1-x}Sn_xTe$ and $Pb_{1-x}Ge_xTe$ at High Temperature," *Journal of the Physical Society of Japan*, vol. 75, no. 6, pp. 64601–1–64601–8, 2006.

[224] D. Damon, "Thermal Conductivity of SnTe Between 100K and 500K," *J.Appl.Phys.*, vol. 37, no. 8, pp. 3181–3190, 1966.

[225] J. Parrott, "The Thermal Conductivity of Sintered Semiconductor Alloys," *J.Phys.C:Solid State Phys.*, vol. 2, pp. 147–151, 1969.

[226] P. Zhu, L. Chen, X. Jia, H. Ma, G. Ren, W. Guo, W. Zhang, and G. Zou, "Thermoelectric Properties of PbTe Prepared at High Pressure and High Temperature," *J.Phys.:Condensed Matter*, vol. 14, pp. 11185–11188, 2002.

[227] P. Zhu, X. Jia, H. Chen, W. Guo, L. Chen, D. Li, H. Ma, G. Ren, and G. Zou, “A New Method of Synthesis for Thermoelectric Materials: HPHT,” *Solid-State Comm.*, vol. 123, pp. 43–47, 2002.

[228] Y. Gelbstein, Z. Dashevsky, and M. Dariel, “Transport Properties of PbI_2-Doped PbTe,” in *Thermoelectrics, 2002. Proceedings ICT ’02. Twenty-First International Conference on*, pp. 5–8, 25-29 Aug. 2002.

[229] W. Scanlon, “Precipitation of Te and Pb in PbTe Crystals,” *Physical Review*, vol. 126, no. 2, pp. 509–513, 1962.

[230] L. Rogers, “The Hall Mobility and Thermoelectric Power of P-Type Lead Telluride,” *Brit. J. Appl. Phys.*, vol. 18, pp. 1227–1235, 1967.

[231] M. Fedorov, E. Gurieva, P. Konstantinov, L. Prokofeva, and Y. Ravich, “Thermoelectrical Figure of Merit in PbTe-Based Solid Solutions with Phonon Scattering by Off-Center Impurities,” in *Thermoelectrics, 2003 Twenty-Second International Conference on - ICT*, pp. 271–274, 17-21 Aug. 2003.

[232] Y. Ravich, B. Efimova, and I. Smirnov, *Semiconducting Lead Chalcogenides.* Plenum Press New York, London, 1970.

[233] R. Allgaier, “Valence Bands in Lead Telluride,” *J.Appl.Phys.*, vol. 32, no. 10, pp. 2185–2189, 1961.

[234] A. Andreev, “The Band Edge Structure of the IV-VI Semiconductors,” *J. de Physique*, vol. 4, no. 11, pp. 50–61, 1968.

[235] M. Cardona and D. Greenaway, “Optical Properties and Band Structure of Group IV-VI and Group V Materials,” *Physical Review*, vol. 133, no. 6A, pp. 1685–1697, 1964.

[236] T. Globus, B. Gelmont, K. Geiman, V. Kondrashov, and A. Matveenko, “Optical Absorption and Band Structure PbTe,” *Sov. Phys. JETP*, vol. 53, no. 5, pp. 1000–1007, 1981.

[237] D. Mitchell, F. Palik, and J. Zemel, “Magneto-Optical Band Studies of Epitaxial PbS, PbSe, and PbTe,” in *Proc. Int. Conf. Phys. Semicond. Paris*, pp. 325–333, 1964.

[238] H. Burkhard, G. Bauer, and W. Zawadzki, “Band-Population Effects and Intraband Magneto-Optical Properties of a Many-Valley Semiconductor: PbTe,” *Physical Review B*, vol. 19, no. 10, pp. 5149–5159, 1979.

[239] C. Hewes, M. Adler, and S. Senturia, “Nuclear-Magnetic-Resonance Studies in PbTe and $Pb_{1-x}Sn_xTe$: An Experimental Determination of $k \cdot p$ Band Parameters and Magnetic Hyperfine Constants,” *Physical Review B*, vol. 7, no. 12, pp. 5195–5212, 1973.

[240] J. Dimmock, “$k \cdot p$ Theory for the Conduction and Valence Bands of $Pb_{1-x}Sn_x/Te$ and $Pb_{1-x}Sn_xSe$ Alloys,” in *Phys. Semimetals Narrow Gap Semicond.*, pp. 319–330, 1971.

[241] J. Conklin, L. Johnson, and j. G.W. Pratt, “Energy Bands in PbTe,” *Physical Review*, vol. 137, no. 4A, pp. 1282–1294, 1965.

[242] F. Herman, R. Kortum, I. Ortenburger, and J. VanDyke, “Relativistic Band Structure of GeTe, SnTe, PbTe, PbSe, and PbS,” *J. de Physique*, vol. 4, no. 11, pp. 62–77, 1968.

[243] L. Johnson, J. Conklin, and j. G.W. Pratt, “Relativistic Effects in the Band Structure of PbTe,” *Physical Review Letters*, vol. 11, no. 12, pp. 538–540, 1963.

[244] P. Lin and L. Kleinman, “Energy Bands of PbTe, PbSe, and PbS,” *Physical Review*, vol. 142, no. 2, pp. 478–489, 1966.

[245] Y. Tung and M. Cohen, “Relativistic Band Structure and Electronic Properties of SnTe, GeTe, and PbTe,” *Physical Review*, vol. 180, no. 3, pp. 823–826, 1969.

[246] S. Kohn, P. Yu, Y. Petroff, Y. Shen, Y. Tsang, and M. Cohen, “Electronic Band Structure and Optical Properties of PbTe , PbSe, and PbS,” *Physical Review B*, vol. 8, no. 4, pp. 1477–1488, 1973.

[247] Y. Tsang and M. Cohen, “Pseudopotential Study of Bonding in the Zinc-Blende and Rocksalt Structures,” *Physical Review B*, vol. 9, no. 8, pp. 3541–3547, 1974.

[248] G. Martinez, M. Schlüter, and M. Cohen, “Electronic Structure of PbSe and PbTe: I. Band Structures, Densities of States, and Effective Masses,” *Physical Review B*, vol. 11, no. 2, pp. 651–659, 1975.

[249] C. Keffer, T. Hayes, and A. Bienenstock, “PbTe Debye-Waller Factors and Band-Gap Temperature Dependence,” *Physical Review Letters*, vol. 21, no. 25, pp. 1676–1678, 1968.

[250] C. Keffer, T. Hayes, and A. Bienenstock, “Debye-Waller Factors and the PbTe Band-Gap Temperature Dependence,” *Physical Review B*, vol. 2, no. 6, pp. 1966–1976, 1970.

[251] Y. Tsang and M. Cohen, “Calculation of the Temperature Dependence of the Energy Gaps in PbTe and SnTe,” *Physical Review B*, vol. 3, no. 4, pp. 1254–1261, 1971.

[252] H. Heinrich, K. Lischka, and H. Sitter, “Experimental Determination of Symmetry of Second Valence Band Maxima in PbTe,” *Physical Review Letters*, vol. 35, no. 16, pp. 1107–1110, 1975.

[253] H. Sitter, K. Lischka, and H. Heinrich, “Structure of the Second Valence Band in PbTe,” *Physical Review B*, vol. 16, no. 2, pp. 680–687, 1977.

[254] J. Dimmock, I. Melngailis, and A. Strauss, “Band Structure and Laser Action in $\mathrm{Pb}_x\mathrm{Sn}_{1-x}\mathrm{Te}$,” *Physical Review Letters*, vol. 16, pp. 1193–1196, 1966.

[255] J. Dixon and R. Bis, “Band Inversion and the Electrical Properties of $\mathrm{Pb}_x\mathrm{Sn}_{1-x}\mathrm{Te}$,” *Physical Review*, vol. 176, no. 3, pp. 942–949, 1968.

[256] S. Ferreira, E. Abramof, P. Motisuke, P. Rappl, H. Closs, A. Ueta, C. Boschetti, and I. Bandeira, “Band Crossing Evidence in PbSnTe Observed by Optical Transmission Measurements,” *Brazilian J. Phys.*, vol. 29, no. 4, pp. 771–774, 1999.

[257] S. Takaoka, S. Shimomura, H. Takahashi, and K. Murase, “Band-Edge Structure of Indium-Doped $\mathrm{Pb}_{1-x}\mathrm{Sn}_x\mathrm{Te}$ Across the Band-Inversion Region Investigated by the Far-Infrared Magnetoplasma Method,” *Physical Review B*, vol. 40, pp. 5642–5648, 1989.

[258] R. Allgaier and j. B.B. Houston, "Hall Coefficient Behavior and the Second Valence Band in Lead Telluride," *J.Appl.Phys.*, vol. 37, no. 1, pp. 302–309, 1966.

[259] P. Dziawa, B. Taliashvili, W. Domuchowski, L. Kowalczyk, E. Lusakowska, A. Mycielski, V. Osinniy, and T. Story, "Structural and Optical Characterization of Epitaxial Layers of CdTe/PbTe Grown on BaF2 (111) Substrates," *Phys.stat.sol.(c)*, vol. 2, no. 3, pp. 1167–1171, 2005.

[260] H. Preier, "Recent Advances in Lead-Chalcogenide Lasers," *Appl. Phys.*, vol. 20, pp. 189–206, 1979.

[261] J. Zemel, J. Jensen, and R. Schoolar, "Electrical and Optical Properties of Epitaxial Films of PbS, PbSe, PbTe, and SnTe," *Physical Review*, vol. 140, no. 1A, pp. A330–A343, 1965.

[262] Y. Varshni, "Temperature Dependence of the Energy Gap in Semiconductors," *Physica*, vol. 34, no. 1, pp. 149–154, 1967.

[263] G. Appold, R. Grisar, G. Bauer, H. Burkhard, R. Ebert, H. Pascher, and H. Haefele, "Inter- and Intraband Magnetooptical Transitions in $\mathrm{Pb}_{1-x}\mathrm{Sn}_x\mathrm{Te}$," in *Inst. Phys. Conf. Ser.*, no. 43, 1979.

[264] I. Melngailis and A. Calawa, "Photovoltaic Effect in $\mathrm{Pb}_x\mathrm{Sn}_{1-x}\mathrm{Te}$ Diodes," *Appl.Phys.Lett.*, vol. 9, pp. 304–306, 1966.

[265] R. Tauber and I. Cadoff, "Thermal and Optical Energy Gaps in $\mathrm{Pb}_{0.93}\mathrm{Sn}_{0.07}\mathrm{Te}$ and $\mathrm{Pb}_{0.85}\mathrm{Sn}_{0.15}\mathrm{Te}$," *J.Appl.Phys.*, vol. 38, no. 9, pp. 3714–3720, 1967.

[266] P. Stiles, E. Burstein, and D. Langenberg, "De Haas-Van Alphen Effect in P-Type PbTe and N-Type PbS," *J.Appl.Phys.*, vol. 32, no. 10, pp. 2174–2178, 1961.

[267] K. Cuff, M. Ellett, and C. Kuglin, "Oscillatory Magnetoresistance in the Conduction Band of PbTe," *J.Appl.Phys.*, vol. 32, no. 10, pp. 2179–2185, 1961.

[268] T. Grasser, S. Selberherr, T. Ayalew, T. Binder, J. Cervenka, K. Dragosits, R. Entner, A. Gehring, M. Gritsch, R. Klima, M. Knaipp, H. Kosina, R. Mlekus, V. Palankovski, R. Rodriguez-Torres, M. Rottinger, G. Schrom, P. Schwaha, M. Stockinger, and S. Wagner, *Minimos-NT 2.1 User's Guide.* Institute for Microelectronics, TU Wien, 2002.

[269] S. M. Sze, *Semiconductor Devices: Physics and Technology.* John Wiley and Sons, Inc., 2nd edition ed., 2002.

[270] R. Allgaier and W. Scanlon, "Mobility of Electrons and Holes in PbS, PbSe, and PbTe Between Room Temperature and 4.2K," *Physical Review*, vol. 111, no. 4, pp. 1029–1037, 1958.

[271] V. Palankovski, M. Wagner, and W. Heiss, "Monte Carlo Simulation of Electron Transport in PbTe," in *Proceedings of the 13th International Conference on Narrow Gap Semiconductors*, 2007.

[272] D. Chattopadhyay and N. Purkait, "Electron Drift Velocity in Lead Telluride at High Electric Fields," *J.Appl.Phys.*, vol. 54, no. 11, pp. 6439–6442, 1983.

[273] D. Chattopadhyay, H. Aichmann, and G. Nimtz, "Negative Differential Mobility in PbTe and PbSnTe at High Electric Fields," *Solid-State Comm.*, vol. 51, no. 3, pp. 151–153, 1984.

[274] A. Krotkus, T. Lideikis, A. Plytnikas, and I. Simkiene, "Hot Electron Conduction of PbTe and $Pb_{1-x}Sn_xTe$," *Solid-State Electron.*, vol. 26, no. 6, pp. 605–609, 1983.

[275] V. Palankovski, M. Wagner, and W. Heiss, *Springer Proceedings in Physics Series*, ch. Monte Carlo Simulation of Electron Transport in PbTe. Springer, 2008. in press.

[276] D. Caughey and R. Thomas, "Carrier Mobilities in Silicon Empirically Related to Doping and Field," *Proc.IEEE*, vol. 52, pp. 2192–2193, 1967.

[277] A. Crocker and L. Rogers, "Interpretation of the Hall Coefficient, Electrical Resistivity, and Seebeck Coefficient of P-type Lead Telluride," *Brit. J. Appl. Phys.*, vol. 18, pp. 563–573, 1967.

[278] C. Hogarth, "Transistor Action in Lead Telluride," *Proc. Phys. Soc. B*, vol. 65, pp. 958–963, 1952.

[279] H. Lyden, "Temperature Dependence of the Effective Masses in PbTe," *Physical Review*, vol. 135, no. 2A, pp. 514–521, 1964.

[280] P. M. Nikolic, K. Radulovica, S. Vujatovica, D. Vasiljevic-Radovica, S. Durica, V. Blagojevica, P. Mihajlovica, D. Urosevica, Z. Dohcevic-Mitrovicb, and O. Jaksic, "Far Infrared and Transport Properties of Single Crystal PbTe Samples Doped with Ce," *Journal of Optoelectronics and Advanced Materials*, vol. 2, no. 5, pp. 465–468, 2000.

[281] E. Rogacheva and I. Krivulkin, "The Temperature and Concentration Dependences of the Charge Carrier Mobility in PbTeMnTe Solid Solutions," *Semiconductors*, vol. 36, no. 9, pp. 1040–1044, 2002.

[282] D. Cammack, A. Nurmikko, j. G.W. Pratt, and J. Lowney, "Enhanced Interband Recombination in $Pb_{1-x}Sn_xTe$," *J.Appl.Phys.*, vol. 46, no. 9, pp. 3965–3968, 1975.

[283] R. Rosman and A. Katzir, "Lifetime Calculations for Auger Recombination in Lead-Tin-Telluride," *Quantum Electronics, IEEE Journal of*, vol. 18, pp. 814–817, May 1982.

[284] E. Heyen, M. Hagerott, A. Normikko, and D. Partin, "Radiative Recombination in PbTe Quantum Wells," *Appl.Phys.Lett.*, vol. 54, no. 7, pp. 653–655, 1989.

[285] M. Baleva, E. Mateeva, M. Petrauskas, R. Tomasiunas, and R. Masteika, "The Energy Profile of Polymorphous PbTe films: II. Recombination in Heterophase PbTe Films at High Levels of Optical Excitation," *J.Phys.:Condensed Matter*, vol. 4, pp. 9009–9014, 1992.

[286] B. Akimov, V. Bogoyavlenskii, V. Vasilkov, L. Ryabova, and D. Khokhlov, "Recombination at Mixed-Valence Impurity Centers in PbTe(Ga) Epitaxial Layers," in *Proceedings of the Conference Nanophotonics 2004*, 2004.

[287] K. Lischka, "Bound Defect States in IV-VI Semiconductors," *Appl.Phys.A*, vol. 29, pp. 177–189, 1982.

[288] G. Span, *Epitaktische Herstellung und Quantentransportuntersuchungen von PbTe-nipi-Strukturen.* PhD thesis, Montanuniversität Leoben, 1996.

[289] W. Shockley and W. Read, "Statistics of the Recombinations of Holes and Electrons," *Physical Review*, vol. 87, no. 5, pp. 835–842, 1952.

[290] K. Herrmann, "Recombination in Small-Gap $Pb_{1-x}Sn_xTe$," *Solid-State Electron.*, vol. 21, pp. 1487–1491, 1978.

[291] G. Garlick, "Recombination Emission in Inorganic Solids," *Reports on Progress in Physics*, vol. 30, no. 2, pp. 491–560, 1967.

[292] I. Mackintosh, "Photon-Radiative Recombination in PbSe, PbTe and PbS," *Proc. Phys. Soc. B*, vol. 69, pp. 115–118, 1956.

[293] J. Vaitkus, M. Petrauskas, R. Tomascaroniumacrnas, and R. Masteika, "Photoconductivity of Highly Excited $A^{IV}B^{VI}$ Thin Films," *Appl.Phys.A*, vol. 54, no. 6, pp. 553–555, 1992.

[294] P. Findlay, C. Pidgeon, R. Kotitschke, A. Hollingworth, B. Murdin, C. Langerak, A. van der Meer, C. Ciesla, J. Oswald, A. Homer, G. Springholz, and G. Bauer, "Auger Recombination Dynamics of Lead Salts under Picosecond Free-Electron-Laser Excitation," *Physical Review B*, vol. 58, no. 19, pp. 12908–12915, 1998.

[295] T. Grasser, *Mixed-Mode Device Simulation.* PhD thesis, Technische Universität Wien, 1999. http://www.iue.tuwien.ac.at/phd/grasser.

[296] H. Ebel, *Thermodynamik.* TU Wien, 6 ed., 2000.

[297] Y. Shinohara, Y. Imai, Y. Isoda, I. Nishida, H. Kaibe, and I. Shiota, "Thermoelectric Properties of Segmented Pb-Te Systems with Graded Carrier Concentrations," in *Thermoelectrics, 1997. Proceedings ICT '97. XVI International Conference on*, pp. 386–389, 26-29 Aug. 1997.

[298] E. Müller, C. Drasar, J. Schilz, and W. Kaysser, "Functionally Graded Materials for Sensor and Energy Applications," *Materials Science and Engineering A*, vol. 362, pp. 17–39, 2003.

[299] G. Span, *Austrian Patent AT 410 492 B.* International Patent Application PCT/AT01/00123, Granted in USA, Russia, Europe.

[300] F. Richou, G. Pelous, and D. Lecrosnier, "Thermal Generation of Carriers in Gold-Doped Silicon," *J.Appl.Phys.*, vol. 51, no. 12, pp. 6252–6257, 1980.

Own Publications

[1] V. Palankovski, M. Wagner, and W. Heiss, *Springer Proceedings in Physics Series*, ch. Monte Carlo Simulation of Electron Transport in PbTe. Springer, 2008. in press.

[2] G. Span, M. Wagner, T. Grasser, and L. Holmgren, “Miniaturized TEG with Thermal Generation of Free Carriers,” *Phys.stat.sol.(rrl)*, vol. 6, pp. 241–243, 2007.

[3] M. Wagner, M. Karner, J. Cervenka, M. Vasicek, H. Kosina, S. Holzer, and T. Grasser, “Quantum Correction for DG MOSFETs,” *J.Comput.Electronics*, vol. 5, pp. 397–400, 2007.

[4] T. Grasser, M. Wagner, and M. Vasicek, “Higher–Order Moment Models for Engineering Applications,” in *Equidiff, Wien*, 2007.

[5] V. Palankovski, M. Wagner, and W. Heiss, “Monte Carlo Simulation of Electron Transport in PbTe,” in *Proceedings of the 13th International Conference on Narrow Gap Semiconductors*, p. 48, 2007.

[6] M. Karner, A. Gehring, S. Holzer, M. Pourfath, M. Wagner, W. Gös, M. Vasicek, O. Baumgartner, C. Kernstock, K. Schnass, G. Zeiler, T. Grasser, H. Kosina, and S. Selberherr, “A Multi-Purpose Schrödinger-Poisson Solver for TCAD Applications,” *J.Comput.Electronics*, vol. 6, pp. 179–182, 2007.

[7] M. Wagner, G. Span, S. Holzer, and T. Grasser, “Thermoelectric Power Generation Using Large-Area Si/SiGe pn-Junctions with Varying Ge Content,” *Semicond.Sci.Technol.*, vol. 22, pp. 173–176, 2007.

[8] M. Vasicek, J. Cervenka, M. Karner, M. Wagner, and T. Grasser, “Parameter Modeling for Higher-Order Transport Models in UTB SOI MOSFETs,” in *12th International Workshop on Computational Electronics Book of Abstracts*, pp. 96–97, 2007.

[9] M. Vasicek, M. Karner, E. Ungersboeck, M. Wagner, H. Kosina, and T. Grasser, “Modeling of Macroscopic Transport Parameters in Inversion Layers,” in *International Conference on Simulation of Semiconductor Processes and Devices 2007*, pp. 201–204, 2007.

[10] M. Wagner, G. Span, S. Holzer, and T. Grasser, “Design Optimization of Large Area Si/SiGe Thermoelectric Generators,” in *International Conference on Simulation of Semiconductor Processes and Devices 2006*, pp. 397–400, 2006.

[11] M. Wagner, T. Grasser, M. Karner, and H. Kosina, “Quantum Correction for DG MOSFETs,” in *11th International Workshop on Computational Electronics Book of Abstracts*, pp. 87–88, 2006.

[12] M. Karner, A. Gehring, S. Holzer, M. Pourfath, M. Wagner, H. Kosina, T. Grasser, and S. Selberherr, “VSP-A Multi-Purpose Schrdinger-Poisson Solver for TCAD Applications,” in *11th International Workshop on Computational Electronics Book of Abstracts*, pp. 255–256, 2006.

[13] S. Holzer, M. Wagner, L. Friembichler, E. Langer, T. Grasser, and S. Selberherr, “A Multi-Purpose Optimization Framework for TCAD Applications,” in *ICCAM 2006 Abstracts of Talks*, p. 76, 2006.

[14] S. Holzer, M. Wagner, A. Sheikholeslami, M. Karner, G. Span, T. Grasser, and S. Selberherr, “An Extendable Multi-Purpose Simulation and Optimization Framework for Thermal Problems in TCAD Applications,” in *Collection of Papers Presented at the 12th International Workshop on Thermal Investigation of ICs and Systems*, pp. 239–244, 2006.

[15] G. Span, M. Wagner, S. Holzer, and T. Grasser, “Thermoelectric Power Conversion using Generation of Electron-Hole Pairs in Large Area p-n Junctions,” in *International Conference on Thermoelectrics*, pp. 23–28, 2006.

[16] M. Wagner, G. Span, and T. Grasser, “Thermoelectric Power Generation Using Large Area Si/SiGe pn-Junctions With Varying Ge-Content,” in *2006 International SiGe Technology and Device Meeting Conference Digest*, pp. 216–217, 2006.

[17] M. Karner, A. Gehring, S. Holzer, M. Wagner, and H. Kosina, “Continuum Versus Quasi-Bound State Tunneling in Novel Device Architectures,” in *Abstracts IEEE 2006 Silicon Nanoelectronics Workshop*, pp. 161–162, 2006.

[18] M. Karner, A. Gehring, M. Wagner, R. Entner, S. Holzer, W. Gös, M. Vasicek, T. Grasser, H. Kosina, and S. Selberherr, “VSP-A Gate Stack Analyzer,” in *WODIM 2006 14th Workshop on Dielectrics in Microelectronics Workshop Programme and Abstracts*, pp. 101–102, 2006.

[19] M. Wagner, G. Span, S. Holzer, V. Palankovski, O. Triebl, and T. Grasser, *SiGe and Ge: Materials, Processing, and Devices*, vol. 3, ch. Power Output Improvement of SiGe Thermoelectric Generators, pp. 1151–1162. The Electrochemical Society; ECS Transactions, 2006.

[20] M. Karner, S. Holzer, W. Gös, M. Vasicek, M. Wagner, H. Kosina, and S. Selberherr, *Physics and Technology of High-k Gate Dielectrics 4*, vol. 3, ch. Numerical Analysis of Gate Stacks, pp. 299–308. The Electrochemical Society; ECS Transactions, 2006.

[21] M. Wagner, G. Span, S. Holzer, O. Triebl, and T. Grasser, “Power Output Improvement of SiGe Thermoelectric Generators,” in *Meeting Abstracts 2006 Joint International Meeting*, p. 1516, Meeting Abstracts 2006 Joint International Meeting, 2006.

[22] M. Karner, S. Holzer, M. Vasicek, W. Gös, M. Wagner, H. Kosina, and S. Selberherr, “Numerical Analysis of Gate Stacks,” in *Meeting Abstracts 2006 Joint International Meeting*, p. 1119, Meeting of the Electrochemical Society (ECS), Cancun, 2006.

[23] M. Karner, M. Wagner, T. Grasser, and H. Kosina, "A Physically Based Quantum Correction Model for DG MOSFETs," in *San Francisco 2006 MRS Meeting Abstracts*, pp. 104–105, 2006.

[24] M. Wagner, M. Karner, and T. Grasser, "Quantum Correction Models for Modern Semiconductor Devices," in *Proceedings of the XIII International Workshop on Semiconductor Devices*, pp. 458–461, 2005.

[25] G. Span, M. Wagner, and T. Grasser, "Thermoelectric Power Generation Using Large Area pn-Junctions," in *The 3rd European Conference on Thermoelectrics Proceedings ECT2005*, pp. 72–75, 2005.

	Author	Co-Author	Total
Journals	2	2	4
Book contributions	1	2	3
Conferences	5	13	18
Total	8	17	25

Table 1: Publication Statistics.

Curriculum Vitae

July 9th, 1979
Born in Vienna, Austria.

June 1998
High school graduation (*Matura*) at the HTBLuVA Mödling, specializing in Energy Engineering and Power Electronics (with honors).

June 1998
Received award *Ehrenring* for extraordinarily successful studies.

September 1998 – December 1998
Held a position as a project engineer at Siemens AG Austria.

January 1999 – September 1999
Compulsory military service, FlFMB Langenlebarn.

October 1999
Enrolled in Electrical Engineering at Vienna University of Technology, Austria.

November 2002
Received award *Leistungsstipendium* for extraordinarily fast and successful studies.

April 2004
Received degree of *Diplom-Ingenieur* (M.Sc.) in Electrical Engineering, specializing in Computer Technology from the Vienna University of Technology (with honors).

May 2004 – August 2004
Trekking tour in the Indian Himalayas.

September 2004
Entered doctoral program at the Institute for Microelectronics, Vienna University of Technology, under the supervision of Prof. *Tibor Grasser*.

June 16th, 2007
Birth of son Jakob.